Lappeenranta
University of Technology

Mariia Polikarpova

LIQUID COOLING SOLUTIONS FOR ROTATING PERMANENT MAGNET SYNCHRONOUS MACHINES

Thesis for the degree of Doctor of Science (Technology) to be presented with due permission for public examination and criticism in the Auditorium 1382 at Lappeenranta University of Technology, Lappeenranta, Finland on the 21st of November, 2014, at noon.

Acta Universitatis
Lappeenrantaensis 597

Supervisor Professor Juha Pyrhönen
Department of Energy Technology
LUT School of Technology
Lappeenranta University of Technology
Finland

Doctor Pia Lindh
Department of Energy Technology
LUT School of Technology
Lappeenranta University of Technology
Finland

Reviewers Associate Professor Juliette Soulard
Department of Electrical Energy Conversion
KTH Royal Institute of Technology
Sweden

Associate Professor David A. Howey
Department of Engineering Science
University of Oxford
The United Kingdom

Opponent Professor Emeritus Tapani Jokinen
School of Electrical Engineering
Aalto University
Finland

ISBN 978-952-265-672-8
ISBN 978-952-265-673-5 (PDF)
ISSN-L 1456-4491
ISSN 1456-4491
Lappeenrannan teknillinen yliopisto
Yliopistopaino 2014

Abstract

Mariia Polikarpova
Lappeenranta 2014
204 pages
Acta Universitatis Lappeenrantaensis 597
Diss. Lappeenranta University of Technology
ISBN 978-952-265-672-8, ISBN 978-952-265-673-5 (PDF),
ISSN-L 1456-4491, ISSN 1456-4491

In the design of electrical machines, efficiency improvements have become very important. However, there are at least two significant cases in which the compactness of electrical machines is critical and the tolerance of extremely high losses is valued: vehicle traction, where very high torque density is desired at least temporarily; and direct-drive wind turbine generators, whose mass should be acceptably low. As ever higher torque density and ever more compact electrical machines are developed for these purposes, thermal issues, i.e. avoidance of over-temperatures and damage in conditions of high heat losses, are becoming of utmost importance. The excessive temperatures of critical machine components, such as insulation and permanent magnets, easily cause failures of the whole electrical equipment. In electrical machines with excitation systems based on permanent magnets, special attention must be paid to the rotor temperature because of the temperature-sensitive properties of permanent magnets. The allowable temperature of NdFeB magnets is usually significantly less than 150 ˚C. The practical problem is that the part of the machine where the permanent magnets are located should stay cooler than the copper windings, which can easily tolerate temperatures of 155 ˚C or 180 ˚C. Therefore, new cooling solutions should be developed in order to cool permanent magnet electrical machines with high torque density and because of it with high concentrated losses in stators.

In this doctoral dissertation, direct and indirect liquid cooling techniques for permanent magnet synchronous electrical machines (PMSM) with high torque density are presented and discussed. The aim of this research is to analyse thermal behaviours of the machines using the most applicable and accurate thermal analysis methods and to propose new, practical machine designs based on these analyses. The Computational Fluid Dynamics (CFD) thermal simulations of the heat transfer inside the machines and lumped parameter thermal network (LPTN) simulations both presented herein are used for the analyses. Detailed descriptions of the simulated thermal models are also presented. Most of the theoretical considerations and simulations have been verified via experimental measurements on a copper tooth-coil (motorette) and on various prototypes of electrical machines.

The indirect liquid cooling systems of a 100 kW axial flux (AF) PMSM and a 110 kW radial flux (RF) PMSM are analysed here by means of simplified 3D CFD conjugate thermal models of the parts of both machines. In terms of results, a significant temperature drop of 40℃ in the stator winding and 28℃ in the rotor of the AF PMSM

was achieved with the addition of highly thermally conductive materials into the machine: copper bars inserted in the teeth, and potting material around the end windings. In the RF PMSM, the potting material resulted in a temperature decrease of 6℃ in the stator winding, and in a decrease of 10℃ in the rotor embedded-permanent-magnets.

Two types of unique direct liquid cooling systems for low power machines are analysed herein to demonstrate the effectiveness of the cooling systems in conditions of highly concentrated heat losses. LPTN analysis and CFD thermal analysis (the latter being particularly useful for unique design) were applied to simulate the temperature distribution within the machine models. Oil-immersion cooling provided good cooling capability for a 26.6 kW PMSM of a hybrid vehicle. A direct liquid cooling system for the copper winding with inner stainless steel tubes was designed for an 8 MW direct-drive PM synchronous generator. The design principles of this cooling solution are described in detail in this thesis. The thermal analyses demonstrate that the stator winding and the rotor magnet temperatures are kept significantly below their critical temperatures with demineralized water flow. A comparison study of the coolant agents indicates that propylene glycol is more effective than ethylene glycol in arctic conditions.

Keywords: cooling system, liquid cooling, thermal design, permanent magnet electrical machines, reliability analysis
UDC 621.313.3:621.3.017:519.248:51.001.57

Acknowledgements

The research documented in this doctoral thesis was carried out at the Institute of Energy Technology (LUT Energy) at Lappeenranta University of Technology between the years 2010 and 2014. The research was funded by the Academy of Finland, the Graduate School of Electrical Energy Engineering (GSEEE), Tukisäätiö, Fortum Foundation and Walter Ahlström Foundation.

I express my sincere gratitude to my supervisor Professor Juha Pyrhönen for introducing me with this interesting research topic and guiding me through the process. I would like to thank my other supervisor Doctor Pia Lindh for collaboration and encouragement over the years. I wish to thank Dr. Janne Nerg and Dr. Pekka Röyttä for their valuable advices and comments.

The comments by the preliminary examiners, Associate Professor Juliette Soulard and Associate Professor David A. Howey, are the most gratefully appreciated. My honoured opponent, Professor Emeritus Tapani Jokinen, I thank you for finding the time for the examination.

Thanks go to my colleague Dr. Pavel Ponomarev, Dr. Yulia Alexandrova, M.Sc. Scott Semken, M.Sc. Ilya Petrov and M.Sc. Lyudmila Popova for cooperative work related to this thesis.

Many thanks are reserved for Christine Silventoinen for her contribution to revise and improve the language of this manuscript. Special thank goes to our faculty secretary Piipa Virkki for managing organizational problem during these years. I also would like to thank Dr. Julia Vauterin-Pyrhönen for her advice to start the PhD in LUT Energy and for her support in the educational process.

I would like to express my thanks to my friends from Saint-Petersburg and Severodvinsk Evgenia Shepeneva, Dina Gaynutdinova, Anna and Mikhail Gerasimov, Alexander Krykov, Mikhail and Liudmila Yachmenova, Ekaterina Fedotova, Svetlana Kreydin, Inna Fomina, Inna Rudakova, Maria Ravier, Vera Bahtina, Anna Parshina, Elena Ivanova, Svetlana Telepaeva, Roman Ledyukov and Tatiana Ledyukova for their suggestions to start PhD and support over the process. Luckily, here in Lappeenranta I was surrounded by bright and cheerful friends, so many thanks go to Pavel Ponomarev, Daria Nevstrueva, Nadezda Kurilets, Dmitry Kuleshov, Lyudmila and Alexander Smirnov, Polina Belova, Sergey Voronin, Andrey Maglyas, Ilya and Daria Pertova, Victorya Kapustina, Natalya Strokina, Yulia Alexandrova, Katteden Kamiev, Alexander Sokolov, Ekaterina Albats, Nikita Uzhegov, Maria Pronina, Ekaterina Sermyagina, Armen Madoyan, Yulia Navalihina, Marina and Egor Nikolaev, Olga Gore, Mikhail Sokolov, Denis Semenov, Kirill Filianin, Kirill Murashko, Elvira Baygildina and others.

Most importantly, I would like to dedicate my deepest appreciation to my loving parents Nina and Victor, my sister Natalya and her husband Dmitry and their children Anna, Andrey and Ekaterina, my brother Evgenii and his wife Victoria and their children Vyacheslav and Alexandra for their love and support.

Mariia Polikarpova
November 2014
Lappeenranta, Finland

Dedicated

to my parents Nina and Victor

Посвящается

моим родителям Нине Викторовне и Виктору Ивановичу

Contents

Abstract

Acknowledgements

Contents

Nomenclature **11**

1 Introduction **17**
1.1 Energy conversion and losses in electrical machines 17
1.2 Heat transfer in electrical machines 19
1.2.1 Conduction 19
1.2.2 Convection and radiation 20
1.2.3 Development of electrical machines with high torque density 24
1.2.4 Weakness of air cooling in high-torque-density applications 28
1.3 Application of liquid cooling in electrical machines 32
1.3.1 Single-phase liquid cooling 35
1.3.2 Two-phase liquid cooling 37
1.3.3 Reliability of the liquid cooling system 40
1.4 Thermal design and analysis of electrical machines 42
1.4.1 Thermal design of electrical machines 42
1.4.1 Thermal design of electrical machines with indirect liquid cooling 57
1.4.2 Thermal design and analysis of electrical machines with direct liquid cooling 65
1.5 Aim and scope of the research 71
1.6 Scientific contribution 73
1.7 List of publications 75

2 Indirect liquid cooling system of an axial-flux permanent magnet synchronous machine **79**
2.1 Description of the machine and its cooling system 79
2.2 Thermal analysis of the machine 83
2.2.1 Losses, thermal conductivities and convection coefficients 83
2.2.2 Thermal design based on CFD thermal modelling 86
2.2.3 Potting material and copper bars 95
2.3 Experimental results and analysis 96
2.4 Conclusions 101

3 Indirect liquid cooling system of a radial-flux permanent magnet synchronous machine **103**
3.1 Machine studied 103
3.2 CFD thermal design of the machine 107

3.3 Liquid jacket and potting material 110
3.4 Experiments 112
3.5 Conclusions 115

4 Direct liquid-cooled high-power low-speed permanent magnet synchronous generator with outer rotor 117
4.1 Description of the generator 118
4.2 Design of a direct liquid cooling system for the generator 119
4.3 Modelling of coolant properties 122
4.4 Thermal analysis of direct-liquid-cooled high-power permanent magnet synchronous generator 129
4.4.1 Thermal conductivities and convection coefficients 129
4.4.2 Thermal analysis based on Lumped Parameter Thermal Network 131
4.4.3 Thermal analysis based on Computational Fluid Dynamics 132
4.5 Experimental validation on a coil prototype (motorette) 136
4.6 Reliability of the generator liquid cooling system 139
4.6.1 Reliability data of the generator cooling loop 140
4.6.2 Reliability data of the generator liquid cooling system 142
4.7 Conclusions 147

5 Oil-immersed permanent magnet synchronous motor 149
5.1 Oil-immersed machine 149
5.2 Thermal analysis of the oil-immersed motor 153
5.2.1 Thermal analysis based on Computational Fluid Dynamics 153
5.2.2 Thermal analysis based on Lumped Parameter Thermal Network 157
5.3 Experimental work 159
5.4 Conclusions 160

6 Conclusions and discussion 163
6.1 Summary of the results of this doctoral thesis 163
6.2 Discussion of the results of this doctoral thesis 166
6.3 Suggestions for future works 167

7 References 169

Appendix A: CFD modelling of radial-flux permanent magnet synchronous machine (Chapter 3) 189

Appendix B: Definition of thermal resistances for DD PMSG (Chapter 4) 191

Appendix C: Definition of thermal resistances for PMSM (Chapter 5) 197

Nomenclature

Latin alphabet

A	availability	-
A	linear current density	A/m
B	magnetic flux density	T
C	constant	-
C	capacitance (in LPTN)	J/K
c_p	specific heat capacity at constant pressure	J/(kgK)
c_v	specific heat capacity at constant volume	J/(kgK)
D	diameter	m
E	dielectric strength	V/m
F	factor	-
F	force	N
f	frequency	Hz
g	acceleration due to gravity	m/s^2
h	height	m
I	current	A
J	current density	A/m^2
k	turbulent kinetic energy	J/kg
K	coefficient	-
K	conductance (in LPTN)	W/K
k_B	Bolzman constant	$m^2 \cdot kg/s^2 \cdot K$
l	length	m
$\dot{m}$	mass flow rate	kg/s
N	number of particles	–
n	synchronous speed	rpm
P	power, heat rate	W
P'	volumetric heat rate	W/m^3
p	pressure	Pa
q	heat flux	W/m^2
R	specific electrical resistivity	$\Omega \cdot m$
R	thermal resistance	K/W
R	reliability	-
r	radius	m
S	source term	-
s	surface, cross-sectional area	m^2
T	temperature	K
T^*	temperature at dimensionless distance from wall	-
T	torque	N·m
t	time	s
U	internal energy	J
UA	unavailability	-

V	volume	m^3
$\dot{V}$	volumetric flow rate	m^3/s
W	width	m
w	dissipation rate of turbulent kinetic energy in Menter's model	-
Y	fluctuating dilatation in compressible turbulence	-
x	x-coordinate (width)	m
y	y-coordinate (depth)	m
y^*	dimensionless distance from wall	-
y^+	dimensionalless wall distance in boundary layer theory	-
z	z-coordinate (height)	m

Greek alphabet

α	thermal coefficient	1/K
α	thermal diffusivity	m^2/s
α	convection heat transfer coefficient	$W/(K \cdot m^2)$
β	thermal coefficient	1/K
Γ	effective diffusivity of k and w in $k - w$ *SST* turbulence model	Pa·s
Γ	blending function in enhanced wall treatment	-
δ	air gap length	m
ε	friction factor	-
ε	dissipation of turbulent kinetic energy	m^2/s^3
κ	absolute value of average surface roughness	m
λ	thermal conductivity	$W/(K \cdot m)$
λ	failure rate	1/year
μ	dynamic viscosity	Pa·s
μ	repair rate	1/year
ν	kinematic viscosity	m^2/s
ξ	pressure loss coefficient in fitting	-
Π	perimeter	m
γ	angle phase shift between A and B_n	rad, °
ρ	density	kg/m^3
σ	electrical conductivity	S/m
σ_F	tangential stress	Pa
τ	viscous stress tensor	-
υ	velocity	m/s
υ^*	dimensionless velocity	-
Φ	dissipation function	-
Ω	angular velocity	rad/s

Dimensionless numbers

Ec	Eckert number
Gr	Grashof number
M	Mach number
Nu	Nusselt number
Pr	Prandtl number
Ra	Rayleigh number
Re	Reynolds number
Ta	Taylar number

Subscripts

a	axial
abs	absorbing
ag	air gap
b	buoyancy
br	breakdown
dw	demineralized water
c	conductor
cd	cooling duct
cond	conductance
const	constant
conv	convection
ch	conductor hole
cf	cooling fluid
Cu	copper
d	dependent
el	electrical
em	electromagnetic
emp	empirical
endw	end -winding
eq	equivalent
f	fluid
fil	filling
fit	fittings
fr	frame
fric	friction
g	geometrical
h	hydraulic
i	system/subsystem component
in	inlet
in	inner
ins	insulation

k	number of failed components/subsystems
ke	kinetic energy
lam	lamination
m	number of operate components/subsystems
mag	magnets
mvg	mean velocity gradient
n	number of components/subsystems
n	local coordinate normal to wall
n	nominal
nac	nacelle
out	outer
p	pressure
par	parallel
pm	permanent magnet
r	rotor
rad	radial
rad	radiating
ref	reference
ry	rotor yoke
s	surface
sf	shaft
ser	series
sl	slot
ss	support structure
sst	stainless steel tube
st	stator
stt	stator tooth
sty	stator yoke
sys	system/subsystem
t	turbulent
tan	tangential
v	volume
vg	velocity gradient
w	wall
w	water
wind	winding

Abbreviations

2D	two dimensional
3D	three dimensional
AC	alternating current
AF	axial flux
DC	direct current
CFD	computational fluid dynamics
DBCS	direct bond copper substrate
DD	direct drive
DD PMSG	direct-drive permanent magnet synchronous generator
DW	demineralized water
DWpH	deionized and pH-controlled water
FEA	finite element analysis
FEM	finite element method
IGBT	insulated gate bipolar transistor
IM	induction machine
LA	liquid-to-air
LC	liquid cooling
LL	liquid-to-liquid
LPTN	lumped parameter thermal network
LJ	liquid jacket
MDT	mean down time
MTBF	mean time between failures
MTTF	mean time to failure
PAO	polyalphaolefin
PMSM	permanent magnet synchronous machine
TC PMSM	tooth-coil permanent magnet synchronous machine
TEFC	totally enclosed fan cooled
RANS	Reynolds-Averaged Navier-Stokes
RF	radial flux
RMS	root mean square
RTD	resistance temperature device
SST	shear stress transport
WJ	water jacket

1 Introduction

1.1 Energy conversion and losses in electrical machines

Electrical machines convert electrical energy into mechanical energy, and vice versa. The main workhorse of the industry is the induction machine (IM), the most common type of electrical machine in the world to date. The nominal efficiency of a 3.8 kW industrial IM was around 85.5 percent at nominal operating point (Puranen, 2006). During the latest 20 years, due to environmental concerns, the industry has been driven towards producing more efficient electrical machines and 4 kW electrical machine should have efficiency 88.6 percent based on the International Efficiency IE3 (IEC 60034-2-1; Technical Data of ABB motors, 2014). However, 250-375 kW IMs can have efficiencies up to 95.8%, as the stator p.u. iron losses and the copper p.u. losses drop with increasing machine power (IEC 60034-2-1; Technical Data of ABB motors, 2014). Permanent magnet electrical machines are considered to be more efficient alternatives to IMs, as the rotor winding Joule losses of the former are eliminated due to the utilization of permanent magnets as the rotor field source (Melfi et al, 2009). The typical nominal efficiency of a 3.93 kW industrial PMSM is approximately 92.3 percent, which gives it a great advantage over IMs (Puranen, 2006).

Over the past decade, tooth-coil permanent magnet synchronous machines (TC PMSMs) have become increasingly popular (Fig. 1.1).

Figure 1.1: Tooth-coil permanent magnet motor.

TC PMSMs feature a special winding construction in which the stator winding is comprised of coils around each or every second stator tooth. In comparison with traditional distributed winding, the tooth-coil winding simplifies the manufacturing process, but the most significant benefit is that it contains very short end-winding regions. This results in a short axial length of the complete machine and reduced stator

copper losses, as the copper volume is smaller than that found in traditional distributed windings (with bulky end windings) (Magnussen and Sadarangani, 2003).

When mechanical energy is converted into electricity or vice versa, both electrical-resistance-caused heat loss generation and magnetic-field-variation-caused losses and mechanical losses occur (Moradnia and Nilsson, 2011). Depending on the design, the heat losses are concentrated in the copper windings with impregnated insulation, in the laminated iron stacks and, to some extent, in the permanent magnets.

In electrical machines, losses can be categorized as follows: 1) copper (Joule) losses in the windings (in the case of PMSMs, Joule losses take place in the stator windings; in the case of IMs, the Joule losses are also generated in rotor windings), 2) iron losses in the magnetic circuit iron material, 3) mechanical losses and 4) additional losses. These losses are dealt with in greater detail below in this section. In industrial IMs, typically 60% of losses are generated in the stator and 40% in the rotor (Saari, 2001), while in machines with excitation based on permanent magnets, about 80% of losses are generated in the stator.

The current I flowing in the stator copper winding generates high Joule losses P_{Cu} internally because of the electrical resistivity R.

$$P_{\mathrm{Cu}} = I^2 \cdot R \tag{1.1}$$

The losses in the active magnetic laminated iron parts due to fast-changing magnetic fields of the machine are caused by eddy currents, hysteresis losses and additional losses (Eq. 1.2) (Ibrahim and Pillay, 2013). The eddy currents in laminations are caused by fast-changing magnetic fluxes in the conducting body according to Faraday's induction law. To reduce the eddy-current losses, thinner laminations are utilized in the construction of an electrical machine. The hysteresis losses are caused by energy losses from the redirection of the magnetic domains in the steel. Iron losses P_{iron} are usually calculated as

$$P_{\mathrm{iron}} = K_{\mathrm{h}} \cdot f \cdot B^{\mathrm{n}} + K_{\mathrm{e}} \cdot f^2 \cdot B^2 + K_{\mathrm{ex}} \cdot f^{1.5} \cdot B^{1.5} \tag{1.2}$$

where f is the frequency, B is the magnetic flux density, n is the Steinmetz constant, which depends on the material type and the flux density (usually 1.6), K_{h} is the hysteresis loss coefficient, K_{e} is the eddy current loss coefficient depending on the material electrical conductivity and the lamination thickness and K_{ex} is the loss coefficient depending on the material microstructure, the conductivity and the cross-sectional area of the lamination. However, it was found that Eq. 1.2 is accurate at certain frequencies and flux density range (Ibrahim and Pillay, 2013). At high frequencies and high flux densities the coefficients in Eq. (1.2) should vary with the frequency and flux density. Eq. (1.2) is also valid for silicone-based laminated steel sheets. For novel soft-magnetic materials (such as Cobalt-based electrical steel sheets,

soft-magnetic-composites and nano-particles magnetic composites) this equation may give inaccurate results.

The rotor losses of a PMSM mainly include the rotor iron losses and the losses in the permanent magnets. In this thesis, the machines analysed have the tooth-coil stator winding construction, by means of which the stator produces magnetic fields containing large amount of harmonics. These harmonics induce pulsating magnetic fields in the rotor, which produce additional eddy current losses in the magnets and iron losses in the rotor iron core. The losses in the permanent magnets are caused by eddy currents, and therefore can be reduced by magnet segmentation.

Mechanical losses in an electrical machine include friction losses in the bearings and between air and machine surfaces caused by the rotor rotation (especially between the rotor surface and air). If there is an on-axis fan arrangement, then mechanical losses includes also windage losses between rotor surface and air (Pyrhönen et al., 2008). The additional losses include all losses which are not accounted for in the above-mentioned losses (AC losses in copper windings, and losses due to skin and proximity effects (particularly important for machine with high electrical frequency)). The losses in the non-active magnetic parts of the machine such as the frame, clamping rings, rotor bushings, shaft, and terminal region are also included in the additional losses (Hämäläinen, 2013).

1.2 Heat transfer in electrical machines

Temperature differences between electrical machine parts and the environment lead to heat transfer because of temperature gradients. The main heat transfer mechanisms also associated with the cooling of electrical machines are conduction, convection and radiation.

1.2.1 Conduction

The material thermal conductivity is caused by the lattice vibration rate of the molecules and the free flow of electrons (Cengel, 2007). The value of the conduction heat transfer rate depends on the material thermal conductivity, the temperature difference between two points of the material and the thickness of the interface between these points.

$$q_{\mathrm{x}} = -\lambda \cdot \frac{\mathrm{d}T}{\mathrm{d}x} \tag{1.3}$$

where λ is the thermal conductivity, x is the characteristic length and T is the temperature. Electrical machines are complex systems consisting of several components connected by various mechanical methods. The materials of machine components have surface roughness, which causes some gaps between the connected components. These gaps are filled with air and/or grease, creating thermal contact resistance. Staton et al. (2005) analysed the effect of the interface gaps between the machine components (such

as gaps between the stator lamination and housing; and between the slot and lamination) on machine thermal behaviour. Typical effective interface gaps and associated contact resistances are listed in the paper (and below in Table 1.1).

Table 1.1 Effective interface gaps between the stator yoke and frame (Staton et al., 2005)

Interface Types of Typical Materials	Effective Interface Gap, mm
Aluminium-Aluminium	0.0005-0.015
Stainless Steel-Stainless Steel	0.007-0.015
Aluminium-Stainless Steel	0.006-0.009
Aluminium-Iron	0.0006-0.006
Average of TEFC IM	0.037

1.2.2 Convection and radiation

Convection is affected by the temperature difference between a surface of solid material, a fluid and the bulk motion of this fluid (Incropera et al., 2007). Convection includes advection, conduction and/or diffusion. Advection is associated with the bulk fluid motion, while diffusion is caused by the random motion of fluid molecules (Incropera et al., 2007). The heat flux transferred by convection in the surface contacting the fluid can be represented by the following equation.

$$q_{\text{conv}} = \alpha_{\text{conv}} \cdot (T_{\text{s}} - T_{\text{f}}) \tag{1.4}$$

where α_{conv} is the convection heat transfer coefficient, T_{s} is the surface temperature and T_{f} is the fluid temperature. The convection heat transfer coefficient is complicated, as it depends on many parameters, such as fluid and heat transfer surface characteristics. In practice, the dimensionless convection heat transfer coefficient known as the Nusselt number is used to reduce the number of total variables (Cengel, 2007). The definition of the Nusselt number is presented by the next equation.

$$Nu = \frac{\alpha_{\text{conv}} \cdot x}{\lambda} \tag{1.5}$$

where α_{conv} is the convection heat transfer coefficient, λ is the thermal conductivity of the fluid and x is the characteristic length of object (diameter or length). The Nusselt number presents a ratio of convection to pure conduction heat transfer. The definition of the Nusselt number Nu depends on the fluid flow regime, the internal or external flow, fluid thermo-physical characteristics, surface geometry, surface roughness and other related characteristics (Incropera et al., 2007).

$$Nu = f(x, Re, Pr) \tag{1.6}$$

where *Re* is the Reynolds number, *Pr* is the Prandl number and x_{bl} is the boundary layer parameter. The Reynolds number *Re* (ratio of the inertia and viscous forces) is used to define whether the fluid flow regime is laminar, transitional or turbulent (Staton et al., 2008). The Prandl number *Pr* (ratio of the momentum and thermal diffusivities) is used to present the fluid characteristics. The magnitude of Reynolds and Prandl numbers can be concluded from their respective definitions:

$$Re = \frac{\upsilon_f \cdot x}{\nu} \tag{1.7}$$

$$Pr = \frac{c_p \cdot \mu}{\lambda} \tag{1.8}$$

where υ_f is the velocity of fluid, ν is the kinematic viscosity of fluid, μ is the dynamic viscosity of fluid, c_p is the specific heat capacity of fluid, λ is the thermal conductivity of fluid and x is the characteristic length.

In the case of high speed machines, the Eckert number is applied to characterize the dissipation. The Eckert number *Ec* provides a measure of the kinetic energy of the flow relative to the enthalpy difference across the thermal boundary layer (Incropera et al., 2007).

$$Ec = \frac{\upsilon^2}{c_p \cdot \left(T_s - T_f\right)} \tag{1.9}$$

where υ_f is the velocity of fluid (flow), c_p is the constant-pressure specific heat of the flow, and T_s and T_f are the respective surface and fluid temperatures. The Mach number *M* is used to characterize the regime (as supersonic, transonic, hypersonic, high-hypersonic and re-entry speeds) (Young et al., 2010).

$$M = \frac{\upsilon_s}{\upsilon_{sound}} \tag{1.10}$$

where υ_s is the velocity of the source relative to the medium and υ_{sound} is the speed of sound in the medium. The Mach number can be used to determine if a flow can be treated as an incompressible flow. In this thesis, low speed machines are studied, so discussion of the dimensionless parameters is not included herein.

Free or natural convection is induced by buoyancy force because of 1) a fluid density gradient (due to a temperature gradient) and 2) a body force (due to a gravitation field) (Incropera et al., 2007). The following equation for the Nusselt number definition can be applied to calculate natural convection on the machine frame outer surface.

$$Nu_{\mathrm{air}} = 0.6 + \left(\frac{0.387 \cdot Ra_{\mathrm{air}}^{1/6}}{\left(1 + \left(\frac{0.599}{Pr_{\mathrm{air}}} \right)^{9/16} \right)^{8/27}} \right) \tag{1.11}$$

where Nu_{air} is the Nusselt number of the air, Ra_{air} is the Rayleigh number of the air and Pr_{air} is the Prandl number of the air. The Rayleigh number is applied to characterize the transition in a free convection boundary layer, which depends on the magnitude of the buoyancy and viscous forces in the fluid.

$$Ra_{\mathrm{air}} = Gr_{\mathrm{air}} \cdot \mathrm{Pr}_{\mathrm{air}} = \frac{g \cdot \beta_{\mathrm{air}} \cdot D_{\mathrm{stfr}}^3 \cdot (T_{\mathrm{stfr}} - T_{\mathrm{air}})}{\nu_{\mathrm{air}} \cdot \alpha_{\mathrm{air}}} \tag{1.12}$$

where Gr_{air} is the Grashof number of the air, Pr_{air} is the Prandl number of the air, g is the gravitation constant (9.81 $\mathrm{m^2/s}$), β_{air} is the coefficient of the thermal expansion of the air (1/303 1/K), α_{air} is the thermal diffusivity of the air, T_{stfr} and T_{air} are the respective stator frame and air temperatures, ν_{air} is the kinematic viscosity of the air, μ_{air} is the dynamic viscosity of the air, λ_{air} is the thermal conductivity of the air and c_{pair} is the specific heat capacity of the air. The Grashof number is used to present the buoyancy force.

$$Gr_{\mathrm{air}} = \frac{g \cdot \beta_{\mathrm{f}} \cdot x^3 \cdot (T_{\mathrm{s}} - T_{\mathrm{f}})}{\nu_{\mathrm{f}}^2} \tag{1.13}$$

In the case of radial flux machines, according to Staton et al. (2008), in conditions of the surface rotation, the Taylor number is more useful for considering the fluid flow regime (laminar, turbulent, or vortex). The fluid flow between two coaxial cylinders is under influence of a centrifugal force created by the rotating cylinder. When this centrifugal force is greater than the fluid viscosity forces, the fluid particles move radially towards the outer cylinder and in doing so carry heat from the inner cylinder towards the outer one (Taylor-Couette flow). Taylor vortices present the movement of fluid particles in the inner-cylinder space. Because of this, the Taylor number is mainly used for determining air flow parameters in an air gap (between the stator and rotor) (Nerg et al., 2013).

$$Ta = \frac{\Omega^2 \cdot r_{\mathrm{m}} \cdot \delta^3}{\nu^2} \tag{1.14}$$

where Ω is the mechanical angular velocity, ν is the kinematic viscosity of fluid, δ is the air gap length and r_{m} is the average of the stator and the rotor radii. To find a

corresponding Taylor-Couette flow form for the air gap geometry, a modified Taylor number Ta_{m} is used (Nerg et al., 2013).

$$Ta_{\mathrm{m}} = \frac{Ta}{F_{\mathrm{g}}} \tag{1.15}$$

$$F_{\mathrm{g}} = \frac{\pi^4 \cdot \left(\frac{2 \cdot r_{\mathrm{sr}} - 2.304 \cdot \delta}{2 \cdot r_{\mathrm{sr}} - \delta} \right)}{1697 \cdot \left(0.0056 + 0.0571 \cdot \left(\frac{2 \cdot r_{\mathrm{sr}} - 2.304 \cdot \delta}{2 \cdot r_{\mathrm{sr}} - \delta} \right)^2 \right) \cdot \left(1 - \frac{\delta}{2 \cdot r_{\mathrm{sr}}} \right)} \tag{1.16}$$

where F_{g} is the geometrical factor, r_{sr} is the average of the stator and rotor radii and δ is the air gap length.

In disk-type axial flux machines, the Nusselt number mainly depends on flow regimes defined by the Reynolds number Re_{afm} and the gap ratio G (Daily and Nece, 1960; Howey, 2012).

$$Re_{\mathrm{afm}} = \frac{\Omega \cdot r^2}{\nu} \tag{1.17}$$

$$G = \frac{\delta}{r} \tag{1.18}$$

where Ω is the mechanical angular velocity, ν is the kinematic viscosity of fluid, r is the rotor radius, δ is the length of the air gap.

Radiation is a heat transfer mode related to emission of energy in the form of electromagnetic waves (Incropera et al., 2007). The heat rate by radiation q_{rad} can be defined by the Stefan-Boltzmann equation.

$$q_{\mathrm{rad}} = \varepsilon_{\mathrm{th}} \cdot \sigma_{\mathrm{SB}} \cdot \left(T_{\mathrm{srad}}^4 - T_{\mathrm{sabs}}^4 \right) \tag{1.19}$$

where $\varepsilon_{\mathrm{th}}$ is the relative emissivity between the radiating and the absorbing surfaces, σ_{SB} is the Stefan-Boltzmann constant ($5.67 \cdot 10^{-8}$ W/m^2·K^4), T_{srad} is the thermodynamic temperature of the radiating surface and T_{sabs} is the thermodynamic temperature of the absorbing surface (Pyrhönen et al., 2008). The radiation heat flux rises quickly alongside the temperature rise of the radiating surface (Eq. 1.9). The temperature difference between the machine surface and environment is usually lower than 40–80 K. Thus, the total amount of transported heat energy by radiation is small (1–2% of the hot spot temperature decrease) in forced convection cases. Therefore, in most thermal

investigations of electrical machines, it is neglected (Bellettre et al., 1997; Hettegger, 2012).

All of the above-described heat transfer mechanisms should be considered during the thermal design of electrical machines to achieve and offer a cooling solution in accordance with the requirements, thereby providing a reduced size, high reliability and improved operational life. The heat removal capability of most cooling solutions is limited by the maximum heat removal rate in certain operating conditions. Several factors contribute to the machine thermal performance, such as geometry, heat losses, and thermophysical properties of materials constituting the machine parts. All designed cooling systems should meet performance requirements by managing the generated heat losses in the physical and operational constraints.

Electrical machines are complex systems consisting of materials with different thermal properties. Industrial machine insulation systems have developed to such a level that copper windings may be classified in thermal classes 155 ˚C and 180 ˚C or even higher. In these cases, the maximum allowable hot spot temperatures of the winding insulation are 155 ˚C or 180 ˚C. However, at temperatures higher than 100 ˚C, many types of industrial permanent magnets cannot withstand all possible operating conditions of permanent magnet synchronous machines. This renders the machine cooling design challenging, as the rotors should stay remarkably cooler than the stators. Traditional cooling methods may lead to over-dimensioning of the machine to meet the low temperature permanent magnet operating conditions. Therefore, a more effective cooling solution should be developed to meet the market requirements for high power and torque density electrical machines.

1.2.3 Development of electrical machines with high torque density

Electrical machines with high torque density are mainly required by sectors for which machine dimensions and weight should be minimized, such as wind farm, truck and hybrid drive sectors. Wind farms have become ordinary sources of electrical energy. The rated powers of up-to-date wind generators are increasing, but seldom exceed 7.5–9 MW (Shi and Lo, 2009; Kowal et al., 2013). The market for wind turbines is wide, and there is demand for more torque density and reliable wind generators. Turbine producers are searching for ways to maximize power and torque density in order to reduce energy costs. Modern inventions in this vein include gearless drive trains, magnetic bearings and permanent magnets for achieving strong reliability, high efficiency and simple rotor construction (Bang et al., 2008; Semken et al., 2012; Kowal et al., 2013). Even high temperature superconductors (HTS) are recommended for lessening generator weight and increasing efficiency (Abrahamsen et al., 2010; He et al., 2014). However, HTS-based electro magnets are expensive to use because of their very low operation temperature (20–55K), which is associated with difficulties in the cooling system (Tomas, 2010; Lewis, 2007). Gearless powerful generators with excitation systems based on permanent magnets are being developed by many producers, such as Avantis, Clipper Wind and Mitsubishi (Shrestha et al., 2008; Semken

et al., 2012). The application of a direct-drive train causes an increase in wind generator dimensions (diameter and length) or in air gap tangential stress to provide the designed high-power capacities. The machine size is limited by readily available transportation and construction techniques (Semken et al., 2012; Kowal et al., 2013). If high temperature superconductors are not used, the tangential stress should be increased by raising the linear current density in the generator stator windings. The consequence is significantly increased Joule heating and the need for more effective heat removal. In this design, the most critical temperatures are located in the stator windings (insulation) and in the rotor-mounted or embedded-permanent-magnets because of the heat flux propagation from the stator towards the rotor.

Electrical machines with permanent magnet excitation systems possess special requirements for the cooling system. In permanent magnet synchronous machines (PMSMs) the heat propagation from the stator winding to the rotor permanent magnets should be minimized because of the temperature sensitive properties of the rare-earth magnets. Permanent magnets have a Curie point or temperature – the temperature at which they become demagnetized or their permanent magnetism changes to induced magnetism – as low as 80 ºC –190 ºC depending on the rare-earth magnet type (Fodorean, 2008; Funieru et al., 2008). Neodium-iron-boron (NdFeB) magnets are used the most because of their high remanent magnetic flux density (up to 1-1.4 T) and high coercive field strength (1000 kA/m) (Howey, 2010), but the allowable operating temperature for these is usually less than 150 ˚C. Other magnets, such as samarium-cobalt (SmCo) magnets, are less temperature sensitive; however, they have a lower remanent flux density and therefore are not used unless high temperature tolerance is needed (Funieru et al., 2008). This means that the generated losses in the stator winding and in the stator iron should be removed through the stator yoke, frame or internally to keep the operating magnet temperature lower than the demagnetization point. Conventional natural air cooling or forced air cooling is not adequate for permanent magnet machines with high torque density, as air removes significant stator losses through the end windings and air gap, and in doing so, transfers heat towards the rotor magnets (Saari, 2001) (Fig. 1.2).

The increasing use of permanent magnets in electrical machines leads to increased interest in the development of liquid cooling solutions because of the magnets' temperature-sensitive properties. Another critical material is the insulation of the copper winding. The stator insulation can withstand temperatures lower than 155 ºC, 180 ºC and 220 ºC with respective classes 155 (F), 180 (H) and 220 (R) based on IEEE standards. However, each 10 K surplus to insulation operation temperature reduces the insulation life span by 30% to 50% (Funieru et al., 2008; Wildi, 2006). High operating temperatures are detrimental, as the electric resistivity of a copper winding increases with the temperature, and more heat losses are subsequently generated. The resistivity of copper in Ω·m as a function of temperature $R_{\mathrm{Cu}}(T)$ is found as

$$R(T) = 1.72 \cdot 10^{-8} \cdot (1 + 0.004 \cdot (T - 293)) \tag{1.20}$$

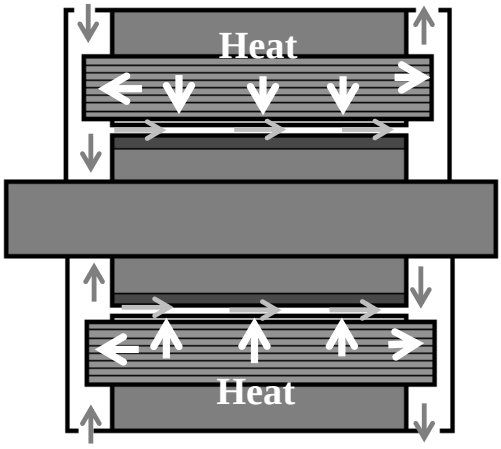

Figure 1.2: Air cooled machine.

Losses in the permanent magnet electrical machines are generated in the active materials – copper winding, laminated steel and permanent magnets. The continuous thermal expansion and contraction owing to machine varying load (wind generator, vehicle motor/generator) can cause critical thermal stresses between the machine materials (Erceg et al., 2012). Table 1.2 lists the linear thermal expansion coefficients for steel, copper, insulation and permanent magnets.

Table 1.2 Coefficients of Thermal Expansion (Erceg et al., 2012; Product Technical Data, TDK, 2011)

Material	Linear Thermal Expansion Coefficient, 1/K
Steel	$11–13 \cdot 10^{-6}$
Copper	$17 \cdot 10^{-6}$
Insulation	$4–25 \cdot 10^{-6}$
Magnet (NdFeB)	$5.2 \cdot 10^{-6}$

The performance of the cooling system should be improved with the increasing torque density of the permanent magnet electrical machines. In conditions of limited space and weight in case of truck and wind turbine applications, the cooling system should guarantee that the machine will stay within acceptable temperature limits of the insulation and permanent magnets. Bruetsch et al. (2008) deduced that up to 73% of damage to electrical machines is caused by over-temperatures.

To avoid exceeding the critical temperatures within the machine, methods for enhancing cooling are needed. It is generally accepted that air cooling systems are easier and more reliable than liquid cooling solutions. However, in some cases, cooling solutions for the highest power machines should adopt indirect or direct liquid cooling to become more

compact and thus more attractive. In the case of electric vehicles, liquid cooling is useful for meeting the high torque densities and desired overload capabilities (Caricchi et al., 1996). Recently, most wind generator manufacturers (e.g., Vestas, Siemens, Alstom, Areva) have started using indirect liquid cooling systems for high power and torque density electrical machines (Kowal et al., 2013). As one can see in Table 1.3, liquid cooling offers some advantages over gas cooling, but it also has drawbacks. Direct liquid systems require a special liquid source and adequate liquid quality to meet system design requirements.

Table 1.3 Convection Coefficients for Different Cooling Methods (Product Technical Data of REO ELECTRONIK AG, 2012; Cengel, 1998)

Cooling Method	Convection Coefficient, $W/(K \cdot m^2)$
Gas Cooling	
- Air	
Natural	5–30
Forced	20–300
- Hydrogen	100–1500
Liquid Cooling	
- Water	
Single-Phase	100–20000
Two-Phase	3000–100000
- Oil	500–2000

Recently, there has been growing interest in the application of materials with high thermal conductance, such as high conductance potting materials (aluminium nitride, high performance epoxy, graphite foam, thermoplastic) (Neal el al., 2000; Rahman et al., 2004; Crescimbini et al., 2005; Hoerber et al., 2011; Yao et al., 2011). These heat conductance materials operating as heat sinks have become popular in electrical machines and potentially result in a more uniform thermal profile (less hot spots) (Seghir-Oualil et al., 2003). The application of a high conductance material allows for balancing of the heat flux or for redistribution of heat towards the cooling system, but it alone does not remove the heat. The heat moves from hot to cool areas without consuming extra cooling power by means of conduction. Rahman et al. (2004) analysed a 25 kW Axial flux Permanent-Magnet Synchronous Machine (AFPMSM) with a liquid jacket and high thermal conductance epoxy between the end windings and frame for electric vehicle propulsion system. However, there is no information available concerning the thermal results. Yao et al. (2011) applied a compound based on aluminium nitride with a thermal conductivity of 40 $W/(K \cdot m)$ to the end winding of a 7kW PMSM and achieved a 20 K reduction of the maximum temperature.

1.2.4 Weakness of air cooling in high-torque-density applications

The thermal management scheme for electrical machines exists to keep their critical components below the required temperature limits, since this has long-term reliability implications (Nategh, 2013). The traditional natural and forced air-cooling systems of electrical machines are the most widely used methods. Air as a coolant is safe and does not require deep treatment or special sourcing because of its abundance. Although air cooling continues to be a widely used method for electrical machine cooling, the use of liquid cooling allows for accommodation of significantly higher heat fluxes (Caricchi et al., 1996). With liquid cooling systems, electrical machines can have higher torque density so that they may be used in such demanding applications as direct-drive high-power permanent-magnet-based generators. Moreover, large, heavy and expensive heat sinks and noisy, powerful fans are required for sufficient air convection capabilities to evacuate high losses (Sharar et al., 2010), while liquid cooling offers a different and more effective cooling solution. At the same level of machine losses, the pumps used to force the liquid through the cooling circuits have lower acoustic noise and vibration levels than open circuit forced air cooling based on powerful fans (Funieru et al., 2008; Costa-Patry, 2011). Liquid cooling systems are mostly of the closed-loop type and therefore have a totally enclosed environment, so this system is almost insensitive to local impacts and offers good controllability (Borges et al., 2008). For example, the cooling systems of offshore wind generators contend with biological-fouling, salty air and salty water. These systems run a high risk of corrosion, so closed cooling systems are required in these applications. Liquid-based cooling systems are able to improve efficiency of electrical machines by reducing machine temperatures, which in turn reduces losses. An improved power-to-size ratio of the electrical machine can be achieved by better efficiency gained due to higher heat removal capacities of the liquid cooling (Table 1.4). However, at low machine ratings the liquid-based cooling system can be more expensive and enormous compared with the air-based cooling system, as more treatment equipment, measuring devices and liquid source are required for its proper operation.

Typical average tangential stress values and linear current density values as functions of the cooling methods are listed in Table 1.4 (Vogt, 1984; Miller, 1994; Rilla, 2012; Semken et al., 2012; Alexandrova et al., 2012; Ponomarev, 2013; Petrov et al., 2013). The values of tangential stress $\sigma_{F\tan}$, of linear current density A and of current density J of the machines studied in this thesis and used during the project work are listed in brackets. In wind turbine generators, the desired efficiency is one of the main factors determining the current density allowed. These machines also have a lower current density at the nominal point, which is determined by the necessity of high efficiency at partial loading. A permanent magnet synchronous generator with a rated power of 8 MW was developed for wind turbine application; because of this, the current density was decided to be lowered in order to provide high efficiency.

Traction drive motors typically have a lower current density and tangential stress at the nominal point. However, they require good cooling at lower speeds, when they operate

at overload, producing high torque. PM electrical machines intended for traction application are normally torque-controlled (Guemo et al., 2013). At increased permanent magnet temperatures, the magnetic polarization decreases and thus the torque drops, so the current density must be increased to provide the required torque. The 100 kW Axial Flux Permanent-Magnet Synchronous Machine (AFPMSM) and 110 kW Radial Flux PMSM (RFPMSM) designed during this work have lower tangential stresses and linear current densities than industrial grade machines with indirect liquid cooling system. Such industrial machines are, however, not dedicated to operate at overload conditions.

Table 1.4 Tangential Stress, Current Loading and Current Density as Functions of the Cooling Method

Cooling Method	Tangential Stress, $\sigma_{F\tan}$ [kPa]	Linear Current Density, A, [kA/m]	Current Density, J [A/mm^2]
Air Cooling (salient pole)	< 50 … 60 (< 30)	< 80 (< 60)	1.5–5
- Passive	-	-	-
- Forced	(8.5_5)	(38_5)	5–10 (3.4_5)
- Forced (design based on stator stacks and radial channels)	-	-	-
Hydrogen Cooling	-	90–110	-
Liquid Cooling (Single-Phase)	> 50	70–200	7–30
- indirect (water jacket)	< 60 (22_1, 33_2)	90–110 (30_1,48_2)	7–10
- direct (immersion oil cooling, direct cooling through hollow strands)	> 60 (80_3; 80_4)	110–200 (130_3;147_4)	10–30 (8_3; 4.8_4)

(1) 100 kW axial flux permanent magnet synchronous machine (Chapter 4),

(2) 110 kW radial flux permanent magnet synchronous machine (Chapter 5),

(3) 26.6 kW oil-immersed permanent magnet synchronous motor (Chapter 7),

(4) 8 MW direct liquid-cooled permanent magnet synchronous generator (Chapter 6),

(5) 50 kW radial flux ferrite magnet synchronous generator (Petrov et al., 2013).

In the case of permanent magnet electrical machines, cooling solutions based on liquid jackets are preferable to forced air cooling, as heat generated in the stator winding and iron should be removed through the outer part to avoid its propagation towards the rotor surface-mounted magnets or rotor embedded-permanent-magnets. For this reason, the axial and radial flux machines presented in this thesis adopt liquid jackets as a cooling

method (even though their tangential stresses and linear current densities are not high (respectively 22–33 kPa and 30–48 kA/m)) to have indirect liquid cooling (50–60 kPa and 90–110 kA/m).

Radial flux electrical machine power is proportional to the rotational speed and the electromagnetic torque T_{em}, which can be expressed based on the rotor volume V_r and the electromagnetic loading viz. tangential stress $\sigma_{F\tan}$ (Pyrhönen et al., 2014):

$$T_{em} = 2 \cdot V_r \cdot \sigma_{Ftan} \tag{1.21}$$

$$\sigma_{Ftan} = \cos\gamma \cdot B_n \cdot A \tag{1.22}$$

The tangential stress is defined by the local value of the air gap magnetic flux density in radial direction (B_n) caused by magnets and currents, linear current density (A) and factor ($\cos\gamma$) as shown in Eq. (1.22). The angle γ describes the phase shift between A and B_n distributions. In electrical machines with an excitation system based on permanent magnets, the air gap magnetic flux density usually stays below 1 T, depending on the magnet type. The limit for air gap magnetic flux density (1 T) is caused by the current material limitations, as the permanent magnet remanent flux density is maximally 1.4 T and the typical steel saturation flux density is 2.2 T. Therefore, the machine power can be increased mainly by the rise of the linear current density A in conditions of constant rotational speed and machine size. However, the linear current density is limited by the utilized cooling capability, operating duty type and the armature reaction-induced reactive voltage drop (Semken et al., 2012; Pyrhönen et al, 2014).

In some high power applications, an air-cooling system is impossible because of the limited physical space for heat sinks, the noisy fans and the absence of a power source high enough for its operation. The forced air cooling of industrial electrical machines is usually provided by a fan installed on the rotor shaft, so the cooling capacity is limited by the machine rotation and fan dimensions (Shi and Lo, 2009). In the case of permanent magnet electrical machines, the magnets mounted on the rotor surface may attract ferromagnetic debris and dust in conjunction with open circuit air cooling (Funieru et al., 2008). This means that open forced-air cooling options become unviable in some applications, requiring special treatment of air to be attractive. In closed air cooling conditions, the circuit air is pumped by a fan attached above the machine and fed by a separate power source. The fan power depends on the air flow rate and pressure drop, so it can be assumed that $P_{fan} \approx v_{air}^3$. The necessary air flow rate is defined by the heat losses generated in the machine being cooled ($P_{loss} \approx P_{cool}$). The heat losses are proportional to the square of the electrical current and the electrical current is proportional to the nominal power of the machine ($P_{loss} \approx P_n^2$). The cooling power P_{cool} is proportional to the air velocity v_{air} and for forced convection it can be assumed that $P_{cool} \approx v_{air}^{4/5}$. Therefore, the fan power P_{fan} is proportional to the machine heat losses P_{loss} and the cooling power P_{cool} and therefore in turn to the machine rated power P_n (Semken et al., 2012).

$$P_{\text{fan}} \hat{=} P_{\text{n}}^{15/2} \tag{1.23}$$

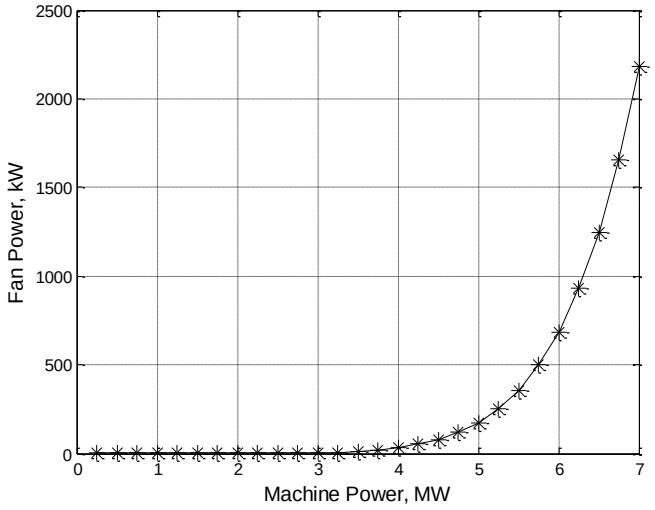

Figure 1.3: Dependence of fan power on machine rated power (Semken et al., 2012).

Electrical machine producers increase the heat transfer surface 1) by using fins, creating cooling holes in the rotor and cooling ducts between the stator stacks, and 2) by designing a clearance between the stator windings in the slots (He et al., 2013). The applications of these modifications yield a larger heat transfer area and result in more effective air cooling. However, pressure losses increase significantly in these machine designs, as air flow has high velocity in the cooling holes and ducts (Fig. 1.3).

Several authors have pointed out the need for moving towards cooling solutions with higher heat capacity capabilities to meet the demands of high density packaging. Hydrogen is used as coolant for the stator and rotor in high-power applications (Product Technical Data, Siemens, 2008; Wolf, 2009). This coolant has a higher thermal conductivity (0.169 W/(m·K)) than air does (0.027 W/(m·K)) and has higher heat capacities, if it operates at pressures lower than 6 bars (Shi and Lo, 2009; Wollf, 2009). However, hydrogen requires a closed-machine construction with sealing of the shaft and a pressure-vessel-type housing (2–3.1 bar) for reliability, as a mixture of hydrogen (4–76%) and air (oxygen) can easily cause an explosion (Gibney et al., 1994). As more machines with high torque density are developed, liquid-based cooling solutions have increasingly come into use (Costa-Patry, 2011; Kim, 2010). However, because of the high cost of the liquid cooling, it is applied only when air cooling is incapable of evacuating the generated losses and a greater heat transfer rate is required than what air

cooling can provide (Saums, 2010). The insulation voltage stress because of higher current density and the forces are higher in electrical machines with liquid cooling because of the higher power density, so a special type of insulation (e.g., epoxy-mica-based insulation) should be considered for these machines (Gybney et al., 1994).

In the following chapter, liquid cooling solutions used in electrical machines are discussed. The basic characteristics, advantages and drawbacks of the various liquid cooling systems are identified.

1.3 Application of liquid cooling in electrical machines

One's selection of a proper cooling system is influenced by the requirements specification set for the cooling solution of the machine to be developed. The requirements specification includes inter alia the coolant type, the dissipated power, the reliability and the cost. For many years, liquid cooling has only been used in specific applications (Ohadi and Qi, 2004; Borges et al., 2008) where air cooling is impossible or does not provide the necessary heat evacuation.

The liquid cooling systems are mainly divided into two types: direct and indirect. A direct liquid cooling system is significantly more efficient compared with an indirect one, as direct cooling offers the opportunity to remove heat directly from the heat source with no intervening thermal conduction resistance (conductor insulation, impregnating resin, slot mainwall insulation, stator yoke, joint between the stator stack and housing, housing material) between the coolant and the hottest machine part (usually the stator of PMSMs or the rotor winding of electrically excited SMs). A direct liquid cooling system is mainly applied in generators with a rated power of more than 100 MW in thermal, hydro and nuclear power plants (Gray at al., 2006; Zhe et al., 2009).

With direct liquid cooling systems, the coolant properties should be precisely controlled, as corrosion and leak events are dangerous. The direct liquid cooling systems of the stator or rotor windings present liquid flows inside the copper conductors or the stainless or brass steel tubes inserted between or inside the copper conductors, thereby evacuating generated heat losses (Vlach et al., 2005; Li et al., 2010; Wang et al., 2010). The direct liquid cooling of a moving rotor winding of electrically excited SMs is more difficult to construct and exploit, compared with the stable direct liquid cooling of a stator winding because of the lower reliability of the feed pipe (Zhe et al., 2009). However, the direct liquid cooling system of the rotor winding of electrically excited SMs offers the opportunity to remove the heat directly from the winding with no intervening thermal conduction resistance caused by the electrical insulation or the laminated steel.

Electrical machines usually have indirect liquid cooling systems to evacuate losses mainly from the stator. These are based on spiral cooling rings or a helix liquid cooling circuit incorporated in the stator frame housing (cooling jacket) along the machine

length and sometimes also inserted in the end shields (Borges et al., 2008; Product Technical Data, ABB LV Motors). The losses generated in the copper winding and the stator iron are evacuated after being transported to the outside frame mainly by conduction or convection through air circulated inside the machine and then cooled externally in a heat exchanger. This most-used indirect liquid cooling system provides effective heat removal from the stator assembly. The forced air cooling is sometimes additionally utilized in this design to alleviate the temperature issue affecting the rotor (Zheng et al., 2008; Jiang and Jahns, 2013). The cooling liquid may also be in direct contact with the stator iron yoke (between the frame and the stator yoke), providing the best contact with the yoke (Sikora et al., 2011) and thus avoiding the uncertain contact resistance between the stator and the cooled frame (thermal paste), which is usually characterized by poor heat conduction capability. Providing a water-tight stator yoke may, however, be a challenge.

The liquid cooling technique offers a high heat-transfer coefficient (<20000 W/m^3), which reduces the temperature rise of the cooled surface to just above the liquid coolant temperature. Compared to air cooling solutions, liquid cooling ones enable a significant increase in the losses that can be sustained without exceeding the temperatures of critical components. Fig. 1.4 presents a comparison of temperature distributions within a stator slot in conditions of forced air cooling, indirect liquid cooling and direct liquid cooling. The illustrated temperature results were simulated by the 2D FEM software Flux. The same heat losses (537 kW/m^3 in case forced air cooling and indirect liquid cooling and 640 kW/m^3 in case of direct liquid cooling) were defined within the copper conductors. In the case of forced air cooling, the convection coefficient (250 W/(m^2·K)) and the air temperature (55 ˚C) in the air gap were defined. The boundary conditions for the indirect liquid cooling were defined by the convection coefficient (1000 W/(m^2·K)) and the air temperature (55 ˚C) in the liquid jacket. In the case of direct liquid cooling, the water temperatures (from 40 ˚C to 60 ˚C) were defined inside the copper conductors.

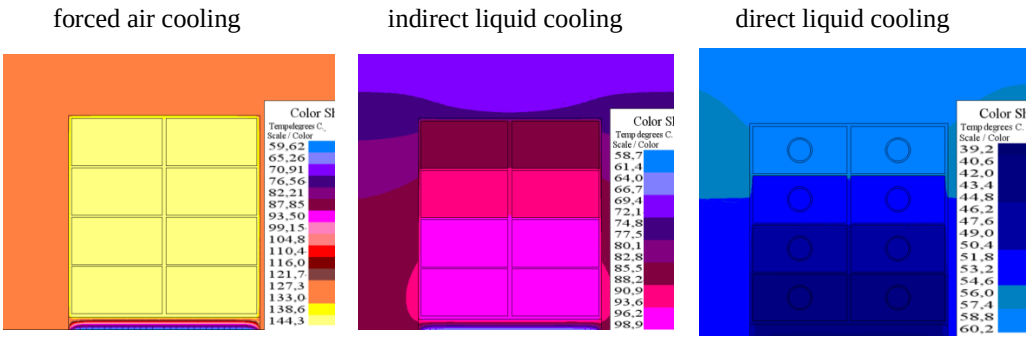

Figure 1.4: Temperature distributions within the stator part in conditions of air cooling (40 mm sub-stacks and 6 mm cooling channels in between), indirect liquid cooling (stator yoke is facing a water pool) and direct liquid cooling (each rectangular conductor has a cooling tube inside).

The conventional liquid cooling systems of electrical machines present two cooling loops connected by a heat exchanger, where the heated liquid is cooled for reuse by

means of an exchange with another fluid (Fig.1.5). The primary cooling loop includes a pump, an expansion tank and fluid treatment equipment, such as a filter, a deionizer and a pH regulating unit (hydrazine adding unit) to facilitate the desired coolant content. The cooling circuits of electrical machines are also in the primary cooling loop. The coolant, driven by a pump, passes through the cooling circuits and acquires heat from various heat sources by virtue of convection. The filter removes particles, scale and organic matter. A deionizer is used for purging the entrained air or other gasses and for eliminating chlorine and other ions from the coolant. The risk of galvanic and other types of corrosion is reduced by using a deionizer. The pH regulating unit regulates the pH value to being slightly alkaline in the range of pH = 8.5. Liquid losses from the system are usually small, but otherwise the liquid-adding system should also be considered in the primary loop. In the secondary loop, the heat rejected from the main coolant dissipates into the outside water/ambient air, so this usually involves pumping or ventilating to force the secondary coolant through. Both cooling loops entail control and measurement equipment offering control over flow, temperature and pressure, depending on the operation conditions. This increases the effectiveness, reliability and cost of the cooling system. The cooling system parameters are modifiable in terms of the ambient conditions and operation regime of the device (through varying the coolant speed, etc.).

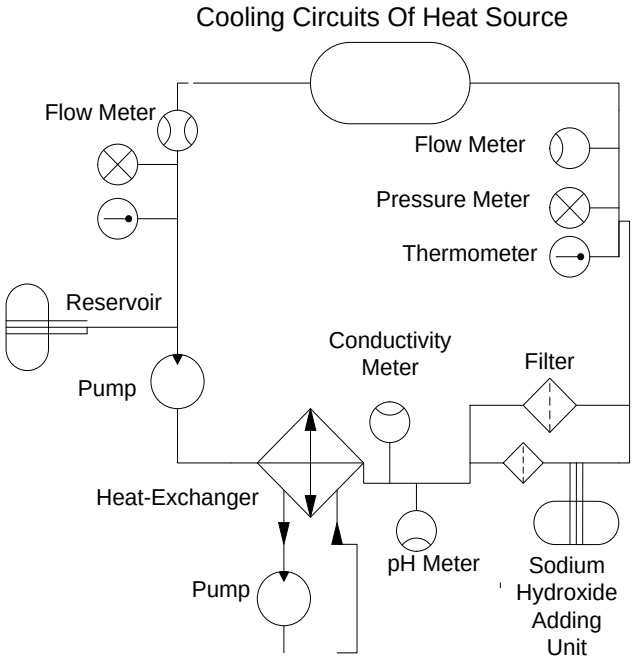

Figure 1.5: Principle scheme of a direct liquid cooling system (Syrett and Stein, 2001).

1.3.1 Single-phase liquid cooling

Producers of electrical equipment prefer single-phase cooling systems for conventional applications, as this technology has an established knowledge base, as well as global availability of water, glycols, oils and additives. There are numerous existing component manufacturers for single-phase cooling and in-depth service knowledge (Saums et al., 2010).

Selection of a proper coolant is crucial in the cooling system design as this affects the entire cooling system performance. The coolant should provide the required heat evacuation and comply with other cooling system requirements, industry needs and performance claims (Saums et al., 2010). Water is the most common and efficient coolant because of its wide availability, low viscosity, high heat capacity and other suitable aspects. Raw water – such as tap water – is not suitable in some applications because of its high corrosiveness, possibility of freezing or boiling and high conductivity. Because of the above-mentioned factors, deionized and pH-controlled water (DWpH) or modified water with antifreeze agents (propylene or ethylene glycols) and inhibitors are used more often in the cooling systems. DWpH is non-conductive ($2 \cdot 10^3\ \Omega \cdot m$), less corrosive and has excellent thermal properties. However, the use of DWpH as a coolant often requires additives for biological control, antifreeze, colorants and other inhibitors to avoid freezing problems and to provide operational safety (Saums et al., 2010). Freezing is a problem in the liquid cooling systems of equipment located in areas where temperatures routinely drop below the freezing point, so coolant used in these systems must have a low freezing point. The most common approach to prevention of freezing is the addition of glycols to water, but this also reduces the overall thermal performance of the cooling solution. Some researchers have pointed to a 28% to 42% reduction in thermal performance from the use of a coolant consisting of mixtures of water and ethylene or propylene glycols compared with the use of pure water (Sharar et al., 2010). The problem of corrosion is solved by coolant treatment and modification with corrosion inhibitors so as to ensure compatibility with other system materials and to satisfy operation parameters such as temperature and high velocity, which intensify the material destruction.

The most commonly used glycols are ethylene glycol and propylene glycol. Ethylene glycol ($HOCH_2CH_2OH$) with certain inhibitors is a popular antifreeze fluid in industrial and automotive applications. However, the presence of automotive-grade glycol inhibitors is undesirable in the direct cooling system of a generator, as they can easily gel and foul the heat exchanger surfaces and significantly reduce the lifespan of pump seals (Yuzwa and Eng, 1990). Propylene glycol ($CH_3CHOHCH_2OH$) is commonly used in the food processing industry, as it is a non-toxic antifreeze fluid. The corrosion inhibitor dipotassium phosphate allows for maintaining a low oral toxicity of the propylene glycol, but it makes it more expensive and more viscous. However, coolant based on low toxic propylene glycol has become more popular in the commercialized cooling systems of power converter and electrical machines (Sharar et al., 2010). Table 1.5 presents the general corrosion and wear data for the corrosion-inhibited Ethylene

Glycol, Propylene Glycol and water with stainless steel and copper (Product Technical Data of Glykosol, 2001; Product Technical Data of Pekasol, 2001). For the cooling system of a generator, the acceptable range of glycol concentration is 48–85% for ethylene glycol-based coolant and 49-85% for the propylene glycol-based one. From an economic standpoint, the concentration of 48–52% is preferable for both glycols, as it ensures good anti-freezing protection (–35 ˚C) at an adequate price (Yuzwa and Eng, 1990). If the freezing temperature is not important, then a lower concentration of glycol could be considered for improving the coolant thermal properties, such as heat capacity and viscosity. A dependence was not found between the corrosion properties of the coolant and the concentration rate of glycol in the coolant.

Even though different oils need less treatment to maintain high resistivity, oils are not often used as a coolant in electrical machines because of their low heat capacity, high viscosity-related friction losses and high pumping power. However, oil coolant can be utilized in low-speed, semi- or totally immersed electrical machines; machines with internal or spray cooling of the rotor or stator winding; and machines with an oil jacket in the frame (Huang et al., 2012; Bennion, 2011; Nategh, 2013). The main advantages of oil are the low resistivity, possibility of operating without a deionizer and functioning as a lubricant (Lim and Kim, 2013). Table 1.5 summarizes the main properties of the single- phase coolants (Saums, 2012; Bennion, 2011; Chevron Phillips Chemical Company LLC, 2008; EVANS, 2013). The problem related to burning liquids is that they add a possible fire load in the system.

Performance improvements to single-phase cooling systems can be obtained using larger heat transfer surfaces by means of mini- or micro-channel design; higher convection coefficients provided by a rise in turbulence intensity; and special fluid delivery methods (Sharar et al., 2010). However, the designs developed require special attention to coolant purity because of the small passages and complex geometry. The cooling systems with mini- or micro-channels have a high pressure drop and are prone to contamination and particulate accumulation (Sharar et al., 2010). The latest trend is to increase the inlet temperature, which results in three benefits: higher pump efficiency, a decrease of its rated power, and weight and size savings on the heat-exchanger side of the cooling system (Sharar et al., 2010; Michel, 2012). However, the outlet temperature of the coolant is limited by the liquid boiling point, which is lower for most liquid coolants (100 ˚C for water and 106–107 ˚C for water and glycol mixes at ambient pressures). Single-phase cooling systems have such limited performance because of the temperature margins of the utilized coolants (high freezing and low boiling temperatures). The permissible coolant temperature rise is only 25–45 ˚C above the inlet temperature (Sharar et al., 2010) because of the boiling and corrosion meters. This translates into the low potential the single-phase cooling solutions have for equipment with concentrated high heat fluxes (such as high-power converters).

Table 1.5. Properties of Coolants.

Fluids	Ethylene Glycol 50%Vol.	Propylene Glycol 50%Vol.	Water	PAO (Synthetic oil)	EVANS Liquid	Oil
Thermal conductivity, W/K·m (at 25ºC)	0.404	0.382	0.6	0.152 (at 40ºC)	0.287 (at 40ºC)	0.147
Thermal expansion coefficient, 1/K	$1.6\cdot10^{-3}$	$2.3\cdot10^{-3}$	$3\cdot10^{-4}$	not available	not available	not available
Specific heat, J/kg·K (at 25ºC)	3341	3649	4279	2261	2511	1600
Dynamic Viscosity, Pa·s (at 25ºC)	$2.5\cdot10^{-3}$	$4\cdot10^{-3}$	$8.5\cdot10^{-4}$	$1.61\cdot10^{-2}$	$1.2\cdot10^{-2}$	$5\cdot10^{-2}$
Density, kg/m^3	1076	1034	997	775	1107	800
Prandl Number	20.7	38.2	6.06	239.5	105	544.2
Flashpoint, ºC	111	99.1	none	226	not available	120
Boiling point, ºC	107.2	222	100	414	190.5	not available
Freezing point, ºC	–34	–28	0	–69	-40	not available

1.3.2 Two-phase liquid cooling

Lately, two-phase cooling systems have been developed extensively. Two-phase cooling has begun to be commercialized in converters with IGBT semiconductors, for which a single phase is not capable of evacuating the highly concentrated losses (Sharar et al., 2010; Howes et al., 2008; Saums, 2010). Compared with single-phase cooling systems utilizing liquid-specific heat capacity (4.2 kJ/kg for water), cooling systems with a phase shift provide high heat dissipation rates at higher operation temperatures and require a considerably smaller coolant volume because of their great latent heats of vaporization (150 kJ/kg for refrigerant) (Costa-Patry, 2011).

The high convection coefficients within two-phase cooling are associated with a latent heat benefit coupled with a buoyancy-driven bubble formation, multi-phase turbulation and mixing within the heat transfer region (Sharar et al., 2010). Systems utilizing boiling enable the evacuation of 2–4 times as much heat compared with systems utilizing the specific heat, or they allow heat fluxes above 120 W/cm^2 (Costa-Patry, 2011). Therefore, power modules could be run with higher operation frequencies without exceeding a junction temperature limit, but providing a relatively isothermal cooling surface with a difference of less than 1˚C (Sharar et al., 2010). The two-phase

cooling systems utilize refrigerants such as R-134a, R-1234ze, R-236fa and R-245fa. Water is seldom used in two-phase cooling systems, as boiling water flow is difficult to control because of the large volumetric difference between the vapour and liquid (Costa-Patry, 2011). Recently, the most commonly used refrigerant R-134a has been substituted by refrigerant R-1234ze, which has similar thermal properties but with significantly lower greenhouse gas emissions. The thermal properties of refrigerants R-134a and R-1234ze are presented in Table 1.6.

Table 1.6. R-134a and R-1234ze saturation properties at 30 ˚C (Costa-Patry, 2011)

Parameter	R-134a	R-1234ze
Pressure	7.7 bar	5.78 bar
Liquid Density	1187.5 kg/m^3	1146.3 kg/m^3
Vapour Density	37.54 kg/m^3	30.56 kg/m^3
Latent Heat	173.1 kJ/kg	162.9 kJ/kg
Liquid Dynamic Viscosity	183 μPas	188 μPas
Vapour Viscosity	13 μPas	12.5 μPas

The common elements of any given two-phase cooling system are the evaporator, pump, condenser/heat-exchanger, liquid-vapor separator (filter/dryer) and expansion tank. Figure 1.6 illustrates the two-phase cooling system developed by Parker (Saums, 2009). The basic element of the two-phase cooling system is a micro evaporator or two-phase cold plate, where heat is transferred to the system by the power device being cooled. This vapour is further carried through the condenser and liquid-vapour separator and exits as liquid. The liquid refrigerant is pumped by a special pump into the micro evaporator. The inert coolants do not cause galvanic effects in this two-phase system, and they are safe for both equipment and personnel in cases of leaks.

In electrical machines, the two-phase system is only applicable in indirect cooling systems, as windings themselves do not offer a site for controlled boiling of the coolant. Instead, a two-phase system in a cooling jacket could be feasible but does not necessarily deliver benefits because the heat transfer is more limited inside the machine. In the work of Camilleri and McCulloch, 2013, the evaporative cooling arranged in the stator for an axial flux permanent magnet synchronous machine is discussed. The evaporative liquid cooling system of an open rotor channel and heat pipe incorporation in the stator yoke have been presented for high-power machines (Zhe et al., 2009; Gieras et al., 2008).

The simplest two-phase device is a heat pipe, which is widely used in laptops; in the power semiconductor industry cooling solutions based on heat pipes also exist (Ivanova et al., 2006; Scowby, 2004). A heat pipe presents a miniature heat exchanger with passive coolant circulation owing to the phase shift and capillary wick. The conventional heat pipe has three sections: an evaporator, an adiabatic section and a condenser (Ivanova et al., 2006). The main advantage of the heat pipes is their capability to transfer heat between two points (pipe ends) with a minimal temperature

difference. Heat pipe capability depends on the dimensions (diameter and length) and the temperature drop between the pipe ends. Heat pipes could easily be utilized in rotating machines (inside the stator teeth, copper winding and rotor yoke) from the manufacturing point of view. However, heat pipe cooling systems do not have a wide application in high power and torque density machines because of the low heat capacity of the heat pipes. The heat transfer capacity of a heat pipe with a diameter of 12 mm and a length of 150 mm is up to 220 W in conditions of 120 K temperature difference (CRS Engineering, 2014). A high number of heat pipes is required to transfer the high losses. In some applications, it is difficult to reduce the amount of heat pipes, as more powerful heat pipes are longer, resulting in larger cooling-system dimensions.

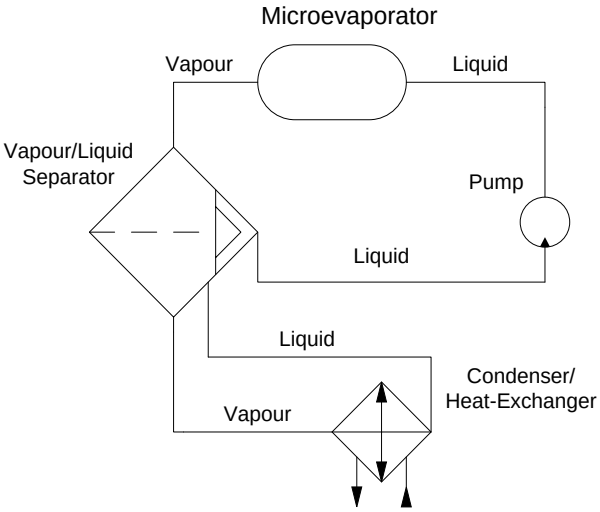

Figure 1.6: Principle scheme of a two-phase liquid cooling system

Over the last few decades, several authors have presented their works on spray cooling utilizing the vaporization latent heat of coolant during operation (Skuriat and Johnson, 2008; Turek et al., 2008). Spray cooling requires the application of nozzles with large driving pressures. This type of two-phase cooling is complex and the spraying devices are prone to clogging, which degrades thermal performance and causes over-temperatures (Sharar et al., 2010). Cooling systems based on spray vaporization do not widely exist in high power and torque density machines because of the difficult construction and control involved.

Several authors have claimed that a single-phase system is preferable in this stage to two-phase systems, because of the former's better control and reliability (Chu, 1999; Michel, 2012). Two-phase cooling systems have different flow regimes and pressure uncertainties, which cause cooling uncertainty, instability and a strong possibility of

dry-out (Sharar et al., 2010). The lack, high cost and low reliability of appropriate equipment (such as the pump) for the two-phase cooling system are other disadvantages (Sharar et al., 2010). However, nowadays many researchers continue working on two-phase systems to make them more reliable and cost-effective, and thereby more attractive for wide usage (Thompson et al., 2009; Saums, 2012).

1.3.3 Reliability of the liquid cooling system

The reliability of the cooling system plays a key role in ensuring the overall reliable operation of the equipment, as a safe and stable cooling operation is essential to power systems. If a liquid cooling system fault occurs, the electrical machine cannot run normally and may even breakdown quickly. Thus, the probability for liquid cooling system faults should be assessed, and preliminary actions should be taken to avoid unexpected cooling faults in the long-term of device reliability. Reliability analysis is especially desired in cooling system design, as an understanding of the cooling system operation parameters, such as failure rate, downtime and availability, helps one to choose the most acceptable cooling solution from operation and service perspectives. The stable operation of the cooling equipment ensures the maximum operation life of the electrical machine and its long-term reliability (an average working lifetime of 25–30 years).

Liquid cooling systems usually have higher manufacturing and maintenance costs than air cooling ones, as more auxiliary system components to provide, treat and control the liquid coolant are necessary, such as a filter, deionizer, pump and/or fan (Borges et al., 2008). However, for removing the same amount of heat, air cooling equipment also consists of many parts and overall may easily have lower reliability metrics compared with powerful liquid cooling equipment. Table 1.7 collects the literature values of failure rates and mean down times of common cooling system components. The coolant should also be changed or reconditioned every 6-12 months (Catalogue of Electro Impulse, 2000). The design of the cooling system should facilitate cleaning and inspection during service to reduce systems downtime (Gutierrez-Alcaraz et al., 2010). The frequency of service and replacements depends largely on the operation conditions and the amount of impurities in the systems. Special attention to coolant purity through continuous filtering is required for systems with small passages or mini- and micro-channels to avoid clogging and contamination.

The most serious drawbacks of the liquid cooling system are corrosion, deposits and potential leaks. Fouling and contamination (e.g., deposits on the metal surface inside the liquid jacket or inside the stainless steel tube in the direct liquid cooling of the stator winding) increase heat flow resistance, which significantly reduces cooling effectiveness and causes electrical components to overheat or even break down. The main results of the corrosion are caused replacement cost and machine downtime. The liquid entering an electrical machine could also easily cause a short circuit and damage the construction. Water and some other fluids are electrically conductive without special treatment, so a system leak could be catastrophic.

Table 1.7 Reliability Parameters of the Cooling System Components (Fraas, 1989; Lees, 1996; Wolpert, 1982; Technical Report, ENEA; Cadwallade, 1998; Technical Report of HSE, 2010; Technical Letter of EATON; Service Catalog of Manifolds, Lebentech; Wagner et al., 1988; Jadhay et al., 2010; Hurst and Ratcliffe, 1994; Catalog of Electro Impulse, 2000)

Component	Failure Rate, per year	Mean Down Time, man-hours
	Primary Side	
Heat Pipe at 60˚C	$6 \cdot 10^{-2}$	0.5
Liquid (Water Based) Pump	$8.64 \cdot 10^{-2}$	5.6
Refrigerant Pump	$1.7 \cdot 10^{-2}$	5.6
Water-Vapour Separator	$2.1 \cdot 10^{-2}$	4
Refrigerated Tank	$1 \cdot 10^{-5}$	24
Liquid Tank (Water Based)	$3 \cdot 10^{-4}$	24
Liquid Filter (Water Based)	$4.32 \cdot 10^{-1}$	4
Expansion Tank	$1.73 \cdot 10^{-3}$	24
Liquid-to-Liquid/Liquid-to-Air Heat Exchanger	$8.64 \cdot 10^{-3}$	10
Connection	$5 \cdot 10^{-6}$	0.5
Manifold	$3 \cdot 10^{-7}$	3
	Secondary Side	
Air Fan	$9.5 \cdot 10^{-2}$	5.6
Centrifugal Pump	$8.64 \cdot 10^{-2}$	5.6
Air Filter	$5 \cdot 10^{-2}$	5
Water Filter	$4.32 \cdot 10^{-1}$	4

The selection of liquid as a coolant results in the incorporation of a deionizer or special filter modules, depending on the type of liquid, to satisfy the pH level, purity, contamination level, freezing point, electrical resistivity and corrosion protection requirements (Saums et al., 2010). Already in the design stage, to avoid or reduce stresses and corrosion issues in specific operation conditions, the following should be carefully considered: the type of liquid, its operating parameters (flow rate, inlet and outlet temperatures, pressure drop, etc.), system pressure, electrical hazard prevention, surface passivation and liquid treatment with additives and corrosion inhibitors, and type of component materials (Ranchy et al., 1998; Saums, 2010). Corrosion, especially at stress points, can easily cause a leakage path.

Liquid hydraulic properties, such as viscosity, density and scaling tendency of the contaminate contained in the liquid, are affected by temperature. For example, pressure losses along the cooling circuit are slightly reduced when the coolant temperature rises, as its density and viscosity drops (Michel, 2012). However, high coolant temperatures can intensify corrosion or fouling between the parts generating heat losses and the coolant (Kadry, 2008). Steel corrosion is intensified by the active ions and oxygen contained in water. These undesirable processes can be reduced by the treatment of

water in vacuum de-aeration filters and by the addition of corrosion inhibitors. The de-aeration allows for reduction of the oxygen content of water and avoidance of corrosion due to oxygen diffusion, especially occurring at higher temperatures. In the case of stainless steel tubes, inter-granular corrosion is prevalent. The stainless steel is usually improperly heat-treated, and therefore the grain boundary areas depleted in chromium are less resistant to corrosion (Melinder, 2010). Low temperature and low chloride concentration of liquid help to preclude the stainless steel cracking. Erosion or metal deterioration from abrasive effects are weaknesses of copper. In the case of high liquid velocity and high temperature, the localization of erosion increases significantly, especially at tube bends (Melinder, 2010). Hence, the working parameters of the liquid cooling system being designed and the possible effects of these should both be carefully considered.

1.4 Thermal design and analysis of electrical machines

1.4.1 Thermal design of electrical machines

Currently, the main thermal design and analysis methods employed are experiments, the lumped parameter thermal network (LPTN), and the Finite Element Method (FEM) and Computational Fluid Dynamics (CFD) methods. Experiments provide the most accurate results, but are expensive compared with thermal analysis methods. Most researchers use the traditional method (which is LPTN) to predict the machine thermal behaviour and further to choose the proper cooling solution, as LPTN does not consume much time or computational resources (Vlach et al., 2005). Thermal analysis using LPNT is based on dividing the machine under study into several components and then representing these by isothermal nodes assumed to be thermally symmetrical in the radial directions to reduce their number (Di Gerlando and Vistoli, 2000). Each node is coupled with its neighbours by means of conduction and convection resistances. The heat flows propagate in the radial and axial directions. The convection and conduction resistances of the components are defined by the basic equations (Nerg et al., 2008):

$$R_{\text{cond}} = \frac{l}{s \cdot \lambda} \tag{1.24}$$

$$R_{\text{conv}} = \frac{1}{s_{\text{s}} \cdot \alpha_{\text{conv}}} \tag{1.25}$$

where l is the length of the body in the heat flow direction, λ is the thermal conductivity, s is the cross-sectional area, s_{s} is the surface area and α_{conv} is the convection coefficient (Mademlis et al., 2000).

The heat losses generated in the different parts of the machine are defined by the power loss vector. The cooling of the machine components is presented by the cooling matrix, with the thermal resistances of the cooling fluid flow passing the nodes (Nerg et al.,

2008). The temperature rises at each node in the steady state are calculated by solving the following equation.

$$[\Delta T] = ([R] + [R_{cf}])^{-1} \cdot [Q] \tag{1.26}$$

where $[R]$ is the square connection matrix containing the thermal resistances of the machine components, $[R_{cf}]$ is the cooling matrix with the thermal resistances of the cooling fluid flow passing the nodes, $[Q]$ is the power loss vector containing the losses at the machine components and $[\Delta T]$ is the temperature rise of the components compared with the initial surface temperature.

In the transient regime, the temperature rises at each node are calculated assuming the thermal capacitances

$$C = V \cdot \rho \cdot c_p$$

$$C_f = \upsilon_f \cdot s \cdot \rho_f \cdot c_{p_f} \cdot \Delta t \tag{1.27}$$

$$[C] \cdot [T] = [K] \cdot [T] + [Q] \tag{1.28}$$

$$\left(\text{heat stored}\right) = \begin{pmatrix} \text{net heat} \\ \text{flow} \end{pmatrix} + \begin{pmatrix} \text{heat} \\ \text{generated} \end{pmatrix}$$

$$\left[T^{t+\Delta t}\right] = \left[T^{t}\right] + \Delta t \cdot [C]^{-1} \cdot \left([K] \cdot \left[T^{t}\right] + [Q]\right)^{-1} \tag{1.29}$$

where C is the thermal capacitance of a machine component, V is the volume of the machine component, C_f is the thermal capacitance of a fluid, υ_f is the average velocity of the fluid, s is the cross-sectional area where the fluid is crossing, ρ is the density of the machine component material, ρ is the density of the fluid, c_{pf} is the heat capacity of the fluid, c_p is the heat capacity of machine component material, $[C]$ is the diagonal matrix of the capacitances of the machine components (J/K), $[T]$ is the vector containing the temperatures at the machine components, $[K]$ is the matrix of the thermal conductance of the machine components (W/K) and Δt is the time step. The rate of the temperature change of each element; i.e., the balance of the heat stored, generated and net heat flow in or out of the machine components (Hey et al., 2011) is presented in Eq. (1.28). Eq. (1.29) presents the difference equation discretized from the differential Eq. (1.28) to define the temperatures of the machine components at each time increment (Hey et al., 2011).

The lumped parameter models are described and experimentally validated in multiple references. One of the first detailed LPTN models with 10 components and 15 nodes was presented by Mellor et al. (1991) for totally enclosed fan cooled (TEFC) design electrical machines (Fig. 1.7 (a)). The presented thermal model was confirmed by experimental temperature data on 75 kW and 5.5 kW induction motors. The authors

concluded that the simulated temperatures were lower than the measured ones because of the surface air gap heat removal roughly estimated by analytical correlations, the mounting methods and other possible reasons. Another thermal network of a 20 kW TEFC induction machine was described by Di Gerlando and Vistoli (1993). The results of the steady state LPTN model were validated on a 3 kW motor prototype with temperature rise differences between 1–3 ºC.

An extensive description of the lumped parameter-based thermal analysis for a radial flux electrical machine with a high-power density was reported by Nerg et al. (2008). As most of the machine structural parts have cylindrical forms, the authors used simplified T-equivalent blocks for their representation. The authors pointed out that the radiation heat transfer processes exist mainly between the end windings, the surrounding medium and the frame. The nodal temperatures were calculated by the construction of a power loss vector, a thermal conductance matrix and an additional cooling matrix for a machine with open circuit cooling. The thermal model presented was validated on three machines: a 430-kW high-speed solid-rotor induction motor with a slitted rotor, a 45-kW low-speed fractional slot PMSM with a laminated rotor core and embedded V-magnets, and a 1.56-MW fractional-slot salient-pole PM synchronous generator. The sensitivity analysis of the developed models was based on the modification of convection coefficients and thermal conductivities by ±30% from the calculated values. It was concluded that in high-speed (high linear speed) machines, the most critical coefficients are the convection coefficients between the stator, the rotor teeth and the air gap and those of the radial conduction of the stator winding. In low-speed applications (low linear speed), the thermal resistance of the stator slot impregnation and the thermal contact resistance between the frame and the stator stack have the greatest effects on the machine thermal behaviour.

Boglietti and Cavagnino (2007) have used thermal network modelling to study the heat transfer between the end winding and the motor frame for three TEFC motors with rated powers of 4, 7.5 and 11 kW. The main idea was to investigate the influence of the construction enhancements, such as short circuit rings with several wafters, fins or tips, which created air whirls inside the motor end caps (Fig. 1.7 (b)). The authors concluded that all motor part over-temperatures decreased with the inner air speed increase, but at high speeds, the inner cooling effects could be less effective (there was less drop in temperature with the wafters application). It was observed that the end winding and the slot winding temperatures had similar values. Only at high rotor speeds is the end winding temperature colder than the slot copper; this is because of the ventilation effect caused by the wafters. In thermal network analysis, it was shown that a linear dependence of the heat transfer coefficients on the inner air speed exists and that the inner ventilation is more effective for a motor containing more free space around the end winding.

Ferreira and Costa (2012) presented an analytical thermal equivalent circuit (steady state conditions) of an axial flux permanent magnet machine for a small-scale, direct-driven wind generation system. The thermal equivalent circuit of the machine was

described in detail. It was concluded that 1) heat in axial flux machine stacks flows only in the axial direction due to the stator silicon steel thermal anisotropy and that 2) from the slots, heat flows to the teeth but not to the stator yoke. The experimental values showed that compared with the measured temperatures, the calculated temperatures were overestimated due to the over-dimensioned thermal resistances.

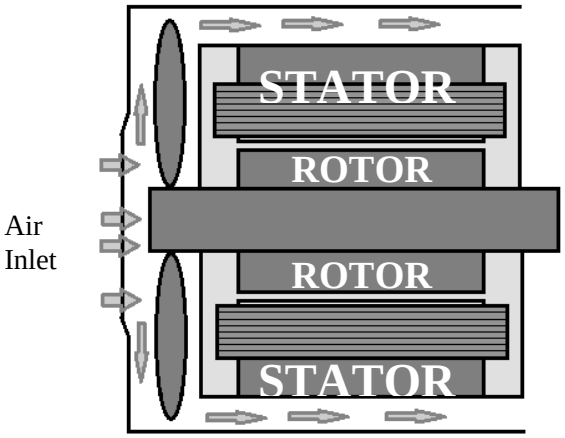

(a)

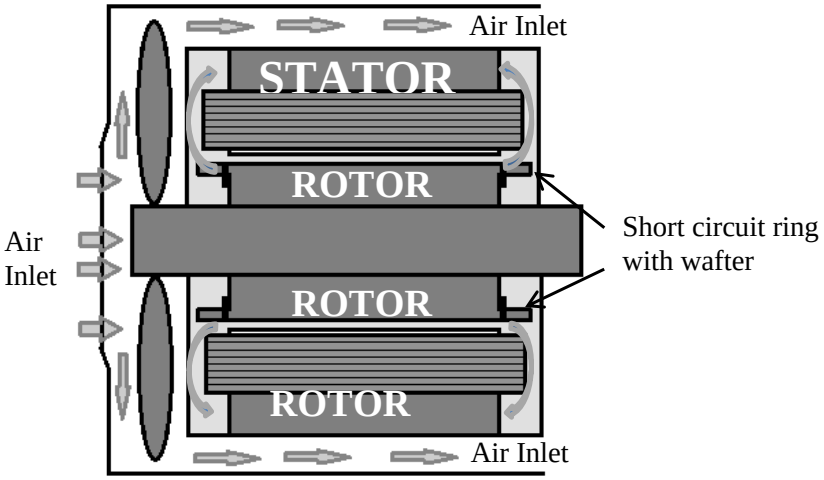

(b)

Figure 1.7: Totally enclosed fan cooling machine (a) (Mellor et al., 1991) and construction enhancements inside the machine end-caps (b) (Boglietti and Cavagnino, 2007).

The convection heat transfer coefficients in the end cap and the air-gap regions, described by the above authors are presented in Table 1.8. The temperature rise of the machine temperatures is shown to present the effectiveness of the cooling method.

Table 1.8 Characteristics of the machines presented in the literature study with TEFC.

Machine and Cooling method	Temperature Rise Stator/Rotor	Convection Coefficient
75 kW induction motors , TEFC (Mellor et al., 1991)	70K/148K	In air gap (Gazley, 1958): $Nu = 2.2$, $Ta \leq 41$ $Nu = 0.23 \cdot Ta^{0.63} \cdot Pr^{0.27}$, $41 < Ta \leq 100$ In stator end cap (Luke, 1923): $\alpha_{conv} = 15.5 \cdot (0.29 \cdot \upsilon_{air} + 1), \upsilon_{air} \approx 7.5 m/s$ In rotor (Mori and Nakayama, 1967): $Nu = 0.83 \cdot (Re \cdot Ra)^{0.2}$
3 kW 50Hz induction motor , TEFC, (Di Gerlando and Vistoli, 1993)	89K/118K	In stator end cap (Symons and Walker's law): $\alpha_{conv} = 10 \cdot (0.54 \cdot \upsilon_r^2 + 1)$ In rotor: $\alpha_{conv} = 4 \cdot (\upsilon_r + 10)$
4,7.5 and 11 kW 2400 rpm induction motors , TEFC, (Boglietti and Cavagnino, 2006)	55K/-	In stator end cap: $\alpha_{conv} = 5.49 \div 6.86 \cdot \upsilon_r$ where υ is the air velocity.

Although the LPTN method is relatively fast and does not require extensive computational resources, it merely yields mean or average temperatures (without hot-spots) of the machine components. Also, a thermal model based on LPTN is unclear concerning thermal contact resistances, convective heat transfer coefficients and fluid domain modelling (Howey, 2010). The growing power of newly developed machines push researchers in their search for hybrid cooling solutions, meaning that more sophisticated and detailed thermal design is required. The temperature of the machine parts may differ significantly depending on locations (Centner and Costa, 2012). The computation method based on the Finite Element Method (FEM) is used to define the detailed temperature distribution within the machine parts and to provide the best cooling configuration. The main disadvantage of FEM design is the impossibility to simulate fluid flows, resulting in the imposition of convection coefficients, which easily results in uncertainty. In FEM, the air gap is defined as solid and has higher thermal conductivity than ordinary air does. The surfaces in the air gap can be considered smooth cylindrical. Then, the experimental results of Ball, Farouk and Dixit (1989) are used to determine the effective thermal conductivity of the air in the air gap. This parameter is defined as the thermal conductivity that the stationary air should have in order to transfer the same amount of heat as the moving air (Mademlis et al., 2000).

$$\lambda_{ag} = 0.069 \cdot (K_r)^{-2.9084} \cdot Re_f^{0.4614 \cdot \ln(3.3361 \cdot Kr)} \tag{1.30}$$

$$K_r = \frac{r_{outr}}{r_{inst}} \tag{1.31}$$

$$Re_f = \frac{r_{outr} \cdot \delta \cdot (n/60)}{\nu_f} \tag{1.32}$$

where δ is the length of the air gap, λ_{ag} is the thermal conductivity of the air in the air gap, Re_f is the Reynolds number of the air, n is the synchronous rotor speed, r_{outr} is the outer rotor radius, r_{outr} is the inner stator radius and ν_f is the kinematic viscosity of air (Mademlis et al., 2000).

A totally enclosed fan-cooled (TEFC) four-pole 1-kW synchronous motor was analysed by Mademlis et al. (2000), by using a 2D FEM thermal steady-state simulation model of one machine pole pitch. The simulated and measured results were both deemed optimal in the categories of loss minimization control and nominal operation. The paper of Marignetti et al. (2012) presents a 2D FEA thermal analysis of an axial flux synchronous permanent magnet machine, including defined convection coefficients on the outer surfaces and air velocity in the air gap (Table 1.8). The stator temperature was similar in both the experimental tests and computation, but the rotor was remarkably hotter in the tests than anticipated due to the air-gap harmonics ignored in the loss simulation.

In FEM thermal analysis, the convection coefficients are calculated using analytical correlations from the literature and are subsequently imposed on the machine back and outer surfaces. This can cause uncertainty concerning the temperature distribution. Tong et al. (2010) conducted both LPTN and FEM analyses on a 2 MW DD permanent magnet wind generator. The cooling system was based on forced air through the frame radial fins. A 3D FE model of one tooth pitch slot was created to predict the temperature distribution. The hottest parts of the machine were the end windings and the rotor embedded-permanent-magnets, whose temperature rises were respectively 94.8 ˚C and 44.8 ˚C, with an ambient temperature of 30 ˚C. The authors showed experimental results on a 10 kW wind generator prototype to validate the computational results. Another paper of Tong et al. (2010) described the cooling system design for a 1.5 MW multibrid PM wind generator, using an equivalent ventilation network and a 3D FEM model. The machine cooling system comprised 24 reinforced air ventilated tenders placed between the stator core and the frame and the forced air cooling of the air gap. The whole machine, with assumed convection coefficients in the air ducts and end surfaces, was modelled by 3D FEM to assess the cooling system performance. The maximum temperature rise of the winding was 80K near the end winding outlet and 84K at the permanent magnets. The calculation results were validated by measurements on a 10 kW PM wind generator.

During the last several decades, CFD thermal analysis has become popular, as it is useful in cases of forced air cooling systems and combined stator liquid jacket and rotor passive/forced air cooling solutions, where air distribution inside the machine is essential. The CFD method allows one to find the temperature distribution within the machine parts (especially in the rotor) with a greater accuracy than with FEM. CFD also simulates the convection coefficient on the machine end surfaces and in the air gap more precisely than FEM does, as the fluid movement is included. With FEM, the convection coefficients are predefined by the user, based on analytical equations. However, high computational resources are required for providing the proper thin mesh to define turbulences and convection coefficients. Many researchers and engineers utilize energy equations and the flow model based on the Navier-Stokes equations for thermal analysis of electrical machines. There are also other turbulence models, such as Large Eddy Simulations and Direct Numerical Simulation (Durst and Karthik, 2011).

The model of a single fluid is presented by the equation of conservation of mass (continuity equation), by the momentum conservation law and by the internal energy conservation law (energy equation) as follows (Howey, 2010; Semenov, 2013):

$$\frac{\mathrm{d}\rho}{\mathrm{d}t} + \rho\vec{\nabla}\cdot\vec{\upsilon} = 0 \tag{1.33}$$

$$\rho\frac{\mathrm{d}\vec{\upsilon}}{\mathrm{d}t} = \rho\cdot\vec{F} + \frac{\partial\vec{\tau}_x}{\partial x} + \frac{\partial\vec{\tau}_y}{\partial y} + \frac{\partial\vec{\tau}_z}{\partial z} \tag{1.34}$$

$$\begin{pmatrix}\text{acceleration}\end{pmatrix} = \begin{pmatrix}\text{body}\\ \text{force}\end{pmatrix} + \begin{pmatrix}\text{momentum}\\ \text{diffusion}\\ \text{with}\\ \text{presureterm}\end{pmatrix}$$

$$\rho\frac{\mathrm{d}U}{\mathrm{d}t} = \vec{\tau}_x\cdot\frac{\partial\vec{\upsilon}}{\partial x} + \vec{\tau}_y\cdot\frac{\partial\vec{\upsilon}}{\partial y} + \vec{\tau}_z\cdot\frac{\partial\vec{\upsilon}}{\partial z} + q_v - \vec{\nabla}\cdot\vec{q} \tag{1.35}$$

$$\begin{pmatrix}\text{enthalpy}\\ \text{change}\end{pmatrix} = \begin{pmatrix}\text{dissipation}\\ \text{function with}\\ \text{presureterm}\end{pmatrix} + \begin{pmatrix}\text{volumetric}\\ \text{heat}\\ \text{source}\end{pmatrix} - \begin{pmatrix}\text{thermal}\\ \text{diffusion}\end{pmatrix}$$

where $\dfrac{\mathrm{d}}{\mathrm{d}t} = \dfrac{\partial}{\partial t} + \dfrac{\upsilon_x\partial}{\partial x} + \dfrac{\upsilon_y\partial}{\partial y} + \dfrac{\upsilon_z\partial}{\partial z},$

ρ is the density of the fluid, t is the time, υ is the velocity of the fluid, F is the resultant volumetric force of the fluid, τ is the stress tensor, U is the internal energy of the fluid (the kinetic energy of fluid molecules, the energy of chemical bonds etc.) defined by caloric equation, q_v is the volumetric heat source and q is the heat flux defined by thermal conduction equation.

$$\vec{q} = -\lambda \cdot \vec{\nabla} T \tag{1.36}$$

$$U = c_{\mathrm{v}} \cdot T \tag{1.37}$$

$$\lambda = \frac{c_{\mathrm{p}}}{Pr} \mu_0 \cdot \left(\frac{T}{T_0} \right)^K \tag{1.38}$$

$$c_{\mathrm{p}} = k_{\mathrm{B}} + c_{\mathrm{v}} \tag{1.39}$$

where U is the internal energy of the fluid, Pr is the Prandtl number, μ_0 is the dynamic viscosity of the fluid at specific temperature, λ is the heat conduction of the fluid, c_{v} is the specific heat capacity of the fluid at constant volume, c_{p} is the specific heat capacity of the fluid at constant pressure, K is the experimentally defined coefficient ($0 \leq K \geq 1$), T and T_0 are the temperature and the specific temperature of the fluid respectively and k_{B} is the specific gas constant or Boltzman constant (8.314 J/(mol·K)).

The components of the stress tensor (normal stresses and shear stresses) could be presented by the Newtonian or viscous fluid model (Durst and Karthik, 2011; Semenov, 2013).

$$\tau_{xx} = -p - \frac{2}{3} \cdot \mu \cdot \left(\frac{\partial \upsilon_x}{\partial x} + \frac{\partial \upsilon_y}{\partial y} + \frac{\partial \upsilon_z}{\partial z} \right) + \frac{2}{3} \cdot \mu \cdot \frac{\partial \upsilon_x}{\partial x} \tag{1.40}$$

$$\tau_{yy} = -p - \frac{2}{3} \cdot \mu \cdot \left(\frac{\partial \upsilon_x}{\partial x} + \frac{\partial \upsilon_y}{\partial y} + \frac{\partial \upsilon_z}{\partial z} \right) + \frac{2}{3} \cdot \mu \cdot \frac{\partial \upsilon_y}{\partial y} \tag{1.41}$$

$$\tau_{zz} = -p - \frac{2}{3} \cdot \mu \cdot \left(\frac{\partial \upsilon_x}{\partial x} + \frac{\partial \upsilon_y}{\partial y} + \frac{\partial \upsilon_z}{\partial z} \right) + \frac{2}{3} \cdot \mu \cdot \frac{\partial \upsilon_z}{\partial z} \tag{1.42}$$

$$\tau_{xy} = \tau_{yx} = \mu \cdot \left(\frac{\partial \upsilon_x}{\partial y} + \frac{\partial \upsilon_y}{\partial x} \right) \tag{1.43}$$

$$\tau_{yz} = \tau_{zy} = \mu \cdot \left(\frac{\partial \upsilon_y}{\partial z} + \frac{\partial \upsilon_z}{\partial y} \right) \tag{1.44}$$

$$\tau_{xz} = \tau_{zx} = \mu \cdot \left(\frac{\partial \upsilon_x}{\partial z} + \frac{\partial \upsilon_z}{\partial x} \right) \tag{1.45}$$

where μ is the dynamic viscosity of the fluid and p is the pressure of the fluid defined by the thermal equation (the systems' internal and external parameters).

$$\mu = \mu_0 \cdot \left(\frac{T}{T_0} \right)^K \tag{1.46}$$

$$p = \rho \cdot k_{\mathrm{B}} \cdot T \tag{1.47}$$

Eq. (1.33) and (1.34) represent the thermodynamic model of perfect gas, which is utilized to model non-reacting flows. The inviscid or ideal fluid can be obtained from the Newtonian or viscous fluid model ($\mu = 0$).

Among the CFD models, the most popular one is the incompressible flow model, in which the continuity equation, the momentum conservation equation and the energy equation are presented in the following forms (Semenov, 2013):

$$\vec{\nabla} \cdot \vec{\upsilon} = 0 \tag{1.48}$$

$$\frac{\partial(\rho \cdot \vec{\upsilon})}{\partial t} + \vec{\upsilon} \cdot \vec{\nabla}(\rho \cdot \vec{\upsilon}) = -\vec{\nabla} p + \mu \cdot \Delta \vec{\upsilon} \tag{1.49}$$

$$\rho \cdot c_{\mathrm{p}} \frac{\mathrm{d}T}{\mathrm{d}t} = \mu \cdot \Phi + q_{\mathrm{v}} + \lambda \cdot \Delta T \tag{1.50}$$

$$\Phi = 2 \cdot \left(\left(\frac{\partial \upsilon_x}{\partial x} \right)^2 + \left(\frac{\partial \upsilon_y}{\partial y} \right)^2 + \left(\frac{\partial \upsilon_z}{\partial z} \right)^2 \right) + \left(\frac{\partial \upsilon_x}{\partial y} + \frac{\partial \upsilon_y}{\partial x} \right)^2 \rightarrow + \left(\frac{\partial \upsilon_y}{\partial z} + \frac{\partial \upsilon_z}{\partial y} \right)^2 + \left(\frac{\partial \upsilon_x}{\partial z} + \frac{\partial \upsilon_z}{\partial x} \right)^2 \tag{1.51}$$

where Δ – is the second-order differential operator, Φ is the dissipation function (the dissipation of the flow kinetic energy into the heat).

The time averaged solution for Navier-Stokes equations or the equation of motion for fluid flow is based on the Reynolds Averaged Navier Stokes (RANS) equations. The RANS equations handle turbulence by time-averaging the flow variables, so velocity, pressure and temperature are presented by a mean variable ($\bar{\upsilon}, \bar{p}, \bar{T}$) and a fluctuating variable (υ', p', T'). The energy equations and momentum in Reynold's Stress Models result in the following form (Launder et al, 1975):

$$\rho \frac{\mathrm{d}\bar{\upsilon}}{\mathrm{d}t} = \rho \cdot g - \nabla \bar{p} + \nabla \tau_{\mathrm{ij}} \tag{1.52}$$

$$\tau_{\mathrm{ij}} = \mu \cdot \left(\frac{\partial \upsilon_{\mathrm{i}}}{\partial x_{\mathrm{j}}} + \frac{\partial \upsilon_{\mathrm{j}}}{\partial x_{\mathrm{i}}} \right) - \rho \left(\overline{u_{\mathrm{i}}' u_{\mathrm{j}}'} \right) \tag{1.53}$$

$$\begin{pmatrix} \text{stress} \\ \text{tensor} \end{pmatrix} = \begin{pmatrix} \text{shear} \\ \text{stress} \end{pmatrix} + \begin{pmatrix} \text{turbulent} \\ \text{stress} \end{pmatrix}$$

$$\rho \cdot c_{\mathrm{p}} \frac{\mathrm{d}\overline{T}}{\mathrm{d}t} = -\frac{\partial}{\partial x_{\mathrm{i}}}\left(q_{\mathrm{i}}\right) + \overline{\Phi} \tag{1.54}$$

$$\overline{\Phi} = \frac{\mu}{2} \cdot \overline{\left(\frac{\partial \overline{\upsilon_{\mathrm{i}}}}{x_{\mathrm{j}}} + \frac{\partial \upsilon_{\mathrm{i}}^{'}}{\partial x_{\mathrm{j}}} + \frac{\partial \overline{\upsilon_{\mathrm{j}}}}{x_{\mathrm{i}}} + \frac{\partial \upsilon_{\mathrm{j}}^{'}}{\partial x_{\mathrm{i}}} \right)^2} \tag{1.55}$$

$$q_{\mathrm{i}} = -\lambda \cdot \frac{\partial \overline{T}}{\partial x_{\mathrm{i}}} + \rho \cdot c_{\mathrm{p}} \cdot \overline{\upsilon_{\mathrm{i}}^{'} T^{'}} \tag{1.56}$$

$$\begin{pmatrix} \text{volumetric} \\ \text{heat} \\ \text{source} \end{pmatrix} = \begin{pmatrix} \text{heat} \\ \text{flux} \\ \text{by conduction} \end{pmatrix} + \begin{pmatrix} \text{turbulent} \\ \text{heat} \\ \text{flux} \end{pmatrix}$$

where i and j are the unit vectors, $\left(\overline{u_i^{'} u_j^{'}}\right)$ is the turbulent inertia tensor and $\left(\overline{\rho u_{\mathrm{i}}^{'} u_{\mathrm{j}}^{'}}\right)$ is the turbulence or Reynolds stress, which is represented by the Boussinesq approximation.

$$-\overline{\rho u_{\mathrm{i}}^{'} u_{\mathrm{j}}^{'}} = \mu_{\mathrm{T}} \cdot \left(\frac{\partial \upsilon_{\mathrm{i}}}{\partial x_{\mathrm{j}}} + \frac{\partial \upsilon_{\mathrm{j}}}{\partial x_{\mathrm{i}}} - \frac{2}{3}\left(\nabla \cdot \vec{\upsilon}\right)\delta_{\mathrm{ij}} \right) - \frac{2}{3}\rho \cdot k \cdot \delta_{\mathrm{ij}} \tag{1.57}$$

where μ_{T} is the turbulent dynamic viscosity of the fluid, k is the turbulent kinetic energy and δ_{ij} is the Kronecker delta.

$$\vec{q} = -\left(\lambda + \lambda_{\mathrm{T}}\right) \cdot \nabla T = -\left(\mu \frac{c_{\mathrm{p}}}{Pr} + \mu_{\mathrm{T}} \frac{c_{\mathrm{p}}}{Pr_{\mathrm{T}}} \right) \cdot \nabla T \tag{1.58}$$

where λ and λ_{T} are the molecular and the turbulent thermal conductivities of the fluid, and Pr and Pr_{T} are the laminar and the turbulent Prandtl numbers of the fluid.

One of the most popular turbulence models is the κ-ε turbulence model, in which the turbulence viscosity coefficient or eddy viscosity is determined by (Chien, 1982)

$$\mu_{\mathrm{T}} = K_{\mu} \cdot \frac{\rho \cdot k^2}{\varepsilon} \tag{1.59}$$

where K_{μ} is the empirical coefficient, k is the turbulent kinetic energy, and ε is the dissipation of the turbulent kinetic energy (the rate at which the velocity fluctuations dissipate). The model transport equations for the κ-ε turbulence model are as follows:

$$\frac{\partial(\rho \cdot k)}{\partial t} + \frac{\partial(\rho \cdot k \cdot \mu_{\mathrm{i}})}{\partial x_{\mathrm{i}}} = \frac{\partial}{\partial x_{\mathrm{j}}}\left(\left(\mu + \frac{\mu_{\mathrm{T}}}{\mathrm{Pr}_{\mathrm{k}}} \right) \frac{\partial k}{\partial x_{\mathrm{j}}} \right) + W_{\mathrm{ke}} + W_{\mathrm{b}} - \rho \cdot \varepsilon - Y_{\mathrm{M}} + S_{\mathrm{k}} \tag{1.60}$$

$$\frac{\partial(\rho\cdot\varepsilon)}{\partial t}+\frac{\partial(\rho\cdot\varepsilon\cdot\mu_{\mathrm{i}})}{\partial x_{\mathrm{i}}}=\frac{\partial}{\partial x_{\mathrm{j}}}\left(\left(\mu+\frac{\mu_T}{\mathrm{Pr}_{\mathrm{k}}}\right)\frac{\partial\varepsilon}{\partial x_{\mathrm{j}}}\right)+C_{1\varepsilon}\cdot\frac{\varepsilon}{k}\cdot(W_{\mathrm{ke}}+C_{3\varepsilon}\cdot W_{\mathrm{b}})\rightarrow$$
$$-C_{2\varepsilon}\cdot\rho\cdot\frac{\varepsilon^2}{k}-Y_{\mathrm{M}}+S_{\varepsilon} \tag{1.61}$$

$$\begin{pmatrix}\text{rate of change}\\ \text{of k or }\varepsilon\end{pmatrix}+\begin{pmatrix}\text{transport}\\ \text{of k or }\varepsilon\\ \text{by convection}\end{pmatrix}=\begin{pmatrix}\text{transport}\\ \text{of k or }\varepsilon\\ \text{by diffusion}\end{pmatrix}+\begin{pmatrix}\text{rate of production}\\ \text{of k or }\varepsilon\end{pmatrix}-\begin{pmatrix}\text{rate of destruction}\\ \text{of k or }\varepsilon\end{pmatrix}$$

where W_{ke} and W_{b} are the generations of turbulent kinetic energy due to the mean velocity gradient and to buoyancy, Y_{M} is the fluctuating dilatation in compressible turbulence; $C_{1\varepsilon}$, $C_{2\varepsilon}$ and $C_{3\varepsilon}$ are model constants, Pr_{k} and Pr_{ε} are turbulent Prandtl numbers for k and ε, and S_{k} and S_{ε} are source terms for k and ε. The model κ-ε turbulence is valid mainly for fully turbulent flows but poor for complex flows with severe pressure gradients, separation and strong streamline curvature (Menter, 1993; Menter, 1994).

The $k - w$ turbulence model is intended for boundary-layer flows in the viscous near-wall region treatment, for streamwise pressure gradient applications and for low Reynolds number flows. It should be avoided outside the shear layer that is a free-stream boundary (Borges and Cezarion, 2012).

$$\frac{\partial(\rho\cdot k)}{\partial t}+\frac{\partial\left(\rho\cdot\vec{\upsilon}_{\mathrm{j}}\cdot k\right)}{\partial x_{\mathrm{j}}}=\frac{\partial}{\partial x_{\mathrm{j}}}\left(\left(\mu+\frac{\mu_{\mathrm{T}}}{\mathrm{Pr}_{\mathrm{k}}}\right)\frac{\partial k}{\partial x_{\mathrm{j}}}\right)+W_{\mathrm{ke}}-C_1\cdot\rho\cdot k\cdot w+W_{\mathrm{kb}} \tag{1.62}$$

$$\frac{\partial(\rho\cdot w)}{\partial t}+\frac{\partial\left(\rho\cdot\vec{\upsilon}_{\mathrm{j}}\cdot w\right)}{\partial x_{\mathrm{j}}}=\frac{\partial}{\partial x_{\mathrm{j}}}\left(\left(\mu+\frac{\mu_{\mathrm{T}}}{\mathrm{Pr}_{\mathrm{w}}}\right)\frac{\partial w}{\partial x_{\mathrm{j}}}\right)+C_2\cdot\frac{w}{k}\cdot W_{\mathrm{ke}}-C_3\cdot\rho\cdot w^2+W_{\mathrm{wb}} \tag{1.63}$$

where w is the dissipation rate of the turbulent kinetic energy (turbulent frequency), W_{kb} and W_{wb} are the generations of turbulent kinetic energy due to buoyancy terms, Pr_{w} are turbulent Prandtl numbers for w, and C_1, C_2 and C_3 are model constants.

The shear-stress transport (SST) $k - w$ turbulence model was developed by Menter (Menter, 1993; Menter, 1994). It is a turbulence model, where the $k - w$ turbulence model is applied in the near-wall region (in a boundary layer) and k and ε turbulence model in the far field (outside of the turbulence) (Kuosa, 2002; Borges and Cezarion, 2012). The ε equation (1.47) is transferred into the w equation (1.49) to provide a smooth change between the models. The $k - w$ SST turbulence model incorporates a damped cross-diffusion derivative term in the w equation or the limited turbulent stress in a boundary layer to avoid unrealistic strain rates and contains the limitation for the turbulence viscosity coefficient to account for the transport of the turbulent shear stress (Kuosa, 2002; Borges and Cezarion, 2012).

$$\frac{\partial(\rho \cdot k)}{\partial t} + \frac{\partial(\rho \cdot k \cdot \mu_{\mathrm{i}})}{\partial x_{\mathrm{i}}} = \frac{\partial}{\partial x_{\mathrm{j}}}\left(\Gamma_{\mathrm{k}} \frac{\partial k}{\partial x_{\mathrm{j}}}\right) + W_{\mathrm{mean\ vg}} - Y_{\mathrm{k}} + S_{\mathrm{k}} \tag{1.64}$$

$$\frac{\partial(\rho \cdot w)}{\partial t} + \frac{\partial(\rho \cdot w \cdot \vec{v}_{\mathrm{i}})}{\partial x_{\mathrm{i}}} = \frac{\partial}{\partial x_{\mathrm{j}}}\left(\Gamma_{\mathrm{w}} \frac{\partial w}{\partial x_{\mathrm{j}}}\right) + W_{\mathrm{w}} - Y_{\mathrm{w}} + S_{\mathrm{cdif}} + S_{\mathrm{w}} \tag{1.65}$$

$$\Gamma_{\mathrm{k}} = \mu + \frac{\mu_{\mathrm{t}}}{Pr_{\mathrm{k}}} \tag{1.66}$$

$$\Gamma_{\mathrm{w}} = \mu + \frac{\mu_{\mathrm{t}}}{Pr_{\mathrm{w}}} \tag{1.67}$$

where $W_{\mathrm{mean\ vg}}$ is the generation of turbulence kinetic energy due to the mean velocity gradients, W_{w} is the generation of w, Y_{k} and Y_{w} are the dissipation of k and w, Γ_{k} and Γ_{w} are the effective diffusivity of k and w, S_{cdif} is the cross-diffusion term, Pr_{k} and Pr_{w} are turbulent Prandtl numbers for k and w, and S_{w} is the source term for w. The SST $k - w$ turbulence model is merited for its good behaviour in adverse pressure gradients and separating flow (Borges and Cezarion, 2012; Durst and Karthik, 2011). There are a fair amount of other turbulent models (κ-ε RNG model, κ-ε realizable model, algebraic stress model, etc.), and each is used for certain types of flows and conditions (Durst and Karthik, 2011). The selection of the appropriate model should be based on the case studied (flow conditions, geometry, etc.) and computational power available. Unfortunately, many researchers and engineers have limited computational resources; therefore, the computational analyses are made using assumptions, which is why the accuracy of the results is diminished.

CFD analysis is popular among researchers working with the thermal design of the synchronous salient pole electrical machine. Pickering et al. (2002) presented the heat transfer analysis of a 1 MVA synchronous salient pole electrical machine with symmetric double-sided ventilation. The field coil faces were extended to give a ribbed surface. A CFD model with two million volume cells was created and simulated by CFD software Fluent 5, using the standard κ-ε turbulence model. The authors concluded that CFD tends to under-predict heat transfer coefficients by 20–30% compared with the tests due to the steady-state approximation of the rotor-stator interaction. The simulation model showed that the convection heat transfer coefficient and the pressure drop through the machine increased by 106% and by 22%, respectively, in the case of a 1mm roughness height, compared with the results of the smooth rotor testing and measured at 16 key locations around one rotor pole. There is no information about the convection coefficient measuring method. Using CFD modelling, Shanel et al. (2003) studied the influence of the supported V-blocks on the temperature distribution along the conductors in the slot for the same 1 MVA air-cooled salient pole generator. The standard κ-ε turbulence model, the multiple- reference frame model for rotor-stator interaction, and the wall functions were used for simulation purposes. It was shown that the wire-wound coils had higher hot spots in the centre than did the strip-on-edge coils,

because of the worse contact with the adjacent turn. The authors calculated the heat transfer coefficients on the machine internal surfaces, assuming air flow, thermal conductance and heat losses within the machine parts. Several modifications to the stator end winding V-blocks, such as different air ducts in the middle and near the winding surface, were presented and assessed. The air ducts near the end winding allowed for reducing the winding temperature by 6 ºC, while the air ducts in the middle of the V-blocks increased the winding temperature by 9.5 ºC, because part of the air was diverted from the end winding in this design. However, the simulation results have not been validated on the machine prototype.

The cooling of the end regions of a 200 kW two-pole strip-wound totally enclosed fan-cooled induction motor was investigated by Micallef et al. (2008). The CFD κ-ε turbulent model was used to simulate the air flow in the end regions. The optimum location of the lower spacers was in line with the rotor end ring. The long narrow shrouded wafters allowed for increasing the thermal resistance between the end winding and the frame by around 6% and for reducing the windage losses by more than 50%. The position of the axial fan above the end winding experienced a reduction of thermal resistance by 19% and an increase of the windage losses by a factor of 2.4. The arrangement of the fan blades close to the end shield allows the direct air flow between the end winding and the frame, therefore reducing the thermal resistance between them by 33%. The models used in the paper were validated by experimental measurements on the coil end winding. The local heat-transfer coefficients on the coil end winding acquired from the experiment were consistent with the CFD simulation results (with a discrepancy of up to 30 W/(m^2·K)).

The doctoral thesis of Howey (2010) presents a novel method of measured surface convective heat transfer in a partially enclosed rotor-stator system using thin film electrical heaters constructed on a printed circuit board. The author studied the heat transfer on the stator surface. 2D and 3D CFD simulations of the air flow were made and checked by experimental work. The study showed that the rotor heat transfer coefficient is higher than the stator heat transfer coefficient in disc type machines, and that the stator heat transfer is sensitive to the gap ratio and outlet, rotor size, rotor speed and roughness (Table 1.9). It was concluded that the inlet boundary conditions should be defined accurately, as these have a crucial influence on results.

Fasquelle et al. (2010) described a 210 kW multiphysical model of an enclosed induction machine with a rated speed of 4500 rpm for railway traction. The forced air flows through several bored ducts in the rotor and stator yoke provided the machine cooling. The CFD analysis of the motor quarter was achieved by the κ-ε turbulence model for three rotational speeds (1500, 2200 and 4000 rpm). The authors showed that the main part of the air mass flow rate (66–71%) was concentrated in the stator slot openings, while the smallest part of the air mass flow rate (6–8%) was in the rotor slot openings. The computational results were validated by experiments under load operation conditions for rotational speeds of 1500, 2200, 3010 and 3500 rpm. It was shown that the temperature gradient on the external wall will reach 60 ºC in a steady

state. The authors concluded that the largest part of the heat evacuation (90%) was assigned to the convection through the stator ducts. The temperature of the rotor copper windings near the internal fan was higher than the temperature of the stator copper windings near the external fan. The sensitivity analysis presented showed that the increase of the convection coefficient from 5 W/(K·m^2) to 15 W/(K·m^2) between the external walls of the magnetic sheets and the end shields allows for decreasing the temperatures of the stator and rotor sheets by 15 ºC and 30 ºC, respectively. The discrepancies between the measured and the simulated results vary between 8 and 14 K, which can be caused by some contact resistances that have not been considered in the model.

Table 1.9 summarizes the characteristics of the electrical machines with the air cooling and the equations utilized for the analytical thermal design. The temperature rises in the stators and rotors, and the coolant flows are listed to demonstrate the effectiveness of the cooling solutions applied.

Table 1.9 Characteristics of the machines presented in the literature study with air cooling.

Machine and Cooling method	Temperature Rise Stator/Rotor (coolant flow)	Convection Coefficient
		Forced Cooling
430 kW 170 Hz induction motor, Forced Air Cooling; 1.5 MW low-speed PMSM, Passive Air (Nerg et al., 2008)	100K/70K (0.37 m^3/s) 90K/-	In air gap (high-speed) (Larjola et al., 1990): $Nu = 0.0214 \cdot (Re_f^{0.8} - 100) \cdot Pr_f^{0.4} \cdot \left(1 + \left(d_h / \delta\right)^{2/3}\right)$ where d_h is the hydraulic diameter of air gap, δ is the length of air gap In air gap (low-speed): $Nu = 2$, Ta_m<1700 $Nu = 0.128 \cdot Ta_m^{0.367}$, 1700<$Ta_m$<$10^4$ $Nu = 0.409 \cdot Ta_m^{0.241}$, 10^4<Ta_m<10^7
1 kW 60000 rpm SRM (11100 kW/m^3), Forced Air Cooling (Brauer and De Doncker, 2011)	60K/- (0.04 m^3/s)	In air gap (VDI-Waermeatlas, 2003): $Nu = \frac{0.037 \cdot Re^{0.8} \cdot Pr}{1 + 2.443 \cdot Re^{-0.1} \cdot \left(Pr^{2/3} - 1\right)}$ In stator slots (VDI-Waermeatlas, 2003):: $Nu = \frac{\left(f/8\right) \cdot \left(Re - 1000\right) \cdot Pr \cdot \left(1 + \left(l^{2/3} / l_{stk}\right)\right)}{1 + 12.7 \cdot \left(f/8\right)^{0.5} \cdot \left(Pr^{2/3} - 1\right)}$ where l is the characteristic length and l_{st} is the stator length
AFPMM (Heat flux at stator front – 500 W/K·m^2), Forced Air Cooling, (Lim et al.,	38 K/- (4 g/s)	For rotor (Wong, 1977): $Nu = 0.15 \cdot Re_w^{4/5} - 100 \cdot \left(\frac{r_{trans}}{r}\right)^2$,

2003)		$r_{trans} = \left(2.5 \cdot 10^5 \cdot \frac{\nu}{\Omega_r}\right)^{0.5}$, where r is the rotor outer radius, r_{trans} is the radius at which the transition occurs from laminar to turbulent flow, and Ω_r is the rotational speed. For rotor (peripheral edge) (Wong, 1977):: $Nu = 0.133 \cdot Re_w^{2/3} \cdot Pr^{1/3}$ For stator (air gap side) (Owen, 1989): $Nu = \frac{0.333 \cdot Q,}{\pi \cdot \nu \cdot r}$ where Q is the volumetric flow rate.
1.5 MW PMSM, Forced Air Cooling (stator axial ducts), (Tong et al., 2010)	80K/- (2.2 m^3/s)	For stator axial cooling duct (Shikun, 2000): $\alpha_{conv} = 28 \cdot \left(\left(0.5 \cdot \upsilon_r\right)^2 + \upsilon_a^2\right)^{0.25} + 1)$, υ_a and υ_r are the axial and radial velocity of air in the axial cooling duct.
		Passive Air Cooling
2.2 kW 1285 rpm AFSPMM (17 kPa), Passive Air Cooling, (Marignetti et al., 2012)	80K/55K	In stator (Becker's law) : $Nu = 0.119 \cdot Re^{2/3}$, $800 < Re < 10^5$ In rotor: $Nu = 0.046 \cdot Re^{0.7} \cdot \left(1 + \frac{8 \cdot Gr}{Re^2}\right)^{0.95}$ (Shimada Eq.) $Nu = 0.073 \cdot Re^{2/3}$ (Dropkin and Carmi)
1500 rpm RFPMSM and 3000 rpm AFPMSM (Howey, 2010; Howey et al., 2012)		In the air gap of a radial flux machine (Becker and Kaye, 1962): $Nu = 0.128 \cdot \left(\frac{Ta^2}{Fg^2}\right)^{0.367}$, $1700 < (Ta^2/Fg^2) < 10^4$ $Nu = 0.409 \cdot \left(\frac{Ta^2}{Fg^2}\right)^{0.241}$, $10^4 < (Ta^2/Fg^2) < 10^7$ $Nu = 0.54 \cdot Ra^{0.25}$, $10^5 < Ra < 10^7$ where Fg is the geometrical factor of the air gap. In the air gap of an axial flux machine (for the rotor side) (Dayli and Nece, 1960):: $Nu = 7.46 \cdot Re_\theta^{0.32}$, $Re_\theta < 10^5$ and $(\delta/D_r) \le 0.01$ $Nu = 0.5 \cdot \left(1 + 5.47 \cdot 10^{-4} \cdot e^{112 \cdot (\delta / Dr)}\right) \cdot Re_\theta^{0.5}$, $Re_\theta < 10^5$ and $0.02 \le (\delta/D_r) \le 0.06$ $Nu = 0.044 \cdot Re_\theta^{0.75}$, $Re_\theta > 10^5$ and $(\delta/D_r) \le 0.01$ $Nu = 0.033 \cdot \left(12.57 \cdot e^{-33.18 \cdot (\delta / Dr)}\right) \cdot Re,_\theta^{0.6 + 25 \cdot (\delta / Dr)^{12/7}}$, $Re_\theta > 10^5$ and $0.02 \le (\delta/D_r) \le 0.06$ where l_{ag} is the air gap length and D_r is the rotor diameter.

Analytical and computational thermal modelling techniques are used for the thermal design of electrical machines. The analytical method based on the lumped parameter thermal network is popular in electrical machine design based on passive air cooling, TEFC and liquid jacket (LJ) cooling. This method is cheap and fast, so it will probably be popular for a long time to come. LPTN is useful as a preliminary thermal design tool for choosing appropriate cooling methods. In the latter stages of machine design, precise computational tools are more applicable as they may define temperature distribution with high accuracy and thereby provide optimal final designs. LPTN is useful for the common machine geometries when the analytical equations for the convection coefficients are accurate. If the convection heat transfer correlations are unknown or invalid (especially in machines with unique geometry), CFD computational methods are more useful than LPTN. Electrical machines with forced air cooling often utilize complex and unique internal geometries (rotor and stator axial ducts, etc.) to increase the efficiency of the forced air flow, so CFD could prove very useful in decision-making concerning the best design thermally speaking and in view of low pressure losses. The computational method is also utilized for optimization of liquid jacket geometry in the machine housing and for analyses of the temperature field within the directly cooled stator and rotor conductors.

1.4.1 Thermal design of electrical machines with indirect liquid cooling

The common indirect liquid cooling system presents cooling tubes incorporated in the stator frame, the stator yoke or the end-rings. All thermal design methods discussed in the previous section are utilized for the thermal analysis of the machine with the indirect liquid cooling system.

LPTN is widely used for the thermal design of electrical machines with cooling systems based on liquid jackets, especially where conventional machine design is concerned. However, thermal modelling of the rotor embedded-permanent-magnets may be problematic, as their geometry and placement can be unique. The LPTN was used to analyse a 6 kW 12-pole automotive starter/alternator (rated tangential stress 20 kPa) and a 5 kW 4-pole electric water pump machine (rated tangential stress 2.8 kPa) with added water jackets in the housings (Fig. 1.8 (a)). In this paper El-Refaie et al. (2004) have recommended the enhancement of the thermal resistance of the rotor embedded-permanent-magnets by replacing the through-shaped magnets with cylindrical segments in a lumped parameter thermal model for a multi-barrier interior PM synchronous machine. Two network nodes representing the magnets were interconnected by thermal resistances for the numbered cylindrical sections and placed at the radial midpoints of the two magnet cavities. However, the modelling results have not been validated on the prototype. Another permanent magnet motor (60 kW and 3500 rpm) with the cooling system based on the stator frame water cooling jacket was analysed in the article of Fan et al. (2010). The lumped parameter network of the machine studied with 9 nodes was constructed based on equations presented in Mellor's article (1991). To simulate the transient temperature distribution in the driving motor, the dynamic thermal equation was adopted. The maximum temperature of the end winding was 63 ˚C at the ambient

temperature of 25 ˚C. The authors concluded that the simulated results were lower than the measured ones because of the assumed heat transfer correlations.

A stator frame liquid cooling system for the axial-field permanent magnet synchronous generator for an HEV drive train was reported by Crescimbini et al. (2003). The cooling of the machine was performed by water flow inside the incorporated aluminium cooling rings in the stator frame and air ventilation of the rotor parts (Fig. 1.8 (b)). The water inlet temperature of 50 ºC allowed for keeping the inner stator parts at temperatures lower than 100 ºC. The 3D simulation results were verified on the generator prototype with a rated power of 15 kW and rated speed of 4500 rpm (and a rated tangential stress of 43 kPa). Zheng et al. (2008) presented and analysed the cooling system of a four-quadrant transducer consisting of a stator and double rotor machine. The cooling of this machine was performed by water flow in twelve evenly distributed channels in the housing and by forced air entering in the air gap. The 2D thermal model of the machine was simulated with imposed water and air temperatures. As a result, the temperatures of the stator winding and the inner rotor winding stayed respectively below 74 ˚C and 177 ˚C at 1 m/s water velocity and 9 m/s air flow speed. The authors reported that the temperature of the stator winding is mainly correlated to the operation parameters of the water cooling system. The forced air cooling system had a significant effect on the rotor temperature but much less so on the stator winding temperature. The paper validates the simulation results through comparisons made with the experiment on the 4QT prototype machine. Another machine cooled by water circulating in the aluminium end plates and by forced air at 40 ˚C, presented in paper of King et al. (2008). The analysed high-speed permanent-magnet synchronous motor is designed to accelerate a high-speed pulse alternator. The water cooling system consisted of six parallel coolant paths located circumferentially in the stator end plates. The presented cooling system allowed a rotor surface temperature rise to 85 ˚C, based on the experiment results.

Kral et al. (2008) presented a thermal model of a 6 kW totally enclosed water-cooled induction motor. The machine under consideration has a cooling system which comprises 22 cooling bars with water flow inside in the housing. The thermal model with constant and transient duty cycles was developed by the authors with the modelling language Modelica. The thermal analysis shows that the stator winding heated to 100 ˚C if the working fluid was heated from 25 ˚C to 45 ˚C. The hottest parts of the rotor were the end windings, with a temperature of 140 ˚C. The test results were compared with the results obtained from the analytical model, and there was a good agreement between the results obtained by the different methods. Another design solution of a stator cooling system for an induction motor was presented by Sikora et al. (2011). The finned water pipes inserted between the stator yoke and the frame allow for cooling of the stator assembly and internal circulating air (Fig. 1.9 (b)). The authors discussed the main advantages of the water-cooled electrical machines over the air-cooled ones, such as higher efficiency, better power-to-dimension ratio and lower noise level. The results of the FEA modelling and accuracy of the dedicated thermal resistance formula were verified on a 7.5 kW induction motor prototype.

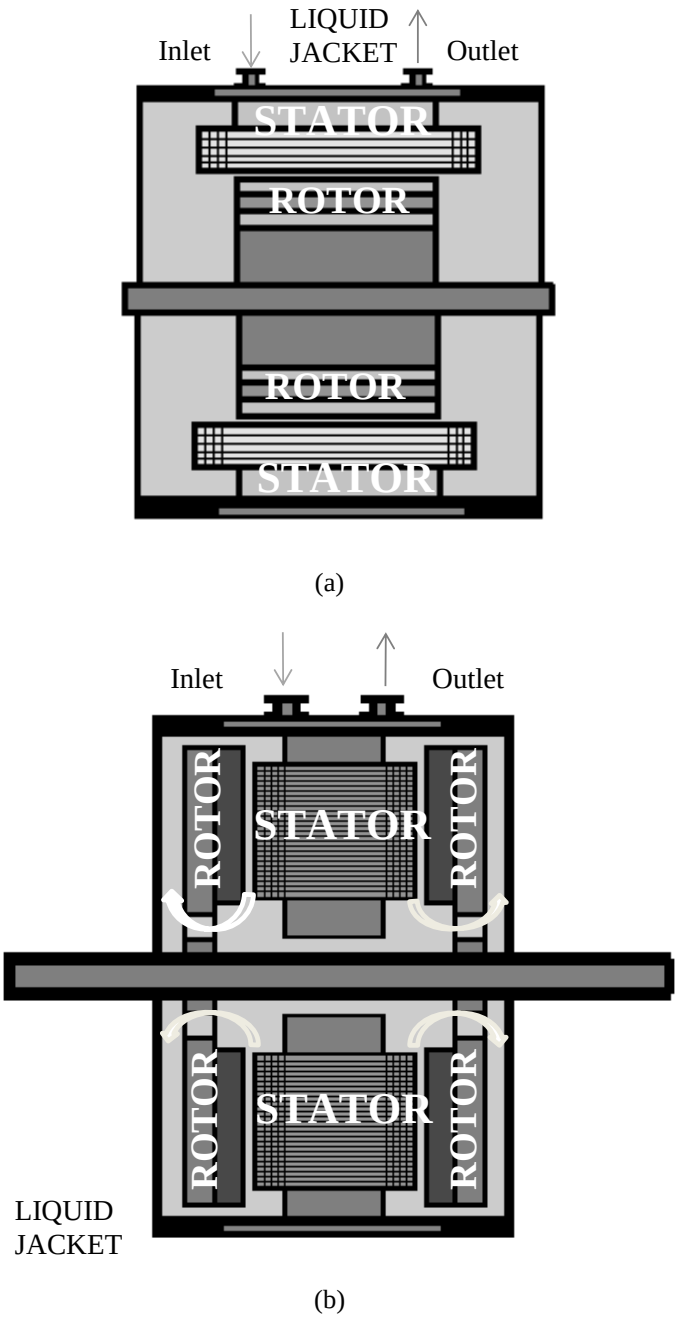

Figure 1.8: Radial flux electrical machine with cooling based on a water jacket (El-Refaie et al., 2004) (a); and axial flux electrical machine with cooling based on a water jacket (Crescimbini, 2003) (b).

In indirect liquid cooling machines, CFD analysis is usually utilized for the liquid jacket design and optimization. However, most of the modelled features have not been verified on the prototypes, so the validity of these results is questionable. The optimization of water flow inside a water-cooled electric motor frame was presented by Borges et al. (2008). The rated power of the machine studied was 75 kW. With the use of CFD techniques, it was shown that having a diffusor on the cooling circuit inlet in place of a pipe and moving this diffusor to the circuit middle part allowed for reducing the load loss by 18%, compared with the initial design.

Thermal modelling of a Slotted Totally Enclosed Axial Flux Machine (STEAM) was described in a paper by Odvarka et al. (2010). The machine consisted of two rotor plates with rotor surface-mounted permanent magnets and a toroidally-wound stator core pack in the middle. The machine cooling system was based on water cooling. An aluminium water jacket was sandwiched in between two slotted stator cores (Fig. 1.9 (a)) to remove 1000 W of heat losses generated in the stator. Coolant flowed in the narrow duct with grooves in the middle of the aluminium jacket, which was shaped like a torus. These grooves intensified the turbulence, subsequently enhancing the heat transfer. The authors presented the analytical and CFD designs of the water jacket parameters in conditions of a water inlet temperature of 65˚C and volumetric flow rate from 5 l/min up to 20 l/min. The total machine stator system was analysed using a lumped-parameter network constructed for one slot pitch by running a transient duty cycle. The optimization of the cooling system depended on the coolant flow rate and the winding temperature resistance. The simulation results were validated by machine tests at two values of load torque and speed: 200 Nm and 2000 rpm, respectively; and 160 Nm and 2500 rpm, respectively. The maximum error of the predicted temperature in light of the test results does not exceed 4K. Huang et al. (2012) presented a numerical study of different-shaped axial cooling channels in the housing applied in traction motors, with lubricant oil as a coolant. The authors executed CFD simulations for the fluid region and compared the duct geometries based on the convection coefficients and pumping power. It was concluded that oval and rectangular channels fare better with low height/width ratios (< 0.1), while oval and elliptical ducts showed better heat transfer coefficients for height/width ratios above 0.3. The oval channel showed the highest dissipating power per temperature difference. The pumping power was highest in the case of the elliptical channel. The ducts had height/width ratios varying from 0.1 to 0.7, and those with the highest height/width ratio had around 100 times more pumping power and around 3 times more cooling power than the 0.1 height-width ratio channels. The authors showed that the rectangular channel should have a small height/width ratio, with smaller than 10% shifted ratios. The paper also listed the definition of Nusselt numbers and Darcy friction factors for rectangular, elliptical and oval ducts. At the end of the paper, the results received by CFD analysis were applied to a 2D steady state model of the machine segment. The maximum temperatures of the stator parts were achieved with the elliptical channels, while the oval channels provided the best cooling. The simulated results have not been validated on a prototype.

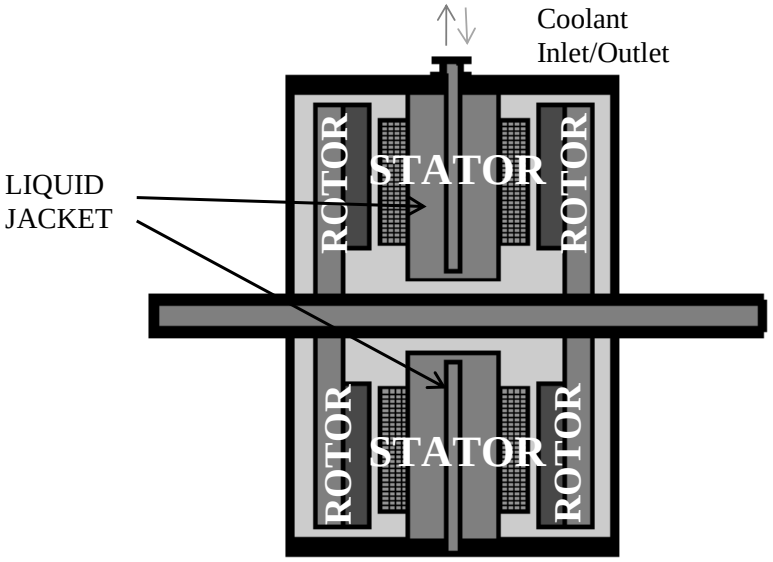

(a)

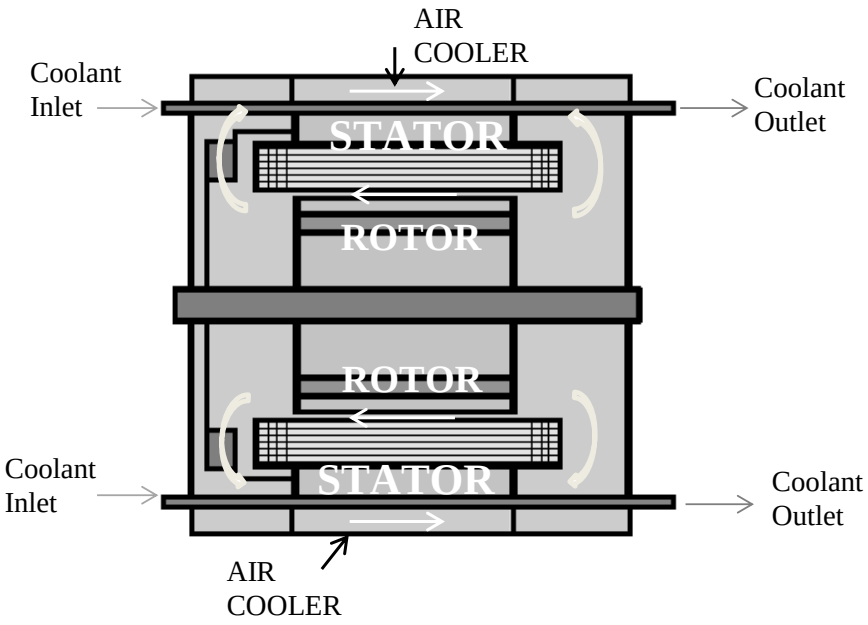

(b)

Figure 1.9: Construction enhancements inside the machine end caps (a) (Boglietti and Cavagnino, 2007), and Electrical machines with cooling based on a water jacket (b) (Sikora et al., 2011).

Schrittwieser et al. (2012) presented a CFD analysis of the fluid flow in the stator ducts of a hydro generator using CFD but without validating the results on a prototype. The models of the generator with the axial stator ducts (the Stage and the Frozen rotor models) were created to analyse the air flow and related heat transfer processes. The combination Shear Stress and κ-ε turbulence model with automatic wall treatment was used to simulate the air flow within the machine. The authors concluded that the highest pressure loss was located in the teeth region, and that the leading side of the slot had a 33% better heat exchange than the trailing side.

Several papers contain both kinds of thermal design – analytical (LPTN) and computational (FEM; CFD) – to achieve more accurate and reliable results. Some of these papers utilize two different thermal analyses because of the infeasibility of testing the prototype. Dajaku and Gerling (2006) reported a novel thermal model for an electrical machine with rotor surface-mounted permanent magnets and a cooling system based on forced water flow in the frame and on serial-circumferentially cooling channels for steady-state and transient conditions. The presented lumped parameter model was verified through comparison with 2D FEM calculations. The paper also analyses the coolant thermal resistance under different operating conditions and the influence of the slot insulation material on the machine thermal behaviour. It was demonstrated that an increase of the convection coefficient in the liquid jacket from 1000 W/(m^2·K) to 6000 W/(m^2·K) results in a 60K temperature drop in the coil side and a 30K temperature drop in the rotor. However, the results have not been validated on the machine prototype. The thermal design of a 6.4 kW motor was presented by Cassat et al. (2002), where a lumped-thermal scheme and a 3D FEM computational model were used to simulate the machine thermal behaviour. The rated speed and synchronous frequency of the studied motor were 149 rpm and 82 Hz, respectively. The convection coefficients on the rotor back surfaces and in the air gap, imposed in 3D FEM and LPTN motor models, were considered according to measurements yielded by an infrared camera in tests. The temperature distribution results of the motor FEM and LPN models were subsequently compared.

Funieru and Binder (2008) presented a numerical thermal modelling of a 500 kW motor with rotor surface-mounted magnets for a railway application. The cooling system of the motor was based on water jacket cooling, with 24 turns around the motor axis. The water volume rate was 15 l/min, and the water inlet temperature was 60 ºC, which kept the winding temperature under 210 ºC. The 3D FEM simulated model presented half of the machine slot in the cross-section and half of the machine length in the longitudinal direction. The air gap region was simulated with equivalent thermal conductivity. The transient numerical and lumped parameter thermal models were presented, and temperature results were compared with results from a test ring. The stator temperatures were in good agreement with the test results, but the rotor temperatures had deviations of typically 10–20% because of the air gap modelling. The no-load operation of the motor, as in the case of a cooling failure, was studied to show that the motor had no overheating.

CFD analysis is widely utilized in papers dealing with analysis and optimization of machines with an unique cooling system geometry or a unique internal structure to intensify the cooling. This computational analysis is employed to define the convection coefficient for a uniquely designed machine, as these coefficients are lacking in the literature.

Seghir-Oualil et al. (2003) studied the thermal behaviour of a permanent magnet synchronous motor having a cooling system based on a frame water jacket and rotor forced air ventilation. The thermal analysis was performed using a nodal network with a description of the thermal conduction and convection in the air gap and on the outer machine surfaces. Based on CFD simulations, the end-regions in the nodal network were identified as two parallel parts with different convection coefficients. The thermal designs showed that the hottest motor parts are the end windings (183 ºC) and the magnets (100ºC), when the inlet water and air temperatures are 40 ºC and 45 ºC, respectively. The sensibility study showed that the airflow rate only influences the magnet temperature. The authors concluded that the end windings' temperature could be reduced by even up to 49 ºC through a thermal bridge between the end windings and the frame water pool (Fig. 1.10 (a)). Additional rotor designs were offered in this paper to significantly cool the rotor magnets, such as triangular fins in the inner rotor part (for a 20K temperature drop), or an auxiliary pipe filled with water or air and placed inside the rotor (respectively for a 50K and 65K temperature drop) (Fig. 1.10 (a)).

A thermal design of a large permanent magnet synchronous machine with a stator comprised of traditional electrical steel laminations and with a stator constructed of soft magnetic composites was developed by Farnia and Hattori (2006). The authors analysed the motor with the cooling system based on the coolant running through the end rings of the stator frame by a stator thermal equivalent model and a stationary simplified 3D machine model. The coolant flowed into the bottom end of the stator and further circulated through the stator slots. The coolant exited from the other side of the machine into a reservoir which acted like a heat sink (Fig. 1.10 (b)). In the numerical modelling, the coolant was not modelled, and the only temperature was imposed on three nodes (at the entrance point, middle point and exit point) to obtain a definition of the stator coil temperature. The computed and measured temperatures of the stator coils were 88 ˚C–113 ˚C and 86 ˚C–115 ˚C, respectively. The sensitivity analysis showed that the most sensitive parameters are the thermal coefficients between the coolant and the components connected to the coolant, especially near the coils.

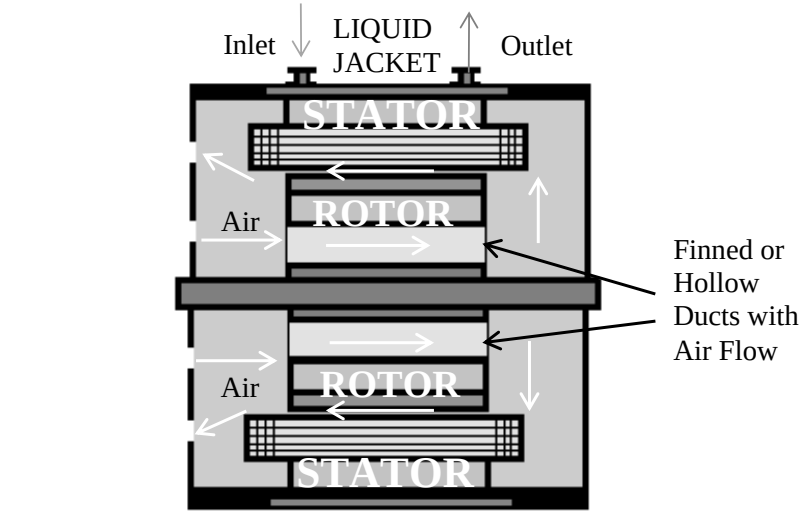

(a)

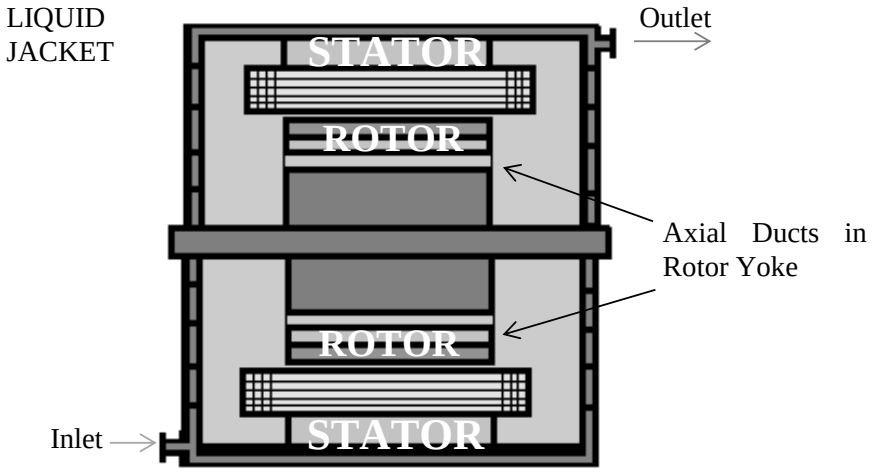

(b)

Figure 1.10: Construction improvements for an indirect liquid-cooled machine (a) (Seghir-Oualil, 2003) and cooling scheme based on a liquid jacket in the frame and end shields (b) (Farnia and Hattori, 2006).

Table 1.10 Characteristics of the machines presented in the literature study with indirect liquid cooling.

Machine and Cooling method	Temperature Rise Stator/Rotor (coolant flow)	Convection Coefficient
31.4 kW 3000 rpm PMDRM (5300 kW/m^3, 43 kPa), Liquid Jacket and Forced Air Cooling, (Zheng et al., 2008)	54K/157K (1 m/s water speed and 9 m/s air speed)	In air gap (Gazley, 1958): $Nu = 2$, $Ta \leq 41$ $Nu = 0.23 \cdot Ta^{0.63} \cdot Pr^{0.27}$, $41 < Ta \leq 100$ $Nu = 0.386 \cdot Ta^{0.5} \cdot Pr^{0.27}$, $Ta > 100$
PMSM, Liquid Jacket and Forced Air Cooling, (Seghir-Qualil et al., 2003)		In air gap (mounted magnets) (Tachibana and Fukui, 1964): $Nu_r = 0.046 \cdot Ta^{0.66} \cdot Pr^{0.33}$, $Nu_a = 0.015 \cdot \left(1 + 2.3 \cdot \left(\frac{2 \cdot \delta_{eq}}{l_r}\right)\right) \cdot Re_a^{0.8} \cdot Pr^{0.33}$, $\delta_{eq} = 4 \cdot \frac{s_{av}}{\Pi_{av}}$, where l_r is the rotor length, and s_{av} and Π_{av} are the average surface and perimeter of the air gap In rotor end cap (Seghir-Ouali et al.,2006): $Nu = 2.85 \cdot 10^{-4} \cdot Re^{1.19}$, $Re_a > 2.77 \cdot 10^5$ In stator end cap (end winding): $Nu = 0.59 \cdot Ra^{0.25}$, $10^4 < Ra < 10^9$ (Mc Adams, 1961) $Nu = 0.27 \cdot Ra^{0.25}$, $3 \cdot 10^5 < Ra < 3 \cdot 10^{10}$ (Mc Adams, 1961) $Nu = 0.54 \cdot Ra^{0.25}$, $10^5 < Ra < 10^7$ (Fishenden et Saunders, 1950) For rotor internal tube (passive air, rotation) (Becker, 1963): $Nu = 0.133 \cdot Re^{0.66} \cdot Pr^{0.33}$, $800 < Re_w < 10^5$

1.4.2 Thermal design and analysis of electrical machines with direct liquid cooling

A direct liquid cooling system comprised of stator and rotor windings is mainly used in the high power generators of thermal, nuclear and hydro power plants. Multiple authors have presented their work on the exploitation analysis of these generators, and some have analysed the coolant chemical composition used for their reliable operation. Oliver et al. (2001) analysed the 25-year experience of the exploitation of 1300 MW liquid-cooled Amos 3 generators. The authors evaluated a brief operation history of the generators and pointed out that the first problems with the stator cooling system had

begun only 16 years after the start of operation. The generator stator copper winding presented a mix of solid copper conductors and hollow stainless-steel tubes. There were 8 hollow strands and 48 solid strands for each bar (Fig.1.11 (a)). It was concluded that the hollow stainless steel conductors provide a lower winding loss and eliminate any problems with the formation of copper oxide, which can contaminate copper tubes. However, the authors did not present any temperature results for the performance of the machine part and the cooling system. The paper describes a new clip design separating the hydraulic cooling water connection from the electrical connection (Fig.1.11 (b)). With this, the stainless steel cooling tubes were individually TIG-welded into the water box and easily inspected for any leaks. The authors presented an end-winding support structure consisting of one inner ring, inner and outer axial blocks interlocked with the bars, and two outer rings. This structure was for withstanding the stresses of a short circuit or out-of-phase synchronization. It was shown that the mixed solid copper and hollow stainless-steel conductors have over 10% fewer losses than copper conductors alone. Irwanto et al. (2009) examined GIGATOP generators with direct water-cooled stator bars and a hydrogen-cooled rotor. The 2-pole generators have a maximum output power of 1400 MW, and the 4-pole generators of 2000 MW. The authors described in detail the main features of the stator, rotor cooling systems, end-winding support structures and insulation systems. The stator copper winding consisted of solid copper bars and stainless steel tubes (as in Fig. 1.11 (a)) cooled by de-ionized water passing through them. The de-ionized water entered and exited the winding over insulating Teflon hoses and water manifolds (Fig. 1.11 (b)). The paper describes the advantages of the composition of solid copper conductors and cooled stainless steel tubes over hollow copper conductors with coolant flow inside, including less corrosion, less leaking and significantly less maintenance. However, the application of the stainless tubes separately from the copper conductors creates an additional thermal resistance between the heat source and the coolant (insulation). It was noted that no additional stresses exist in the design composed of cooled stainless steel tubes and copper conductors, as copper and stainless steel have similar thermal expansion coefficients. The improved flexible connections were described, and an analysis of stator end winding operation vibration was presented.

A study of dissolved copper oxides in deionized water in liquid-cooled generators was presented in the paper of Dortwegt and Maughan (2001). The authors explained that the maximum corrosion rate occurs in the oxygen concentration range of 200–300 ppb (0.2–0.3 ppm), and the corrosion rate is minimized at pH values approaching 8.5 and greater. The formation of copper ions mainly occurs when the pH values are below 7.0, where the temperature influence is also noticeable. Therefore, the authors performed the water pH control by changing the caution resin module from hydrogen to sodium and back in the deionizer. The changing of the positively charged water ions by hydrogen ions increases the water pH value. To keep the pH below the limited value, the caution resin (in the deionizer) should be moved in sodium form in order to change the positively charged water ions with sodium ions. 7.5 pH and water resistivity of

around 5–8 MΩ·cm are optimal parameters, as in this case the corrosion rate is reduced to 10 – 20% of the original rate.

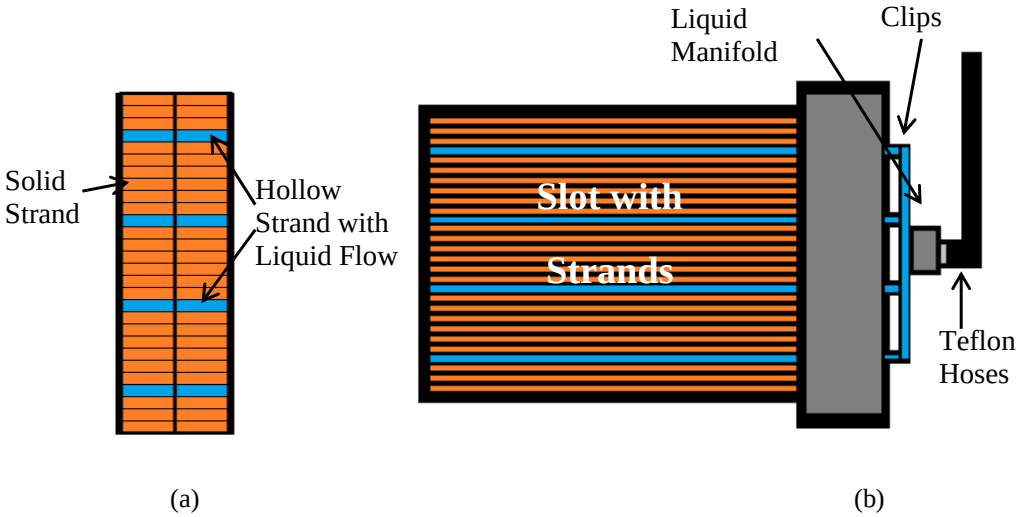

Figure 1.11: Stator bar (a) and clip designs (b) (Oliver et al., 2001; Irwanto et al., 2009).

Svoboda and Palmer (2008) presented another extensive chemistry analysis on the dependence between the copper oxide solubility, pH value and temperature for hollow copper conductors of a water-cooled generator. The authors concluded that the solubility of copper oxides is dependent on pH and, to a lesser degree, on temperature in the generator water-cooling system. It was indicated that the solubility of copper oxides (Cu_2O, CuO) increases alongside an increasing temperature at neutral pH, and that the solubility of CuO may slightly decrease with increasing temperatures at acidic pH. The paper indicates that copper oxides (Cu_2O, CuO) are always present in the generator stator cooling system, with Cu_2O dominating in low-oxygen systems, and CuO dominating in high-oxygen systems. The authors described how accumulation of deposits preferentially occurs in areas of increased turbulence, such as in the inlets, outlets and bends of the hollow conductors. Based on test results, the copper oxides release rate increases with increasing temperature for the pH range of 6.5–7. Experimental data on the solubility of copper oxides depending on pH values at temperatures of 50 ºC and 100 ºC was presented. It was concluded that the solubility of copper oxides increases with temperature rises at neutral pH, and decreases at acidic and intermediate alkaline pH.

A study examining the water chemistry system used for the stator winding cooling system of alternators at a thermal power station was presented by Larin et al. (2011). The authors list the main parameters influenced by the rate of corrosion, including such indicators as pH value and temperature of cooling water, content of the oxidizer, total mineralization and catalysts of corrosion phenomena. The generator stator cooling

system had a closed-water loop, where five percent of the circulating water flow was converted in the ion exchange filter. In the cooling loop analysed, the coolant was pumped through a mixed-bed filter composed of a strong-acid cation-exchange resin and a strong-base anion-exchange resin to increase its pH to the standardized value of 8.5 +/– 0.5. Based on the experience of the district power station exploitation, the authors noticed that temporary excursions to below the permissible value of water pH had occurred, accompanied by the occurrence of free carbon dioxide in water. The specialist from the power station added sodium hydroxide into cooling water to increase its pH value, but this also did not prevent periodic excursions to pH values below the standardized limits. The authors recommended the application of a NaOH automated metering system for the circulation water to maintain the specified value of electrical conductivity (1–2 mS/cm).

Most papers present the thermal analysis of direct liquid cooling only by creating a model of the copper conductors with imposed coolant temperatures or convection coefficients due to limited computational resources. Papers presenting direct liquid cooling systems usually do not validate their results on prototypes. The validation of results is problematic because the machines in question are large and expensive; it is difficult to construct full models and manufacture prototypes.

Azizi et al. (2009) examined the influence of wiring structures and cooling systems on the temperature and the insulation age of the stator slot wiring. They studied a 1 MVA synchronous generator with three phases and 24 slots. 2D FEM electrical and thermal designs of the stator slot with round or rectangular conductors in conditions of natural air cooling or direct water cooling were presented. The authors concluded that circular conductors have a better heat transfer exchange with the surroundings and a longer insulation age than do the rectangular ones in the stator. In the case of circular conductors, the wiring temperatures were respectively 5-7 K lower in conditions of air and water cooling. Because of the lower temperature, these windings had 1.25 and 6 times the original insulation age.

The study of Kargar et al. (2010) examines heat conduction within a composed solid material of a rotor direct-cooled sector with constant internal heat generation. In the thermal model, the insulation and convection boundary conditions were imposed on symmetry lines and on the fluid cooling sides, respectively. Furthermore, the coolant effect on the maximum insulation temperature of the direct cooled rotor for water, air and hydrogen as a coolant were studied. The applications of water, hydrogen and air have the effect of 0.14, 0.23 and 0.26 respective temperature rises within the rotor slot.

Wang et al. (2010) reported the calculation of the winding bar temperature for the water cooling stator used in 777 MVA Three-Gorge Hydro-Generators. The stator of the generator had 510 slots, 1020 bars and more than 2000 water-joints. Every bar consisted of 6 water cooled hollow strands and 24 solid strands. The inlet and outlet water temperatures in the cooling circuit were 38 ˚C and 65 ˚C, respectively. The authors presented the formulas for the convection coefficient definition in the air gap, water

duct and end cap regions (Table 1.11), which correspondingly resulted as 106 W/(m^2·K), 10988 W/(m^2·K) and 77 W/(m^2·K). The 2D numerical model of the stator slot was simulated by ANSYS software using imposed water temperatures in the hollow strands as boundary conditions. It was concluded that the proportion of relative error between the heat taken away by water and the total heat generated in bar is less than 5% in every outlet-water temperature-point.

Table 11 presents the Nusselt number correlations used for the thermal analysis of the direct liquid cooling electrical machines.

Table 1.11 Characteristics of the machines with direct liquid cooling presented in the literature study

Machine and Cooling method	Temperature Rise Stator/Rotor (coolant flow)	Convection Coefficient
777 MVA synchronous generator, Stator Direct Liquid Cooling, (Wang et al., 2010)		For air flow (Gnielinski, 1976) $Nu = 0.0214 \cdot (Re_f^{0.8} - 100) \cdot Pr_f^{0.4} \cdot \left(1 + (d/l)^{2/3}\right) \cdot \left(T_f / T_w\right)^{0.45}$ $0.6 < Pr_f < 1.5$, $0.5 < (T_f/T_w) < 1.5$, $2300 < Re_f < 10^6$, For water flow (Gnielinski, 1976) $Nu = 0.012 \cdot (Re_f^{0.8} - 100) \cdot Pr_f^{0.4} \cdot \left(1 + (d/l)^{2/3}\right) \cdot \left(Pr_f / Pr_w\right)^{0.11}$ $0.5 < Pr_f < 500$, $0.05 < (Pr_f/Pr_w) < 20$, $2300 < Re_f < 10^6$ d is the duct diameter of and l is the duct length
19 kW 1500 rpm PMSM (3560 kW/m^3, 30 kPa), Liquid Jacket, Direct Oil Cooling (Nategh, 2013)	100K/35K (0.1 m^3/h)	For stator end windings (direct oil cooling, laminar flow): $Nu = 0.664 \cdot Re^{1/2} \cdot Pr^{1/3}$, $Nu = 0.3 + \frac{0.62 \cdot Re^{1/2} \cdot Pr^{1/3}}{\left(1 + \left(\frac{0.4}{Pr}\right)^{2/3}\right)^{1/4}} \cdot \left(1 + \left(\frac{Re}{282000}\right)^{5/8}\right)^{4/5}$.

Li et al. (2010) presented a 3D FEM temperature field model of a water-cooled stator bar in a QFSN-220-2 turbogenerator, in which hollow strands were blocked differently. The stator bar of the generator studied was composed of six conducting wire groups, with four solid conductors and one hollow conductor per group. The turbulent water flow inside the conductor with an inlet velocity of 0.902 m/s, temperature of 28.25 ºC and outlet pressure of 1 bar defined the boundary conditions for the stator bar model. The basic heat loss (28.2 kW/m^3) and additional loss of the stator bar were taken into consideration. The outlet temperatures of the top and bottom bars were respectively 50.5 ºC and 44.5 ºC. The authors showed that the respective temperatures of the top and bottom bars rise from 4.6 K and 3.4 K to 22.1 K and 16.1 K if one to three of the parallel hollow strands are completely blocked.

Centner and Sabelfeld (2012) presented the thermal behaviour of a 6 MW synchronous machine. The authors studied the temperature distribution within the rotor conductors, comparing cases of direct and indirect cooling. A lumped parameter thermal network of the generator was constructed and described in detail in the article. The simulation models showed that the temperature of the directly-cooled winding is distributed almost evenly (there is a 4% difference between the winding in the centre of the slot and the end-winding) over the complete length of the rotor. In the case of the indirect-cooling method, a 40% temperature difference existed between the winding in the centre of the slot and the end-winding. The temperature rise of the rotor winding with indirect air cooling was 20% higher than that with the direct-cooled winding.

The doctoral thesis of Nategh (2013) presents the thermal effects in a 19 kW PMSM with a rated speed of 1500 rpm for automotive traction. An LPTN of the whole machine and 3D CFD simulations on the liquid flow in the housing were done and checked by experimental work. The cooling solution based on the oil jacket in the housing and direct cooling of the end-winding (Fig. 1.12) was also analysed (Table 1.11). The study showed that the application of the impregnation materials with higher thermal conductivity (epoxylite and SbTCM) reduce the stator winding hot-spots by 20–40 K. The thermal effect of the lamination thickness and amount of alloy contents was up to 10 K in the hot-spot temperatures of the rotor and the stator winding. The simulations were validated by the tests performed on the machine.

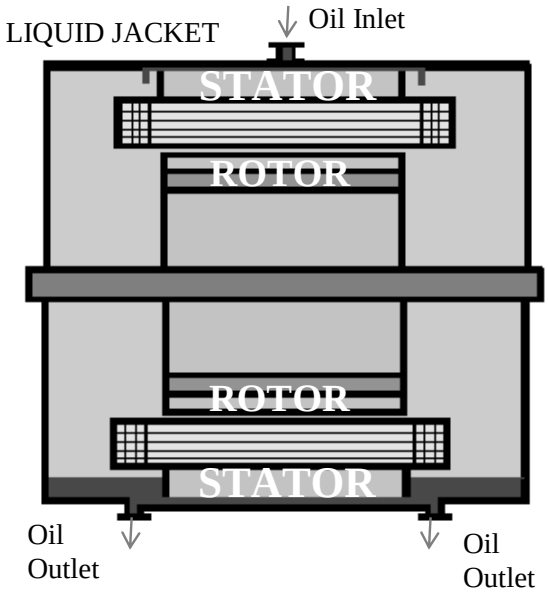

Figure 1.12: Scheme of direct oil cooling (Nategh, 2013).

Permanent magnet electrical machines with indirect liquid cooling systems have been widely analysed by both researchers and engineers. Most have employed CFD only for the liquid jacket optimization and design, but they have subsequently applied the CFD results to the LPTN of the whole machine model. CFD analysis of the machine model has also been broadly applied when machine designs are unique or when the air flow needs to be optimized in the highest powered machines. However, most of these results have not been validated on machine prototypes. It is obvious that there is a lack of information concerning the design and the optimization of electrical machines with direct liquid cooling due to the rarity of this machine design.

Concerning permanent magnet electrical machines developed for vehicle and wind power applications, indirect and direct liquid cooling systems have become popular, and more validated results concerning their design and optimization are required. Vehicle permanent magnet electrical machines are designed to endure short overloads, so effective direct and indirect liquid cooling solutions are necessary. The development of wind energy has increased demand for direct-drive permanent magnet electrical generators with the highest power (> 6-8 MW) due to their reliability. However, limitations exist for the transportation and installations of these generators, especially in offshore sites. New cooling solutions are required for these machines so that their size may be reduced to meet the market requirements.

1.5 Aim and scope of the research

This doctoral thesis discusses cooling systems and thermal issues of tooth-coil permanent magnet synchronous electrical machines with high torque density, as these are important and vital for product quality, workability and reliability. Technological progress has resulted in the development of new tools, such as computational methods, which enable the fast and precise study of electrical machine thermal behaviour. In the design stage of an electrical machine, knowledge of the temperature distribution allows for the evaluation of machine performance, preventing breakdown due to excessive temperatures of critical components such as insulation or permanent magnets.

In the literature there are a lot of reports focusing on the thermal analysis of electrical machines based on LPTN and rarely on CFD. However, there is a lack of works analysing the direct liquid cooled electrical machines taking into account the whole machine. Several papers have been devoted to studying the coolant agents for the direct liquid cooled machines. Electrical machines with an indirect cooling system based on a liquid jacket are analysed widely in the literature, but the high conductance materials applied as improved heat paths to the liquid jacket have so far been studied only in a couple of papers, although this cooling scheme can be effective, especially in case of high torque density electrical machines.

Liquid cooling solutions and their application in tooth-coil permanent magnet electrical machines with high torque density is the focus of this work. Different liquid cooling solutions enhancing heat transfer are characterized and analysed herein. The aim of this

research is to find and assess the most effective practical liquid cooling systems for certain high-torque-density permanent magnet electrical machines. An evaluation of the applicability and accuracy of different methods in the heat transfer analysis of these machines is conducted. The main tools for thermal analysis of the machines presented in this work are 1) lumped parameter thermal network (LPTN), and 2) numerical modelling (Finite Element Analysis (FEA) and Computational Fluid Dynamics (CFD)). This study includes theoretical analyses, numerical simulations and experiments. Most of the presented liquid cooling solutions are verified by test results of machine prototypes.

The executed research is discussed in eight chapters. Their structure and content are summarized as follows:

Chapter 1 introduces the basics of heat transfer in electrical machines, a literature survey and an overview of the liquid cooling technologies for electrical machines. The latest developments in electrical machines and cooling solutions for them are discussed. A literature survey concerning thermal modelling of electrical machines is presented. Numerous papers with general considerations about different machines' thermal designs based on LPTN, FEM and CFD are described. Special attention is paid to effects of cooling systems. The advantages and drawbacks of liquid cooling types are discussed. The liquid coolants used most are described and analysed. The reliability analysis of the different components forming the liquid cooling loop is presented in the end of this chapter.

Chapter 2 presents a high-torque-density axial flux permanent magnet machine with 100 kW rated power and 1500 rpm rated speed for application to off-road working vehicles. This chapter contains the optimizing of the cooling scheme, aiming at the avoidance of hot spots in the stator winding and the permanent magnets. The cooling improvements with the water jacket and high conductance materials (copper bars and potting material) are presented and illustrated here. The thermal field is calculated with computational resources, with the aim of presenting total machine thermal performance. The thermal impact of the number of copper bars and potting material location is discussed, and CFD thermal modelling of the machine model is employed to determine this impact. The simulation is validated by comparisons with the experiments presented on the machine prototype.

In **Chapter 3**, the focus is on the development of an efficient cooling solution for a 110 kW radial flux permanent magnet synchronous machine with high torque density for application to off-road working vehicles. The cooling systems are based on a liquid jacket incorporated into the frame and on the potting material arranged around the end windings. A 3D CFD thermal model of the machine part is proposed for providing the estimation of its thermal behaviour under conditions of the cooling solution developed. A machine prototype is used to assess the effects of two different potting materials. The total cooling system and cooling system components are examined using a CFD thermal computational model, and conclusions concerning their influence are presented. Several

considerations for the design and construction of the cooling scheme based on the liquid jacket and the potting materials are given in this chapter. The experimental test results are discussed and analysed.

In **Chapter 4**, the main focal point is the development of a cooling solution and thermal analysis of an 8 MW direct-drive permanent magnet synchronous generator (DD PMSG) for offshore wind turbines application. The obvious method for achieving a significant reduction in weight and size in a high-torque, low-speed machine is to improve the cooling system of the stator windings, where losses dominate. Internal liquid cooling of the windings is considered, as this can provide an adequate temperature for the copper winding and the permanent magnets. This chapter provides basic design equations for using direct liquid cooling for the stator copper winding with direct internal cooling by means of hollow conductors. The performance of various cooling fluids developed for liquid cooling is investigated and assessed in order to optimize the coolant. Thermal designs are based on CFD -thermal modelling and simplified thermal network for computing the thermal behaviour of the studied machine are described in detail in this chapter. The reliability measures of the developed direct liquid cooling solution are analytically determined based on published failure and repair rates of cooling system components. A detailed description of a coil prototype (motorette) and test results are presented.

Chapter 5 presents a direct cooling method with oil employed as a coolant for an electrical motor with an integrated hydraulic pump. For this purpose, a 26.6 kW oil-immersed permanent magnet synchronous machine is described and evaluated from a thermal-analysis standpoint. In order to find the hot spots within the machine under study with greater accuracy, CFD -thermal-based design is advanced. The lumped parameter thermal network for a machine with this type of cooling scheme is presented. Furthermore, a machine prototype was built and tested to validate the simulated results and demonstrate the advantages of this cooling solution.

In **Chapter 6**, a summary of the main results of the present doctoral thesis with general conclusions is provided. Recommendations for future research work are proposed.

1.6 Scientific contribution

The applicability and accuracy of methods of different heat transfer analysis for analysing certain tooth-coil permanent magnet synchronous machines with high torque density are assessed and re-evaluated. High-torque-density axial and radial flux permanent magnet electrical machines with direct and indirect liquid cooling solutions are analysed from a thermal perspective to provide methods for defining the operating temperatures of critical machine parts under conditions of high losses and constrained dimensions. Based on innovative thinking, new heat transfer means and direct liquid cooling for low power machines are proposed for PMS machines with high torque density. Special liquid cooling solutions, such as 1) adoption of copper bars and potting

material, 2) direct liquid cooling of the stator winding and 3) oil-immersed cooling, are designed and analysed here.

This thesis contributes to solving several issues related to the liquid cooling system design, assessment and thermal modelling of electrical machines. The merits and drawbacks of different types of liquid cooling systems and coolants are discussed. It provides basic design equations for using indirect (liquid jacket) and direct liquid cooling (liquid flow inside the copper conductors and oil-immersed) systems. The assessment of the thermal capabilities of the various liquid cooling systems is introduced by the heat transfer (based on FEA) and mass transfer (based on CFD) simulations inside the permanent magnet electrical machines. Thermal models based on LPTN are described for machines with direct liquid cooling. Also discussed herein is a method for carrying out a reliability analysis of the liquid cooling systems based on the literature values of failure rate and mean down time of their basic components.

The present work contributes to liquid-cooled machine design in the following ways:

- Proposal of an indirect liquid cooling system with a water jacket incorporated into the frame for a 100 kW axial flux permanent magnet synchronous machine and for a 110 kW radial flux permanent magnet synchronous machine with high torque density. Use of materials of high thermal conductance (copper bars and potting material) is proposed and assessed for boosted effectiveness of the cooling solutions developed. It is shown that materials of high thermal conductance impede rotor over-temperatures and provide efficient cooling of the stator winding, even without the application of forced air cooling. The effect of the liquid jacket performance on the temperatures of machine components is evaluated. The CFD thermal simulations of the heat transfer inside the machines studied are described in detail in Chapters 2 and 3.
- Proposal of a direct liquid cooling system of the stator copper winding for an 8 MW direct-drive permanent magnet synchronous generator with high torque and low speed for remote operation in offshore wind turbines. This unique cooling solution for wind generators is recommended as a way to significantly reduce the machine dimensions, and to slightly reduce the cost of the rated point efficiency of the machine. The design methodology of the stator winding with internal direct liquid cooling is presented and described. Special attention is paid to the coolant selection and to the developed cooling system reliability. The CFD thermal model and the lumped parameter thermal network for the machine with this type of cooling scheme are presented in Chapter 4.
- Proposal of direct-immersion oil cooling for a 26.6 kW permanent magnet synchronous motor for application to off-road vehicles. This unique cooling method is presented as a particularly effective and useful solution for an integrated system comprised of a motor and hydraulic pump. The CFD thermal simulations and LPTN is presented to analyse the machine performance in Chapter 5.

The thermal analysis methods and theoretical considerations concerning cooling system optimization applied and reported in this thesis were verified via experimental measurements on a copper tooth-coil (motorette) and various prototypes of electrical machines. The validated approaches may also be applied to the design and analyses of other permanent magnet electrical machines with high torque density.

1.7 List of publications

This section lists conference and journal publications related to the work presented in this thesis in which the author is the main author:

1. Polikarpova, M., Röyttä, P., Semken, S., Nerg, J. and Pyrhönen, J., "Thermal Design and Analysis of a 6 MW Direct-Water-Cooled Permanent Magnet Synchronous Generator for High-Power Direct-Drive Wind Turbine Applications", ICREPQ, Spain, 2011.
2. Polikarpova, M., Alexandrova, J. and Pyrhönen, J., "Direct Water Cooling of Stator Winding of 6 MW Synchronous Generator", XVIII School-Seminar of Young Scientists and Specialists under the leadership of RAS Academician Professor A. I. Leontiev, Russia, 2011.
3. Polikarpova, M., Lindh, P., Pyrhönen, J. and Nerg, J., "Application of Finite Element Methods to the Thermal design of the Fractional Slot Permanent Magnet Synchronous Motor", ISEF, Portugal 2011.
4. Polikarpova, M., Röyttä, P., Alexandrova, J., Semken, S., Nerg, J. and Pyrhönen J., "Thermal Design and Analysis of an 8 MW Direct-Water Cooled Direct Drive Permanent Magnet Synchronous Generator for High-Power Wind Turbine Application", ICEM, France, 2012.
5. Polikarpova, M., Lindh, P. and Pyrhönen, J., "Thermal Design and Analysis of Fractional Slot Permanent Magnet Synchronous Motor", vol. 6, issue 2, pp.181-187, International Review of Mechanical Engineering (IREME), 2012.
6. Polikarpova, M., Semken, S. and Pyrhönen, J., "Reliability Analysis of A Direct-Drive Liquid Cooling System of Direct-Drive Permanent Magnet Synchronous Generator", Reliability and Maintainability Symposium, January, 2013.
7. Polikarpova, M., Röyttä, P. and Pyrhönen, J., "Liquid Internal Cooling of High-Power Synchronous Permanent Magnet Generator Winding in Arctic Conditions", International Review of Mechanical Engineering (IREME), vol. 7, issue 2, pp.301-307, 2013.
8. Polikarpova, M., Lohtander, M., Popova, L., Musikka, T., Juntunen, R., Silventoinen, P., Varis, J., Pyrhönen, O., and Pyrhönen, J., "Reliability Analysis

of Liquid Cooling Systems' Mechanical Components for 3 MVA Power Converter", Mechanica, vol. 19, issue 4, pp.417-423, 2013.
9. Polikarpova, M., Ponomarev, P. and Pyrhönen, J., "Oil-Immersion Direct-Liquid-Cooling of Permanent-Magnet Synchronous Motor", in Proceedings UK Heat Transfer Conference, pp.115-1-115-8, UK 2013.
10. Polikarpova, M., Lindh, P., Tapia, J.A. and Pyrhönen, J., "Application of Potting Material for a 100 kW Radial Flux PMSM", ICEM, Germany 2014.
11. Polikarpova, M., Lindh, P., Gerada, C., Rilla, M., Naumanen, V. and Pyrhönen, J., "Thermal Effects of Stator Potting in an Axial-Flux Permanent Magnet Synchronous Generator", Applied Thermal Engineering, accepted, 2014.

The major parts of the above publications, including cooling system design, machine thermal designs, construction and simulations of LPTN and CFD models and measurements of the prototype machines were provided by the author. The thermal design and the analytical analysis of the generator cooling system in Publications 1-2, 4, 7 were made in cooperation with Dr. Pekka Röyttä. The electromagnetic designs and the loss calculation of the studied machines were made by Dr. Yulia Alexandrova in Publications 1-2, 4; Dr. Pia Lindh in Publications 3, 5, 10 and 11; Dr. Hanna Jussila and Dr. Pia Lindh in Publications 11; Dr. Pavel Ponomarev in Publication 9. The mechanical design of the generator was made by Scott Semken in Publications 1-2 and 4. The experimental tests were made in cooperation with Dr. Pia Lindh in Publications 3, 5, 10-11 and with Dr. Yulia Alexandrova and Scott Semken in Publications 4. The tests were made by Dr. Pavel Ponomarev in Publication 9. The thermal design and reliability analysis of the converter cooling systems were made by the author in Publications in 6 and 8. The electromagnetic design of the converter was made by Lyudmila Popova and the mechanical design of the converter was made by Dr. Mika Lohtander in Publication 8.

The following list includes other publications which the author contributed to, where the author is a co-author:

1. Röyttä, P., Polikarpova, M., Pyrhönen, J. and Nerg, J., "Liquid Internal Cooling of Electric Machine Windings in Arctic Conditions", International Conference on Electrical Machines, Italy, 2010.
2. Ponomarev, P., Polikarpova, M., Heinikainen, O. and Pyrhönen, J., "Design of Integrated Electro-Hydraulic Power Unit for Hybrid Mobile Working Machines", EPE, UK, 2011.
3. Ponomarev, P., Polikarpova, M., and Pyrhönen, J., "Thermal Design of Directly-Oil-Cooled Permanent Magnet Synchronous Machine", ICEM, France 2012.
4. Alexandrova, J., Semken, S., Polikarpova, M., Pyrhönen, J., "Defining Proper Initial Geometry of an 8 MW Liquid-Cooled Direct-Drive Permanent Magnet

Synchronous Generator for Wind Turbine Applications Based on Minimizing Mass", ICEM, France, 2012.

5. Ponomarev, P., Polikarpova, M., Heinikainen, O. and Pyrhönen, J., "Design of Integrated Electro-Hydraulic Power Unit for Hybrid Mobile Working Machines", SPEEDAM, Italy, 2012.
6. Semken, S., Polikarpova, M., Röyttä, P., Alexandrova, J., and Pyrhönen, J., "Direct-Drive Permanent Magnet Generator For High-Power Wind Turbines – Benefits and Limiting Factors", IET Renewable Power Generation, vol. 6, issue 1, pp.1-8, 2012.
7. Lindh, P., Nerg, J., Pyrhönen, J., Polikarpova, M., Jussila, H. and Rilla, M., "Interior Permanent Magnet Motors with Non-Overlapping Concentrated Windings or With Integral Slot Windings For Traction Application", Electrical Review, issue 5, 2012.
8. Petrov, I., Polikarpova, M., Pyrhönen, J., "Rotor Surface Ferrite Magnet Synchronous Machine for Generator Use in a Hybrid Application – Electro-Magnetic and Thermal Analysis", IECON, Austria 2013.
9. Popova, L., Musikka, T., Juntunen, R., Polikarpova, M., Lohtander, M., Pyrhönen, J., "Design and Modelling of Low-Inductive Busbars for a Three-Level ANPC Inverter", International Review of Electrical Engineering, vol. 9, issue 1, 2014.
10. Debruyne, C., Polikarpova, M., Pyrhönen, J., Desmet, J. And Vandevelde, L., "Evaluation of the Efficiency of Line-Start Permanent-Magnet Machines as a Function of the Operating Temperature", Transactions on Industrial Electronics, vol.61, issue 8, pp.4443-4454, 2014.
11. Pyrhönen, J., Lindh, P., Polikarpova, M., Kurvinen, E., and Naumanen, V., "Heat-Transfer Improvements in an Axial-Flux Permanent-Magnet Synchronous Machine", Applied Thermal Engineering, accepted, 2014.

In Publications 1 and 4 the author has contributed in the design of the generator direct liquid cooling system. In Publications 2-3, 5 the author has made the LPTN analysis and 3D FEM thermal analyses of the machine. In Publication 6 the author has contributed in the thermal analyses of DD PMSG and has made the economic analysis of the wind turbine installation. In Publications 7 and 8 the author has made the CFD analyses of the developed machines and their cooling solutions. In Publication 9 the author has contributed in the thermal analysis of the designed converter. In Publication 10 the author has made the LPTN of the machine. In Publication 11 the author has contributed in the thermal design and analyses of a PM traction motor.

2 Indirect liquid cooling system of an axial-flux permanent magnet synchronous machine

This chapter is devoted to developing an indirect liquid cooling system based on a water jacket and high conductance materials for a 100 kW axial flux electrical machine.

2.1 Description of the machine and its cooling system

Axial flux machines have become increasingly popular in electric vehicles, bicycles and other applications where high torque density and compact design are necessary (Scowby et al., 2004; Howey, 2010; Odvarka, 2010). This type of machine, due to its special configuration, usually utilizes inherent self-ventilation, but the effect of this cooling method on machine operation characteristics is significant. The rotating rotor disks are located along the whole diameter, and the arrangement of multiple gaps in the rotor body and its support structure provides the high turbulence of the air flow inside; heat removal is therefore based on convection (Ferreira, 2012). However, low rotational speeds are undesirable for this machine type, as the poorly cooled volumetric end windings cause high resistive losses due to high temperatures (Ferreira, 2012). Therefore, an alternative cooling solution consisting of a speed-independent cooling system with a high heat removal rate is required for high-torque-density axial flux electrical machines for truck application.

The machine studied is a two-stator-one rotor axial flux permanent magnet synchronous machine with a rated power of 100 kW and a rated speed of 1500 rpm for highly integrated systems with constrained allocation space. The design of the machine includes two slotted stators, with a rotor situated in between. The machine has 12 open slots with double-layer tooth-coil windings in the stators and 10 poles in the rotor, making the flux fluctuations in the rotor magnets – and subsequently the losses in them – high (Fig. 2.1).

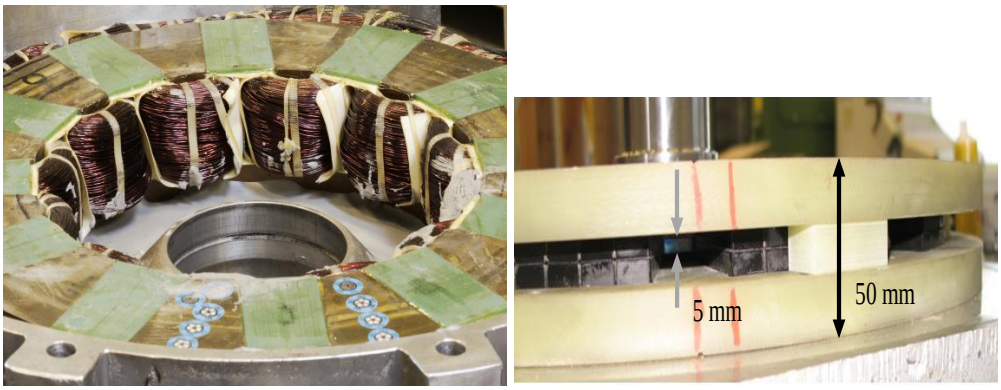

Figure 2.1: Stator and rotor of the machine studied.

The permanent magnets (NdFeB) are embedded in a composite rotor. They have thin lamination stacks on their surfaces to conduct the magnetic flux tangentially when the magnets are off the teeth areas in order to reduce the flux density fluctuations in the magnets. Table 2.1 provides the nominal parameters and the geometrical data of the machine.

Table 2.1 Characteristics of the AF PM machine

Parameter	Quantity
Rated Power	100 kW
Rated Speed	1500 rpm
Line to line voltage	500 V
Rated phase current	164 A
Number of phase	3
EMF factor (back emf / nominal voltage)	1
Tangential Stress at the rated point	33 kPa
Linear current density at the rated point	48 kA/m
Current density at the rated point	6 A/mm^2
Peak output power to rated output power ratio (overload capability) at nominal speed	1.5
Load angle	38 deg.
Power Factor	0.92
Rated electrical efficiency (designed)	95%
Number of slots and poles	12, 10
Active mass of machine	200 kg
Geometrical data	
Stator Outer Diameter	390 mm
Stator Inner Diameter	250 mm
Length of Air Gap	2.5 mm
Length of Stator Stack	190 mm
Length of Stator	70 mm
Slot Opening	40 mm

The calculated heat losses distribution within the machine is presented below in Table 2.2. The high current density causes high Joule losses in the stator copper winding. During machine operation, the eddy currents, hysteresis and additional magnetic fields (armature reaction caused harmonic flux components) produce large losses in the active magnetic iron parts of the machine stator, the rotor and the permanent magnets. Owing to the tooth-coil stator winding construction, the stator magnetic fields containing a great amount of harmonic components cause additional eddy current losses in the rotor. Large additional friction losses are precipitated by the special machine configuration (two air gaps and an abundance of holes in the rotor structure), resulting in significant windage losses.

Table 2.2 Heat sources of the machine at rated speed

Source Position	Quantity
Stator Copper Windings	2160 W
Stator Cores	900 W
Rotor Ferromagnetic Parts	200 W
Permanent Magnets	450 W
Additional Losses (mechanical losses in the air gap, AC copper losses, microhysteresis losses in the iron, etc.)	2785W

A hybrid cooling system was designed and developed for the machine. Initially the system consisted of two liquid-cooled frames (one per stator) and copper bars incorporated in the stator teeth (1 copper bar (8mm in diameter) per tooth). The composite rotor structure was designed to act as a fan (with air space between the permanent magnet poles and between the glass fibre parts). This design should have provided intensive air circulation by rotation, thereby ensuring cooling. Unfortunately, the rotor ducts were machined to be significantly smaller than what the initial design had required, and the fixing elements were drilled to a depth of 5 mm instead of the 15 mm designed depth (Fig. 2.1). The fan effect was almost totally lost, causing significant problems in the rotor cooling. It was impossible to enlarge the rotor ducts without a new rotor, which could not be manufactured.

The extra heat transfer elements – copper bars incorporated in the stator teeth (2 bars per tooth) and potting material connecting the end windings to the liquid-cooled frame – were added for the machine cooling because of the rotor manufacturing error (Fig. 2.2). The high conductance elements were applied to provide better cooling, which is particularly desirable in overloading conditions. This study considers the actual prototype structure. The overall cooling system design approach of the machine is illustrated in Fig. 2.2 (half of the machine is illustrated).

Most of the copper bars are embedded in the teeth and the stator yoke, but the extremities (outer ends of the bars) are immersed in the liquid water jacket for direct cooling (Fig.2.2). Most of the heat of the stator windings moves towards the teeth, which together with the heat losses generated in the teeth, is transported by the copper bars to the outside water jackets in the housings. The system of three copper bars per tooth was chosen based on acceptable loss of the flux-carrying cross-sectional area and mechanical strength. A higher number of copper bars could cause breakage of the stator teeth.

From the electromagnetic point of view, eddy-current losses in the copper bars vertically embedded inside the teeth are negligible due to the low penetration of the magnetic field caused by the high permeability of the surrounding lamination material and the low gradients of magnetic flux density in the copper bars.

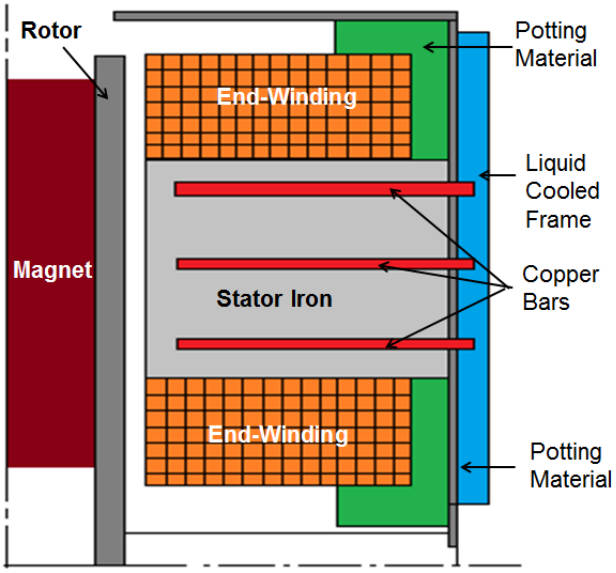

Figure 2.2: Scheme of the machine hybrid cooling system (not to scale).

The potting material (of no electrical significance) provides high heat conductivity and thereby redistributes the losses generated in the end windings towards the liquid jacket (heat does not move towards the rotor magnets). Attached between the end windings and the water-cooled frame, high conductance materials alleviate the thermal issue from the end winding by establishing a heat transfer path that delivers heat towards the cooled frame. The properties of the potting material (Ceramacast 675N by Aremco) are presented in Table 2.3 (Technical Data Sheet of AREMCO, 2010).

Table 2.3 Properties of Ceramacast 675N by Aremco, USA

Parameter	Quantity
Thermal Conductivity	100 W/(K·m)
Dielectric Strength	300 kV/m
Specific Electrical Resistivity	$1 \cdot 10^{11}$ Ω·m
Limited Temperature	1200 °C
Heat Capacity (Aluminium Nitride)	740 J/(K·kg)
Density (Aluminium Nitride)	3260 kg/m^3

In order to achieve high heat transfer rates (of up to 10000 W/(m^{2}K) in the liquid jacket, the application of water as a coolant in the frame housing has been considered. The

liquid cooling duct, shaped as a rectangle and with a cross-section size of $9 \cdot 10^{-4}$ m^2, is sandwiched in between two metal cores in each machine frame, with outer and internal stator liquid jacket diameters of 0.166 m and 0.015 m, respectively. The liquid-filled channel in the stator housing provides a large wetted surface and subsequently a high heat evacuation rate. The water flow is pushed by a pump through the inlet duct in the frame and picks up the heat generated in the machine by means of convection and conduction before exiting from the frame outlet ducts.

2.2 Thermal analysis of the machine

The proposed hybrid cooling of the axial flux permanent magnet machine is assessed based on CFD thermal computational designs of simplified machine models. CFD thermal analysis was selected for the machine modelling, as this method allows for including the mass transfer that is critical for the temperature simulation, especially in the rotor with the temperature-sensitive magnets. Thermal analysis based on FEA could yield good results for the stator, but it was impossible to simulate the rotor part correctly (the air gap is defined by the thermal conductivity). The machine studied has a unique design (i.e., application of the potting material), so it is difficult to assess the convection coefficient in the end cap spaces if LPTN and FEA are to be applied.

Three modifications of the cooling systems and the effects of these on the machine thermal behaviour are studied. The sensitivity analysis of the machine includes the determination of the machine thermal performance with varying numbers of copper bars and locations of potting material. The analysis is carried out numerically, using CFD thermal analysis.

2.2.1 Losses, thermal conductivities and convection coefficients

Several factors contribute to proper machine thermal performance modelling, such as correct heat losses distribution, thermal properties of machine solid parts, and correct convection coefficients on the outer and inner boundaries between machine surfaces and fluids. The losses distribution within the machine parts, as based on the measured current and power in the tests, are listed in Table 2.4 for 75%, 100% and 120% loads. The additional losses are high in the machine studied because of the two air gaps design and the manufacturing defects (the different lengths of the air gaps (1 mm and 3 mm) are a result of the faulty manufacturing). The magnet remanent flux density has been considered to be constant.

Table 2.4 Heat losses at different loads (whole machine) at 1200 rpm

Machine Part	75% load	100% load	120% load
Stator Iron	675 W	900 W	1800 W
Copper Winding	1114 W	2160 W	3100 W
Rotor Iron	150 W	200 W	400 W
Permanent Magnet	225 W	450 W	900 W
Additional	2636 W	2785 W	2800 W
Total	4800 W	6492 W	9000 W

The machine parts are constituted of materials whose thermal conductivities are either isotropic or anisotropic. Anisotropic conduction is associated with the composite structure of the machine parts. The stator teeth and yokes are split up into many laminations to reduce the eddy current losses in the magnetic circuit caused by the magnetic flux alternation. The laminations are connected to each other by the lamination insulation surfaces and possible air in the middle, both having low thermal conductivity, which results in poor thermal conductivity in the radial direction. Each conductor of the stator winding is impregnated by insulation whose thermal conductivity is only 0.26 W/(K·m), so it causes very poor conduction in the radial and tangential directions in the slots, and in the radial and axial directions in the end windings. Table 2.5 lists the thermal conductivities in different directions of the materials used (Mademlis et al., 2000; Ibtiouen et al., 2001; Technical Data Sheet Of AREMCO, 2010). The thermal contact conductance has not been considered in the models.

Table 2.5 Thermal conductivities of the materials used in the machine

Material of Model Component	Thermal Conductivities, W/(K·m), Direction, cylinder coordinates		
	r(radial)	θ(tangential)	z(axial)
Iron lamination	4.43	39	39
Stator Copper Winding in slot	0.8	0.8	386
Stator Copper End-Winding	0.8	386	0.8
Solid Aluminium	237	237	237
Permanent Magnets (NdFeB)	9	9	9
Glass Fibre	0.43	0.43	0.43
Copper Bars	400	400	400
Potting Material (Ceramacast 675N by Aremco)	100	100	100
Epoxy Resin	0.26	0.26	0.26

The analytical calculation of the two-phase solid-to-solid mixture of Maxwell (1954) can be used for equivalent thermal conductivity for the copper winding (Hong, 2011). The thermal conductivity of the rotor and stator laminations may be defined in the same manner.

$$\lambda_{eq} = \frac{\lambda_{ins} \cdot \left(\lambda_{Cu} + 2 \cdot \lambda_{ins} - 2 \cdot s_{sl} \cdot F_{space} \cdot \left(\lambda_{ins} - \lambda_{Cu}\right)\right)}{\lambda_{Cu} + 2 \cdot \lambda_{ins} + F_{space} \cdot \left(\lambda_{ins} - \lambda_{Cu}\right)} \tag{2.1}$$

where λ_{eq} is the equivalent thermal conductivity of the winding, λ_{Cu} is the thermal conductivity of the copper, λ_{ins} is the thermal conductivity of the insulation, F_{space} is the copper space factor, and s_{sl} is the cross-section of the slot.

The totally enclosed housing disables any ambient air flow and thus deteriorates the convection heat transfer inside the machine. A small natural convection exists on the outer sides of the housing and can be determined by the following equations (Incropera et al., 2007). The Churchill and Chu correlation is used for the Nusselt number calculation. This equation is valid for horizontal cylinders and $Ra \leq 10^{12}$ (Incropera et al., 2007). The Rayleigh number of the air flow on the outer surface of the machine frame is $1.035 \cdot 10^{8}$.

$$\alpha_{convfr/air} = \frac{\lambda_{air} \cdot Nu_{air}}{D_{stfr}} \tag{2.2}$$

$$Nu_{Dair} = \left[0.6 + \left(\frac{0.387 \cdot Ra_{air}^{1/6}}{\left(1 + \left(\frac{0.599}{Pr_{air}}\right)^{9/16}\right)^{8/27}} \right) \right]^2 \tag{2.3}$$

$$Ra_{air} = \frac{g \cdot \beta_{air} \cdot D_{stfr}^3 \cdot \left(T_{stfr} - T_{air}\right)}{\nu_{air} \cdot \alpha_{air}} \tag{2.4}$$

$$Pr_{air} = \frac{c_{pair} \cdot \mu_{air}}{\lambda_{air}} \tag{2.5}$$

where k_{air} is the thermal conductivity of the air, Nu_{air} is the Nusselt number of the air, D_{stfr} is the length of the stator frame, Ra_{air} is the Rayleigh number of the air, Pr_{air} is the Prandl number of the air, g is the gravitation constant (9.8 m^2/s), β_{air} is the coefficient of the thermal expansion of the air (1/303 1/K), α_{air} is the thermal diffusivity of the air, T_{stfr} and T_{air} are the stator frame and air temperatures, ν_{air} is the kinematic viscosity of the air, μ_{air} is the dynamic viscosity of the air, λ_{air} is the thermal conductivity of the air and c_{pair} is the specific heat capacity of the air.

Heat dissipation out of the machine occurs mostly through the back liquid jackets in the housings. The convection coefficient in the frame ducts can be calculated from the definition of the Nusselt number via the Gnielinski correlation (Incropera et al., 2007). The Gnielinski correlation is valid over a large Reynolds number range, including the

transition region in the circular smooth tube ($0.5 \leq Pr_{\text{fluid}} \leq 2000$ and $3000 \leq Re_{\text{D}} \leq 5\,000\,000$) (Incropera et al., 2007). The Reynolds number of the coolant flow in the liquid jacket is 3180. The equation has a margin of error of 10% or less.

$$\alpha_{\text{conv w/duct}} = \frac{\lambda_{\text{w}} \cdot Nu_{\text{w}}}{D_{\text{duct}}} \tag{2.6}$$

$$Nu_{\text{w}} = \frac{\frac{\varepsilon}{8} \cdot (Re_{\text{w}} - 1000) \cdot Pr_{\text{w}}}{1 + 12.7 \cdot \left(\frac{\varepsilon}{8}\right)^{0.5} \cdot \left(Pr_{\text{w}}^{2/3} - 1\right)} \tag{2.7}$$

$$Re_{\text{w}} = \frac{\rho_{\text{w}} \cdot \upsilon_{\text{mean,w}} \cdot D_{\text{duct}}}{\mu_{\text{w}}} \tag{2.8}$$

$$\varepsilon = 0.11 \cdot \left(\frac{\varepsilon_{\text{ss}}}{D_{\text{duct}}} + \frac{68}{Re_{\text{w}}}\right)^{1/4} \tag{2.9}$$

where Nu_{w} is the Nusselt number of the water, ε is the friction factor, Re_{w} is the Reynolds number of the water flow, Pr_{w} is the Prandl number of the water, λ_{w} is the thermal conductivity of the water, ρ_{w} is the density of water, $\upsilon_{\text{m,w}}$ is the mean flow speed of the water, μ_{w} is the dynamic viscosity of the water, ε is the friction factor and ε_{ss} is the stainless steel surface roughness ($1.327 \cdot 10^{-6}$ m). The friction factor is defined by the Aldsul correlation (Eq.2.9) for the Colebrook equation (Incropera et al., 2007). The water flow was set to 6.2 l/min, so the convection coefficient is 480 W/(m^2·K) for water properties at 17°C. This value of the water flow rate was defined in the preliminary specifications, as the designed machine should be applicable to highly integrated vehicle modules.

2.2.2 Thermal design based on CFD thermal modelling

A simplified simulation model based on computational thermal design takes into account the geometry, the material parameters, the losses and the boundary conditions equivalent to a real machine. The 3D CFD thermal simulated model includes half of the machine slot in the cross-section and half of the machine length in longitudinal direction. As mentioned above in section 2.1, because the fan effect in the rotor structure was ruined during manufacturing, the CFD thermal model of the rotor part was created without the desired ducts and the fixing elements. The bearing and end shields were excluded from the model. For simulation purposes, using Gambit software, a tetrahedral mesh with 94 000 nodes, 1 120 000 faces and 440 000 cells were created within the machine model (Fig. 2.3).

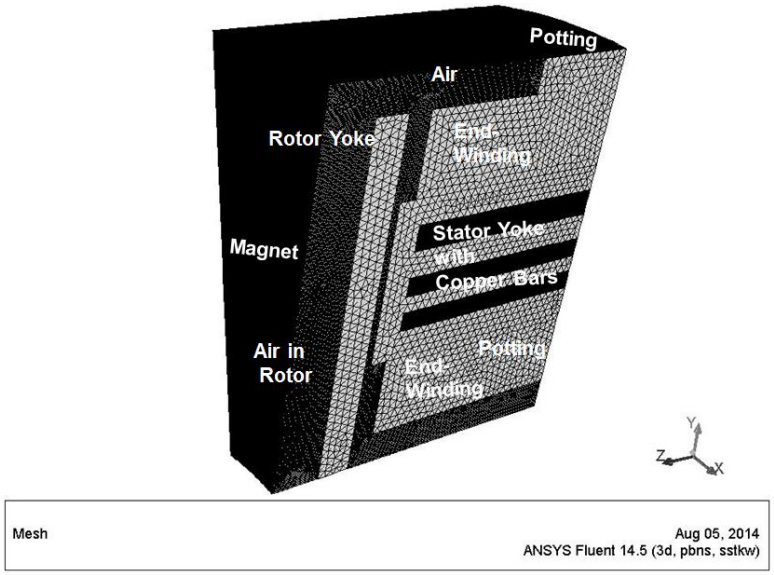

Figure 2.3: Mesh created for the machine model.

The CFD thermal modelling was implemented using the κ-ω SST turbulence Menter model and the energy models of the commercial software Fluent 14.5. The κ-ω SST turbulence model was applied because the model equations behave appropriately in both the near-wall and far-field zones. The blending function and the cross-diffusion derivative term (added in the ω equation) are applied to the κ-ω SST turbulence model to handle two models (Fluent 6.3 Documentation). The Rotation Reference Frame (with a speed of 157 rad/s) is applied to simulate air flow inside the rotor structure. The viscous heating module is considered to include the air friction losses in the simulations, although it is insignificant in this case because of the low air speed. The default values of the κ-ω SST turbulence model constants were used.

In the machine thermal model, the boundary conditions, such as the convection coefficients and coolant temperatures in the frame (respectively 480 W/(m^2·K) and 17 ˚C) and on the outer surface (respectively 3 W/(m^2·K) and 22 ˚C) were imposed. The convection coefficients were defined by Eq. (2.2)-(2.9). The volumetric heat losses presented in Table 2.4 were imposed as heat sources of the simplified machine parts. The interface gap between the stator iron and the housing was assumed to be 0.015 mm (Staton et al., 2005). The interface gap was defined by the wall thickness, and the air thermal conductivity (0.03 W/(m·K)) was applied to the interface gap (the wall thickness). The wall thickness (5 mm) with the steel thermal conductivity (16 W/(m·K)) was also applied to the outer machine surface. The small gap between the copper bars and stator lamination was defined by the wall thickness (0.1 mm) and the grease thermal conductivity (0.2 W/(m·K)). The thin glue layer applied for the permanent magnet attachment was not taken into account in the model, as its thermal resistance is low and

can therefore be neglected. The thermal conductivity of the epoxy (used as a glue) is 1 W/(m·K) and the glue layer is 0.1 mm, so the thermal resistance of the glue layer is 0.01 K/W.

The surface roughnesses were defined on the boundary surfaces inside the machine (back surfaces, surfaces in the air gap region). The surface roughness was assumed to be 25 μm for the stator windings and 5 μm for other surfaces. The surface roughness affects the convection heat transfer coefficient between the internal air flow and the machine parts, as it causes disturbances into the viscous sublayer of the boundary layers (Pickering et al., 2002). The fluid side heat transfer convection coefficient is defined based on the local conditions (turbulence level, temperature and velocity profiles) in software Ansys Fluent 14.5 (Ansys 14.5 Theory Guide)

$$\alpha_{\mathrm{conv}} = \frac{q}{T_{\mathrm{ref}} - T_{\mathrm{wall}}} \tag{2.10}$$

where q is the heat flux density at wall, T_{ref} is the local fluid temperature (the adjusted cell temperature) and T_{wall} is the wall temperature. The heat transfer is defined using Fourier's law at the wall for laminar flow (Eq.2.11) and the law-of-the-wall for temperature derived using the analogy between heat and momentum transfer for turbulent flow (Eq. 2.12) in Fluent 14.5 (Ansys 14.5 Theory Guide).

$$q = \lambda_{\mathrm{f}} \left(\frac{\partial T}{\partial n} \right)_{\mathrm{wall}} \tag{2.11}$$

where n is the local coordinate normal to the wall, λ_{f} is the thermal conductivity of fluid.

The law of the wall presents the relationship between the velocity profile and wall shear stress in the turbulent boundary layers (Eq. 2.13) (Ansys, 2011). Based on this theory there are three sub layers near by the wall: laminar viscous sub layer, buffer layer with viscous and turbulence effects and logarithmic layer with mixing effect caused by turbulence (Fig.2.4).

$$\upsilon^* = \frac{1}{K_{\mathrm{K}}} \cdot \ln\left(K_{\mathrm{emp}} y^* \right)$$

$$\upsilon^* \equiv \frac{\upsilon_{\mathrm{P}} \cdot K_{\mu}^{1/4} \cdot k_{\mathrm{P}}^{1/2}}{\tau_{\mathrm{w}} / \rho}$$

$$y^* \equiv \frac{\rho \cdot K_\mu^{1/4} \cdot k_P^{1/2} \cdot y_P}{\mu} \tag{2.12}$$

where K_K is von Karmar constant (0.4187), K_{emp} is an empirical constant (9.783), y^* is the dimensionless distance from the wall, v^* is the dimensionless velocity, y_P is the distance from point P to the wall, v_P is the velocity at the first near-wall node P, K_μ is an empirical coefficient, k_P is the turbulent kinetic energy at the first near-wall node P, τ_w is the wall shear stress (Pa), T_P is the temperature at the first near-wall node P, c_p is the specific heat capacity of the fluid, ρ is the density of the fluid, μ is the dynamic viscosity of the fluid (Ansys 14.5 Theory Guide).

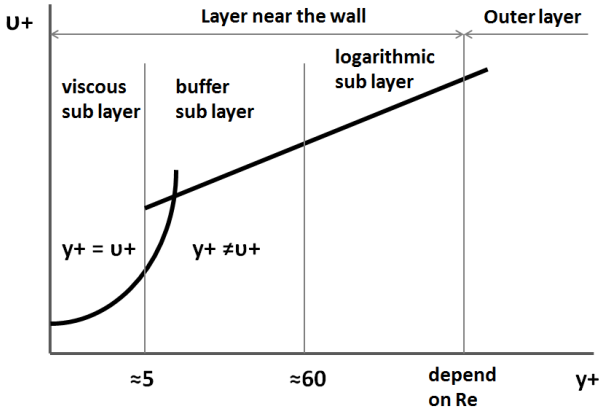

Figure 2.4: near wall modelling in RANS (Ansys, 2011).

In Ansys Fluent the dimensionless distance from the wall y^* is applied assuming that it is approximately equal to y^+. The *y plus* (y^+) is used in the boundary-layer theory and is defined as the dimensionless wall distance for a wall-bound flow.

$$y^+ = \frac{y \cdot v_{fr}}{\nu} \tag{2.13}$$

$$v_{fr} = \sqrt{\frac{\tau_w}{\rho}} \tag{2.14}$$

$$\tau_w = \mu \cdot \left(\frac{\partial v}{\partial y} \right)_{y=0} \tag{2.15}$$

$$\upsilon^{+} = \frac{\upsilon}{\upsilon_{\mathrm{fr}}} \tag{2.16}$$

where y is the distance to the nearest wall, υ_{fr} is the friction velocity at the nearest wall, v is the kinematic viscosity of the fluid, ρ is the fluid density at the nearest wall, τ_{w} is the wall shear stress (Pa), μ is the dynamic viscosity of the fluid and υ is the flow velocity parallel to the wall. The *y plus* is used as a grid-independent criterion or to assess the mesh for flow pattern.

The law-of-the-wall employs the logarithmic law (Eq. 2.17; Fig.2.4) for the turbulent region where effects of turbulence dominate conduction (Ansys 14.5 Theory Guide)

$$T^{*} \equiv \frac{\left(T_{\mathrm{w}} - T_{\mathrm{P}}\right) \cdot \rho \cdot c_{\mathrm{p}} \cdot K_{\mu}^{1/4} \cdot k_{\mathrm{P}}^{1/2}}{q}$$

$$T^{*} = Pr_{\mathrm{y}^{*}} + \frac{\rho \cdot Pr \cdot K_{\mu}^{1/4} \cdot k_{\mathrm{P}}^{1/2} \cdot \upsilon_{\mathrm{P}}^{2}}{2 \cdot q} \quad \left(y^{*} < y_{\mathrm{t}}^{*}\right)$$

$$T^{*} = Pr_{\mathrm{t}} \cdot \left[\frac{1}{\kappa}\ln(Ey^{*}) + P\right] + \frac{\rho \cdot K_{\mu}^{1/4} \cdot k_{\mathrm{P}}^{1/2} \cdot \upsilon_{\mathrm{P}}^{2}}{2 \cdot q} \cdot \left(Pr_{\mathrm{t}} \cdot \upsilon_{\mathrm{P}}^{2} + (Pr - Pr_{\mathrm{t}}) \cdot \upsilon_{\mathrm{c}}^{2}\right) \quad \left(y^{*} > y_{\mathrm{t}}^{*}\right)$$

$$P_{\mathrm{smooth}} = 9.24 \cdot \left[\left(\frac{Pr}{Pr_{\mathrm{t}}}\right)^{3/4} - 1\right] \cdot \left[1 + 0.28 \cdot e^{-0.007 \cdot \frac{Pr}{Pr_{\mathrm{t}}}}\right] \tag{2.17}$$

where T^{*} is the temperature at the dimensionless distance y^{*} from the wall, y_{P} is the distance from point P to the wall, T_{P} is the temperature at the first near-wall node P, ρ is the density of the fluid, c_{p} is the specific heat capacity of the fluid, k_{P} is the turbulent kinetic energy at the first near-wall node P, K_{μ} is an empirical coefficient, q is the wall heat flux, Pr is the Prandl number of the fluid, Pr_{t} is the turbulent Prandl number, $Pr_{\mathrm{y}^{*}}$ is the turbulent Prandl number at the dimensionless distance y^{*} from the wall, υ_{P} is the velocity at the first near-wall node P, υ_{P} is the mean velocity magnitude at $y^{*}=y_{\mathrm{t}}^{*}$, μ is the dynamic viscosity of the fluid (Ansys 14.5 Theory Guide).

Two basic methods are applied to consider the flow near the wall in Ansys Fluent 14.5. The Low Reynolds' number method is used to capture the viscous effect in the sub layer, so very refined mesh is required in this case. The low Reynolds' number method requires *y plus* values below 2 and the κ-ω turbulence model is recommended. Another method is wall function method, where the boundary layer is not resolved and thereby

the mesh needs not to be refined. The wall function method requires a mesh with *y plus* above 30 and the *κ-ε* turbulence model is recommended. If *y plus* is between 2 and 30 (buffer zone) the enhanced wall function (enhanced wall treatment) is applied and the *κ-ω* SST turbulence model could be used (Ansys, 2012). The enhanced wall function (enhanced wall treatment) presents the combination of the Low Reynolds' number method and the wall function method according to the relative weightage (Eq. 2.18) (Ansys 14.5 Theory Guide; Kader, 1981). However, this method guarantees reasonable representation of velocity profiles only in the region where *y plus* is between 3 and 10 and in other *y plus values* ($11 < y^+ < 30$) the correctness is lower (Ansys, 2012).

$$\upsilon^+ = e^{\Gamma\upsilon} \cdot \upsilon^+_{\text{lam}} + e^{1/\Gamma\upsilon} \cdot \upsilon^+_{\text{t}}$$

$$\Gamma_{\upsilon} = -\frac{0.01 \cdot \left(y^+\right)^4}{1 + 5 \cdot y^+}$$

$$T^+ = e^{\Gamma_{\text{T}}} \cdot \upsilon^+_{\text{lam}} + e^{1/\Gamma_{\text{T}}} \cdot \upsilon^+_{\text{t}}$$

$$\Gamma_{\text{T}} = -\frac{0.01 \cdot \left(Pr \cdot y^+\right)^4}{1 + 5 \cdot Pr^3 \cdot y^+} \tag{2.18}$$

where Γ_{υ}, Γ_{T} are the blending functions for υ^+ and T^+ correspondingly, υ^+_{lam} is the laminar dimensionless velocity, υ^+_{t} is the turbulent dimensionless velocity, T^+_{lam} is the laminar thermal wall function, T^+_{t} is the turbulent thermal wall function (Ansys 14.5 Theory Guide).

According to Menter (2003) and based on industrial experience, in cases of complex geometry (e.g., the sector of an electrical machine), the *κ-ω* SST turbulence model is the best choice. It is capable of handling a wide range of *y plus* values with acceptable errors (Menter et al., 2003). The constructed 3D model of the machine segment (Fig. 2.3) has *y plus* = 6 for the walls of the stator and rotor in the air gap region and *y plus* = 2 for other walls of the stator and rotor.

The application of the potting material in the end winding naturally caused low air circulation between the end winding and the internal side of the liquid jacket incorporated in the machine frame. Fig. 2.5 (a) shows that the air velocity between the end winding and the internal side of the frame is insignificant (1-3 m/s), meaning the thermal resistance of this region is high. The air circulation around the lower end winding is higher (3-9 m/s) due to its placement near the rotating shaft. The application of the potting material in this region provides a heat conductance path for better cooling of the machine stator. Fig. 2.5 (b) illustrates the air velocity distribution in the potting material application. The air velocity is higher inside the machine, as the air flow has less space for circulation (the spaces in the end-winding region are limited by the

potting). Fig. 2.5 also illustrates the wall function convection coefficients in the potted and non-potted machine models. The higher convection coefficients (230-260 W/(m^2·K)) on the end winding surfaces (Fig. 2.5 (b)) are associated with a higher air velocity in the potted stator.

(a) Air velocity distribution inside the machine and convection coefficients on outer surfaces of the machine parts (without the potting material)

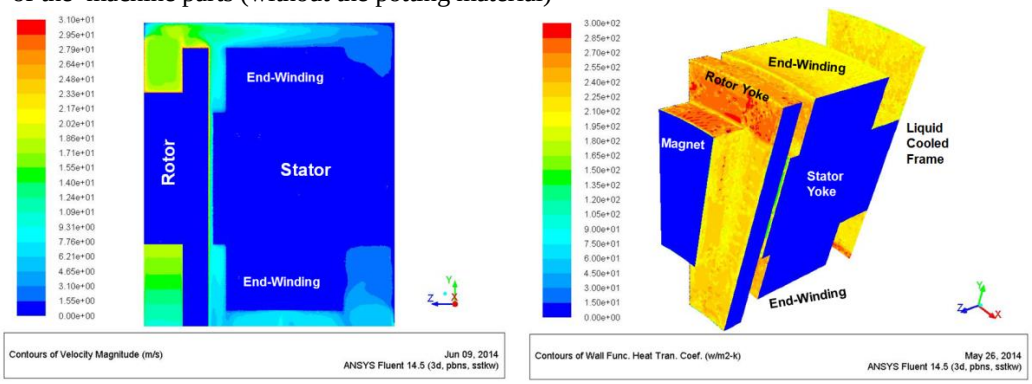

(b) Air velocity distribution inside the machine and convection coefficients on outer surfaces of the machine parts (with potting material)

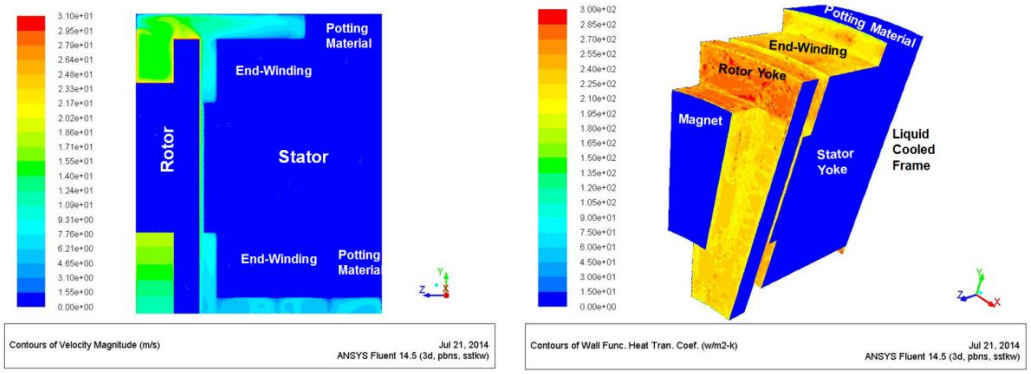

Figure 2.5: Air velocity distribution and convection coefficients on the surfaces of outer machine parts.

Next, three types of modifications made to the machine cooling system are compared from thermal point of view in Fig.2.6 at 100% load. The first model (a) adopts a water jacket (WJ) incorporated in the frame; the second model (b) adds the three copper bars inserted in the teeth; the third model (c) adopts all the cooling scheme components (the water jacket, the three copper bars and the potting material in the clearance between the end-windings and the frame). Table 2.6 indicates the temperature results for the machine parts at different loads.

(a) Temperature distribution within machine parts (the cooling system is based on WJ)

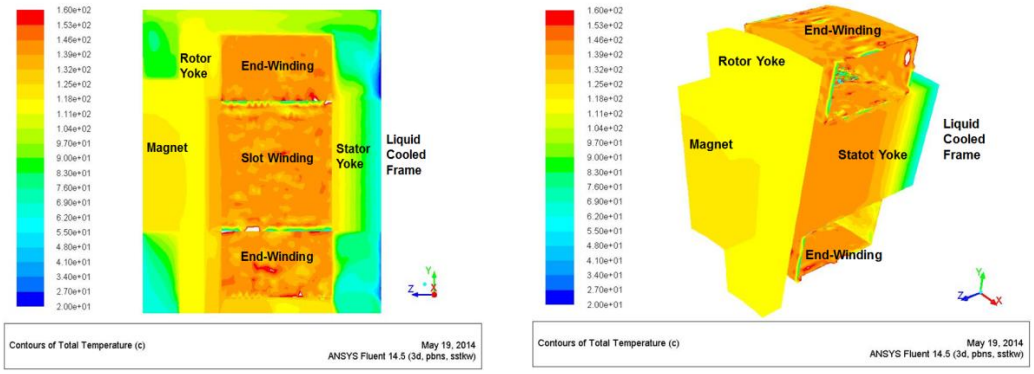

(b) Temperature distribution within machine parts (the cooling system is based on WJ and three copper bars per tooth)

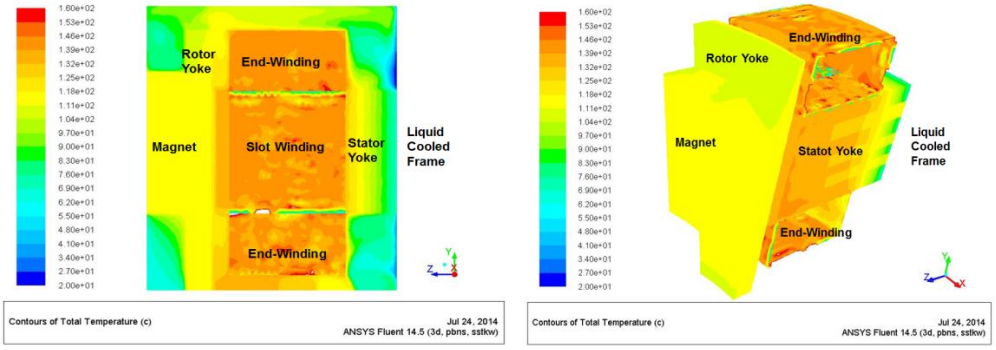

(c) Temperature distribution within machine parts (the cooling system is based on WJ, potting materials and three copper bars per tooth)

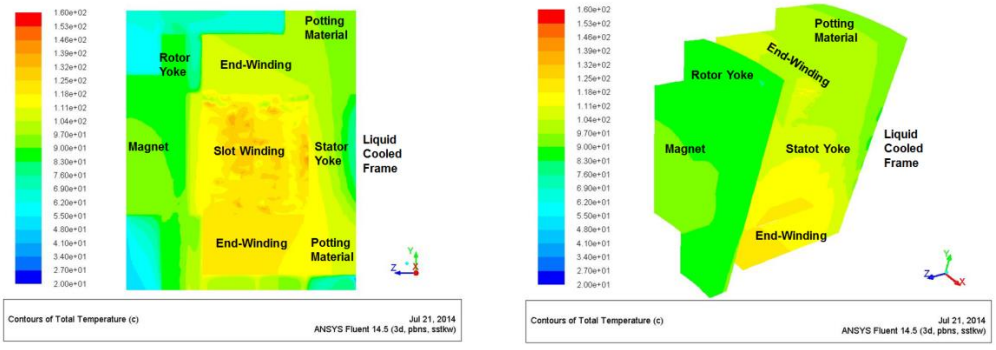

Figure 2.6: Temperature distributions within the machine parts according to the different cooling methods at 100% load.

The application of the copper bars inserted in the stator teeth and stator yoke mainly reduces the temperature of the stator iron by 10 K (Fig. 2.6 (a) and (b)). The resulting temperature drop in the stator winding is 8-10 K (Table 2.6). The cooler stator iron in turn produces a drop in temperature (up to 10 K) in the embedded permanent magnet (Fig. 2.6 (a) and (b)). However, at 75% and 120% loads, the copper bar application only causes a 3-5 K temperature drop in the rotor (related to the restricted cooling of the rotor) (Table 2.6). The rotor is cooled only by the air circulation, the cooling capacity of which is limited in this design (without forced air cooling). In Fig. 2.6 (c), the resulting temperature distribution from the addition of the potting material and the copper bars is shown. The application of the potting material reduces the stator winding temperature by 10-15 K (Fig. 2.6 (b) and (c)). The highest temperature drop, 18-20 K, is in the upper end windings, as more potting material is applied there (Fig. 2.6 (c)). The rotor temperatures are reduced by 15-20 K (Fig. 2.6 (b) and (c)), as the air circulation increases and the air temperature decreases by 20-30 K.

Table 2.6 Temperature distribution within machine parts (simulated results)

Machine component	Average Temperature (75% load→100% load→120% load)		
	With the cooling system based on the water jacket	With the cooling system based on the water jacket and three copper bars per stator tooth	With the cooling system based on the water jacket, three copper bars per stator tooth and end winding potting materials
Stator iron	120˚C →130˚C →137˚C	111˚C →120˚C →127˚C	100˚C →107˚C →125˚C
Air in Air Gap	120˚C →125˚C →143˚C	113˚C →115˚C →135˚C	80˚C →100˚C→120˚C
End-winding	138˚C →150˚C →165˚C	128˚C →142˚C →150˚C	110/120˚C →115/125˚C →130/140˚C
Slot Winding	138˚C →150˚C →165˚C	128˚C →142˚C →150˚C	120˚C →125˚C →140˚C
Rotor Iron	102˚C →115˚C →146˚C	100˚C →111˚C →141˚C	83˚C →90˚C →115˚C
Magnets	102˚C →125˚C →155˚C	100˚C →115˚C →152˚C	83˚C →97˚C →125˚C

Based on CFD thermal analysis results, the copper bars mostly influence decreases in the stator iron and the slot winding temperatures, while the potting material decreases the temperatures of the entire machine.

2.2.3 Potting material and copper bars

In the previous section, three cases of the cooling scheme are presented and analysed. This section presents the use of thermal analysis to determine the winding and permanent magnet temperatures associated with different numbers of copper bars and differing potting material locations.

The thermal analysis was conducted using the commercial FEM software Fluent. The resulting simplified 3D model represents only a forty-eighth part of the total machine and comprises the stator yoke, the stator tooth, the slot wedge, the copper winding, the copper end winding, the insulation, the inserted copper bars and the potting material. An accurate thermal model of the machine is achieved by defining the boundary conditions (the convection coefficients in the frame and outer surface) and the imposed volumetric heat losses. The simulation parameters are the same as those discussed in Section 2.2.2. The effects on temperature of the number of copper bars and the potting material location at 100% load are listed in Table 2.7.

Table 2.7 Temperature distribution within the stator iron and winding at 100% load (simulated results)

Type of Modification of Cooling Scheme based on Liquid Jacket	Average Temperature	
	Rotor Mounted Magnets	Slot Winding/ End Windings
Without copper bars or potting material	125˚C	150˚C/150˚C
One copper bar (d=8mm)	120˚C	146˚C/146˚C
Three copper bars (d_1=8mm and $d_{2,3}$=6 mm)	115˚C	142˚C/142˚C
Potting of half of the end-winding space	110˚C	140˚C/136˚C
One copper bar (d=8mm) and potting of half of the end-winding space	108˚C	130˚C/130˚C
Three copper bars (d_1=8mm and $d_{2,3}$=6 mm) and potting of half of the end-winding space	97˚C	125˚C/120˚C
One copper bar (d=8mm) and potting of the whole of the end-winding space	95˚C	130˚C/130˚C
Three copper bars (d_1=8mm and $d_{2,3}$=6 mm) and potting of the whole of the end-winding space	93˚C	125˚C/120˚C

The potting material and copper bars significantly influence the machine temperatures. The potting of half of the space between the end winding and the frame allows for a reduction of the end winding temperature by 14 ˚C and the rotor temperature by 10 ˚C. The application of copper bars mainly reduces the slot copper winding temperature,

with a drop of 4 ˚C or 8 ˚C corresponding to one or three copper bars per tooth. The temperature of the embedded permanent magnet drops by 5-10 ˚C with the application of the copper bars. The design optimization of this cooling system is constrained by the desire to keep the number of the copper bars in a range allowing simple manufacturing, low extra losses in teeth and sufficient mechanical durability.

A significant temperature drop can be attained through the joint application of the copper bars and potting material. The potting of half of the end winding space and the added copper bars allow for a reduction of the winding temperature by 20-30 ˚C and the rotor temperature by 17-28 ˚C, depending on the number of copper bars. The potting of the whole end winding space can provide a reduction of the rotor temperature by 5-12 ˚C, depending on the number of copper bars.

2.3 Experimental results and analysis

An axial flux machine prototype was manufactured for practical verification of the proposed cooling solutions. The machine models presented in Fig. 2.6 were thus tested. Initially, the machine prototype was measured in conditions of the water jacket operation. The stators were built in such a way that they had 12 solid steel plates welded on the yokes and milled to achieve good contact on the housing cooled by water. The idea was to leave a flow path for circulating air flow inside the machine so that the rotor would work as a two-sided fan circulating air among the magnets, the end windings, behind the stators and then back to the rotor fan inlet. The rotor supporting structure was made of impregnated class fibre, and there was a steel hub for the rotor. Unfortunately, the hub was manufactured incorrectly, so it almost totally closed off the fan intake. It was not possible to arrange for a new rotor during the work. Therefore, the machine practical performance was unable to meet the original needs; it could, however, be used to verify the effectiveness of the other aforementioned cooling arrangements.

To improve the cooling performance, the above-mentioned copper bars were inserted in both stators, and one of the two stators was partially potted (Fig. 2.2). These modifications of the machine prototype allowed for receiving more useful data for the analysis and verification of the computation results.

The machine was tested with an ASC800 inverter and IM load machine. It was assumed that the inverter has a high frequency; therefore, the non-sinusoidality of the inverter voltage has not been taken into account. The prototype machine has two stators and one rotor. The facility water was used as a coolant during the tests (Fig. 2.8). This water is full of oxygen, the main driving force for steel corrosion, so in a real application, only a mix of water and glycol should be adopted. Several measurements were made using the same machine but incorporating the different combinations of the cooling solutions. First, measurements of the machine with the added liquid jacket were taken. Then, the copper bars were inserted into the same machine and the measurements were obtained again. Finally, one of the stators of the prototype machine was potted and the machine was measured again. The rotor temperature was not measured during the tests. The

temperatures of the stator winding were measured with 28 Pt-100 sensors. The margin of error of the measuring device (Resistance Temperature Device (RTD), Pt-100, class B) is ± 0.3 ºC at 0 ºC (DIN 43760). The measurement locations for one coil of phase U are shown in Fig. 2.9.

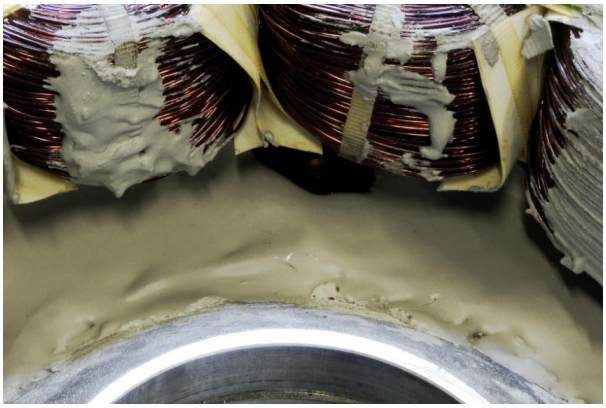

Figure 2.7: Potting material location between the end winding and frame.

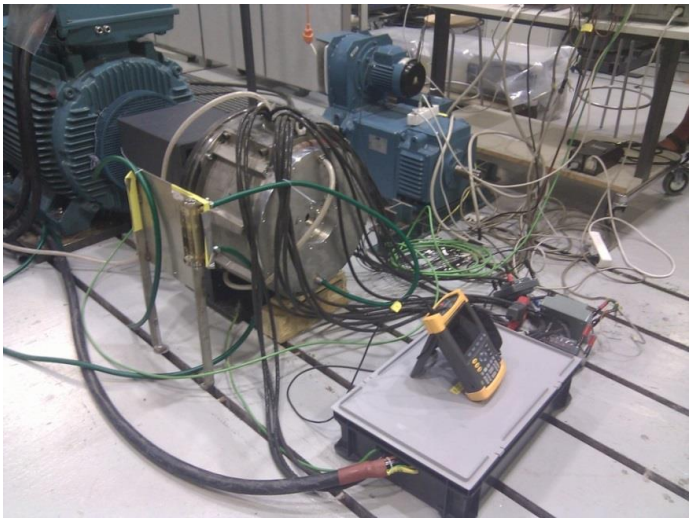

Figure 2.8: Test bench setup for the axial flux machine.

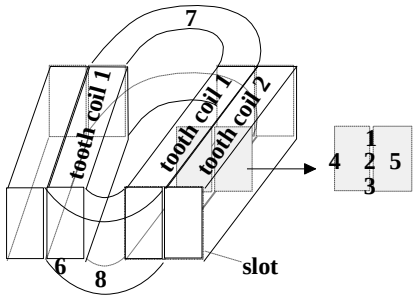

Figure 2.9: Placement of sensors inside the stator.

a. End-Winding temperature (Air Gap Side) at 75% load

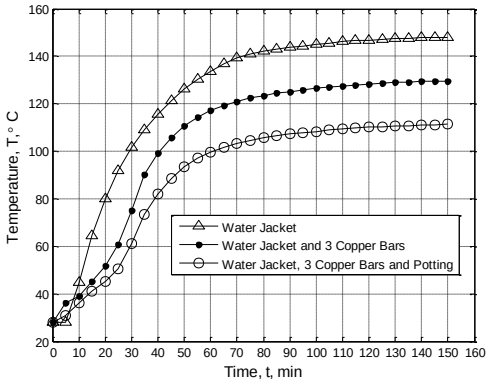

b. End-Winding temperature (Air Gap Side) at 120% load

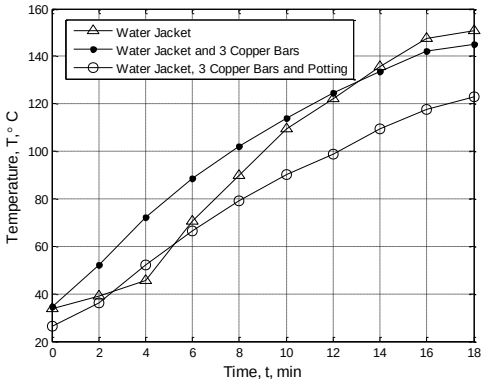

c. End-Winding temperature (Frame Side) at 75% load

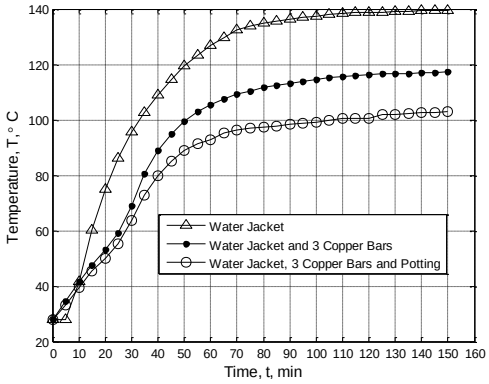

d. End-Winding temperature (Frame Side) at 120% load

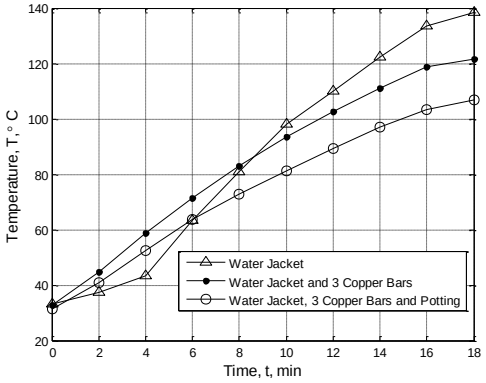

Figure 2.10: Temperature rises of the end winding during tests

(margin of error of the RTD: ± 0.3 ºC at 0 ºC).

a. Slot Winding temperature (upper part) at 75% load

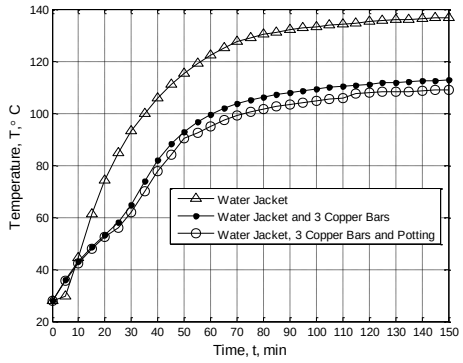

b. Slot Winding temperature (upper part) at 120% load

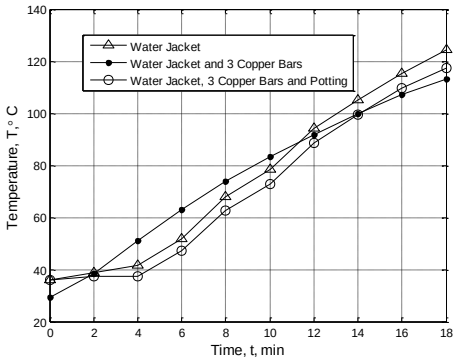

c. Slot Winding temperature (bottom part) at 75% load

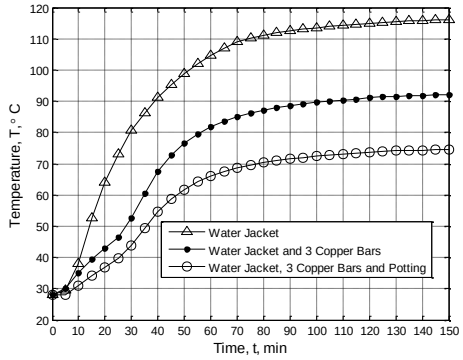

d. Slot Winding temperature (bottom part) at 120% load

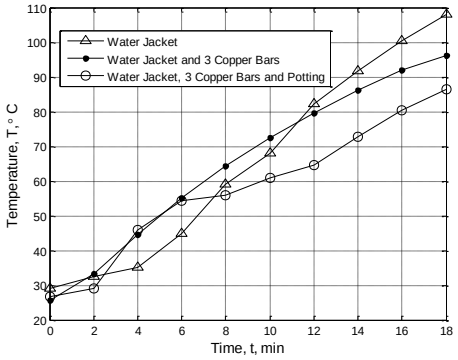

e. Slot Winding temperature (middle part) at 75% load

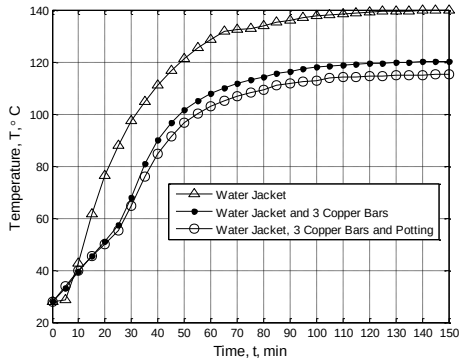

f. Slot Winding temperature (middle part) at 120% load

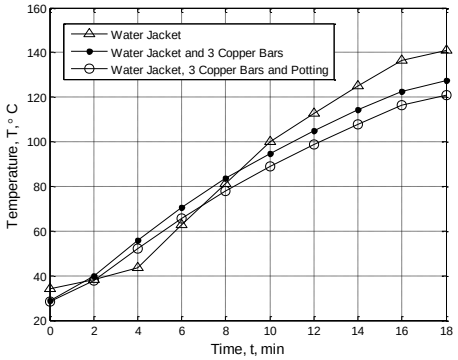

Figure 2.11: Temperature rises of the slot winding during tests

(margin of error of the RTD: ± 0.3 ºC at 0 ºC).

The simulated temperatures of the axial machine (Tables 2.8) are compared with the measured values. The deviation is on the order of 2–5 K, depending on the location. The highest deviation between the measured and the computational results is in the end winding region. The thermocouples were attached to the end winding outer surface, and that is why the influence of other parameters, such as air, was significant. The same losses for the machine parts were applied to the CFD thermal modelling, but in the case of lower temperatures, the losses decrease as copper resistivity decreases. This causes slightly overestimated temperatures for the applications of the copper bars and potting material (Table 2.8).

Table 2.8 Temperature distribution within machine parts (simulated and measured results)

Machine component	Average temperature at 75% load (measured/simulated)		
	With the cooling system based on the water jacket	With the cooling system based on the water jacket and three copper bars per stator tooth	With the cooling system based on the water jacket, three copper bars per stator tooth and end-winding potting materials
End-winding	143˚C /138˚C	125˚C /127˚C	110˚C /115˚C
Slot Winding (middle part)	140˚C /138˚C	122˚C /127˚C	118˚C/120˚C

The simulated temperature results generated by 3D models using CFD thermal analysis are validated by the test results on the machine prototype, albeit with a discrepancy of up to 2–5 K, especially in the end winding region. There are four possible explanations for this temperature discrepancy. First, the cooling surface of the end winding has a complex geometry. In the CFD thermal computations presented herein, the end winding region is defined as a rectangle with constant surface roughness in order to reduce expensive computational efforts. This may explain the overestimated temperatures, because a real end winding has a variable real surface roughness, and therefore, a larger heat transfer surface. Secondly, there exists a difference between the boundary conditions and material properties (thermal conductivities) defined in the CFD thermal simulation and the actual ones exhibited during the tests. In the last test, the machine contained both potted and non-potted stators, so the stator with potting was heated by the hotter stator without potting. In the CFD thermal computation, only one stator was simulated because of limited computational resources. Thirdly, errors were caused by the unstructured mesh, the turbulence model applied in the CFD thermal analysis and the analytical equation for the convection definition. Finally, there likely were unknown manufacturing defects, such as low contact thermal conductance.

The application of copper bars yields a maximum temperature drop of about 20 ˚C in the stator slot winding (Fig.2.11 a, c, e), and 15 ˚C in the stator end winding (Fig.2.10 a, c) in the tested designs. The temperature drop along the slot winding is obvious and accounts for about 15 ˚C in the upper part (close to the air gap region) and 25 ˚C in the bottom part (close to the stator yoke) (Fig. 2.11). The application of the potting material provides the slot winding temperature drop of 3–15 ˚C (Fig. 2.11). The temperature drop is significant in the bottom part of the slot winding, as the potting material is located only in the region between the end winding and the frame (Fig.2.11 c). The temperature drop of the end winding is 14–17 ˚C and the most significant temperature drop is in the potted part of the end winding (Fig. 2.10 a, c).

The test results were only implemented for 75% and 120% loads. The tests at 120% load were short, as over-temperatures may cause breakdown of class-F insulation at 155 ˚C and possible magnet demagnetization at 150 ˚C. Higher additional losses were identified during the tests because of the manufacturing defects (i.e., the differing lengths (1 mm and 3 mm) of the air gaps). The axial flux machine with two stators is demanding from a manufacturing perspective. The presented experimental and simulated results prove that the proposed cooling scheme with the liquid jacket, the copper bars and the potting materials provides much better cooling capability than the cooling scheme based on the liquid jacket alone.

This particular prototype was not very successful, and a fair amount of heat transfer problems were present. One of the major problems related to axial flux machine technology is that there is no possibility for a good shrink-fit between the stator yoke and the frame, which would enable a high thermal flux conductance from the stator to the frame. This feature renders the cooling of the machine difficult. In this case, this adverse effect was compensated for by the copper bars, which enabled good heat transfer from the stator stack to the water jacket. However, the problem of cooling the rotor remains, as air circulation must be relied upon, and the only way of arranging a path for the rotor-cooling air flow is to have free space between the stator yoke and the frame, which again weakens the stator cooling. Unfortunately, no definite answer to the question of whether or not it is fully suitable was found, due to the manufacturing issues with the prototype.

2.4 Conclusions

This study has shown that the proposed hybrid cooling solution (liquid jacket with the potting material and the copper bars) is a better solution than the cooling solution based only on the liquid jacket. The applied potting material and the copper bars significantly help in reducing the end winding temperature by increasing the heat conductance path between the liquid-cooled frame and the winding. To fully exploit the advantages of a liquid cooling jacket and high conductance material (potting material and copper bars), a hybrid cooling scheme for obtaining sufficient levels of cooling has been proposed and analysed. The three copper bars inserted in the stator iron reduce the temperature of

the stator copper winding by 15-20 ˚C. The CFD thermal analysis has demonstrated that three copper bars per stator tooth can provide a 4 ˚C temperature drop in the stator winding compared with the temperature measured in conditions of one copper bar per stator tooth. However, a large number of copper bars may increase the fabrication cost and result in mechanical reliability problems. The potting material serves to avoid the high thermal resistance between the end winding and the internal side of the liquid-cooled frame containing air, whose velocity and turbulence are low in this region. Thus, application of Ceramacast 675N causes a 20 ˚C temperature drop in the stator end winding, depending on the volume of the attached potting. The cooling scheme consisting of the water jacket, total potting of the end winding region and the application of the three copper bars per stator tooth allow for a temperature reduction of the stator winding by up to 40 ˚C, compared with the temperatures resulting from the cooling scheme based only on the water jacket. In this case, the temperature of the rotor decreases by 20-25 ˚C according to CFD thermal analysis, but this has not been validated by the measurements, as the rotor was not measured in the tests.

The above-presented results of the experiments indicate that the operating temperature of the most critical machine part – the copper winding insulation – is under the limited values. It may be concluded that the temperature of the embedded magnets is high because of the manufacturing mistake. This study proves that the cooling system based on the liquid jacket does not provide reliable operation of a closed-type axial flux permanent magnet machine with high torque density, especially in the overloads. The cooling system based on the liquid jacket should include also forced air cooling or the special construction of the rotor operating as a fan. The cooling system of the stator introduced and discussed in this chapter may easily be adapted to other axial flux permanent magnet synchronous machines with high torque density.

3 Indirect liquid cooling system of a radial-flux permanent magnet synchronous machine

This chapter is dedicated to the development of an indirect liquid cooling solution for a 110 kW radial flux permanent magnet synchronous machine. The designed cooling system should have the capability to keep the stator winding and the rotor-embedded-permanent magnets at temperatures lower than the accepted thermal limits. The simplified thermal models of the machine studied are simulated with the commercial software Fluent 14.5. The influence of potting material on temperature is also analysed in this section from a thermal standpoint. CFD-thermal modelling and prototype testing were utilized for this analysis.

3.1 Machine studied

The machine studied is a 110 kW radial flux tooth-coil winding permanent magnet synchronous machine with a rated current of 146 A and voltage of 500 V. Table 3.1 lists the machine characteristics.

Table 3.1 Characteristics of the RF PM machine

Parameter	Quantity
Rated Power	110 kW
Rated Speed	1500 rpm
Line to line voltage	500 V
Rated phase current	146 A
Number of phases	3
EMF factor (back emf / nominal voltage)	0.87
Rated Tangential Stress	22 kPa
Linear current density	30 kA/m
Current density	5 A/mm^2
Peak output power to rated output power ratio (overload capability) at nominal speed	2.6
Load angle	40 deg.
Power Factor	0.94
Rated electrical efficiency	96%
Number of slots and poles	24, 16
Active mass of machine	160 kg
Geometrical data	
Stator Outer Diameter	433 mm
Stator Inner Diameter	330 mm
Length of Air Gap	1.5 mm
Length of Stator	190 mm
Magnet Width × Height	45 × 12 mm^2
Slot Width × Height	27.5 × 33.5 mm^2

In the machine, the stator copper winding and the stator core losses account for more than two-thirds of the machine total losses (Table 3.2). The large number of poles in the rotor and the high rotational speed required are associated with the high frequency of the magnetic field variation in the iron parts. This high frequency, together with high flux density, produces a considerable amount of iron losses, which in some operating points can be even higher than the copper losses. Because of a manufacturing mistake, the rotor stack-supporting end rings were fabricated from black iron instead of stainless steel, which caused high extra losses in the rotor (values are given in brackets).

Table 3.2 Heat Losses

Heat Source	900 rpm, 560 Nm	1200 rpm, 700 Nm	1500 rpm, 700 Nm
Stator Copper Winding	1000W	1600W	1600W
Stator Core	720 W	1140 W	1440 W
Rotor Core	480 W (+400W)	760 W (+1000W)	960 W (+1400W)
Permanent Magnets	300 W	330 W	360 W
Mechanical Losses	300 W	500 W	600 W
Additional Losses (mechanical losses in the air gap, AC copper losses, microhysteresis losses in the iron, etc.)	300 W	400 W	500 W

As most of the losses are concentrated in the stator and as hot spots can easily occur in the windings, a water jacket was selected as a cooling solution (Fig. 3.1). The coolant passes through a series of channels (series connected) with a size of 4 mm × 40 mm and a total length of 5.4 m in the stator frame (Fig. 3.1). The coolant is a 50/50 mixture by volume of water-ethylene glycol. However, the applied water jacket does not provide efficient heat removal from the end winding region because of the high thermal resistance created by air. The over-temperatures of the end windings are a common issue in machines with natural air cooling. The 6-8 K temperature drop in the end windings is due to the potting of the end winding region. Two different types of potting materials are analysed in this work; the thermal characteristics of these are listed in Table 3.3 (Technical Data Sheet of AREMCO, 2010).

Table 3.3 Thermal Properties of Potting Materials

Parameter	Ceramacast 675N	High Temperature Epoxy 2315
Dielectric Strength, kV/m	$1.2 \cdot 10^4$	$1.9 \cdot 10^4$
Specific Electrical Resistivity, Ω·m	$1 \cdot 10^{11}$	$1 \cdot 10^{14}$
Limited Temperature, ºC	1200	185
Heat Capacity, J/(K·kg)	740	1000
Density, kg/m^3	3260	1800
Thermal Conductivity, W/(K·m)	100	58

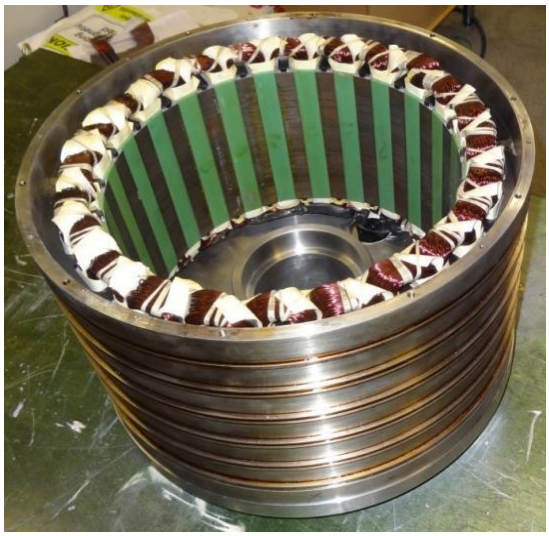

Figure 3.1: The machine studied.

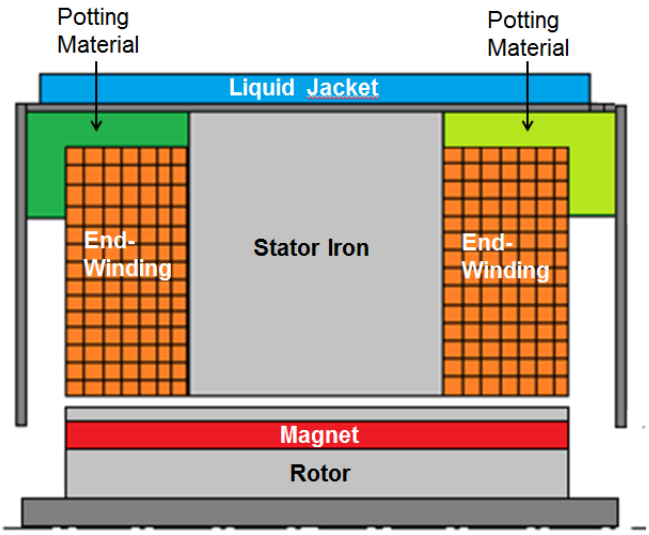

Figure 3.2: Cooling system scheme.

The rotor with the embedded permanent magnets (NdFeB) is shown in Fig. 3.2. The permanent magnets were split into eight pieces to reduce the losses in them. However, the losses in the rotor are high because of the manufacturing mistake (the stack-supporting end rings are fabricated from black iron, not shown in Fig.3.2).

The performance of the liquid jacket is illustrated in Fig. 3.3, which incorporates the following assumptions for the convection coefficient and the calculations of pressure losses. Regarding the convection coefficient, the Reynolds number ranges from 1500 to 10600, depending on the coolant flow rate in the liquid jacket (Fig. 3.3).

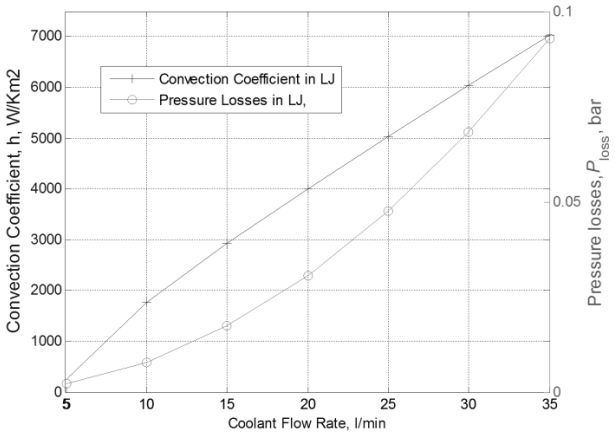

Figure 3.3: Performance of the liquid jacked (LG).

The coolant flow is Ethylene Glycol 50%Vol (at 50˚C). The convection coefficient was calculated from Eq. (2.6)-(2.9) and Eq.(3.1). In the case of the transient and turbulent flows ($Re \geq 2300$), the Gnielinski correlation (Eq.2.7) was applied for the Nusselt number calculation (Incropera et al., 2007). For the laminar flow, the Nusselt number was assumed to be constant and equals 4.36, which is valid for a circular tube with a uniform surface heat flux and fully developed conditions (Incropera et al., 2007). The friction factor ε is defined by the formulas for laminar (Eq. 3.1), transition and turbulent flow regimes (the Aldsul correlation for the Colebrook equation is presented in Eq. 2.9).

$$\varepsilon = \frac{64}{Re_{\mathrm{D}}} \tag{3.1}$$

where Re_{D} is the Reynolds number of the coolant flow (Incropera et al., 2007).

Eq. (3.2) presents the Darcy-Weisbach equation, which is employed for the calculation of the pressure loss due to friction p_{lossfric} for the fully developed flow. Eq. (3.3) is used for the calculation of the pressure loss in the fittings p_{lossfit}.

$$p_{\mathrm{loss\ fric}} = \frac{\rho_{\mathrm{f}} \cdot u_{\mathrm{f}}^2}{2} \cdot \left(\frac{l_{\mathrm{cd}} \cdot \varepsilon}{D_{\mathrm{duct}}} \right) \tag{3.2}$$

$$p_{\text{loss fit}} = \frac{\rho_f \cdot u_f^2}{2} \cdot \Sigma\xi \tag{3.3}$$

where ρ_f is the density of liquid (1000 kg/m^3), u_f is the mean flow speed, ε is the friction factor, l_{cd} is the duct length and $\Sigma\xi$ is the sum of the pressure losses coefficients in the fittings (inlet and outlet are respectively 0.5 and 1). The friction factor is defined by Eq. (2.9) and Eq. (3.1). The stainless steel surface roughness is assumed to be $1.327 \cdot 10^{-6}$ m.

3.2 CFD thermal design of the machine

A computational model of the machine studied with the liquid jacket and the potting material applied around the end windings was created and simulated to describe the feasibility of this cooling solution. CFD thermal analysis was selected for the machine modelling to depict 1) the influence of the potting material application on the air flow distribution inside the machine, and subsequently (2) the temperature distribution in the rotor and stator.

The CFD thermal model of the machine presents a segment of it (one tooth pitch) and includes the stator and rotor yokes (upper and lower parts), magnet incorporated in the rotor, slot winding, wedge, end winding, potting and air (Fig. 3.4). The model presents only half of the machine length, in the longitudinal direction. Fig. 3.4 illustrates the simulated machine model mesh with 260 000 nodes, 5 400 000 faces and 2 600 000 cells.

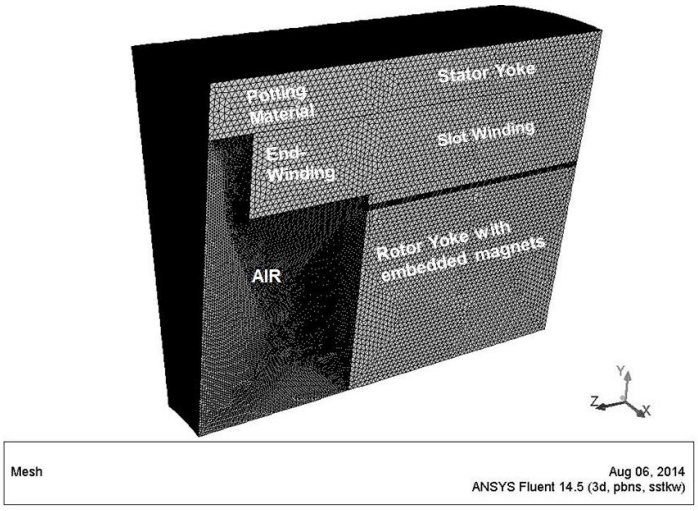

Figure 3.4: Mesh created for the machine model.

For the air region, the κ-ω SST turbulence model of commercial software Ansys Fluent 14.5 was applied. This turbulence model was employed because it is capable of handling a wide range of *y plus* values (assuming some error), and the model equations behave appropriately in both the near-wall and far-field zones. In cases of complex geometry (e.g., the sector of an electrical machine), the κ-ω SST turbulence model is the right choice according to Borges and Cezarion, 2012. The energy and the viscous heating modules were applied, although the air friction is insignificant in this case (due to low air speed). The default values of the Fluent model constants were used. The constructed machine model has *y plus* = 6.5 for the walls of the stator in the air gap and all rotor walls and *y plus* = 2 for the stator walls in the end cap region.

The thermal properties of the machine components are as those presented earlier in Table 2.5 and Table 3.3. The thermal conductivity of the slot copper winding in tangential and radial directions is 0.58 W/(K·m) (Eq. 2.1). The machine model takes as input the heat losses listed in Table 3.2 (at operation point, 1500 rpm and 700 Nm) and the thermal boundary conditions. To simulate the real application environment, the uniform convective heat transfer coefficient and liquid temperature (25 l/min - 50 ºC and 5050 W/m^2·K) were applied on the outer surface of the stator yoke. The convection coefficient has been evaluated using Eq. (2.6-2.8) and Eq. (3.1). The Reynolds number of the coolant flow in the liquid jacket is 7580, so the Gnielinski correlation can be assumed valid with the assumptions. The properties of Ceramacast 675N claimed by the producer were applied for the potting region (Table 3.3). The interface gap between the stator iron and the housing was assumed to be 0.01 mm (Staton et al., 2005). The interface gap was defined by the wall thickness, and the air thermal conductivity (0.03 W/(m·K)) was applied to the interface gap (the wall thickness). The glue applied for the permanent magnet attachment was not taken into account in the model, as its thermal resistance (0.1 mm epoxy layer with the thermal conductivity 1 W/(m·K)) is low (0.12 K/W) and can, therefore, be neglected. The surface roughness was defined for the machine parts as 25 μm for the stator windings, and as 5 μm for other surfaces.

Fig. 3.5 shows the temperature and the velocity fields within the machine parts for the potted and non-potted stators. The figures of velocity distribution inside the machine show that the velocity values are higher (by 40%) in the end cap region in the case of the machine with the potted stator, as the air flow has less space for circulation (the spaces in the end winding region are limited by the potting material). In the end cap region near the end windings, the air velocity is 3-5 m/s and 6-9 m/s in the respective non-potted and potted machines (Fig. 3.5 a, b). Therefore, higher convection coefficients occur in the end cap region in the potted machine design.

The temperature distributions within the potted and non-potted machines are illustrated in Fig. 3.5 and listed in Table 3.5.

(a) Temperature distribution within the potted machine parts

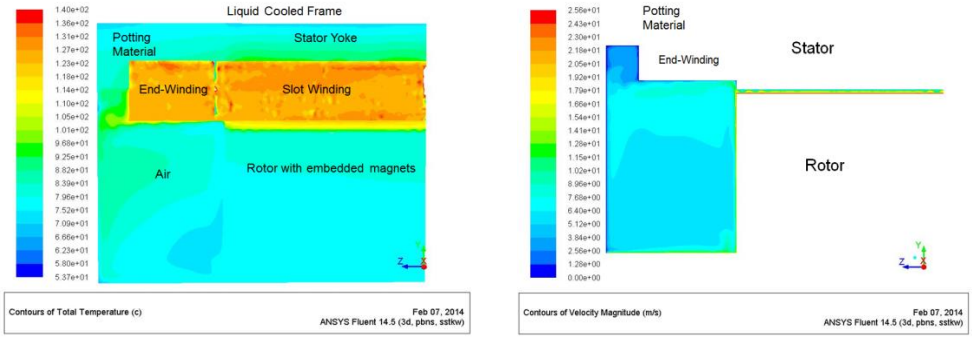

(b) Temperature distribution within the non-potted machine parts

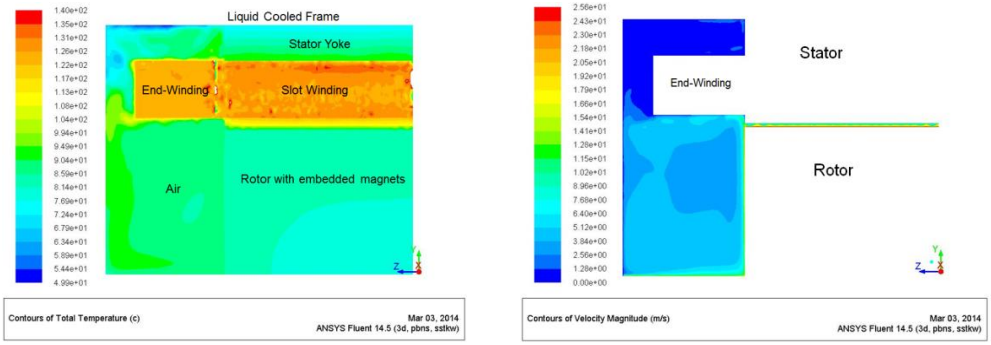

Figure 3.5: Temperature distribution within the machine parts and the air velocity field, in simulated conditions of the different cooling solutions.

As can be seen in them, the application of the potting material in the end winding region allows for a 6 K temperature reduction of the end windings and the slot winding temperature. The potting material attached to the end winding and the stator yoke on one side and to the internal frame side on another works as a thermal bridge. In the case of the potted machine design, the temperatures of the stator winding stay below 125 ºC, and the magnet temperature (below 80 ºC) is under the capability of most magnet grades. The lower internal air temperature and higher air velocity in the end cap provide lower temperatures of the rotor embedded-permanent-magnets (77 ˚C) and the rotor iron (70˚C) in the potted machine design compared with the non-potted one (Fig. 3.5 a, b). The application of the potting material provides a 10–11 K temperature drop in the rotor embedded-permanent-magnets and the rotor yoke (Table 3.5).

Table 3.5 Temperature distribution within the potted and non-potted machine designs

Machine Part	Non-Potted Stator	Potted Stator
Stator Yoke	85˚C	80˚C
Stator Slot	131˚C	125˚C
End Winding	126˚C	120˚C
Air in End cap	90˚C	80˚C
Rotor Embedded Magnets	88˚C	77˚C
Rotor Yoke	80˚C	75˚C

3.3 Liquid jacket and potting material

In the parametric study, the CFD thermal model developed for the radial flux PMSM and the analytical model of the liquid jacket are used to analyse the influence of the cooling jacket performance and the potting material location on the machine thermal behaviour.

The optimization of the liquid jacket is based on the different cross-section parameters of the cooling duct (Fig.3.6). The Reynolds number of the coolant flow in the liquid jacket ranges from 1500 to 7700, depending on the duct dimensions and the coolant flow. Therefore, Eq. (2.6–2.9) and (3.1-3.3) can be assumed valid with the assumption that the coolant flow has been fully developed.

The convection coefficient increases significantly when the dimensions of the liquid jacket duct are reduced or/and the flow rate increases (Fig. 3.6), which cause the rising of the coolant velocity in the liquid jacket. However, the rise of the coolant velocity is also associated with the increase of pressure losses.

The CFD thermal model presented in the previous section was used to explore the machine thermal performance under various heat dissipation conditions. The heat losses generated at the rated point (1500 rpm and 700 Nm) were applied to the machine parts (Table 3.2). Uniform convection coefficients (5050 and 10000 W/(m^2·K)) associated with the coolant and coolant temperature (50 ºC) on the machine outer surface were applied as boundary conditions to simulate the temperature distributions within the machine models (Fig.A.1 in Appendix A and Table 3.6). These simulated temperature distributions were then used to assess the liquid jacket performance in the machine hot spots. The increase of the convection coefficient from 5050 W/(m^2·K) to 10000 W/(m^2·K) on the surface, representing the effect of liquid cooling jacket, could provide a 3 K temperature drop in the slot winding and in the rotor embedded-permanent-magnets for the non-potted machine. In the case of the potted machine, the temperature drop is 3 K in the slot winding. The performance of the liquid jacket mainly influences the stator temperature. The rotor temperature depends on the internal air temperature, which decreases insignificantly with the convection coefficient increase in the liquid jacket (1-2 K temperature drop of internal air if the convection coefficient

increases from 5050 W/(m^{2}K) to 10000 W/(m^{2}K)). This temperature sensitivity related to liquid jacket performance is depicted in Table 3.6.

(a) (b)

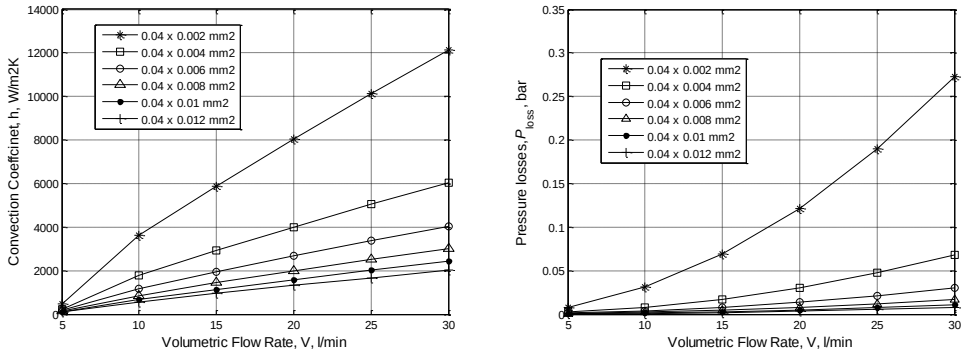

Figure 3.6: Liquid jacket performance with different cooling duct dimensions (a) – convection coefficient in the liquid jacket; (b) – pressure losses in the liquid jacket).

Table 3.6 For potted and non-potted machine designs, temperature distribution indicating liquid jacket performance

Machine Part	Non-Potted Stator		Potted Stator	
Convection Coefficient	5050 W/(m^{2}K), 50 ºC	10000 W/(m^{2}K), 50 ºC	5050 W/(m^{2}K), 50 ºC	10000 W/(m^{2}K), 50 ºC
Stator Yoke	85˚C	80˚C	80˚C	76˚C
Stator Slot	131˚C	128˚C	125˚C	122˚C
End Winding	126˚C	123˚C	120˚C	119˚C
Air in End cap	90˚C	88˚C	80˚C	80˚C
Rotor Embedded Magnets	88˚C	85˚C	77˚C	76˚C
Rotor Yoke	80˚C	78˚C	75˚C	75˚C

Furthermore, the influence of the potting material location on the machine hot spots may be analysed using the CFD thermal model. The heat losses generated at the rated point (1500 rpm and 700 Nm) and uniform convection coefficient and coolant temperature (5050 W/(m^2·K) and 50 ºC) on the machine outer surface were input. The temperature and velocity fields for different volumes of the potting material applied around the end winding region are illustrated in Fig. A.2 in Appendix A and listed in Table 3.7.

Table 3.7 Temperature distribution within the (partially and wholly) potted and non-potted machine designs

Machine Part	Potted Stator (upper part of the end-winding region)	Potted Stator (half of the end-winding region)	Potted Stator (the end-winding region is totally potted)
Stator Yoke	80˚C	77˚C	77˚C
Stator Slot	125˚C	123˚C	123˚C
End Winding	120˚C	118˚C	118˚C
Air in End cap	80˚C	79˚C	79˚C
Rotor Embedded Magnets	77˚C	76˚C	76˚C
Rotor Yoke	75˚C	75˚C	75˚C

The increase of the potting material volume causes a reduction of the air region volume and thereby a higher velocity and higher convection coefficient in the end cap region. The CFD thermal modelling results indicate that the total potting of the end winding region only provides a modest 2-3 K temperature drop in the stator winding region relative to the temperature when only the upper part of the end winding region is potted. The internal air temperature and subsequently the rotor temperature decrease insignificantly and to a somewhat lesser extent when either half or the whole of the end winding region is potted than when the upper part of the end winding region is potted.

3.4 Experiments

A 110 kW machine prototype was manufactured to verify the computational electromagnetic and thermal results. An experimental investigation was carried out with ethylene glycol as a coolant under various operating conditions. The experimental set up used for evaluating the thermal and electromagnetic performance of the machine studied is illustrated in Fig. 3.7.

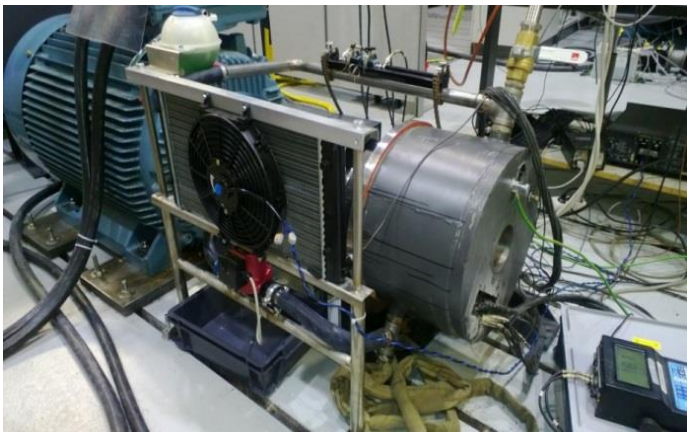

Figure 3.7: Test bench setup for the radial flux machine.

The stator end windings were potted with two different potting materials: Ceramacast 675N, with a thermal conductivity of 100 W/(m·K); and the high temperature epoxy 2315, with a thermal conductivity of 58 W/(m·K). Half of the end winding regions were potted (Fig. 3.5 (a)). The 50/50 mixture of water and glycol was pumped from the reservoir into the machine frame and further through a heat exchanger. The auxiliary equipment of the cooling system under study includes the pump, heat exchanger and flow meter (Figure 3.8).

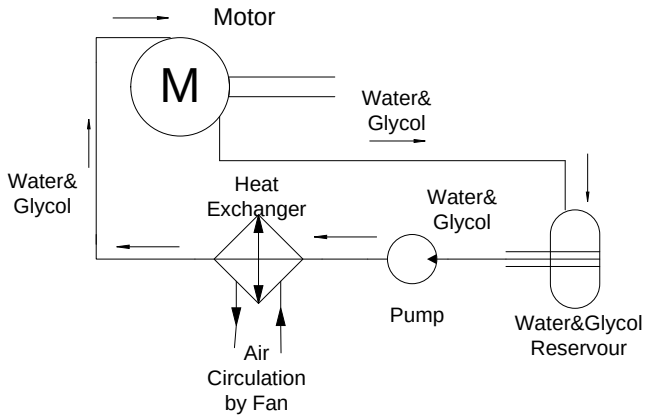

Figure 3.8: Cooling circuit in test bench setup.

The coolant flow rate was set at 16 l/min for 4 hours and was then increased to 25 l/min for 1 hour (Fig.3.9). However, the flow speed may be increased to dissipate more heat losses during overloading conditions. The temperature distribution of the PMSM running under load conditions for over 5 hours is shown in Figure 3.9.

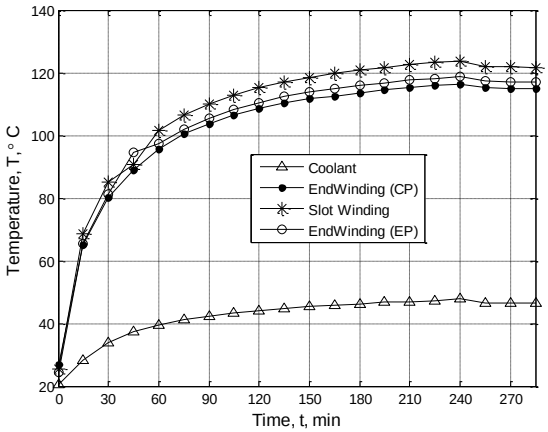

Figure 3.9: Temperature rises of the slot and end windings (potted with Ceramacast 675N) during tests (the margin of error of Pt-100 is ± 0.3 ºC at 0 ºC).

The measurement was carried out for a rotating speed of 900 rpm, an rms current of 113 A, a line-to-neutral voltage of 400 V and a torque of 560 Nm. The calibrated Pt-100 sensors were inserted in the slot winding and in the end windings to record the temperature of the tested machine. The margin of error of Resistance Temperature Device (Pt-100, class B) is ± 0.3 ºC at 0 ºC (DIN 43760). The slot-winding temperature stabilized at 123 ºC, and the end winding temperature at 116–118 ºC. The end winding potted with Ceramacast 675N material was 2–3 K colder than the end winding potted with the high temperature epoxy 2315.

The CFD thermal model of the machine was simulated at the testing machine parameters (900 rpm, 560 Nm). The liquid jacket performance (48 ºC and 3200 W/(m^2·K) defined by Eq. 2.6-2.9 had the same liquid jacket geometry and flow rate 16 l/min) as in the experiment (Fig. 3.10). The same modelling parameters as described in Section 3.2 were applied.

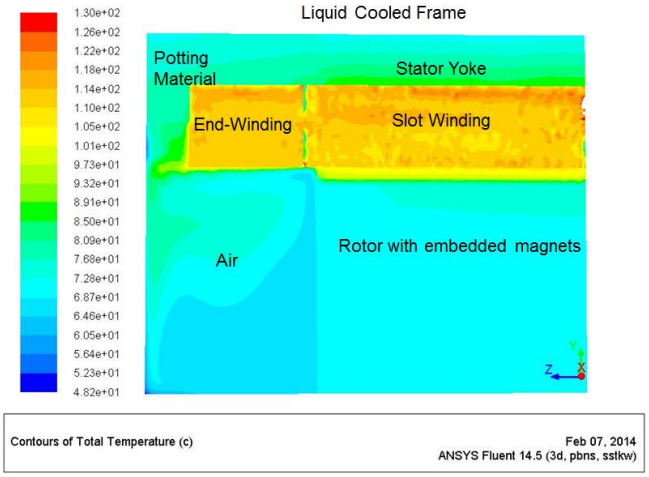

Figure 3.10: Temperature distribution within the machine parts (900 rpm, 560 N·m).

The winding temperature results from the CFD thermal model agree with the temperature results of the testing. The discrepancy between the measured and simulated results (2-4 K) is only found in the slot-winding region (Fig. 3.9 and Fig.3.10). The assumed winding conductivity and the interface gap between the stator yoke and the liquid jacket incorporated in the frame might be the main reasons for the discrepancy, but other possible explanations include errors caused by the computational modelling, by the measuring equipment and by unknown manufacturing defects.

3.5 Conclusions

The 110 kW permanent magnet synchronous machine presented here is dedicated to working temporarily with high torques in a traction application, so more heat losses will be generated in the constrained physical volume. The goal was to keep the sensitive machine components (insulation and permanent magnet) below certain temperature threshold values. The cooling solution is based on a liquid jacket and high conductivity heat transfer paths to it (potting material).

The CFD thermal model of the machine segment was used to analyse the temperature distribution within the machine parts in conditions of different cooling system performance. The analysis reveals that utilization of heat conductive material can provide a 6 K temperature reduction of the stator copper winding and a 10 K temperature drop in the rotor embedded-permanent-magnets. It should be noted that the total potting of the end winding region could yield a 2-3 K temperature drop in the stator winding relative to the temperature when only the upper part of the end winding region is potted. The improvement of the liquid jacket performance (reflected in the increase of the convection coefficient) could provide a 3 K temperature drop in the stator winding. The application of the total potting of the end winding region (compared with the case in which only the upper part of the end winding region is potted) and the improvement of the liquid jacket performance result in an insignificant decrease of the internal air temperature and therefore do not cause a temperature drop in the rotor.

In the machine prototype, two different potting materials were analysed (Ceramacast 675N, with a thermal conductivity of 100 W/(m·K) and the high temperature epoxy 2315, with a thermal conductivity of 58 W/(m·K)). The potting material Ceramacast with its higher thermal conductivity could only provide a 2–3 K lower temperature of the end winding region.

The validation of the computational results using the experimental data on the machine prototype was also presented. The modelling results for the temperature distribution follow the trend in the experimental data fairly well; there was only a 2-4 K discrepancy in the slot winding. This discrepancy was likely caused by 1) the errors in the CFD thermal modelling assumptions (regarding the turbulence model, unstructured mesh, assumed thermal conductivities, thermal contact resistances, etc.); 2) the measurement error; and 3) unknown manufacturing defects. However, the results presented in this part are noteworthy because of the feasibility of their utilization for practical applications in automotive and other industries. The potting material provides for the reliable operation of the end winding without the application of forced air cooling.

4 Direct liquid-cooled high-power low-speed permanent magnet synchronous generator with outer rotor

Wind turbine power is steadily increasing nowadays, and the possibility of realization of machine power of up to 10–20 MW is currently being discussed. Wind turbine power is presently available at close to 10 MW (Semken et al., 2012; Kowal et al., 2013). Enercon has offered its 7.5 MW DD turbine since 2007 (De Vries, 2012). In 2013, Vestas described in a publication a new semi-geared drive with a 9 MW permanent magnet generator (Snieckus, 2013). The largest generators are planned to be installed in offshore applications, which would require the design of more powerful and reliable generators. Direct-drive permanent magnet synchronous generators (DD PMSG) for wind farms with a rated power of slightly more than 4 MW are available on the market, but competitively speaking, these machines are heavy and enormous in comparison to installations based on more conventional generators and gearboxes. The torque (and in this case) power production in a machine are directly proportional to the air gap tangential stress $\sigma_{F\ \tan}$; i.e., they are proportional to the product of the air gap normal flux density B_δ and the stator linear current density ($\sigma_{F\tan} = \cos\gamma \cdot B_\delta A_s$). This means that an obvious way to reduce the weight of a PMSG is to increase the linear current density A_s by increasing the current density J_s in the stator winding. That causes high heat losses in the winding, which can be dangerous for both the stator coil insulation and for the rotor surface permanent magnets, which have temperature sensitive properties. Thus, the development of compact high-power direct-drive wind turbine generators necessitates the design of a more effective internal cooling system to ensure the safe operation of the rotor permanent magnets.

A traditional air cooling system is no longer applicable for generators with high tangential stress, as it does not allow for removal of the generated heat losses or ensure proper operation of the rotor mounted permanent magnets. Hence, direct liquid cooling (LC) system of the stator winding has become a useful solution, as it can provide an adequate temperature of the winding and the rotor mounted-permanent-magnets. The operating magnet temperature must in all cases be lower than 120–150 ºC for NdFeB (Fodorean and Miraoui, 2008). In practice, if the generator rotor must also tolerate a possible short circuit, the magnet operating temperature must be normally, depending on the material selection, even less than 100˚C. In an offshore site, closed water cooling systems can help the internal components of the wind turbine nacelle to avoid the maritime air moisture and corrosion atmosphere inside the generator. However, a direct liquid cooling system complicates the generator design, so its design requires special attention.

4.1 Description of the generator

The machine is a low-speed, concentrated non-overlapping fractional-slot winding (tooth-coil), three-phase liquid-cooled direct-drive (LCDD) synchronous generator with a rated power of 8 MW (Fig. 4.1). An electromagnetic concept of a similar machine with an inner rotor is presented in a paper by Alexandrova et al. (2012, 2014). The generator design includes a tooth-coil multiple-phase segmented construction.

Table 4.1. General data of the LCDD outer rotor PM generator.

Parameter	Quantity
Rated Power	8 MW
Rated Speed	11 rpm
Line to line voltage	3.3 kV
Rated phase current	1110 A
Number of phase	6
EMF factor (back emf / nominal voltage)	0.74
Tangential Stress	80 kPa
Linear current density	147 kA/m
Current density	4.8 A/mm^2
Peak output power to rated output power ratio (overload capability) at nominal speed	1.6
Load angle	35 deg.
Power Factor with $i_d = 0$	0.63
Rated electrical efficiency	92.5%
Number of stator slots and rotor poles	144, 120 (12/10)
Total generator with bearing mass	80 t
Geometrical data	
Rotor Outer Diameter	7900 mm
Air Gap Diameter	6940 mm
Length of Air Gap	8 mm
Length of Stator	1150 mm
Magnet Width × Height	146 × 28 mm^2
Slot Width × Height	76 × 73 mm^2

The low torque and high power of the generator imply impressive dimensions, as the produced torque is proportional to the square of the air gap diameter. To reduce the weight of the generator, the fairly high linear current density (A_s = 147 kA/m) is considered. The stator outer bore diameter is 6.9 m, and the stator length is 1.15 m. In the generator, the main heat sources are the copper losses and to a lesser extent, the iron losses, because of the stator frequency. The copper losses are the largest because high electric currents are running through the copper windings. Because of the eddy currents and the hysteresis, some iron losses appear in the machine. The heat generation distributes itself unevenly among the conductors in the stator slot, and despite the low

frequency, some skin and proximity effects exist in the solid copper conductors. The losses are too high to be removed by air cooling, because of the low heat capacity of air. Table 4.2 lists the heat sources in the generator.

The total copper losses of the generator are 530 kW and the core loss is about 10 kW, resulting in 21.5 kW/m^2 specific heat flow on the stator surface. The high heat losses in the winding endanger the insulation, and they may deteriorate the operation of the rotor surface-mounted permanent magnets, which have temperature sensitive properties. The heat losses are too high to be removed by air cooling (because of the low heat capacity of air cooling). The temperature of the winding is more than 200 ˚C in natural air cooling (as simulated by the LPTN presented in both this chapter and Appendix 1). From a mechanical perspective, forced air cooling is challenging because of the large dimensions. The bulk coils present additional difficulties, as there are large cross-sectional areas of coils. The high number of turns around every stator tooth is considered to be due to the very low rotational speed. Therefore, a direct liquid cooling system for the stator winding is considered.

Table 4.2. Heat sources of the LCDD generator.

Heat Source Position	
Stator Copper Windings	530 kW
Stator Core	10 kW
Rotor Core	1.2 kW
Permanent Magnets	30 kW
Additional losses (mechanical losses in the air gap, AC copper losses, microhysteresis losses in the iron etc.)	40 kW

4.2 Design of a direct liquid cooling system for the generator

The above-mentioned problem of high ohmic losses is solved through direct water cooling of the stator winding and natural air cooling of the rotor for the PMSG.

The usual direct liquid-cooled windings present a series of connected hollow copper conductors with liquid coolant inside them. This had been the most used design for internally cooled windings before the last couple of decades. However, according to the exploitation experience presented in a Technical Letter of GE (2001) and paper of Worden and Mundulasi (2001), there have been many failures of the cooling systems based on hollow copper windings – leakages in the clip-to-strand connections due to the crevice-corrosion mechanism, a loose seal and copper erosion. Copper conductors have a high tendency for erosion of the tube surface in certain conditions. High water velocity, high-temperature fluid and suspended solids in fluid can cause an impingement attack and destruction of the oxide layer formed on the inner copper conductor surface, especially in areas where fluid changes direction. The critical parameters are 90 ˚C and 1 m·s^{-1}, beyond which problems start occurring (Milinder,

2010; Svoboda and Palmer, 2008). The design of the stator winding with stainless steel tubes inside of the hollow copper conductors allows for increasing the cooling system performance and reliability. In case of stainless steel tubes the higher velocity of water flow compared to the values available with copper can be adopted, and simpler (from the mechanical perspective) clip-to-strand connections can be used. Compared with copper tubes, stainless steel tubes suffer to a much greater extent from most of the corrosion types. However, under certain conditions, stainless steel can also be subject to corrosion, such as crevice-related pitting corrosion or stress corrosion cracking (Kadry, 2008; Technical Handbook of Raccorderie Metallische, 2011). A high temperature liquid flow can cause the breakdown of the protective oxide layer on the tube surface, resulting in crevice-related pitting corrosion. Therefore, the temperature of liquid flow should be kept at a temperature lower than 100 ºC (Technical Letter of Fineweld Tube; Technical Letter of Fisher Group, 2009). Stress corrosion cracking of the stainless steel tube is a result of the chloride solution in the coolant, so all plastic connections and other possible sources of chloride should be avoided.

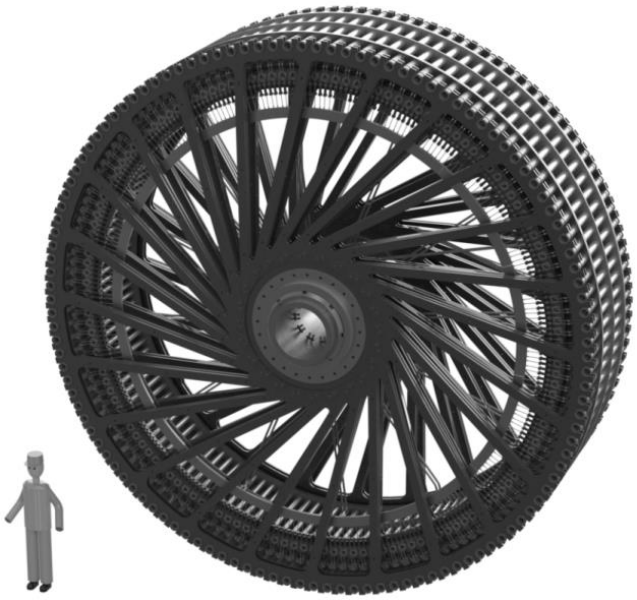

Figure 4.1: Outer rotor LC DD permanent magnet generator (Semken et al., 2012).

The direct water cooling system is designed to remove the copper and iron losses in the stator (Fig.4.2). The cooling system consists of 144 parallel cooling circuits which ensure a uniform temperature along the copper conductor surface. Each cooling circuit contains 20 tubes connected in series. The stator winding is designed with hollow rectanglar copper conductors of 15 mm by 18 mm dimensions, with extruded stainless steel tubes of 7 mm by 0.75 mm inside of them.

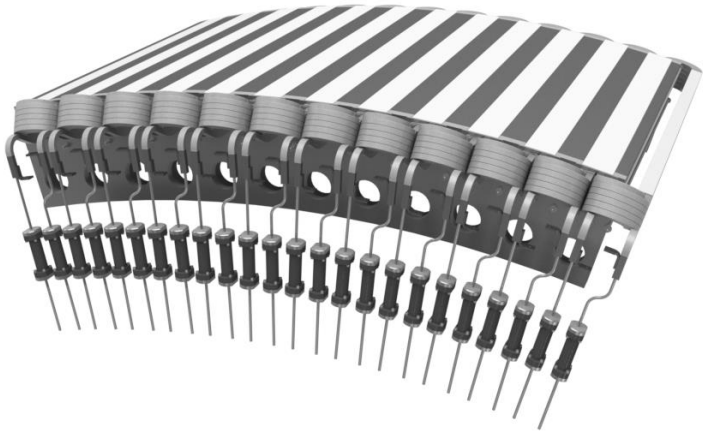

Figure 4.2: Stator segment (Semken et al., 2012).

Figure 4.2 presents the temperature increase and pressure losses in a 25 meter total-length coil with demineralized or deionized pH-controlled water (DWpH) flowing along the cooling circuit.

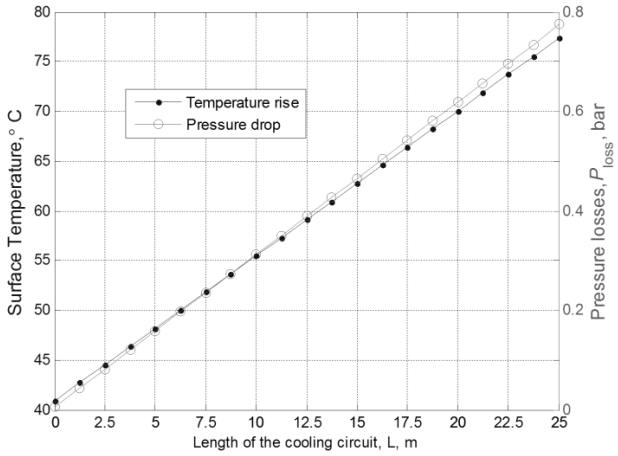

Figure 4.3: Temperature of the inner conductor surface and pressure losses along one cooling circuit (analytical calculation).

The temperature of DWpH is 40 ˚C, and the flow rate is 1 m/s. The outlet temperature of DWpH is up to 80–90˚C to prevent tube corrosion (Technical Letter of Fineweld Tube; Technical Letter of Fisher Group, 2009). Such cooling system parameters (the deionized water velocity is 1 m/s, and the inlet/outlet temperatures are 40 ˚C and 80 ˚C, respectively) allow for keeping the temperature of the stator winding lower than 90 ˚C, and that of the permanent magnets even under 60 ˚C. The outlet temperature of the

cooling DWpH is determined by the inlet temperature of DWpH and the cross-section of the copper conductor in conditions of the constant heat rate (Incropera et al., 2007).

$$T_{\mathrm{dw}} = T_{\mathrm{dw0}} + \frac{P}{c_{\mathrm{pdw}} \cdot s_{\mathrm{sst}} \cdot \rho_{\mathrm{dw}} \cdot \upsilon_{\mathrm{dw}}} \tag{4.1}$$

where T_{dw}, T_{dw0} are the temperatures of inlet and outlet DWpH flows, P is the heat rate, c_{pdw} is the heat capacity of DWpH, ρ_{dw} is the density of DWpH, υ_{dw} is the velocity of DWpH, and s_{sst} is the cross-section area of the stainless steel tube. The temperature to which the copper conductor can be cooled is mainly determined by the convective heat transfer coefficient and the heat exchange rate.

$$T_{\mathrm{s}} = T_{\mathrm{dw}} + \frac{P}{\pi \cdot D_{\mathrm{sst}} \cdot l_{\mathrm{c}} \cdot \alpha_{\mathrm{conv\,dw/c}}} \tag{4.2}$$

where T_{s} is the temperature of the internal stainless steel conductor surface, which varies as a function of the position , D_{sst} is the inner diameter of the extruded stainless steel tube, l_{c} is the conductor length, which defines the position, and $\alpha_{\mathrm{conv\ dw/c}}$ is the convective heat transfer coefficient between DWpH and the tube extruded in the conductor. The constant water properties at 60 ˚C were considered for the temperature rise and pressure losses calculation (Fig. 4.3). The convection heat transfer is obtained by Eq. (2.6–2.9), which is assumed valid in this case, as the Reynolds number of the coolant flow in a stainless steel tube is 11200. The total pressure losses of DWpH are determined by the pressure losses along the length of the conductors and in the fittings (bends, inlet and outlet junction of the conductors / cooling circuit); see Eqs. (3.1)-(3.3) and Eq. (2.9) (Incropera et al., 2007). The equations for the calculation of pressure losses are applied with the assumption that the coolant flow is fully developed. The stainless steel surface roughness is assumed to be $1.327 \cdot 10^{-6}$ m.

The temperature rise and the pressure losses along the cooling circuit were simulated with the constant values of the coolant properties (Fig. 4.3). The next section presents the thermal analysis of the cooling system with higher accuracy, as the change in coolant properties depends on the coolant temperature.

4.3 Modelling of coolant properties

Water is the best coolant for many energy conversion applications, but limitations may arise when it is used as a coolant in the cooling system of a wind turbine generator. The arctic operating conditions of machines impose special requirements for the fluid. At temperatures below 0 ºC water freezes and expands, which can result in a failure in the cooling system. The freezing problem can be solved through the mixing of the cooling water with glycols and antifreeze additives (i.e., chemical treatment).

The properties of glycols, such as Ethylene Glycol (50 volume %), Propylene Glycol (50 volume %), and water are listed in Table 1.5 (Product Technical Data, KUHLSOLE GmbH, 2011).

Table 4.3. General corrosion and wear data.

Fluids	Wear data of stainless steel, gm^{-2}
Ethylene Glycol 35% Vol.	–0.1
Propylene Glycol 50% Vol.	–0.04
Water at 14ºdH	–0.5

Ethylene Glycol with 50% Vol., Propylene Glycol with 50% Vol., and DWpH fluid are next analysed and further compared. These fluids were chosen on the basis of their thermo physical characteristics, which can be suitable for the direct cooling of the stator winding of an electrical machine. In fact, the main requirements were satisfaction of the working temperature range of the copper conductors (a low freezing temperature and high flash temperature) and low corrosion activity in contact with the stainless steel (Table 4.3). Although there are many coolants on the market, only some can be applicable in direct winding cooling of electrical machines.

The models of the fluids studied are presented in Table 4.4.

Table 4.4. Models of the fluids studied.

Fluids	Temperature range	Max. deviation of specific properties, %
Ethylene Glycol 50% Vol.	–30…100ºC	0.5
Propylene Glycol 50% Vol.	–30…100ºC	0.5
Demineralized water	0…100ºC	0.2

The property models of the fluids were constructed in a MATLAB program on the basis of their main thermo physical characteristics, with certain deviation. The values of the density, thermal conductivity, specific heat and dynamic viscosity vary depending on the temperature and solute mass fraction. These parameters are simulated by the models presented in the literature (Lugo at al., 2001; Milinder, 2010). The reference properties of the studied fluids were taken from Products Technical Data offered by M. Conde Engineering, 2002. The deviations of the thermo physical parameters of the studied fluids and their constructed models fluctuate between 0.2 and 1 %, depending on the fluid. The largest fluctuations are in dynamic viscosity – about 1%. The fluctuations of other parameters are negligible. The completed calculations can thus be considered to produce a high degree of accuracy, as the deviations of parameters of the constructed models and the impact of the studied fluids on the results are insignificant.

One-dimensional heat conduction in a steady state is governed by the following equation.

$$\frac{\mathrm{d}}{\mathrm{d}x}\left(s_\mathrm{c}\cdot\lambda\cdot\frac{\mathrm{d}T}{\mathrm{d}x}\right)+S=0 \tag{4.3}$$

where x is the axial coordinate, s_c is the cross sectional area of the conductor, λ is the heat conductivity of the material, T is the temperature, and S is the source term. To solve the temperature distribution in a winding, the winding is divided into small control volumes between which the temperature variation is thought to be linear. The source term is comprised of the electric losses and the heat convection to the cooling fluid. The electric loss rate, $P_{\mathrm{Cu},}$ comprises Joule losses generated in the winding.

$$P_\mathrm{Cu}=R_\mathrm{AC}\cdot I^2 \tag{4.4}$$

$$R_\mathrm{AC}=R_\mathrm{DC}\cdot K_\mathrm{AC} \tag{4.5}$$

where R_AC is the AC resistance, R_DC is the DC resistance, K_AC is the AC resistance coefficient (in this case about 1.2 (Pyrhönen, 2013)) and I is the current RMS value. The electric conductance of the material varies with temperature. Thus, the DC resistance R_DC of the material is calculated separately at each control volume.

$$R_\mathrm{DC}=\frac{1+\alpha\cdot\left(T_\mathrm{s}-T_\mathrm{ref}\right)}{\sigma_\mathrm{ref}}\frac{x}{s_\mathrm{c}} \tag{4.6}$$

where α is temperature coefficient, σ_ref is the electrical conductivity at the reference temperature, $T_{\mathrm{ref}\,,}$ and x is the axial length of the control volume. The heat convection rate from the surface, P_conv, is calculated with the convection heat transfer coefficient α_conv.

$$P_\mathrm{conv}=\alpha_\mathrm{conv}\cdot\left(T_\mathrm{s}-T_\mathrm{f}\right)\cdot\Pi\cdot x \tag{4.7}$$

where T_f is the mean fluid temperature at the given axial location, and Π is the wetted perimeter. To determine the convection heat transfer coefficient, the definition of the Nusselt number and the Gnielinski (1988) correlation for the Nusselt number were used (Eq. (2.6)–(2.9)) when the Reynolds number exceeded 2300. Concerning the laminar flow, the Nusselt number was assumed constant and equals 4.36, which is valid for a circular tube with uniform surface heat flux and laminar, fully developed flow conditions (Incropera et al., 2007). The pressure losses of the coolants are determined from the pressure losses along the length of the conductors and in the fittings by Eqs. (3.1)-(3.3) (Incropera et al., 2007). The stainless steel surface roughness is assumed to be $1.327\cdot10^{-6}$ m.

The discretization of the simulated cooling circuit is done according to the classic work of Patankar (1980). The boundary conditions assumed were that there was a constant temperature at the fluid inlet and zero heat flux to the exterior at the outlet. In this case,

the calculation domain was divided into 20 control volumes of equal length (1.25 m). Due to space constraints, the details of discretization are excluded from this thesis, but they are presented in the paper of Polikarpova et al. (2013). A central difference scheme was used and the resulting coefficient matrices were solved with the MATLAB programming language and with Gaussian elimination. The source term S in Eq. (4.8) is divided into constant, S_{const}, and temperature dependant, S_{d}, parts.

$$S = S_{\mathrm{const}} + S_{\mathrm{d}} \cdot T \tag{4.8}$$

One should notice that the source term is actually heat flux, meaning that the units are Watts per meter. Combining Eq. (4.4)–(4.8) the source term becomes

$$S = \frac{\left[1+\alpha\cdot\left(T_{\mathrm{s}}-T_{\mathrm{ref}}\right)\right]\cdot I^2}{\sigma_{\mathrm{ref}}}\frac{x}{s_{\mathrm{c}}} - \alpha_{\mathrm{conv}}\cdot\left(T_{\mathrm{s}}-T_{\mathrm{f}}\right)\cdot \Pi \tag{4.9}$$

This can be divided into the constant term

$$S_{\mathrm{const}} = \frac{\left(1+\alpha\cdot T_{\mathrm{ref}}\right)\cdot I^2}{\sigma_{\mathrm{ref}}\cdot s_{\mathrm{c}}} + \alpha_{\mathrm{conv}}\cdot T_{\mathrm{f}}\cdot \Pi \tag{4.10}$$

And the temperature dependent term

$$S_{\mathrm{d}} = \frac{\alpha\cdot I^2}{\sigma_{\mathrm{ref}}\cdot s_{\mathrm{c}}} - \alpha_{\mathrm{conv}}\cdot \Pi \tag{4.11}$$

The equation above yields an interesting limiting condition: the value of S_{d} should always be negative, or a thermal runaway (i.e., the feedback from the surface temperature rise will be positive) is bound to happen. As may be noticed, the algorithm will use the mean fluid temperature in calculating the heat transfer. It is calculated through the domain from the following equation:

$$T_{\mathrm{f,i}} = T_{\mathrm{f},0} - \sum_i \frac{P_{\mathrm{conv},i}}{\dot{m}\cdot c_{\mathrm{p},i}} \tag{4.12}$$

where $T_{\mathrm{f},\,0}$, $T_{\mathrm{f},\,\mathrm{i}}$ are the temperatures of inlet and outlet flows, $P_{\mathrm{conv},\,\mathrm{i}}$ is the heat convection rate from the surface, $c_{\mathrm{p},\,\mathrm{i}}$ is the heat capacity of the flow and $\dot{m}$ is the mass flow in kg s^{-1}. This form implies that the mean fluid temperature must be iterated. The maximal difference of the mean fluid temperature at the same point between the iteration steps was used as a convergence criterion.

Fig. 4.4 presents the comparison of Ethylene Glycol (50 volume %), Propylene Glycol (50 volume %) and DW as coolants for the direct cooling system of the stator copper winding with the extruded stainless steel tubes. The comparison values are summarized in Table 4.5. The values of the density, thermal conductivity, dynamic viscosity, heat capacity and Prandl number were defined by the models of coolants presented above.

(a) Temperature rise of fluid along the cooling circuits

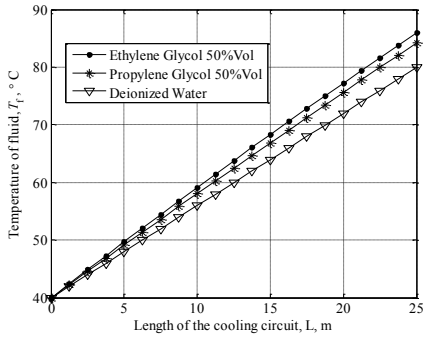

(b) Convection coefficient between fluid and tube surface along the cooling circuits

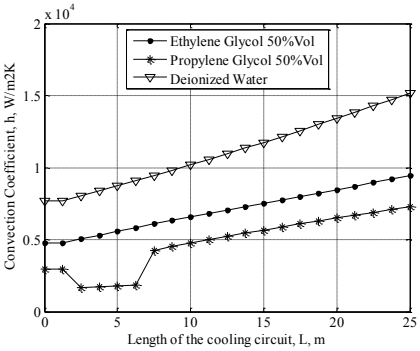

(c) Temperature rise of tube surface in the cooling circuits

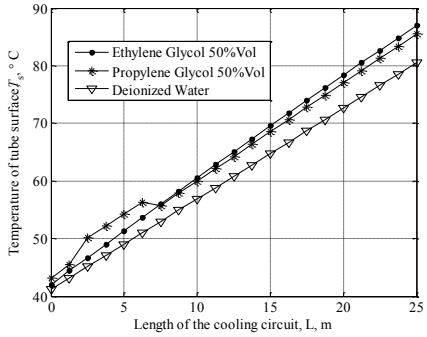

(d) Joule losses within the copper conductors in the cooling circuits

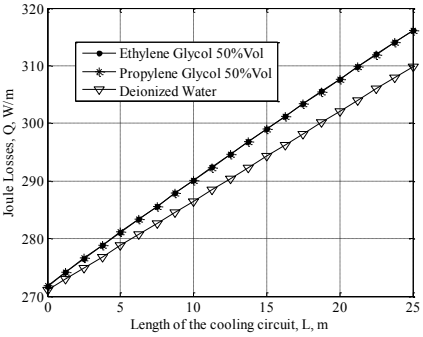

(e) Hydraulic losses of fluids along the cooling circuits

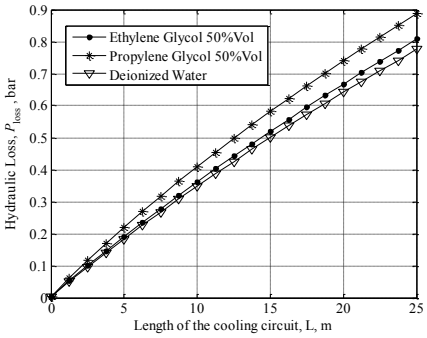

(f) Pump capacity for pumping the fluids along the cooling circuits

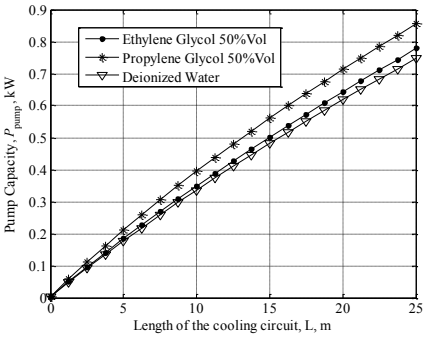

Figure 4.4: Comparison of properties for Ethylene Glycol 50% Vol., Propylene Glycol 50% Vol., and DW.

Table 4.5. Properties of Ethylene Glycol 50% Vol., Propylene Glycol 50% Vol., and DW as coolants for the direct liquid cooling system of the stator winding (at the end of the cooling circuit).

Coolant Property	Ethylene Glycol 50% Vol.	Propylene Glycol 50% Vol.	DW
Outlet temperature of the Fluid, ºC	86	84.2	79.9
Temperature of the Tube Surface at the outlet, ºC	87	85.5	80.5
Convection Coefficient, W/(m^2·K)	9400	7200	15000
Joule Losses within the Copper Conductor, W	316	316	310
Hydraulic Loss of Fluid, bar	0.807	0.888	0.778
Pump Capacity, kW	0.78	0.86	0.75

When one compares the outlet temperature of DW in Table 4.5 (79.9˚C) with the temperature in Fig. 4.3 (76.7 ˚C) reflecting constant DW properties, it can be noticed that the error of the assumed constant coolant properties is 3.2 K. The pressure losses inside the cooling circuit are 0.775 bar in the case of constant DW properties (Fig. 4.3), and 0.778 bar in the case of the temperature-dependent DW properties.

As seen in the figures and Table 4.5 above, DWpH is the most useful fluid from both thermal and hydraulic points of view. The glycol mixes have higher hydraulic losses and temperature rises compared with DWpH because of their higher dynamic viscosity and resulting flow transition nature (Fig. 4.4(a) and 4.4(c)). The temperatures of the 50 % Ethylene Glycol solution and the 50 % Propylene Glycol solution are similar, although the former showed a slightly weaker performance (Fig. 4.4(a)). Assuming the correlations are valid, the heat transfer coefficient of Propylene Glycol is lower than that of Ethylene Glycol because of its lower Prandl number and specific heat. Because of the friction factor definition based on Eq. (2.9) and (3.1), there are some abrupt changes in the calculated convection coefficients for Propylene Glycol (Fig. 4.4 (b)) where there are flow regime changes (for laminar, transition and turbulent flow regimes). This reason also accounts for the abrupt change in the graph of the calculated hydraulic losses for Propylene Glycol (Fig. 4.4 (c)).

When one considers the performance of the electric machine, it is enlightening to observe how the Joule loss generation rate develops as a function of the position along the winding. When one compares Fig. 4.4(a) and Fig. 4.4(d), it becomes evident that the loss generation rate is linearly dependent on the surface temperature of the copper and stainless steel. The Joule losses generated could be slightly reduced by reducing the temperature. An easy way to do this is to increase the mean fluid velocity. This, however, generates more pressure loss and wear in the winding cooling tubes. The hydraulic power dissipation in the windings per unit length is given in Fig. 4.4(e). This figure can be used to judge whether it would be wise to increase the flow speed to decrease the Joule losses. The hydraulic loss generation rate of Propylene Glycol is the greatest because of its high viscosity, and this affects the pump capacity, so the use of Propylene Glycol reduces the cooling system performance. Fig. 4.4(f) illustrates the

pump capacity per unit length, assuming a pump efficiency of 71% of the Grundfos centrifugal pump CR-15 for the generator cooling system characteristics (Technical Data, Grundfos, 2013).

Thus, water is the best fluid for a direct water cooling system of the stator winding in conditions of an ambient temperature down to 0ºC. In arctic conditions, mixes of Propylene Glycol or Ethylene Glycol and water should be considered. Propylene Glycol is nontoxic and has better thermal and corrosion resistance properties compared with Ethylene Glycol, but is less effective due to the large hydraulic losses. The concentration of glycol could be considered below 50%, thereby improving the cooling system performance, but this also causes lower freezing temperature points (lower than – 30 ºC) for this mix of water and glycol. Figure 4.5 presents the cooling system performance for different concentration rates of water and glycol (Product Technical Data, M. Conde Engineering, 2011). The concentration rate of glycol should be considered based on the environment of the wind turbine installation location (the lowest temperature).

(a)

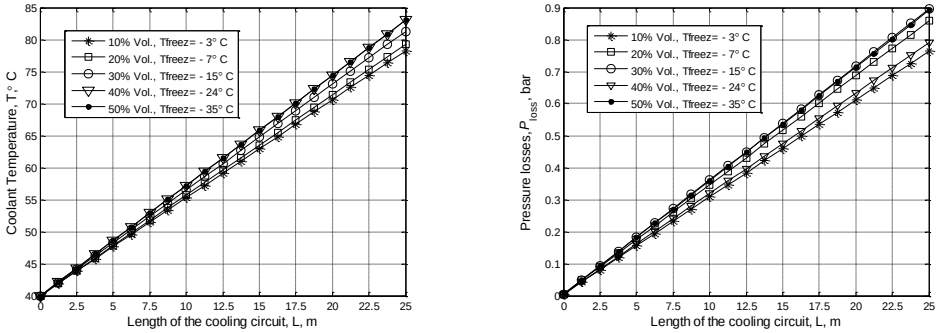

(b)

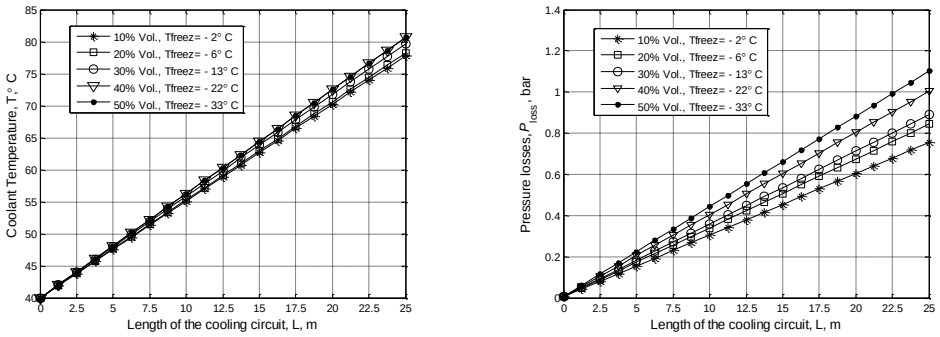

Figure 4.5: Temperature rise and pressure losses for different ratios of water and glycol (a – Ethylene Glycol; b – Propylene Glycol).

4.4 Thermal analysis of direct-liquid-cooled high-power permanent magnet synchronous generator

The thermal modelling approach to a DD PMSG includes numerical simulations of temperature distribution within the machine. After the analytical determination of the coolant performance, the temperatures of the machine parts are further calculated by means of LPTN and CFD thermal modelling. CFD thermal analysis was selected for the machine modelling because of the unique machine design. As a machine prototype has not been constructed, LPTN thermal analysis was applied to validate the CFD thermal modelling.

4.4.1 Thermal conductivities and convection coefficients

The thermal conductivities of the materials constituting the different parts of the generator are simulated with uniform or non-uniform conduction in the case of the rotor iron, stator copper winding, stator tooth and yoke. The non-uniform conduction is associated with the composite structure of the machine parts, and can be defined based on Eq. 2.1. The number of conductors in a slot is 20. Each conductor has an extruded stainless steel tube with the coolant inside, and is impregnated by Nomex insulation with a thickness of 0.25 mm and a thermal conductivity of 0.2 W/(K·m). These design properties cause poor conduction inside the slot, in both the radial and tangential directions. Table 4.6 lists the thermal conductivities of the used materials in different directions (Mademlis et al., 2000; Ibtiouen et al., 2001).

Table 4.6. Thermal conductivities within the machine parts

Material of model components	Thermal Conductivities, W/(K·m), Direction, cylinder coordinates		
	radial	tangential	axial
Iron	39	39	4.43
Aluminium	237	237	237
Permanent magnets	9	9	9
Glass fibre	0.3	0.3	0.3
Nomex	0.2	0.2	0.2
Epoxy resin	0.26	0.26	0.26

The LPN thermal model of the machine is simulated based on the empirical formulations of the convection coefficients in the air gap and the end regions. The convection between the end parts and air is intensified by the rotation of the rotor. The air flow rate in the nacelle is defined by the following equation.

$$\dot{V}_{\mathrm{nacair}} = \pi \cdot r_{\mathrm{nac}}^2 \cdot l_{\mathrm{nac}} \cdot N_{\mathrm{airexchange}} \tag{4.13}$$

where r_{nac} is the nacelle radius, l_{nac} is the nacelle length, and $N_{\mathrm{airexchange}}$ is the number of air exchanges (1/hour). The flow rate of stagnant air is considered based on an

assumption that a typical air exchange per hour is 1 for a nacelle with two openings on opposite sides (Bearg, 1993). A special filter system should be considered to prevent a salty environment.

The most complex task is the calculation of the convection coefficients in the endcap regions. The following empirical equations introduced by Incropera (2007) and Elkins (1997) were used to define the forced convection on the outer rotor surface, the end surfaces of the stator and the rotor. Eq. (4.14) determines the turbulent flow over the constant heat flux surface (valid for $Re \leq 1\ 000\ 000$). Eq. (4.16) determines the flow over the cylinder (valid when $Pr_{\text{fluid}} \geq 0.7$ and $40\ 000 \leq Re_{\text{D}} \leq 400\ 000$). These correlations can be assumed valid, as the Reynolds numbers for the air flow over the stator and the rotor are $1.8 \cdot 10^5$ and $8.66 \cdot 10^5$, respectively.

$$Nu_{\text{outr/air}} = 0.0163 \cdot Re^{0.8}_{\text{outair}} \tag{4.14}$$

$$Re_{\text{outair}} = \frac{r_{\text{outr}}^2 \cdot \pi \cdot n}{60 \cdot \nu_{\text{air}}} \tag{4.15}$$

$$Nu_{\text{ends/air}} = 0.027 \cdot Re_{\text{air}}^{0.805} \cdot Pr_{\text{air}}^{1/3} \tag{4.16}$$

$$Re_{\text{air}} = \frac{D_{\text{st}} \cdot U_{\text{nacair}}}{\nu_{\text{air}}} \tag{4.17}$$

where $Nu_{\text{out/air}}$ is the convective heat transfer coefficient between the rotor and air, Re_{outair} is the Reynolds number of air in the rotor region, Pr_{air} is the Prandl number of air, n is the rotor synchronous speed, r_{outr} is the outer radius of the rotor, ν_{air} is the kinematic viscosity of air, $Nu_{\text{ends/air}}$ is the convective heat transfer coefficient between the stator and air in the endcap region, Re_{air} is the Reynolds number of air in the stator endcap region, D_{st} is the stator diameter, and υ_{nacair} is the air velocity in the wind turbine nacelle. The convection coefficient in the air gap is defined by the following equations (Kuosa et al., 2004).

$$Nu_{\text{ag}} = 0.0204 \cdot (Re_{\text{ag}}^{0.8} - 100) \cdot Pr_{\text{air}}^{0.4} \cdot \left(1 + \left(\frac{D_{\text{hag}}}{l_{\text{st}}}\right)^{0.66}\right) \tag{4.18}$$

$$Re_{\text{ag}} = \frac{D_{\text{hag}} \cdot \upsilon_{\text{agair}}}{\nu_{\text{air}}} \tag{4.19}$$

$$D_{\text{hag}} = l_{\text{ag}} \cdot \left(\frac{8}{3}\right)^{0.5} \tag{4.20}$$

$$\upsilon_{\text{agair}} = \left(\left(\frac{\Omega_{\text{r}} \cdot r_{\text{inr}}}{2} \right)^2 + \upsilon_{\text{nacair}}^2 \right)^{0.5} \tag{4.21}$$

where Nu_{ag} is the convective heat transfer coefficient in the air gap region, Re_{ag} is the Reynolds number of the air in the air gap region, Pr_{air} is the Prandl number of air, D_{hag} is the hydraulic diameter of the air gap, υ_{agair} is the air velocity in the air gap region, v_{air} is the kinematic viscosity of the air, l_{ag} is the length of the air gap, r_{inr} is the inner radius of the rotor, υ_{nacair} is the air velocity in the wind turbine nacelle, and Ω_{r} is the angular velocity of the rotor. These convection coefficient values are rough, as they do not include the flow created by the rotor support structure rotation.

4.4.2 Thermal analysis based on Lumped Parameter Thermal Network

Thermal analysis using LPN is based on dividing the generator into several components – the frame, the stator yoke, the stator teeth, the stator copper coils, the air gap, the rotor yoke, the rotor embedded-permanent-magnets, the air in the hollow support structure, the end cap air and the shaft. The stator copper coil is divided into three regions: the copper winding in the slot, copper end-winding and coolant. Fig. 4.6 shows an equivalent network of thermal resistances and power sources for the generator studied.

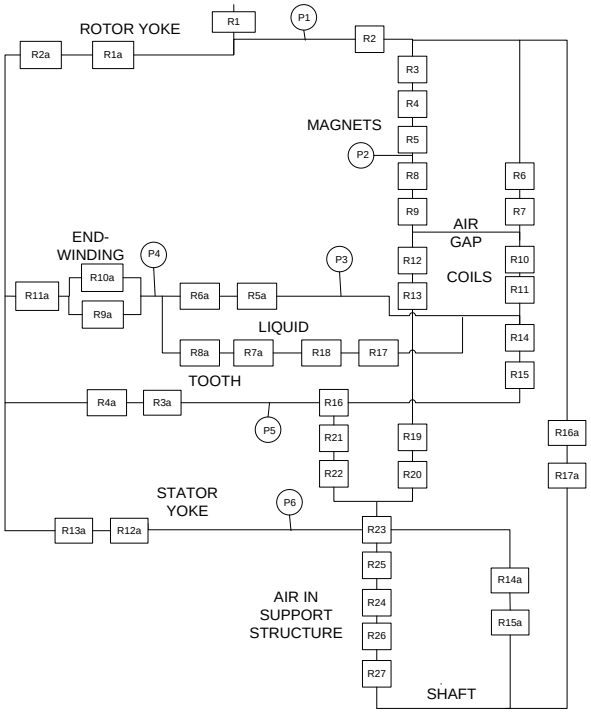

Figure 4.6: Lumped-parameter model of the generator (steady-state).

The detailed equations of the convection and conduction thermal resistances of the machine parts are presented in Appendix 1. The power loss vector contains copper losses, iron losses, permanent magnet losses, friction and additional losses separated between the generator components. A specific code developed with a Matlab program was used to compute the temperature rise. The cooling matrix is defined by the cooling resistances of liquid flow in the stator winding, and by the air flows in the air gap and in the rotor support structure. The calculated temperatures of the generator parts (Eq. 1.24-1.26) are collected in Table 4.7. It should be noted that the lumped parameter model shows the average temperatures of the generator parts. The average temperatures of the stator winding and the coolant are respectively 58 ºC and 57 ºC. Furthermore, finite–element software is used to provide a detailed temperature distribution within the studied generator.

4.4.3 Thermal analysis based on Computational Fluid Dynamics

A computational thermal analysis of DD PMSG is conducted using the commercial software Fluent. CFD thermal design is useful for cases of fluid flow inside the machine parts. It allows obtaining of the temperature distribution within the machine without a definition of the convection heat transfer coefficient in the air-gap and air of the hollow support structure by empirical equations. However, this model requires more computational resources; therefore, the geometry is simplified. The 3D-model of the generator represents only part of the machine because of the machine symmetry. A small slice is selected to be able to generate the most dense mesh and in doing so achieve the most reliable results. This CFD thermal analysis was conducted to simulate the average temperature of the stator slot and the temperatures of the rotor. Because of the limited computational resources, it was impossible to create in one sole model an actual design including the stator slots, the end windings containing liquid passages and the rotor structure. Therefore, two models were created: the first only comprised the stator part (1/144th part) without the end windings, and the second comprised the machine part, with the temperature of the stator copper winding defined from the previous model results.

Fluent 14.5 software for FEM was employed to create a 3D model simulation showing the temperature distribution within the copper conductors with the internal water flow (Fig.4.7). The mesh contained 247 000 nodes. The κ-ω SST turbulence module and energy modules were used for the simulation. The κ-ω SST turbulence model was applied because it can handle a wide range of *y plus* values (assuming some error), and the model equations behave appropriately in both the near-wall and far-field zones. The default values of the Fluent model constants were implemented. The stator segment model has $y\ plus = 53$ for the internal walls of the copper conductors.

The assumptions of the inlet velocity and the temperature of the demineralized water were based on the results presented in Fig.4.4 (a). It was also assumed that there would be no heat transfer between neighbouring conductors. The outer surfaces of the copper conductors were assumed to be insulated with double-coated Nomex tape (0.25 mm).

The slot insulation thickness was assumed to be 1 mm. The copper conductors were constructed without stainless steel tubes because of limited computational resources. The surface roughness of the stainless steel tube was assumed to be 3.2 μm. The stainless steel tubes were by the wall thickness (0.75 mm) and the stainless steel thermal conductivity (16 W/(m·K)). The stainless steel surface roughness was assumed to be $1.327 \cdot 10^{-6}$ m. The volumetric copper losses (640 kW/m^3), iron losses (4.7 kW/m^3) were assumed to be within the model parts. The convection coefficients and air temperature (30˚C) were defined on the stator yoke surface and in the air gap as 17 W/(m^2·K) and 53 W/(m^2·K), respectively (Appendix B).

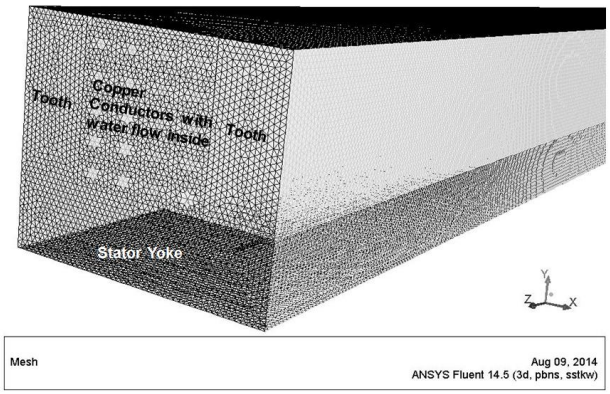

Figure 4.7: Mesh for the stator part model.

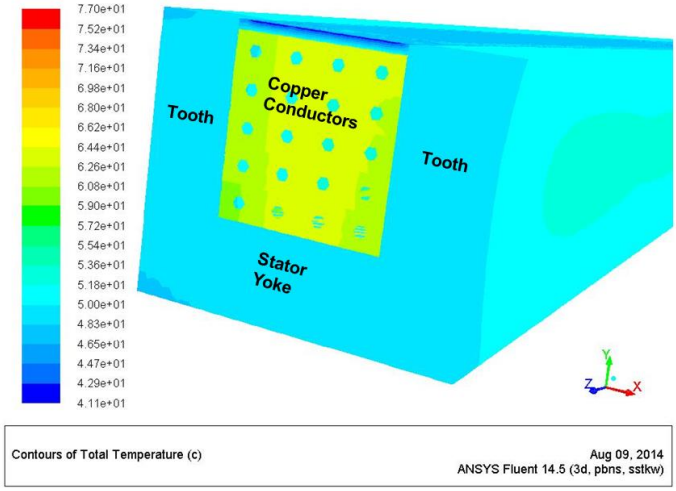

Figure 4.8: Temperature distribution within the stator parts.

Fig. 4.8 shows that the average temperature of the conductors is about 60 ˚C. This temperature is further used to simulate the rotor temperatures. The simplified 3D model

(Fig. 4.9) represents only one-hundred-forty-forth (1/144th) of the generator. The generator model comprises the stator yoke, the stator tooth, the slot wedge, the copper winding, the copper end winding, the insulation, the rotor iron, the rotor with the magnet and the air gap. For simulation purposes, tetrahedral mesh with 241 000 nodes, 2 330 000 faces and 1 111 000 cells was created with the generator model in Gambit (Fig.4.9). The model of the machine segment (Fig. 4.9) has *y plus* = 3 for the stator and rotor in the walls.

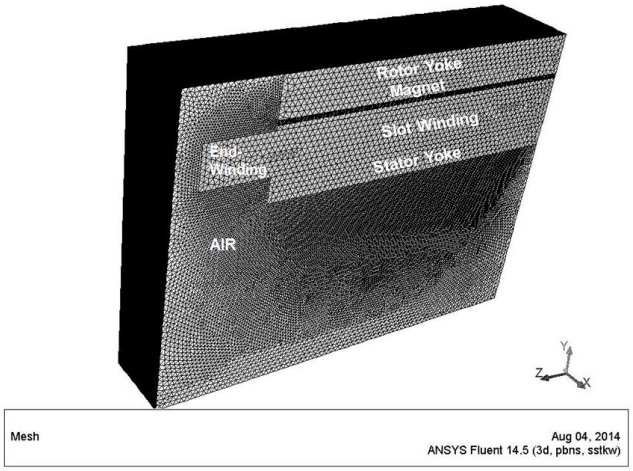

Figure 4.9: Mesh for the generator model.

Figure 4.8 shows the temperature field and the velocity field of the generator resulting from the simulation of the 3D Fluent 14.5 software. The κ-ω SST turbulence module and energy modules are used for the simulation. The κ-ω SST turbulence model was applied because it can deal with a wide range of *y plus* values (assuming some error), and the model equations behave appropriately in both the near-wall and far-field zones. The default values of the Fluent model constants were used.

The stator and rotor iron stacks have non-uniform conductivities because of their laminated structure. The heat losses presented in Table 4.2 are imposed as heat sources of the simplified generator parts. The rotor surfaces and the support structure (left wall) have a rotation speed of 11 rpm. The surface roughness was assumed to be 25 μm for the stator windings and 5 μm for other surfaces. To simulate a real application environment, the uniform convective heat transfer coefficient and air temperature (18 W/m^2·K and 30 ºC based on Eq. 4.14-4.15) were applied on the outer surface of the rotor yoke. Fig.4.10 illustrates the temperature distribution within the generator studied. The air velocity and the convection coefficient are presented in Appendix B (Fig.B.2).

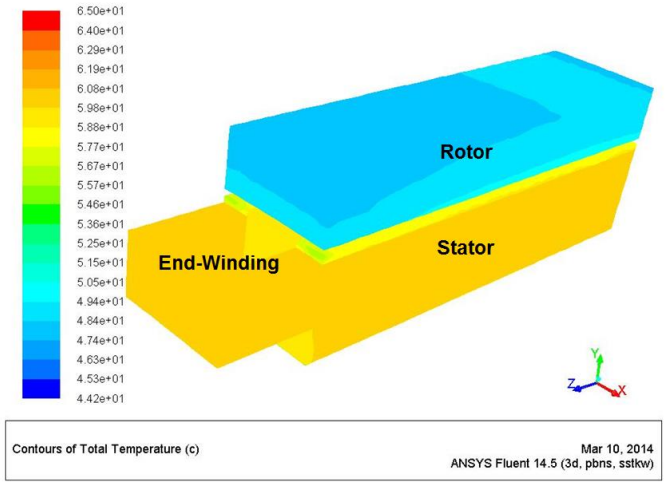

Figure 4.10: Temperature distribution within the generator.

The obtained temperature distribution with the machine parts from the LPN and CFD thermal analyses are presented in Table 4.7. The discrepancy between the temperature results is 2-3 K, which is mainly attributable to the assumed convection coefficients in LPTN. The wind generator usually operates below its rated point, as the blade pitch control is applied in the wind turbine. Therefore, actual generator temperatures will be lower than those presented in Table 4.7.

Table 4.7 Temperatures of the PMSG under study, at 30°C ambient temperature and at the rated point.

Model Components	Simulated Average Temperature, ˚C	
	LPN	CFD-thermal
Stator Yoke	57	50-60
Stator Tooth	60.5	54-60
Stator Winding (average)	62	60
Coolant (average)	60.5	-
Air Gap	50.5	48
Rotor Mounted Magnets	47	50
Rotor Yoke	47	48
Shaft	32	-

As may be seen in the table, the direct water cooling system of the stator copper winding is an effective cooling method at the rated point, as the temperature of the permanent magnets is limited to 50 ºC, and the average temperature in the winding is 60-62 ºC based on the CFD and LPN thermal analysis. The low permanent magnet

temperature allows for using high remanence magnets, which helps in creating a high tangential stress. Based on the analytical simulation, the maximum winding temperature is limited to 80 ºC. However, assuming that the conductors influence each other, the maximum temperature of the conductors is just 65 ºC. Such a temperature can be regarded as an advantage, as the stator copper loss is the dominating one, and this low operating temperature guarantees a significantly lower stator resistance for the machine, compared to machines operating at 130 ºC, for example. Because of the highly effective cooling, the machine is not thermally limited, but its peak torque is limited by the synchronous inductance. Therefore, the machine operates at a lower temperature than normally but is still remarkably lighter than an air-cooled counterpart. The cooling solutions developed for the stator winding are capable of removing higher losses and providing the cooling for a higher current density than in the machine studied. In this particular generator design, the high efficiency of the generator (reflected in high energy output) was the target value.

4.5 Experimental validation on a coil prototype (motorette)

A coil prototype in the form of a motorette was constructed to validate the workability of the system designed for direct liquid cooling. The motorette comprises two thermally parallel and electrically series connected coils and a magnetic stack (Fig. 4.11), emulating a small part of the stator. Each coil consists of eight 15 mm × 15 mm conductors (and four turns), with 7 × 1 mm extruded tubes inside of them and a total length of 6 m. The inlet and outlet of the stainless steel cooling tubes are joined with a manifold. For cooling purposes, synthetic oil (polyalphaolefin, PAO) was considered to avoid using a water deionizer. PAO has high viscosity ($4.15 \cdot 10^{-3}$ m^2/s) and lower heat capacity (2301 J/(kg·K)) than water, so the application of PAO deteriorates the performance of real generator cooling system (Product Technical Data, FUCHS, 2012).

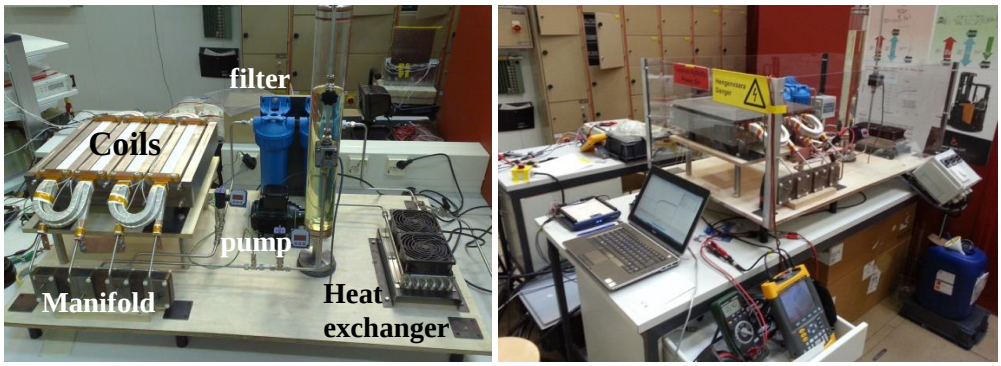

Figure 4.11: Coil prototype test bench setup.

The tubing, hard plumbing, component quick-disconnects for field maintenance, coolant filters, heat exchanger, pump and other components were selected to meet the system

design requirements (Fig. 4.11). The filter and heat exchanger are included in the cooling loop to filter out particles and cool down the coolant.

Fig.4.12 illustrates the performance of the cooling system for water, Ethylene Glycol (50% Vol.), PAO, and EVANS waterless liquid (EVANS is based on proprietary blends and additives). The temperature rise and the pressure losses are simulated by Eqs. (2.6)–(2.9), (3.1)-(3.3), (4.1)-(4.2) and the liquid properties from Table 1.5 were assumed. The copper losses generated in the stator winding were corrected based on Eq. (4.5)–(4.6), depending on the operation temperature range. The stainless steel surface roughness is assumed to be $1.327 \cdot 10^{-6}$ m.

(a) (b)

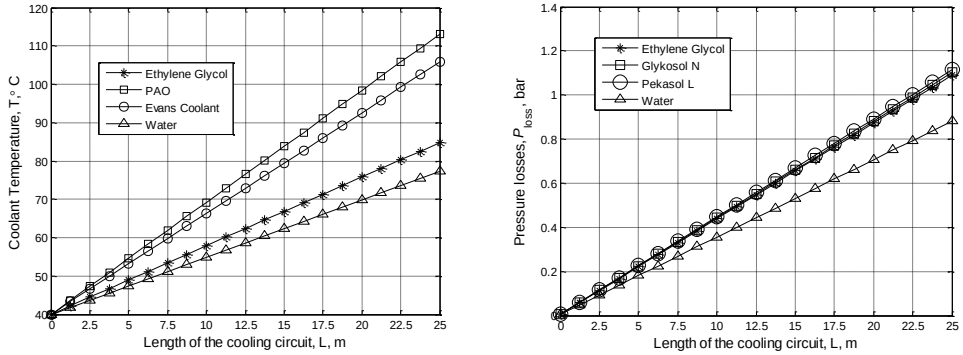

Figure 4.12: Temperature rise of coolant (a) and pressure losses (b) along one cooling circuit (analytical calculation).

To generate heat losses within the copper conductors, the coils were connected in series to a high frequency synchronous generator with a maximum frequency of 550 Hz and a rated current of 140 A. An appropriate 1000 A source was not available. This high frequency and the attached steel plate above the coil were used to respectively create larger losses in the coils and additional high losses in the steel and in the stainless steel tube inside the copper bars. In the real generator, the rated current in a segment is 1000 A at 11 Hz, so losses in the stainless steel tubes will be small. This test did not demonstrate the real conditions of the generator under study, but it did show the effectiveness and workability of the cooling system.

A total of eight thermocouples (Resistance temperature Device (RTD)) were attached to the copper conductors at the site of the inlet, outlet and near the steel to measure their respective temperatures. The input and output PAO temperatures and pressures were measured during the tests from outside the coils by the sensors (Type K termocoules). The generated losses were defined by the voltage and current measured values. In the copper conductors and stainless steel tubes, 180 W heat losses were generated. The steel plate attached above the coil additionally generated 2800 W. The PAO flow rates were

measured using a flow meter series connected to the cooling circuit. Thus, the generated heat losses were evacuated by the coolant, with a velocity of 1.7 m/s and by natural convection, as the coil prototype has not been isolated. The temperatures were stabilized in 5 hours (Fig. 4.13).

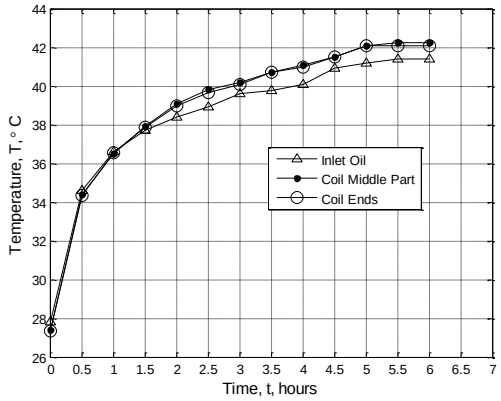

Figure 4.13: Temperature rise of coolant and coil parts during the tests.

At the end of the test, the pump pushing the coolant in the cooling circuit of the coils was switched off and then switched on again to demonstrate the cooling effectiveness (Fig. 4.14). The direct oil cooling provided a 0.04-0.07 K/s cooling of the copper conductors, meaning a 11-22 K temperature drop of the copper conductors over 5 min.

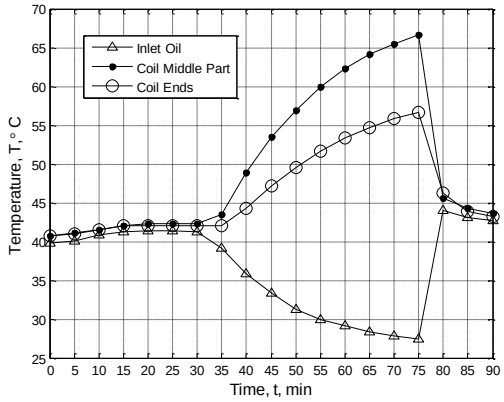

Figure 4.14: Temperature rise of the coolant and coil parts during the tests when the flow was switched off and then on again.

The experimental temperature results deviate from the results calculated from Eq. (4.1)–(4.7) (Fig. 4.15). The measured total pressure drop (2 bars) includes pressure drops in the cooling circuit of the coil and in the manifolds. The calculated value of the

pressure losses in the cooling circuit of the coil is 0.6 bars, so the manifold causes a high pressure drop. The discrepancy between the simulated and measured values of the temperature rise may rise from the simulation assumption, as the influence of the conductors on each other was not included in it. Another explanation for the discrepancy is manufacturing defects (a real surface has greater roughness), resulting in a higher convection coefficient and heat transfer surface. The test setup was not insulated from the environment, so some of the generated heat losses were removed by passive air convection during the tests. The temperature rise and pressure losses within the coils tested only partly validate the analytically calculated values, but these do demonstrate the workability of the designed cooling solution (Fig. 4.15). The Resistance Temperature Device (Pt-100, class B) for the coil temperature measurement has an error margin of ± 0.3 ºC at 0 ºC (DIN 43760). The coolant temperature was measured using a Type K thermocouple (DIN class A) with standard limits of error at 0.35 ºC or 0.06% at 0 ºC.

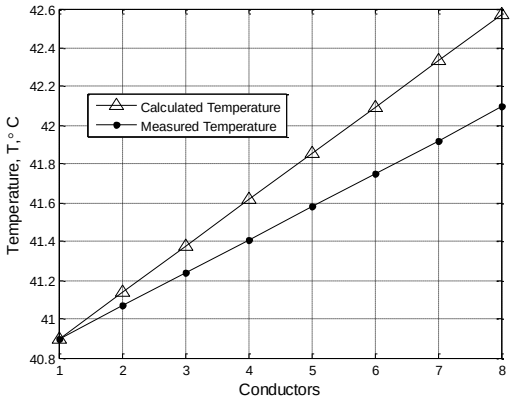

Figure 4.15: Calculated and measured temperatures of the coolant along the test cooling circuit (the standard limit of error of the Type K thermocouple at 0 ºC is 0.06 %).

4.6 **Reliability of the generator liquid cooling system**

The move to liquid cooling raises a reliability question. Is a liquid-cooled (LC) DD PMSG as reliable as an air-cooled DD PMSG? This is the question addressed by this part, which documents the reliability analysis for an 8 MW LC DD PMSG. The analysis considered the LC DD PMSG and its liquid cooling loop and secondary cooling in order to manage the coolant temperature in the primary loop. Both liquid-to-liquid and liquid-to-air secondary cooling solutions were analysed. Reliability is important in the design of an LC DD PMSG cooling system. Proper, long-term operation of the machine depends on effective and consistent cooling of its component parts. Inadequate cooling adversely affects the reliability, which in turn reduces the electrical machine's availability to generate electrical power, reducing revenue. Understanding cooling

system failure modes and which areas are most prone to failure is critical in achieving a robust generator design and optimizing wind turbine availability.

4.6.1 Reliability data of the generator cooling loop

Reliability considerations play an important part in the design and analysis of the cooling system concepts. The LC DD -PMSG cooling system is separated into two subsystems: the primary generator cooling system and the secondary system that removes heat from the primary (Liquid to Liquid (LL) or Liquid to Air (LA)). The reliability analysis divides the generator cooling systems into series- and parallel-connected components. Both the LL and LA secondary side components are calculated in the same manner. The subsystems do not have redundant components.

The presented cooling systems consist of several repairable components with constant failure and repair rates, so reliability evaluations include the repair effects (mean down time). The reliability analyses are executed using the main reliability metrics, such as *Mean Time Between Failures (MTBF)*, *Mean Down Time (MDT)*, *Mean Time To Failure (MTTF)*, failure rate, reliability and availability (Villemeur, 1992). Two types of repairable system are used: a series system with *n* components, and a parallel *m/n* system (identical components – active redundancy) (Villemeur, 1992). The parallel *m/n* system operates when at least *m* out of *n* components are operating. This system is used for the calculation of water filters and parallel connected sets of air filters, heat exchangers and fans.

Product data for reparable components often contain two reliability metrics: failure rate and Mean Down Time (MDT). Failure rate is the frequency with which a component or system fails per time interval (e.g., 1/hour). MDT is the expected time interval (in minutes, hours, days, years, etc.) for detecting and repairing the fault of the component and putting it back into service. In this calculation, the time for changing the unrepaired component (with a new one) was assumed as the MDT of the component (for the filter). The term 'component unavailability' refers to the inability of a component to be in a state to perform a required function (Villemeur, 1992). The following equations are used to calculate the total system unavailability *UA*, repair rate μ and failure rate λ for the series system and parallel *m/n* system (Villemeur, 1992).

$$UA_{\text{sersys}}(\infty) \approx \sum_{i=1}^{n} \frac{\lambda_i}{\mu_i} \tag{4.22}$$

$$\mu_{\text{sersys}}(\infty) \approx \frac{\sum_{i=1}^{n} \lambda_i}{\sum_{i=1}^{n} \frac{\lambda_i}{\mu_i}} \tag{4.23}$$

$$\lambda_{\text{sersys}}(\infty) \approx \sum_{i=1}^{n} \lambda_i \tag{4.24}$$

$$UA_{\text{parsys}}(\infty) \approx \sum_{i=1}^{m-1} C_{\text{n}}^{\text{k}} \cdot \left(\frac{\lambda_i}{\mu_i} \right)^{\text{n-k}} \tag{4.25}$$

$$\mu_{\text{parsys}}(\infty) \approx \frac{(n-m+1) \cdot \mu_i \cdot C_n^{m-1} \cdot \mu^{m-1} \cdot \lambda^{n-m+1}}{\sum_{i=0}^{m-1} C_n^k \cdot \mu_i^k \cdot \lambda^{n-k}} \tag{4.26}$$

$$\lambda_{\text{parsys}}(\infty) \approx \frac{m \cdot \lambda_i \cdot C_n^m \cdot \mu_i^m \cdot \lambda_i^{n-m}}{\sum_{k=m}^{n} C_n^k \cdot \mu_i^k \cdot \lambda_i^{n-k}} \tag{4.27}$$

$$C_{\text{n}}^{\text{m}} = \frac{n!}{m!(n-m)!} \tag{4.28}$$

where UA_{sys} is the subsystem or system limiting unavailability, m is the number of operate components/subsystems for proper system operation, n is the number of components/subsystems, k is the number of failed subsystems, λ_i and μ_i are the failure rate and repair rate of system/subsystem component i respectively and λ_{sys} and μ_{sys} are the failure rate and the repair rate of the total subsystem or system respectively.

Mean Time To Repair (*MTTR*) is the expected operating time interval (in minutes, hours, days, years, etc.) for the component repair. Mean Time Between Failures (*MTBF*) is the expected operating time interval (in minutes, hours, days, years, etc.) between the component repairs. The total system *MTTR*, *MDT* and *MTBF* for series and parallel m/n system are calculated using Eq. (4.29-4.31) (Villemeur, 1992).

$$MTTR_{\text{sys}} = \frac{1}{\lambda_{\text{sys}}} \tag{4.29}$$

$$MDT_{\text{sys}} = \frac{1}{\mu_{\text{sys}}} \tag{4.30}$$

$$MTBF_{\text{sys}} = MTTR_{\text{sys}} + MDT_{\text{sys}} \tag{4.31}$$

The repairable component or system is characterized by two main reliability measures, reliability and availability, which can be defined by Eq. (4.32-4.33) (Villemeur, 1992; Cadwallade, 1998). The component availability *A* is the ability of a component to be in a state to perform a required function (Villemeur, 1992). The component reliability *R* is the probability that the component can perform a required function for a given time interval *t*.

$$R(t) = e^{-\lambda_{\text{sys}} \cdot t} \tag{4.32}$$

$$A_{\text{sys}} = 1 - UA_{\text{sys}} \tag{4.33}$$

The literature values of the failure rates and mean down times of the components of the cooling systems presented in Table 1.6 and in Table 4.9 are used in the calculation of the reliability metrics. The validity of these values depends on exploitation conditions, manufacturing, etc. It is difficult to find correct reliability values without real condition measurements, but the further results (Table 4.10) are correct assuming the validity of the values in Tables 1.7 and 4.8.

Table 4.8 Reliability parameters of the generator cooling system (Technical Report, HSE, 2010; Lees, 1996; Technical Letter, EATON, 2012)

Auxiliary Component	Failure Rate, per year	Mean Down Time, man-hours
Primary Side		
Stainless-Steel Tube, tooth coil	$4.6 \cdot 10^{-7}$ per m	1 per m
Connection	$5 \cdot 10^{-6}$	0.5
Manifold	$3 \cdot 10^{-7}$	3
Up/Down Tube in LL Cooling System (D =78 mm, l =100/120 m)	$6 \cdot 10^{-6}$ per m	1 per m
Tube in LA Cooling System (D =16 mm, l =50 m)	$6 \cdot 10^{-6}$ per m	4

4.6.2 Reliability data of the generator liquid cooling system

The primary liquid cooling loop is sized to remove temperature build-up in the stator windings and surrounding steel laminations. To manage the primary coolant temperature, secondary cooling can be based on liquid-to-liquid (LL) or liquid-to-air (LA) heat exchangers. In either case, the primary loop is made of the same auxiliary components: a deionizer, a centrifugal pump, a water reservoir, liquid filters, and an expansion vessel (Fig.4.16). The secondary cooling side includes auxiliary components for cooling the main fluid, such as a pump and water filter (LL) or air fans and an air filter (LA) (Fig.4.17).

In addition to its auxiliary components, the generator cooling loop consists of its plumbing, which in this case is made of stainless steel tubing, tube connections, and manifolds. The failure of any auxiliary component of the generator loop or any part of its plumbing parts is considered a failure of the cooling system. Within the generator, the cooling system is divided into 12 identical parallel circuits, one for each of the 12

stator segments. Each of these circuits features a single inlet tube leading into an inlet manifold that connects to 12 conductor inlet tubes, one for each coil. Exiting the coils, 12 outlet tubes connect to the outlet manifold, which then recombines the flows into a single outlet tube. Thus, every coil has a coolant inlet and outlet, so for each stator segment, there are 12 inlet and outlet pairs connected in parallel to incoming and outgoing coolant manifolds. The inlet and outlet connections must be galvanically isolated from each other and from the remainder of the coolant system, so an insulated mechanical connection must be used between the conductor coils and the coolant manifolds. The 288 mechanical connections of the 144 copper coils in the primary loop form are its major weakness from the standpoint of reliability, as these connections are subject to potential corrosion or sealing issues (Technical Letter of GE, 2001; Irwanto et al., 2009). Figure 4.16 illustrates a schematic representation of the stator segment flow. The reliability parameters for the circuit are defined by Eqs. (4.22)-(4.27). Each generator segment comprises a cooling circuit with m = 12, n = 12, and k = 1. The reliability parameters of the 12 parallel circuits of the LC DD-PMSG loop are defined by Eqs. (4.22)–(4.34), with m = 12, n = 12, and k = 1.

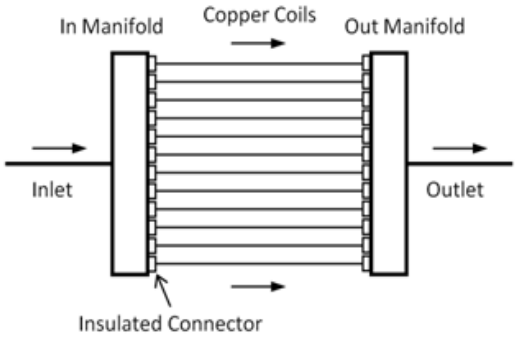

Figure 4.16: Schematic representation of a primary coolant flow path for a single stator segment.

For the LA approach, liquid-to-air heat exchangers connect the primary liquid loop with the secondary side. The auxiliary components on the secondary side include air filters and the blowers that force air through the heat exchangers. Five fan and filter units (21 m^3 volume of one unit) serve five heat exchangers of 0.6 m^3 total volume to ensure adequate cooling. Offshore applications call for specialized filtering of the corrosive sea air. Fig. 4.17 (a) offers a simplified illustration of the LA exchange approach. For LL heat exchange, primary and secondary liquid loops connect through a liquid-to-liquid heat exchanger. The auxiliary components of the secondary loop include liquid filters (0.08 m^3 volume of one unit) and a centrifugal pump. Fig. 4.17 (b) offers a simplified illustration of the LL exchange approach. Because liquid-to-liquid cooling is more effective (as liquid coolant has high heat capacity), a single heat exchanger unit with a typical size of 0.17 m^3 is needed; the secondary side of the liquid-to-liquid cooling system is simpler and inherently more reliable. For offshore installations, there is the

opportunity to use seawater as the secondary side coolant. However, using seawater as a coolant presents some challenges. Its salt content makes it corrosive and electrically conductive, and seawater has a high biological content. A special treatment system is needed to prevent fouling and clogging of the pump and heat exchanger if seawater is used (Gutierrez-Alcaraz et al., 2010).

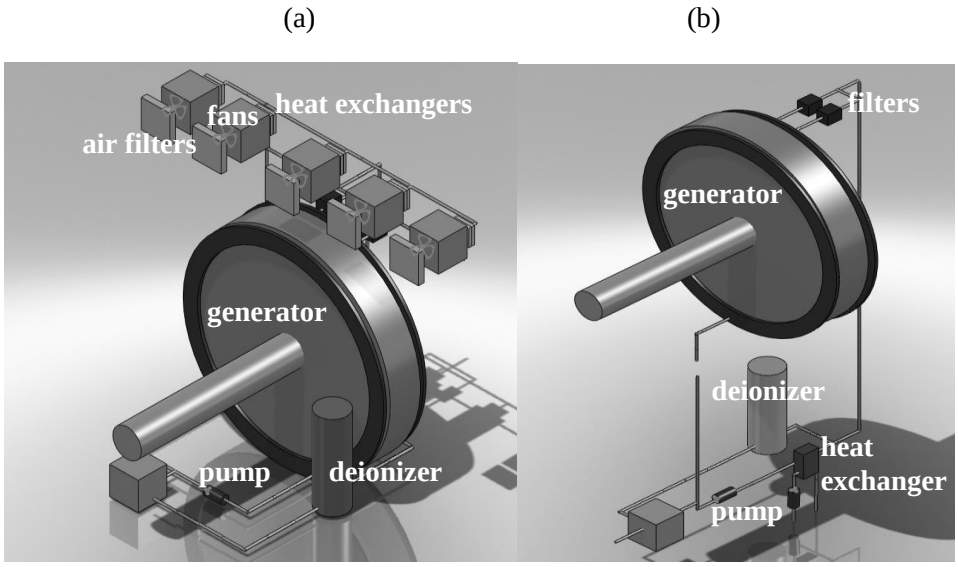

Figure 4.17: Generator and cooling system based on a liquid-to-air heat exchanger (a) and liquid-to-liquid heat exchanger (b).

The reliability of the LL and LA primary and secondary sides depends on auxiliary component reliabilities. The auxiliary components in either case are connected in series. Only multiple components of the same type are connected in parallel (i.e., water and air filters, fans, and air-to-water heat exchangers). The treatment equipment (filters and deionizer) for the primary and secondary side cooling fluids, air or water, were also included for this reliability analysis. The failure rates and *MDT* for the auxiliary equipment of LL and LA primary and secondary sides have been taken from the literature and they are summarized in Table 1.7 (Lees, 1996; Service Catalogue of Manifolds, Lebentech; Wagner et al., 1988; Hurst, 1994; Fraas, 1989; Wolpert, 1982; Cassady, 1989, Jadhay, 2010). These component reliability values are used to calculate the metrics of the primary and secondary side cooling systems, and the reliability of the LC DD-PMSG cooling system as a whole. According to Table 1.7, the failure rate is high for the deionizer, water/air filter, air fan, and centrifugal pump because they have shorter design working lifetimes. These components must be serviced and changed out as they reach the end of their lifetimes: every year for the deionizer and water filter; every 10 years for the centrifugal pumps and air fans. The main reliability parameters of the generator cooling loop and the LC DD-PMSG cooling systems based on LL and LA systems and including all their components are presented in Table 4.9. These values

were calculated from Eqs. (4.22)-(4.32), using the values of the failure rates and MDT presented in Tables 1.7 and 4.8.

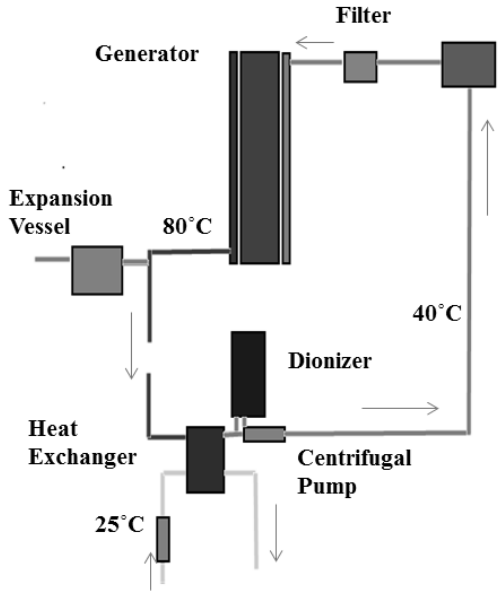

Figure 4.18: Water-based cooling system of main liquid.

Table 4.9 Reliability parameters of the generator cooling systems

Parameters	Generator Cooling Loop	Primary Cooling Loop		Total Cooling System	
		Liquid-to-Air	Liquid-to-Liquid	Liquid-to-Air	Liquid-to-Liquid
Failure Rate, per year	$3.1 \cdot 10^{-3}$	1.9	1.8	2.4	2.4
MTTF, years	322	0.54	0.55	0.43	0.43
MDT, man-hours	13	4.3	4.3	4.5	4.3
MTBF, years	322	0.54	0.55	0.43	0.43
Availability	≈1	≈ 0.9991	≈ 0.9991	≈ 0.9988	≈ 0.9989
Unavailability	$4.68 \cdot 10^{-6}$	$1 \cdot 10^{-3}$	$8.8 \cdot 10^{-4}$	$1.2 \cdot 10^{-3}$	$1.1 \cdot 10^{-3}$

Fig. 4.19 presents the reliability of the generator cooling loop (4.9 a) and the LC DD PMSG primary sides based on LL and LA heat exchangers (4.9 b) during 30 years of exploitation. The reliability of the generator cooling loop drops from 0.998 to 0.937. The reliability of the primary loop based on LA heat exchangers drops significantly during the operating period. The LA system exhibits this relatively poor performance because of the five identical liquid-to-air heat exchangers, which increase the overall failure probability. The LL system includes only one liquid-to-liquid heat exchanger. The curve of the LA primary cooling loop is not straight because of the five parallel-connected LA heat exchangers (Eq.4.25-4.27).

The more sophisticated models require many variables and associated parameters to represent the principal damage mechanisms in the life equations. The variables include elastic, inelastic, and total strain-ranges; dissipated strain energy; temperature; frequency; hold time; strain rate; and mean stress (Tomas, 2010).

(a) (b)

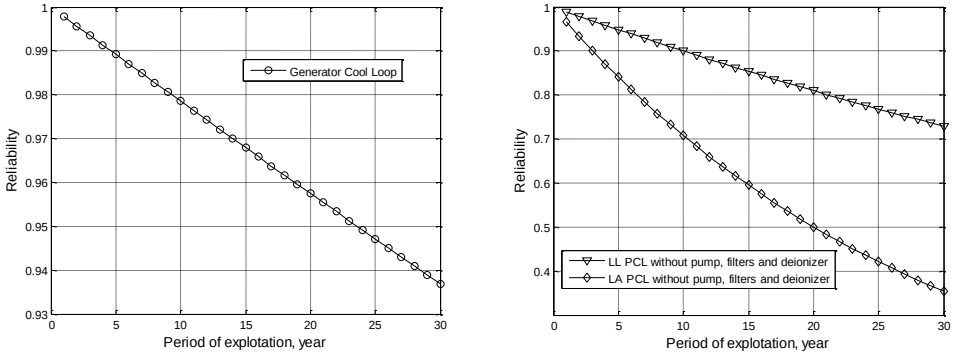

Figure 4.19: Reliability of the generator cooling loop (a) and LL and LA primary cooling sides (b) over a 30 years of their exploitation.

On average, in a wind turbine having a technical availability of 98%, the highest amounts in total number of system or component failures, expressed as percentages, are as follows: electrical system (23%), plant control system (18%), sensors (10%), mechanical brakes (8%), hydraulic system (8%), yaw system (8%), rotor blades (7%), rotor hub (6%), housing (4%), generator (4%), gearbox (4%) (Hahn et al., 2006). However, failures of the gearbox and generator have the longest downtimes – 6 and 7 days, respectively (Hahn et al., 2006). The annual failure rate of a wind turbine increases from 1.7 failures per year to 3 failures per year when the rated power rises from below 600 kW to 888 kW. Wind turbines with a rated power above 1000 kW experience 7.5 failures per year (Hahn et al., 2006). The reliability of an average generator based on a gearbox drops from 0.9389 to 0.1511 over 30 years (0.09 failure rate per year (Hahn et al., 2006)), so the liquid cooling system reduces its reliability by 3.5% ($3.1 \cdot 10^{-3}$ additional failures in the cooling loop per year). However, the gearbox

reliability drops from 0.9337 to 0.1277 over 30 years (0.098 failure rate per year (Smolders et al., 2010)), so the wind turbine containing a generator and a gearbox is more prone to unavailability than is a direct-drive Permanent Magnet Synchronous Generator with direct liquid cooling.

4.7 Conclusions

The direct-drive permanent magnet synchronous generator is more reliable than the high-speed power generator presently on the market. The use of the internal cooling system of the stator winding allows for reducing the tremendous dimensions of DD PMSGs. Larger DD PMSGs must be liquid cooled to meet upcoming power capacity demands without exceeding the practical limits for size, weight, and capital cost. However, liquid cooling is a new technology for wind turbines, and its impact on reliability must be evaluated. This part presents a description and analysis of the direct water cooling system of the stator copper winding. The system removes the heat losses of the stator winding (530 kW), thereby ensuring an adequate temperature of the copper conductors (up to 80˚C) and the safe operation of the rotor surface-mounted permanent magnets (up to 50˚C) at the rated point. The thermal analysis of the generator has been made at the rated point, as this is the most sensitive point. The blade pitch control applied in the wind turbine excludes the possibility of generator overload.

The thermal models of the PMSG studied were generated by LPN and CFD thermal modelling. The CFD thermal design allows one to obtain more detailed temperature distribution within the copper conductors in the slot, the rotor permanent magnets and the rotor yoke. Unfortunately, it was impossible to simulate the whole generator model without the assumed convection coefficients based on the analytical correlations. The model of the generator stator with the DW flow was simulated first, and the resulting temperature for the copper winding was then applied to the stator slot of the whole machine model. The CFD thermal modelling showed that the stator slot temperature may be up to 65 ˚C. The test results of the tooth-coil (motorette) also demonstrated that there was an overestimation of the copper temperature in the analytical correlations. The tests ascertained the effectiveness and workability of the cooling system.

The reliability analysis for a liquid-cooled 8 MW DD PMSG coupled with primary and secondary liquid coolant systems is presented here. Reliability was calculated analytically and assessed based on the reliability metrics of *MTBF*, *MDT*, *MTTF*, failure rate and availability. Both liquid-to-liquid and liquid-to-air secondary side cooling solutions were analysed. Reliability metrics were calculated and assessed in terms of constant failure and repair rates. The analysis concluded that the cooling system for the LC DD PMSG has an average reliability (i.e., probability to perform the required function) of 0.96 over a 30-year design lifetime (with $3.1 \cdot 10^{-3}$ failures in the cooling loop per year). Assuming that the reliability metrics are valid, the total cooling system of the generator (including primary and secondary cooling loops) reduces the wind generator reliability by 3.5%. This is insignificant compared to gearbox reliability, the

application of which reduces the generator reliability by almost 100%. Four to five hours of servicing are required every five months to change out consumed parts and shorter life components, such as filters, the deionizer, fans and pumps. An LC DD PMSG cooling system based on a liquid-to-air heat exchange between the primary and secondary sides is less reliable than an equivalent system based on a liquid-to-liquid heat exchange, because the liquid-to-air system includes multiple heat exchanger units, each with short-life components. Cooling system reliability could be improved by designing in redundancy; however, the economic feasibility of this approach must be studied.

The thermal and reliability analysis methods presented herein may be applied in electrical machine design with a direct liquid cooling system. The LPN method is the best for the preliminary analysis of temperature distribution within the machine studied. In the last stages of the machine design, FEM and CFD analyses with validation by experiments should be carried out to define the hot spots in the machine parts. CFD thermal analysis is also necessary for defining the cooling system parameters.

5 Oil-immersed permanent magnet synchronous motor

This chapter presents a 26.6 kW tooth-coil embedded-permanent-magnet synchronous electrical machine with direct-immersion oil used as the coolant method. This means that the machine is completely filled with oil. It is intended for off-highway, hybrid working vehicles which require a source of hydraulic power for their main hydraulic actuators. The coolant is taken from the working hydraulic circuit, which eliminates the need for a separate cooling circuit in the system. The electromagnetic concept of this machine is fully presented in the works of Ponomarev et al. (2011, 2013). This cooling system was proposed to alleviate the temperature issue concerning the stator winding and the rotor permanent magnets. The thermal model of the machine based on LPTN is presented to assess the cooling system performance. The thermal field of the machine is calculated with the CFD thermal method in order to present the oil velocity distribution and to locate the hot spots inside the machine's critical parts. The results of the machine tests are illustrated and compared with the simulated values.

5.1 Oil-immersed machine

The rated power and speed of the machine in question are 26.6 kW and 1500 rpm, respectively. Neodymium-iron-boron magnets are adopted for the machine excitation because of their high energy product. A detailed architecture of the radial flux machine is shown in Fig.5.1. Table 5.1 lists the main dimensions of the machine.

Figure 5.1: Oil-immersed radial flux machine (Ponomarev et al., 2011).

Table 5.1 Characteristics of Machine Studied

Parameter	Quantity
Rated Power	26.6 kW
Rated Speed	1500 rpm
Line to line voltage	400 V
Rated phase current	43 A
Number of phase	3
EMF factor (back emf / nominal voltage)	0.93
Tangential Stress at the rated point	22 kPa
Linear current density	30 kA/m
Current density	5 A/mm^2
Peak output power to rated output power ratio (overload capability) at nominal speed	2.6
Load angle	44 deg.
Power factor	0.87
Rated electrical efficiency	95%
Number of slots and poles	18, 16
Total machine mass with bearings	93 kg
Geometrical data	
Stator Outer Diameter	380 mm
Stator Inner Diameter	260 mm
Length of Air Gap	3 mm
Length of Stator Stack	63 mm
Total Stator Length	115 mm
Magnet Width × Height	43 × 12 mm^2
Slot Width × Height	44 × 34 mm^2

This machine employs direct-immersion oil cooling (see Fig. 5.2). The configuration of the cooling circuit ensures an oil volume rate of 4 l/min and an inlet oil temperature up to 80 ˚C. The integrated pump circulates the oil through the machine to remove the generated heat. Oil enters through the frame end, cools the machine internal surfaces, removes the majority of heat losses, and exits from another frame end. The cooling unit (heat exchanger) can be attached to the cooling circuit. The oil cooling system should be able to filter, purify and control the coolant to any desired level during the machine run. The stator windings and the permanent magnets are coated with epoxy to avoid corrosion issues. The impregnation material for the stator winding is polyester-based resin. The oil (Ultramax HVLP46) parameters are listed in Table 5.2.

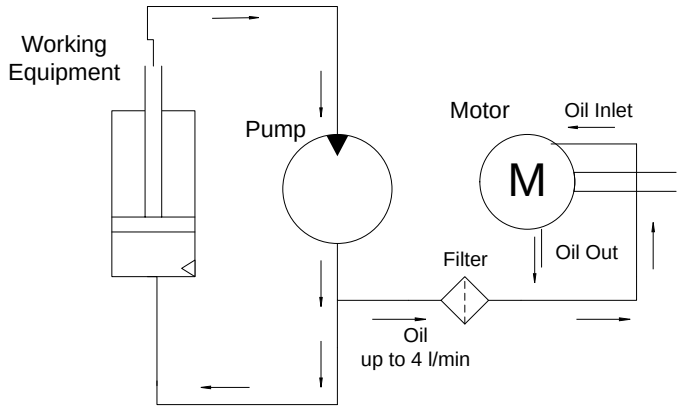

Figure 5.2: Cooling scheme of the machine.

Table 5.2. Properties of Ultramax HVLP46 (Product Technical Data,Valvoline)

Typical Property	
Dynamic Viscosity, Pa·s (at 40ºC/ at 80ºC)	$40 \cdot 10^{-3}/7 \cdot 10^{-3}$
Specific Heat Capacity, J/kg·K	2300
Thermal Conductivity, W/m·K	0.185
Density, kg/m^3	866
Flashpoint, ºC	>221
Freezing point, ºC	-42

The coolant fills up all the space inside the electrical machine, directly flushing the copper end windings and, in doing so, removing the heat directly from the place it emerges the most. For the tests, all of the spaces inside the machine were inspected to verify that it was indeed completely filled with oil. The machine was filled via the down duct, and the oil exited via the upper duct. The direct oil cooling allows for achieving a very compact design for an electrical machine with high torque density, due to the great current loading of the windings. The permanent magnets are also thermally protected, as the coolant flushes all the rotor surfaces. However, oil cooling does have drawbacks, such as oil drag force and oil friction losses, especially at high speeds. The oil friction losses P_{friction} can be defined by

$$P_{\text{friction}} = F_{\text{drag}} \cdot r \cdot \Omega \tag{5.1}$$

where oil drag force F_{drag} is calculated based on Petroff's law from Eq.5.2 (Dukkipati, 2007; Stachowiak and Batchelor, 2005).

$$F_{\text{drag}} = \frac{\mu_{\text{oil}} \cdot s_{\text{r}} \cdot 2 \cdot \pi \cdot r \cdot \Omega}{l_{\text{ag}}} \tag{5.2}$$

where r is the radius measured from the rotor axis to the centre of the gap between the stator and the rotor, Ω is the mechanical angular velocity, μ_{oil} is the dynamic viscosity of the oil, s_{r} is the area of the rotor wetted surface and l_{ag} is the length of the gap between the stator and the rotor. The oil drag force in the machine under study is thoroughly discussed in Ponomarev's doctoral thesis (2013). For the specific machine at hand, based on Eq. (5.2), the friction torque is 3.64 N·m at 500 rpm and 11 N·m at 1500 rpm when the oil temperature is 40ºC. However, such high friction torque is required at the machine start; furthermore, the oil will be heated by the friction losses and the friction torque will subsequently decrease.

In order to decrease the friction losses in the air gap, the height of the gap is increased and the stack length of the machine is minimized, which requires the usage of expensive permanent magnets with high remanence. The friction losses in the gap between the rotor and the stator are presented in Fig. 5.3 for different speed ranges and different oil temperatures. The decrease of the oil viscosity due to friction losses is not taken into account in Fig. 5.3.

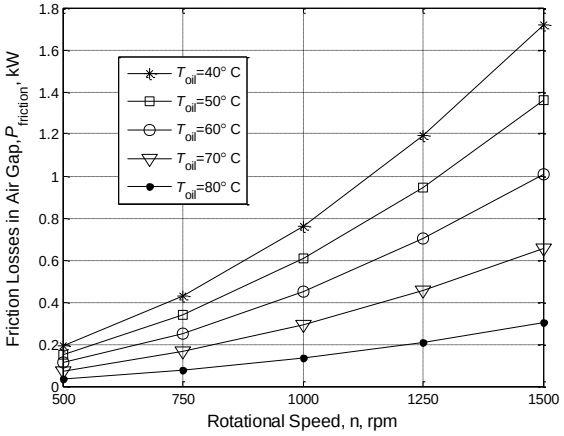

Figure 5.3: Friction losses in the gap between rotor and stator.

It is obvious that high speeds are dangerous for electrical machines with immersion liquid cooling because of the resulting high friction losses. However, oil immersion cooling is useful in low-speed electrical machines with high torque density.

5.2 Thermal analysis of the oil-immersed motor

The 3D thermal model of the machine geometry and mesh is created using Gambit software. The slice (representing 1/36th) of the machine is selected for modelling to reduce computation efforts. The mesh constructed contains 75 500 nodes, 880 000 faces and 350 000 cells. The 3D machine model includes the stator yoke, slot winding, end windings, wedge and rotor yokes (upper and lower parts, with a magnet incorporated in between them) (Fig.5.4). The machine model in question is calculated by using the energy and κ-ω SST modes of ANSYS multiphysical software (Fluent 14.5). The κ-ω SST turbulence model was applied because it can handle a wide range of *y plus* values (assuming some error), and the model equations behave appropriately in both the near-wall and far-field zones. The default values of Fluent model constants were used. The rotation for the rotor surface is included. The *y plus* value is below 6 for the oil flow near the stator and rotor surfaces.

Table 5.3. Losses in the motor.

Heat Source Position	at 100% load
Stator Copper Windings	1750 W
Stator Core	100 W
Rotor Core	150 W
Permanent Magnets	100 W
Friction Losses	100 W

5.2.1 Thermal analysis based on Computational Fluid Dynamics

The 3D thermal model of the machine geometry and mesh is created in software Gambit. The slice (representing 1/36th) of the machine is selected for modelling to reduce computation efforts. The mesh constructed contains 75 500 nodes, 880 000 faces and 350 000 cells. The 3D machine model includes stator yoke, slot winding, end-windings, wedge and rotor yokes (upper and down parts) with magnet incorporated in between them (Fig.5.4). The machine model in question is calculated by using the energy and κ-ω SST modes of ANSYS multiphysical software (Fluent 14.5). The κ-ω SST turbulence model was applied, it handles wide range of y plus values assuming some error and the model equations behave appropriately in both the near-wall and far-field zones. The default values of Fluent models' constants were used. The rotation for the rotor surface is included. The constructed machine model has *y plus* = 6.5 for the walls of the stator in the air gap and all rotor walls and *y plus* = 4 for the stator walls in the end cap region.

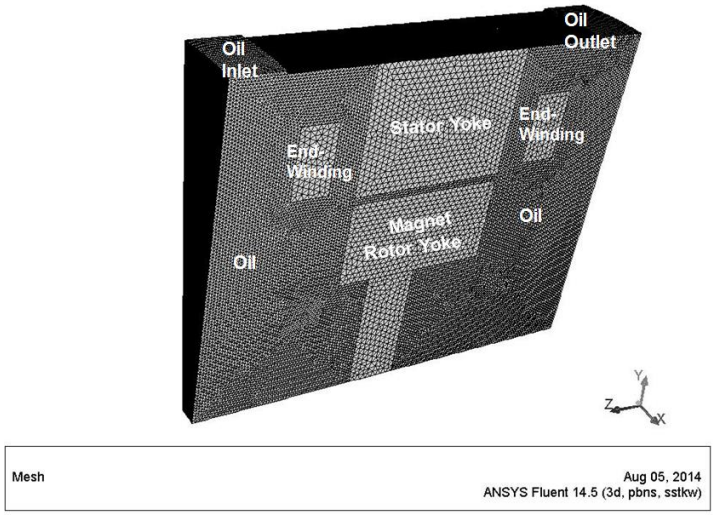

Figure 5.4: Mesh for the machine model.

Identifying the correct thermal conductivities of the materials constituting the machine parts is especially beneficial for ensuring proper thermal analysis. Table 5.4 lists the material properties (Mademlis et al., 2000; Ibtiouen et al., 2001; Product Technical Data,Valvoline). The thermal conductivity of the stator winding is defined by Eq. (2.1).

Table 5.4 Thermal conductivities of materials used in machine

Material of the Model Component	Thermal Conductivities, W/(K·m), Direction, cylinder coordinates		
	r(radial)	θ(tangential)	z(axial)
Iron	39	39	4.43
Stator Copper Winding in Slots	0.7	0.7	386
Stator Copper End-Winding	0.7	386	0.7
Permanent Magnets	9	9	9
Glass Fibre	0.43	0.43	0.43
Oil (50ºC)	0.185	0.185	0.185

In the machine modelling, conditions similar with the test are used. The cooling oil flow is set to 8 l/min to ensure an adequate temperature of the machine's critical parts. For the thermal model, the ohmic, core and magnet losses (Table 5.3) are taken into account. The thermal model includes the viscosity heating (friction losses). The surface roughness was assumed to be 25 μm for the stator windings and 5 μm for other surfaces. The heat flow through the outer frame (natural convection) is insignificant, but the convection coefficient 3.7 W/K·m^2 is assumed to be on the outer frame of the machine model (from Eqs. (2.2)-(2.5)). The effect of the glue thermal resistance for the permanent magnet attachment has been neglected, as its value, assuming 0.1 mm epoxy layer with the thermal conductivity of 1 W/(m·K), is 0.2 K/W. The Churchill and Chu

correlation applied for the Nusselt number calculation (Eq.2.3) is valid for this case, as the Rayleigh number of the air flow on the machine outer surface is $1 \cdot 10^8$. Heat was transported by the flowing oil entering the machine at 50 ˚C. The oil flow, forced through by the rotor rotation, becomes turbulent, thereby improving the heat transfer removal. Fig. 5.5(a) presents the oil velocity field and Fig. 5.5(b) displays the convection coefficients on the back surfaces of the machine parts.

(a)

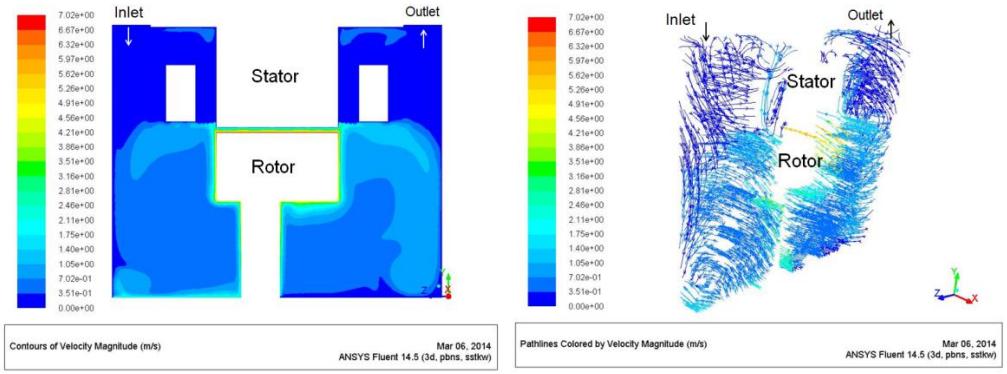

(b)

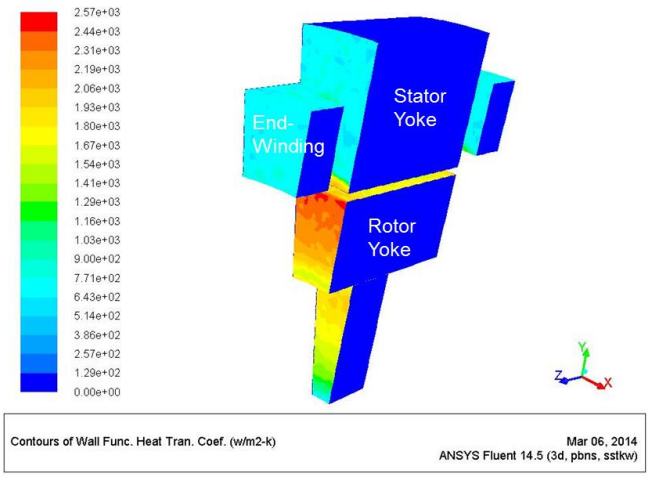

Figure 5.5: Oil velocity field inside the machine (a), and convection coefficients on the back surfaces of the machine (b).

As seen in Fig. 5.5 (b), the convection heat transfer coefficients are very high on the rotor surfaces (2000 W/(K·m^2)) because of the thermal properties of the oil and the speed of the rotor surface. The end sides of the stator have low convection heat transfer coefficients (600-700 W/(K·m^2)) compared with the rotor convection coefficients. The

synthetic oil has high viscosity, which results in a low propagation of turbulence vortices. The stator convection coefficients could be increased by raising the rotor rotational speed, but this in turn causes an increase of additional losses (friction losses) because of the significant oil viscosity. Fig. 5.6 presents the steady state distribution of temperature within the machine part (a) and in the cross-section of the machine model (b).

(a)

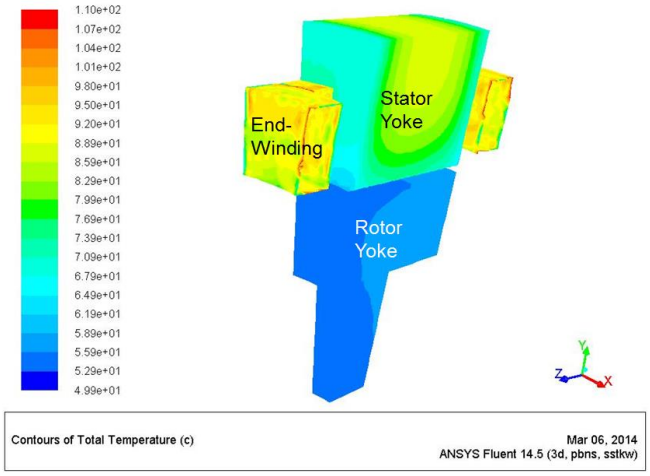

(b)

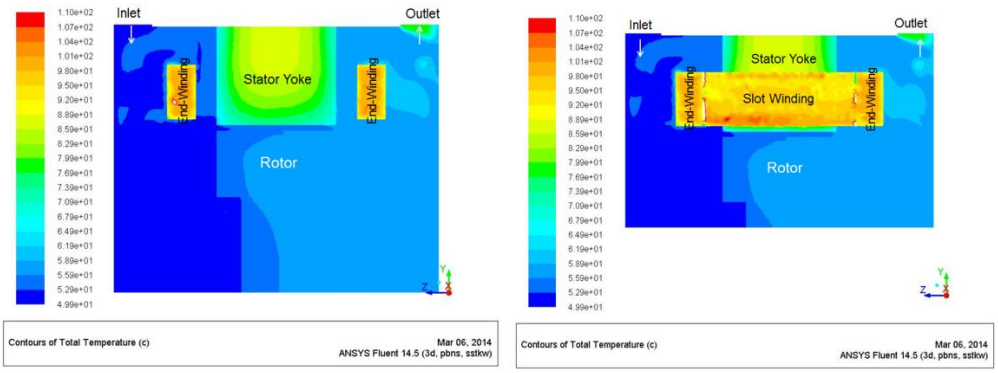

Figure 5.6: Temperature distribution on the machine outer surfaces (a), and temperatures in the machine cross-section (b).

The hottest spots (95-98 ˚C) are found within the stator slot winding and the end windings, in accordance with what is be expected in conditions of high copper losses, low thermal conductivity of the winding and insignificant convection coefficient. The high convection coefficient and low losses cause the low temperature of the rotor

(56-60 ˚C). The resulting temperature profile proves the high effectiveness of the designed cooling system.

5.2.2 Thermal analysis based on Lumped Parameter Thermal Network

Lumped parameter models of the machines are described and experimentally validated in many references (e.g., see Chapter 1 of this work); however, these models only give the average temperatures without discretization to show hotspot temperature. A lumped parameter thermal model of the machine is realized in order to define the temperature field and subsequently to compare with the temperature results obtained by the CFD thermal modelling. The equations in Appendix 2 are used for the calculation of the conduction and convection resistivity parameters as well as the utilization of those for the definition provided by Eq. (1.24)-(1.26) of the temperature rises in the machine parts. A steady-state lumped parameter thermal network with 8 power sources, 47 conduction and convection thermal resistances is shown in Fig. 5.7. The temperature distribution was simulated at steady-state, so the heat capacitances have not been applied. The symmetry makes it possible to divide the machine into elements that are concentric around the shaft.

A Matlab computer code was developed for the calculation of the machine thermal network (Fig. 5.7). The input parameters for the program are the dimensions, material properties, rotational speed, losses within the machine parts and coolant inlet specifications (Tables 5.1-5.4). The cooling matrix is used to model the coolant flow. Convection between the motor parts and oil is intensified by the rotation of the rotor and the working of the pump. The most complex task is the calculation of the convection coefficients in the end cap regions. The convection coefficients on the stator end-surfaces and the rotor end-surfaces are defined by Eqs. (5.3)–(5.6) (Incropera, 2007; Hilpert, 1933; Zukauskas, 1972). The following equations were used to define the convection in the end spaces of the stator yoke. The inlet oil flow rate (8 l/min) was used to assume oil velocity on the surface. Eq. (5.3) is valid for the oil flow over the cylinders ($Pr_{\mathrm{oil}} \geq 0.7$ and $4\,000 \leq Re_{\mathrm{D}} \leq 40\,000$). Eq. (5.5) is valid for the cylinders in the cross flow ($0.7 \leq Pr_{\mathrm{oil}} \leq 500$ and $1 \leq Re_{\mathrm{D}} \leq 1\,000\,000$). These correlations can be assumed valid, as the Reynolds numbers for the oil flow over the stator and the rotor are $5 \cdot 10^3$ and $2.42 \cdot 10^5$, respectively.

$$Nu_{\mathrm{endst/oil}} = 0.193 \cdot Re_{\mathrm{oilst}}^{0.618} \cdot Pr_{\mathrm{oil}}^{1/3} \tag{5.3}$$

$$Re_{\mathrm{oilst}} = \frac{\dot{V}_{\mathrm{oil}}}{\nu_{\mathrm{oil}} \cdot \pi \cdot l_{\mathrm{endcap}}} \tag{5.4}$$

$$Nu_{\mathrm{endr/oil}} = 0.076 \cdot Re_{\mathrm{oilr}}^{0.7} \cdot Pr_{\mathrm{oil}}^{0.36} \cdot \left(Pr_{\mathrm{oil}} / Pr_{\mathrm{oilr}} \right)^{1/4} \tag{5.5}$$

$$Re_{\mathrm{oilr}} = \frac{D_{\mathrm{r}} \cdot \upsilon_{\mathrm{r}}}{\nu_{\mathrm{oil}}} \tag{5.6}$$

where $Nu_{\mathrm{endst/oil}}$ is the convective heat transfer coefficient between the stator end surfaces and oil, Re_{oilst} and Re_{oilr} are the Reynolds numbers of the oil in the endcap regions of the stator and the rotor, Pr_{oil} is the Prandl number of the oil in the end cap region, Pr_{oilr} is the Prandl number of the oil at the rotor surface, D_{r} is the rotor diameter, $\dot{V}_{\mathrm{oil}}$ is the volumetric oil flow rate at m^3/s, r_{induct} is the inlet duct radius and ν_{oil} is the kinematic viscosity of the oil.

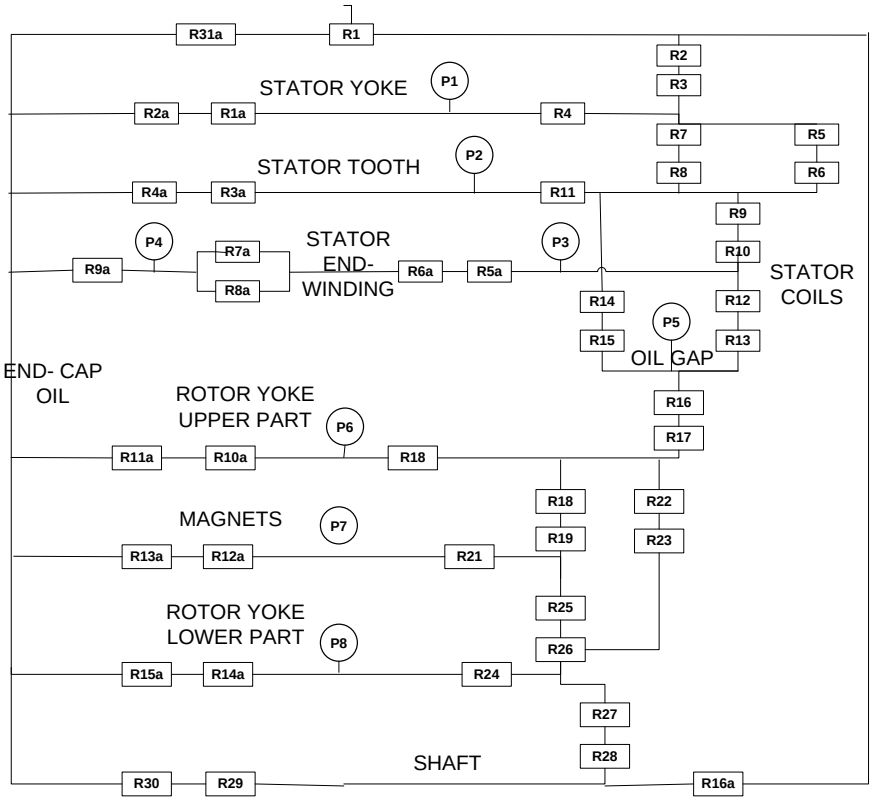

Figure 5.7: LPTN model of the oil-immersed motor (in steady-state without heat capacities).

Table 5.5 lists the temperature resulting from the LPTN and CFD thermal analyses. The temperature results obtained by LPTN agree with those obtained by the CFD motor thermal analysis, with differences ranging from 4-10 K. The greatest temperature differences are found in the stator iron and the rotor iron, and are caused by the uncertainty of the oil velocities in the end cap regions of the rotor and the stator (Eq. (5.2), (5.4)). In the LPTN analysis, it was assumed that half of the oil flow goes through the back surface of the stator, and the total oil flow goes through the back

surface of the rotor. However, the oil velocity distributions in the end cap region (Fig. 5.3 (a)) show that oil velocities are low on the back surfaces of the rotor and the stator, and that is why the stator iron and the rotor iron are hotter in the CFD thermal analysis than in the LPTN analysis. The temperature of the rotor and stator iron can be reduced by the placement of the inlet and outlet ducts near the stator.

Table 5.5 Temperatures of machine parts

Machine Part	Average Temperature (hot-spot)	
	LPTN	CFD
Copper Winding	102˚C	97˚C (100˚C)
Copper End-Winding	100˚C	95˚C (98˚C)
Stator Iron	70˚C	80˚C (85˚C)
Rotor Iron	52˚C	59˚C
Permanent Magnets	52˚C	59˚C
Oil in End-Region/Oil in Air Gap	53˚C/53˚C	52-59˚C

5.3 Experimental work

All computational considerations were verified by experimental measurements on the machine prototype. The machine prototype was tested at 66 A phase current. The heat input was measured indirectly through the voltage and current. The experimental scheme of the liquid cooling circuit is illustrated in Fig. 5.8.

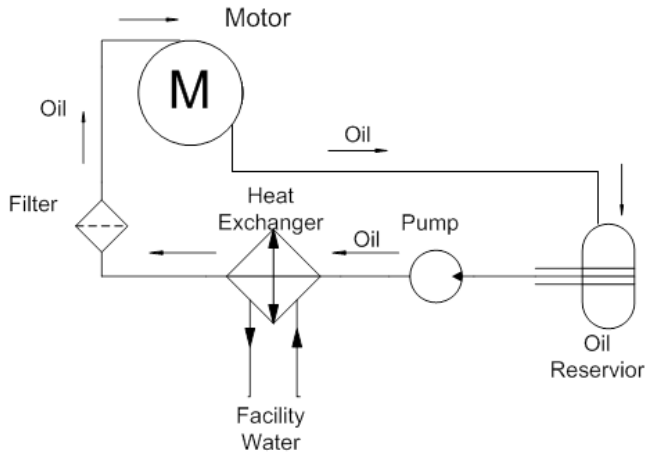

Figure 5.8: Experimental cooling scheme used for the machine tests.

The oil flow was set to 8 l/min for the machine under study. Three thermocouples (Pt-100 (class B) with an error margin of ± 0.3 ºC at 0 ºC (DIN 43760)) were glued between the winding and the stator yoke in different coils in order to measure the average temperatures. The measurements were carried out with the inlet temperature of

the oil at 50˚C and the flow rate at 0.1154 kg/s. The outlet temperature of the oil was up to 55˚C. The centrifugal pump was used to force the coolant from a tank into the tested machine through the cooler, forming a closed loop circuit. A flow meter measured the volume flow rate of oil through the cooling circuit to control its constant value. The thermocouples were connected to a recording device to monitor the temperature more accurately.

The measured temperatures stabilized in half an hour, and the average temperature value was 90 ˚C in the region between the stator yoke and the winding. It is difficult to compare these temperatures with those resulting from the LPTN analysis, as it gives the temperature of the stator yoke and the slot winding as 70 ˚C and 102 ˚C, respectively. From the CFD thermal analysis, the temperature in the region between the stator yoke and the winding is 88-93 ˚C. Thus, the experimental temperature value has a minor discrepancy (2-3 K) with the estimated temperature values from CFD thermal analysis. The discrepancy between the measured and simulated temperatures can be attributed to such factors as wrong modelling assumptions and instrumental error (± 0.3 ºC at 0 ºC). The modelling of the electrical machine part contains many assumptions, such as the unstructured mesh and the applied turbulence model in CFD thermal modelling and the analytical equation for the convection definition in the LPTN modelling. The measured temperatures are local, while LPTN analysis allows for defining the average temperature of the body, and thermal analysis based on CFD thermal analysis provides the temperature distribution with differences of up to 10˚C in the region in question.

5.4 Conclusions

This chapter has addressed the development of thermal analyses of a permanent magnet synchronous electrical motor with direct-immersion oil cooling. The key advantage of this cooling method is the possibility for high convection coefficients in the endcap region (up to 700 W/m^2·K for the stator and up to 2000 W/m^2·K for the rotor) and in the gap between stator and rotor (up to 2000 W/m^2·K). In this way, the cooling system ensures an efficient removal of heat losses and adequate temperatures in the machine studied. The machine may even be heavily overloaded due to its extremely efficient direct cooling and can – at lower than the rated speed – provide torque up to 5 times the nominal over long periods of time, if the coolant flow is increased.

The temperature results for the machine parts were obtained using two different thermal design methods: CFD thermal, the computational method; and LPTN, the analytical method. CFD thermal design is useful for cases of fluid flow inside a machine, as it allows for obtaining the temperature distribution within the machine without the need for the definition of the convection heat transfer coefficient in the air gap and yoke surfaces rendered by empirical equations. The temperature between the stator yoke and the winding was measured from the machine prototype tested at 100% load. The calculated and measured temperatures show good agreement. For the PMSM, in conditions of an 8 l/min oil flow with an inlet oil temperature of 50 ˚C, the stator

winding temperature was kept below 120 ˚C and the magnet temperature below 60 ˚C, with 2.2 kW heat losses. Thus, direct-immersion oil cooling can indeed be used for high heat flux removal capability in electrical machines with high torque density.

6 Conclusions and discussion

In this doctoral thesis, several direct and indirect liquid cooling solutions have been presented and analysed. The work describes both the design of these cooling systems and the thermal analyses of various high-torque-density permanent magnet electrical machines incorporating direct or indirect liquid cooling. The most important aspects of liquid cooling systems have been summarized herein.

In low-speed permanent magnet electrical machine design, progress made towards higher power, smaller dimensions and lower mass has created the problem of how to remove the heat losses in high-torque-density machines. Such machines are required for off-road working vehicles and offshore wind turbines, for example. In the case of high-torque-density electrical machines with short overloads, the most basic air-cooling solutions for thermal management require a great deal of physical space (for high-power fans, heat sinks, etc.), and that is why liquid cooling solutions are required. The temperature sensitive components of permanent magnet electrical machines, such as permanent magnets and insulation, may fail or lose their operation properties at high temperatures. Therefore, over-temperatures can result in a short lifetime and low reliability for a machine. Indirect and direct liquid cooling solutions allow for improving the thermal performance by providing high heat transfer rates and by eliminating noise and the large space needed for powerful air cooling systems. However, the application of a liquid cooling system translates into the necessity for taking maintenance precautions for safe machine operation.

6.1 Summary of the results of this doctoral thesis

The overall objective of this thesis was two-fold: 1) to design direct and indirect liquid cooling systems for tooth-coil permanent magnet electrical machines, and 2) to create and employ accurate thermal models for assessing the effectiveness of the thermal performance of these applied cooling systems. CFD thermal modelling of the heat transfer inside the machines and reliable LPTN simulations were both applied.

In the introduction to the work, the basics of heat transfer, performance of cooling solutions in electrical machines and literature survey on thermal design methods were presented. It was also demonstrated that the liquid cooling system design should include such aspects as temperature, liquid content and corrosion control to provide the best possible performance and reliability and thereby avoid shutdown of the whole system.

Indirect liquid cooling systems were studied based on a 100 kW axial flux permanent magnet synchronous machine and a 110 kW radial flux machine. For the axial flux PMSM, the effects of an added water jacket and high thermal conductance materials were studied. Copper bars were inserted in the teeth to conduct heat from them to the liquid jacket, and potting material was applied around the end winding to improve their heat transfer towards the water jacket. According to the test results, the stator winding

maximum temperature decreased by approximately 40 ˚C with the cooling scheme based on the added water jacket, potting material and copper bars as compared to that of the original cooling system design based only on the water jacket. An axial flux permanent magnet synchronous machine with two stators was constructed to analyse the different cooling schemes. The error between the calculated and the measured values for the stator winding was only about 2-5 ˚C, which validates the presented methodology of CFD thermal simulations of the fluid flow and heat transfer inside the machines. The discrepancy was caused by incorrect modelling of the end winding region, unstructured mesh and erroneous modelling assumptions (regarding thermal conductance and thermal contact resistance). The computational analysis showed that the rotor temperature decreased by approximately 28 ˚C with the cooling scheme based on the added water jacket, potting material and copper bars. The parametric study based on the applied thermal analysis demonstrated that the application of three copper bars per tooth results in a temperature drop of 4 ˚C in the stator slot compared with the design having just one copper bar per tooth. A rotor temperature drop of 5 ˚C can be obtained when the whole region (rather than half of the region) around the stator end winding is potted (in the design with the three copper bars). Therefore, the simulated and measured results presented herein validate the significant improvement of the cooling performance provided by the high conductance materials.

The cooling solution of the 110 kW radial flux machine was based on the use of a liquid jacket and a thermal bridge (potting material) placed in it in order to sink the generated losses from the end winding. The developed 3D CFD thermal model of the machine segment, the analytical model of the liquid jacket and the test results were used to design and analyse this indirect cooling system. The highly thermally conductive potting material conducted the generated heat from the end winding to the circulated liquid, thereby inducing a 6 K temperature drop in the stator winding and a 10 K temperature drop in the rotor embedded-permanent-magnets, based on the CFD thermal modelling. The parametric study related to the applied thermal analysis revealed that the total potting of the end winding region and the increase of the convection coefficient in the liquid jacket could provide a 2-3 ˚C temperature drop in the stator winding. In the machine prototype, two different potting materials (Ceramacast 675N with a thermal conductivity of 100 W/(m•K) and high temperature epoxy 2315 with a thermal conductivity of 58 W/(m•K)) were analysed. The potting material with the higher thermal conductivity could only provide a 2-3 ˚C lower temperature of the end winding region. The modelling results for the temperature distribution in the end winding region follow the trend in the experimental data quite well, with a 2-4 ˚C discrepancy in the slot winding mainly due to incorrect modelling assumptions (concerning thermal contact resistances).

A direct liquid cooling system of an 8 MW direct-drive permanent magnet synchronous generator with total heat losses of 610 kW was also designed. It was analysed with the creation and use of 1) CFD thermal simulations of the fluid flow and heat transfer inside the machines and 2) reliable LPTN simulations. It was shown that the liquid flow inside the stator copper winding provides efficient cooling in conditions of high concentrated

heat losses (530 kW), thereby avoiding the high temperature flux propagation towards the rotor permanent magnets. The design principles of the direct liquid cooling system for the copper winding with the inner stainless steel tubes were described in detail. In conditions of the demineralized water mass flow of 3.42 kg/s with an inlet temperature of 40 ˚C, the winding and the rotor magnet temperatures are kept below 80 ˚C and 50 ˚C, respectively. The reliability analysis of cooling circuit parts of the generator was used to show the advantage of liquid cooling for wind farm application. The analysis concluded that the cooling system for the designed generator has an average reliability of 0.96 over a 30 year design lifetime. The tests on the laboratory setup on the tooth coils (motorette) were focused on studying the feasibility of implementing effective thermal management with direct liquid cooling. The simulated temperatures were validated against the measured temperatures, with some discrepancy because of the simulation assumptions and the impossibility of avoiding environmental effects during testing.

The study on the comparison of Ethylene Glycol (Vol. 50 %) and Propylene Glycol (Vol. 50%) used as coolant agents for copper conductors with inner stainless steel tubes showed the deterioration of the cooling system performance compared to water cooling. However, if the wind turbine is situated in areas where temperatures drop below the freezing point of demineralized water, a mix of water and glycol should be considered to prevent the coolant from freezing. As a coolant, propylene glycol is more effective because of its superior thermal properties, but less due to bigger hydraulic losses resulting from its higher dynamic viscosity. Ethylene Glycol has worse corrosion-resistance properties, as the wear of the copper and stainless steel tube increases with its application.

Also analysed was direct-immersion oil cooling for a 26.6 kW tooth-coil permanent magnet synchronous machine with high torque density intended for off-highway, hybrid working vehicles. This unique cooling system provides good cooling capability without the extra cost of a separate cooling agent, as the oil circulating in the hybrid vehicle is also used for the motor cooling. The CFD thermal simulations of the fluid flow and heat transfer inside the machines and reliable LPTN simulations were created for analysing the PMSM. Based on this methodology, the stator winding temperature was kept below 102 ˚C and the magnet temperature below 60 ˚C, with 2.2 kW heat losses in conditions of an 8 l/min oil flow with an inlet temperature of 50 ˚C. It was shown that high rotational speeds cause a significant rise of friction losses inside the machine, especially in the air gap, so direct-immersion oil cooling should be applied in machines with low speed. This cooling solution was tested and verified on an actual machine prototype, and had a 2-3 ˚C discrepancy with the thermal modelling, mainly due to the computational assumptions.

6.2 Discussion of the results of this doctoral thesis

Thermally speaking, this thesis provides a new verification of thermal results based on CFD thermal simulations of the heat transfer inside the machines, LPTN simulations and experimental testing. The results presented herein demonstrate that indirect and direct liquid cooling systems are useful solutions for PMSMs with high torque density. The indirect liquid cooling system based on the liquid jacket alone is an effective cooling solution, but during short overloads, a high-torque-density PMSM is prone to over-temperatures in its temperature-sensitive parts (the stator winding and permanent magnets) due to the thermal resistance between the heat source and the coolant. High conductance materials, such as potting material and/or copper bars, are effective passive cooling solutions to reduce temperatures of the rotor and windings for machines with cooling systems based only on a liquid jacket. Direct liquid cooling of the stator winding is a useful cooling method for DD PMS wind generators. It reduces the machine dimensions and weight, thereby meeting market requirements concerning transportation and installation limits. Direct-immersion oil cooling is highly effective for low-speed PMSMs, as it may be used in high-torque-density machines which can safely withstand overloads. Of interest is that off-road working vehicle PMS machines could incorporate direct liquid cooling of the stator winding, as this would help prevent the high friction losses in the air gap at high speeds.

The modelling presented in this thesis was done using a general-purpose PC with a 2.5 GHz, two-core 64-bit processor and 12 GB of memory. The presented results were simulated used illustrated meshes, which are the finest possible at the utilized computer. To check the grid independence only coarser meshes were simulated, that shown that the temperature differences are insignificant (up to 1-2 ˚C) and the results can be assumed as grid independent. The four analysed cases show that the described methodology can yield accurate estimations of the local temperatures in the measured prototypes. The discrepancy between the simulated and the measured temperatures is up to 5 ˚C. It was mainly caused by the unstructured mesh, the simplified geometry, the computational assumptions and the measurement device error.

LPTN is a good thermal design tool, as it allows one to select an appropriate cooling solution and to calculate machine temperatures quickly. However, it is difficult to define the convection coefficients, especially in the end cap regions, when there is a unique geometry and cooling solution (e.g., in the DD PMSG with an outer rotor). It is difficult to predict the coolant flow distribution inside the machine (e.g., in the direct-immersion oil cooling of a PMSM), which is crucial for the convection coefficient definition and in turn, the temperature definition. Thus, CFD thermal analysis is preferable to LPTN and FEA, as it allows for simulating the temperature distribution within the rotor and stator in cases of unique machine design. CFD thermal design is also useful during the design process of the total machine, as it is significantly cheaper than performance of experiments on various machine prototypes. This tool was especially useful for the thermal modelling of the PMSM with the cooling system based on the liquid jacket and the high conductance materials, as it is possible to create a machine slice and assess the

effect of the coolant solution on the stator and rotor temperatures. However, it is difficult to take into account all the constructional elements and create the whole machine model with a good mesh because of the limited computational resources. What helps to increase overall system effectiveness during the design process and to prevent the waste of cooling energy during machine operation are the following three considerations: 1) accurate design of the cooling system geometry (including the geometry of the ducts in the liquid jacket, the placement of the inlet and outlet ducts, the dimensions of the stainless steel tubes in the direct liquid cooling systems, etc.), 2) proper coolant types and 3) operational characteristics of the liquid cooling system.

6.3 Suggestions for future works

The rapid growth of high torque and power density electrical machines affects mechanical structures, cooling capacities and cooling technologies. If only traditional cooling devices are used with high-power units, the mechanical sizes and power required for cooling will increase sharply. Therefore, innovative methods for cooling should be researched for future applications. For example, a combination of traditional and two-phase cooling methods offers promising potential for future solutions.

Effective cooling is one of the main ways in which increased power generation in modern electrical machines may be sustained, so future studies should deal more with examining the effects of various fluids and solid materials. Using the thermal modelling approach of LPTN, FEM and CFD analyses, optimization of electrical machine geometry can be achieved to provide better heat evacuation capabilities (through applications of fins, flow direction elements etc.). CFD thermal modelling can be useful in the thermal analysis of high-speed machines, where temperature distribution is critical, particularly in the case of the rotor.

The following topics should be studied in future works:

- The application of a two-phase cooling solution for high-torque-density electrical machines used in special applications (e.g., military, airspace and sports)
- The effects of machine geometry on conditions of direct-immersion oil cooling (including possibilities for avoiding friction losses via use of a separator in the air gap)
- Development of a cooling solution for high temperature superconductor (HTS) electrical machines

7 References

Abrahamsen, A.B., Mijatovic, N., Seiler, E., Zirngibl, T., Traholt, C., Norgard, P.B., Pedersen, N.F., Andersen N.H., Ostergrad, J. (2010). Superconducting wind turbine generators. In *Superconductor Science and Technology*, vol. 23, pp.1-8.

Alexandrova, J., Semken, S., Polikarpova, M., Pyrhönen, J. (2012). Defining proper initial geometry of an 8 MW liquid-cooled direct-drive permanent magnet synchronous generator for wind turbine applications based on minimizing mass. *International Conference on Electrical machines*, pp.1250-1255.

Alexandrova J. (2014). *Wind Turbine Direct-Drive Permanent Magnet Generator with Direct Liquid Cooling for Mass Reduction*. Doctoral Thesis, Acta Universitatis Lappeenrantaensis, Finland.

Ansys 14.5 Theory Guide. [Retrieved 2014], url:http://www.arc.vt.edu

Ansys 14.5.Review Course. [Retrieved 2014], url: https://www.scribd.com/doc/138960383/Fluent-Intro-14-5-L13-ReviewCourse

Azizi, D., Gholami, A. and Abbasi, V. (2009). Selection the optimum cooling scheme for generators based on the electro-thermal analysis. In *International Journal of Electrical and Electronics Engineering*, vol. 3, pp.408-413.

Ball, K.S., Farouk, B., Dixit, V.C. (1989). An Experimental Study of Heat Transfer in a Vertical Annulus with a Rotating Cylinder. *International Journal of Heat and Mass Transfer*, 32, pp.1517-1527.

Bang, D., Under, H.P., Shrestha, G. and Ferreira, J. (2008). Promising direct-drive generator system for large wind turbines. In *Wind Power to the Grid Seminar (EPE-WECS)*, pp.1-10.

Becker, K.M. (1963). Measurement of convective heat transfer from a horizontal cylinder rotating in a tank of water. *International Journal Heat Mass Transfer*, 6, pp.1053-1062.

Bellettre, J., Sartre, V., Biais, F. and Lallemand, A. (1997). Transient state study of electric motor heating and phase change solid-liquid cooling. In *Wind Power to the Grid Seminar (EPE-WECS)*, pp.1-10.

Bennion, K. (2011). *Electric motor thermal management*. National Renewable Energy Laboratory.

Brauer, H.J. and De Doncker, R.W. (2011). Thermal modeling of a high-speed switched reluctance machine with axial air-gap flow for vacuum cleaners. In *Proceedings of Conference on Power Electronics and Applications*, pp. 1-10.

Bruetsch, R., Tari, M., Froehlich, K., Weiers, T. and Vogelsang, R. (2008). Insulation failure mechanisms of power generators. *IEEE Electrical Insulation Mechanism*, 24 (4), pp.17-25.

Boglietti, A. and Cavagnino, A. (2007). Analysis of the end-winding cooling effects in TEFC induction motors. In *IEEE Transactions on Industry Applications*, 43 (5), pp.1214-1222.

Borges, S.S., Cezario, C.A. and Kunz, T.T. (2008). Design of water cooled electric motors using CFD and thermography techniques. *International Conference on Electrical Machines*, pp.1-6.

Borges, S.S. and Cezario, C.A. (2012). CFD and thermography techniques applied in cooling systems designs. *Applied Computational Fluid Dynamics*, pp.135-154.

Cadwallade, L.C. (1998). *Selected component failure rate values from fusion safety assessment tasks*. Idaho National Engineering and Environmental Laboratory, USA, pp.3-62.

Campbell, J.B., Tolbert, L.M. and Ayers, C.W. (2007). Two-phase cooling method using the R134a refrigerant to cool power electronic devices. In *IEEE Transactions on Industry Applications*, 43 (3), pp.648-656.

Camilleri, R. and McCulloch, M.D. (2013). Investigating mechanisms for an evaporative cooled in-wheel AFPM machine. *13th UK Heat Transfer Conference*, pp.144-1-144-10.

Caricchi, F., Crescimbini, F., Di Napoli, A. and Marcheggiani, M. (1996). Prototype of electric vehicle drive with twin water-cooled wheel direct drive motors. *27th Annual IEEE Power Electronics Specialists Conference*, pp.1926-1932.

Cassat, A., Espanet, C. and Wavre, N. (2002). BLDC motor stator and rotor iron losses and thermal behavior based on lumped schemes and 3D FEM analysis. In *Conference Record of the Industry Applications Conference*, (4), pp.2469-2476.

Catalogue of Heat Pipes. *High-performance thermal solutions heat-pipes & engineering systems for power electronics*. [Retrieved 2010], url: www.heat-pipes.com.

Catalogue of Cooling Equipment. *Cooling equipment for electronics*. Electro Impulse. [Retrieved 2000], url: www.electro-impulse.com.

Chin, Y.K. and Staton, D.A. (2004). Transient thermal analysis using both lumped-circuit approach and finite element method of a permanent magnet traction motor. *AFRICON*, 2, pp.1027-1035.

Chu, R.C. (1999). A review of IBM sponsored research and development projects for computer cooling. *15th IEEE SEMI-THERM Symposium*, pp.151-165.

Cengel, Y.A. (2007). *Heat Transfer and Mass Transfer*: *A Practical Approach*. NY: McGraw Hill, pp.23-841.

Centner, A.P. and Costa, A.F. (2012). Coupled fluid-thermal network modeling approach for electrical machines. *International Conference on Electrical Machines*, pp.1236-1239.

Costa-Patry, E. (2011). *Cooling high heat flux micro-electronic systems using refrigerants in high aspect ratio multi-microchannel evaporators*. Doctoral Thesis n 5225, EPFL, Switzerland.

Crescimbini, F., Di Napoli, A., Solero, L. and Caricchi, F. (2003). Compact permanent-magnet generator for hybrid vehicle applications. In *Conference Record of the Industry Application Conference*, 1, pp.576-583.

Dajaku, G. and Gerling, D. (2006). An improved lumped parameter thermal model for electrical machines. *17th International Conference on Electrical Machines*, pp.1-6.

Ball, K.S., Farouk, B., Dixit, V.C. (1989). An experimental study of heat transfer in a vertical annulus with a rotating cylinder. *Int.J.Heat Mass Transfer*, 32, pp.1517-1527.

De Vries, E. (2012). *Enercon E-126 7.5 MW still world's biggest*. [Retrieved 2012], url: www. windpowermonthly.com.

Di Gerlando, A. and Vistoli, I. (1993). Improved thermal modeling of induction motors for design purposes. *6th International Conference on Electrical Machines and Drives*, pp.381-386.

Dortwegt, R. and Maughan, E.V. (2001). The chemistry of copper in water and related studies planned at the advanced photon source. In *Proceedings of Particle Accelerator Conference*, pp.1456-1458.

Dukkipate, R. (2007). *Mechanism and machine theory*. New Age International (P) Limited.

Durst, F. and Karthik, T.S.D. (2011). Turbulence models and their applications. In *10th Indo Germal Winter Academy*.

Elkins, C.G. (1997). *Heat transfer in the rotating disk boundary layer*. Doctoral Thesis, Stanford University.

EL-Refaie, A.M., Harris, N.C., Jahns, T.M. and Rahman, K.M. (2004). Thermal analysis of multibarrier interior PM synchronous machine using lumped parameter model. In *IEEE Transactions on Energy Conversion*, 19 (2), pp.303-309.

Erceg, I., Sumina, D. and Vrazic, M. (2012). Modification of synchronous generator cooling system control. *International Conference on Electrical Machines*, pp.370-375.

Fan, J., Zhang, C., Wang, Z., Dong, Y., Nino, C.E., Tariq, A.R. and Strangas, E.G. (2010). Thermal analysis of permanent magnet motor for the electric vehicle application considering driving duty cycle. In *IEEE Transactions on Magnetics*, 46 (6), pp.2493-2496.

Farnia, D.K. and Hattori, T. (2006). Electromagnetic and thermal modeling of a permanent magnet synchronous machine with either a laminated or SMC stator. *JMAG Users Conference*, pp.1-32.

Fasquelle, A., Le Besnerais, J., Harmand, S., Hecquet, M., Brisset, S., Brochet and P., Randria, A. (2006). Coupled electromagnetic acoustic and thermal-flow modeling of an induction motor of railway traction. In *Applied Thermal Engineering*, 30, pp.2788-2795.

Fenot, M., Dorignac, E., Giret, A. and Lalizel, G. (2013). Convective heat transfer in the entry region of an annual channel with slotted rotating inner cylinder. *Applied Thermal Engineering*, 54, pp.345-358.

Ferreira, A.P. and Costa, A.F. (2012). Thermal analysis of an axial flux permanent magnet machine. *International Conference on Electrical Machines*, pp.1480-1485.

Fishenden, M. and Saunders, O.A. (1950). *An introduction to heat transfer*. Oxford, UK.

Fodorean, D. and Miraoui, A. (2008). Permanent magnets thermal operation limits in a hybrid rxcited synchronous machine used on wide speed applications. *International Conference on Optimization Of Electrical and Electronic Equipment*, pp.21-26.

Fraas, A.P. (1989). *Heat exchanger design*. John Wiley & Sons, England.

Funieru, B. and Binder, A. (2008). Thermal design of a permanent magnet motor used for gearless railway traction. *Annual Conference of Industrial Electronics*, 4, pp.2061-2066.

Galea, M., Gerada, C., Raminosoa, T., Wheeler, P. (2000). A thermal improvement technique for the phase windings of electrical machines. In *IEEE Transactions on Industry Applications* 48 (1), pp.79-87.

Gazley, C. (1958). Heat transfer characteristics of rotating and axial flow between concentric cylinders. *Transactions ASME*, pp.79-89.

Gerlando, A. and Vistoli, I. (2000). Improved thermal modeling of induction motors for design purposes. In *IEEE Transactions on Energy Conversion*, 15 (2), pp.135-142.

Gibney, J.J. (1994). *Technical Letter: GE Generators – An Overview*. GE Power Systems, USA.

Gieras J.F., Wang, R.-J. and Kamper M.J. (2008). *Axial flux permanent magnet brushless machines*. Springer, pp. 251-280.

Gnielinski, V. (1976), New equations for heat and mass transfer in turbulent pipe and channel flow. *Forschung in Engenieuwesen,* 41 (1), pp. 8-16.

Gray, R. F., Montgomery, L., Nelson, R., Pimpkin, J., Joki-Korpela, S. and Caguiat, F. (2006). Designing the cooling systems for the world's most powerful turbogenerator. In *IEEE Power Engineering Society General Meeting*.

Guemo, G. G., Chantrenne, P. and Jac, J. (2013). Application of classic and T lumped parameter thermal models for permanent magnet synchronous machines. *Electric Machines & Drives Conference*, pp.809-815.

Gutierrez-Alcaraz, J.M., De Hann, S.W.H. and Ferreira, J.A. (2010). Seawater based cold plate for power electronics. In *Conference Publications for Energy Conversion Congress and Exposition*, pp. 2985-2992.

Gosse, J. (1981). *Guide technique de thermique.* Dunod Paris, pp. 168-169.

Hafner, M., Schöning, M. and Hameyer, K. (2008). Automated sizing of permanent magnet synchronous machines with respect to electromagnetic and thermal aspects. In *Proceedings of the International Conference on Electrical Machines*, pp.1-6.

Hahn, B., Durstewitz, M. and Rohling, K. (2006). Reliability of wind turbine. Experiences of 15 years with 1500 WTs. *ISET*.

Hämäläinen, H. (2013). *Identification of some additional loss components in high-power low-voltage permanent magnet generators*. PhD thesis, Lappeenranta University of Technology, Finland.

Hey, J., Howey, D.A., Martinez-Botas, R. and Lamperth, M. (2011). Transient thermal modelling of an Axial Flux Permanent Magnet (AFPM) machine with model parameter optimization using a Monte Carlo method. *Vehicle Thermal Management Systems*, 10, Woodhead Publishing.

Hettegger, M., Reinbacher-Köstinger, A. and Biro, O. (2012). Characterizing the convection wall heat transfer on convoluted shapes in the end-region of an induction machine. *International Conference on Electrical Machines*, pp.1217-1224.

Hey, M., Reinbacher-Köstinger, A. and Biro, O. (2012). Characterizing the convection wall heat transfer on convoluted shapes in the end-region of an induction machine. *International Conference on Electrical Machines*, pp.1217-1224.

Hilpert, R. (1933). *Forsch. Geb. Ingenieurwes.* p. 205.

Hong, C. (2011). *Thermal modelling of the ventilation and cooling inside axial flux permanent magnet generators*. Doctoral Thesis, School of Engineering and Computer Science Durham University, UK.

Hoerber, J., Mueller, M., Franke, J., Ranft, F., Heinle, C., and Drummer, D. (2011). Assembly and interconnection technologies for MID based on thermally conductive plastics for heat dissipation. *34th International Spring Seminar on Electronics Technology*, USA.

Howes, J.C., Levett, D.B., Wilson, S.T., Marsala J. and Saums, D.L. (2008). Cooling of an IGBT drive system with vaporizable dielectric fluid (VDF). *24th IEEE SEMI-THERM Symposium*, USA.

Howey, D.A. (2010). *Thermal design of air-cooled axial flux permanent magnet machines*. Doctoral Thesis, Imperial College London, UK.

Howey, D.A., Childs, P.R.N. and Holmes, A.S. (2012). Air-gap convection in rotating electrical machines. In *IEEE Transactions on Industrial Electronics*, 59 (3), pp.1367-1375.

Huang, Z., Marquez, F., Alakula, M. and Yuan, J. (2012). Characterization and application of forced cooling channels for traction motors in HEVs. *International conference on electrical machines*, pp.1210-1216.

Hurst, N.W. and Ratcliffe, K. (1994). Development and applications of a structural audit technique for the assessment of safety management systems. *Hazards*, 12, p.315.

Ibrahim, M. and Pragasen, P. (2013). Core loss prediction in electrical machine laminations considering skin effect and minor hysteresis loops. In *IEEE Transactions on Industry Applications*, 49 (5), pp.2061-2068.

Ibtiouen, R., Nouali, N. and Benhaddadi, M. (2001). Application of lumped parameters and finite element methods to the thermal modeling of an induction motor. In *Proceedings of IEEE International Electronic Machines and Drives Conf*erence, pp. 505-507.

Incropera, F.P., Dewitt, D.P., Bergman, T.L. and Lavine, A.S. (2007). *Fundamentals of Heat and Mass Transfer*. 6th edition. USA, John Wiley & Sons, pp.320-440.

Irwanto, B., Steigleder, K., Perros, O. and Verrier, M. (2009). Large 60 Hz turbogenerators: mechanical design and improvements. *Electric Machines and Drives Conference*, pp.471-476.

Ivanova, M., Avenas, Y., Schaeffer, C., Dezond, J.B. and Schulz-Harder, J. (2006). Heat pipe integrated in direct bonded copper (DBC) technology for cooling of power electronics packaging. In *IEEE Transactions on Power Electronics*, 21 (6), pp.1541-1547.

Jiang, W. and Jahns, T.M. (2013). Development of efficient electromagnetic-thermal coupled model of electric machines based on Finite Element Analysis. *Electric Machines and Drives Conference*.

Kader, B. (1981). Temperature and concentration profiles in fully turbulent boundary layers. *Int. J. Heat Mass Transfer*, vol.24 (9), pp. 1541-1544.

Kadry, S. (2008). Corrosion analysis of stainless steel. *European Journal of Scientific Research*, vol.4, pp. 508-516.

Kamiev, K. (2013). *Design and testing of an armature-reaction-compensated permanent magnet synchronous generator for island operation*. Doctoral Thesis, Acta Universitatis Lappeenrantaensis, Finland.

Kargar, A., Kianifar, A. and Mohammadiun, H. (2010). Two-dimensional heat conduction of direct cooling in the rotor of an electrical generator (numerical analysis). *World Academy of Science, Engineering and Technology*, 43, pp.716-721.

Kim, Y., Joshi, Y., Fedorov, A., Lee, Y.-J. and Lim, S.-K. (2010). Thermal characterization of interlayer microfluidic cooling of three-dimensional integrated circuits with nonuniform heat flux. *Heat Transfer*, 132, pp.1-9.

King, J.K., Kobuck, R.M. and Repp, J.R. (2008). High speed water-cooled permanent magnet motor for pulse alternator-based pulse power systems. *14th Symposium on Electromagnetic Launch Technology*, pp.1-6.

Kolondzovski, Z. (2010). *Thermal and mechanical analysis of high-speed permanent-magnet electrical machines*. Doctoral Thesis, Aalto University, Finland.

Kral, C., Haumer, A. and Bäuml, T. (2008). Thermal model and behavior of a totally-enclosed-water-cooled squirrel-cage induction machine for traction applications. *IEEE Transaction on Industrial Electronics*, 55 (10), pp.3555-3565.

Kuosa, M. (2002). *Numerical and experimental modelling of gas flow and heat transfer in the air gap of an electric machine*. Doctoral Thesis, Lappeenranta University of Technology, Finland.

Kuosa, M., Sallinen, P. and Larjola, J. (2004). Numerical and experimental modelling of gas flow and heat transfer in the air gap of an electrical machine. *Journal Of Thermal Science*, 13 (3), pp.48-55.

Kylander, G. (2005). *Thermal modelling of small cage induction motors*. Doctoral Thesis, School of Electrical and Computer Engineering, Chalmers University of Technology, Sweden.

Kowal, D., Sergeant, P., Dupre, L. and Vandenbossche, L. (2013). The effect of the electrical steel properties on the temperature distribution in direct-drive PM synchronous generators for 5 MW wind turbines. *IEEE Transaction on Magnetics*, 49 (10), pp.5371-5377.

Launder, B.E., Reece, G.J., and Rodi, W. (1975). Progress in development of a Reynolds-Stress turbulent closure. *Journal of Fluid Mechanics*, 68 (3), pp.537-566.

Larin, B.M., Larin, A.B., Korotkov, A.N. and Opari, M.Y. (2011). Water chemistry of the system for cooling the electrical generator stator of the power unit at a thermal power station. *Thermal Engineering*, 58 (7), pp.552-555.

Lees, F.P. (1996). *Loss prevention in the process industries*. Elssevier, UK.

Lewis, C., Muller, J. (2007). A direct drive wind turbine HTS generator. In *IEEE Power Engineering Society General Meeting*, pp.1-8.

Li, J., Liu, Z. and Fu, J. (2010). Research on temperature field of turbogenerators on hollow strands blocked. In *IEEE International Conference on Computer Science and Information Technology*, pp.513-517.

Lim, C.H., Airoldi, G., Bumby, J.R., Dominy, R.G., Ingram, G.J., Mahkamov, K., Brown, N.L., Mebarki, A. and Shanel, M. (2010). Experimental and CFD investigation of a lumped parameter thermal model of a single-sided, slotted axial flux generator. *International Journal of Thermal Science* , 49, pp.1732-1741.

Lim, D.H. and Kim, S.C. (2013). Thermal performance of oil spray cooling system for in-wheel motor in electric vehicles. *Applied Thermal Engineering*, 10, pp.1-11.

Lindström, J. (1999). *Thermal model of a permanent–magnet motor for a hybrid electric vehicle*. Technical Report, Chalmers University of Technology, Sweden.

Lugo, R., Fournaison, L., Chourot, J.-M. and Guilpart, J. (2001). An excess function method to model the thermophysical properties of one-phase secondary refrigerants. *International Journal of Refrigeration*, 25, pp. 916-923.

Luke, G.F (1923). The cooling of electrical machines. *Transactions AIEE*, pp. 1278-1288.

Mademlis, C., Margaris, N. and Xypteras J. (2000). Magnetic and thermal performance of a synchronous motor under loss minimization control. *IEEE Transaction on Energy Conversion*, 15 (2).

Magnussen, F. and Sadarangani C. (2003). Winding factors and joule losses of permanent magnet machines with concentrated windings. *IEEE International Electric Machines and Drives Conference*, 1, pp.333-339.

Marignetti, F., Colli, V.D. and Coia, Y. (2008). Design of axial flux PM synchronous machines through 3D coupled electromagnetic thermal and fluid-dynamical finite-element analysis. *IEEE Transactions on Industrial Electronics*, 55 (10), pp.3591-3601.

Marcinichen, J., Olivier, J. and Thome, J. (2011). Reasons to use two-phase refrigerant cooling. *Electronics Cooling Magazine*, pp. 22-27.

Maxwell, J. (1954). *A Treatise on Electrical and Magnetism*. 3rd ed., Dover, New York.

Mc Adams, W.H. (1961). *Transmission de la chaleur*. Dunod Paris.

Melfi, M.J., Evon, S. and Mcelveen, R. (2009). Induction versus permanent magnet motors. *IEEE Industry Applications Magazine*, November-December, pp.28-35.

Melinder, A. (2010). *Properties of secondary working fluids for indirect systems*. International Institute of Refrigeration (IIR), France.

Mellor, P.H., Roberts, D. and Turner, D.R. (1991). Lumped parameter thermal model for electrical machines of TEFC design. *IEE Proceedings on Electric Power Applications*, 138 (5), pp.205-218.

Menter, F.R. (1993). Zonal two equation k-w turbulence models for aerodynamic flows. *24th Fluid Dynamics Conference*.

Menter, F.R. (1994). Two-equation eddy-viscosity turbulence models for engineering applications. *AIAA Journal*, 32 (8), pp.1598-1605.

Menter, F.R., Kuntz, M. and Langtry, R. (2003). Ten years of industrial experience with the SST turbulence model. *Turbulence, Heat and Mass transfer*, 4.

Micallef, C., Pickering, S.J., Simmons, K.A. and Bradley, K.J. (2008). Improved cooling in the end region of a strip-wound totally enclosed fan-cooled induction electrical machine. In *IEEE Transactions on Industrial Electronics*, 55 (10), pp.3517-3524.

Michel, B. (2012). *State-of-art of computer cooling technologies*. IBM Zurich Research Laboratory.

Misc. (2003). *VDI-Wärmeatlas*. 9th ed., VDI, Ed..

Moradnia, P. and Nilsson, H. (2011). A parametric study of the air flow in an electric generator through stepwise geometry modifications. *ECCOMAS Thematic Conference*, pp.1-20.

Mori, Y. and Nakayami, W. (1967). Forced convective heat transfer in a straight pipe rotating about a parallel axis. *Int. J. Heat Mass Trans.*, 10, pp.1179-1194.

Nategh, S. (2013). Thermal analysis and management of high-performance electrical machines. Doctoral Thesis, KTH School of Electrical Engineering.

Neal, G.D., Kwon, O., and Lieu, D.K. (2000). Ceramic filled thermoplastic encapsulation as a design feature for a BLDC motor in a disk drive. *Asia-Pacific Magnetic Recording Conference*.

Negrea, M. and Rosu, M. (2001). Thermal analysis of a large permanent magnet synchronous motor for different permanent magnet rotor configurations. *IEEE International Electric Machine and Drives Conference*, pp.777-781.

Nerg, J., Rilla, M. and Pyrhönen, J. (2008). Thermal analysis of radial-flux electrical machines with a high power density. In *IEEE Transactions on Industrial Electronics*, 55, pp. 3543 – 3554.

Nishimura, Y., Oonota, M. and Momose, F., (2008). Thermal management technology for IGBT modules. *FUJI Electric Review*, 56 (2), pp. 79-84.

Odvarka, E., Brown, N.L., Mebarki, A., Shanel, M., Narayanan, S. and Ondrusek, C. (2010). Thermal modelling of water-cooled axial-flux permanent magnet machine. 5th *International Conference on Electonics, Machines and Drives*, UK, pp.1-5.

Ohadi, M. and Qi, J. (2004). Thermal management of harsh-environment electronics. *20th IEEE Semiconductor Thermal Measurement and Management Symposium*, pp. 231-240.

Oliver, J., Michalec, J., Zimmerli, B., Joho, R., Krick, N. and Huber, A. (2001). Generator winding design – Amos 3 with 25 years experience. In *IEEE Transactions on Energy Conversion*, 16 (1), pp.87-91.

Owen, J.M. (1989). An approximation solution for flow between a rotating and stationary disk. *ASME Journal of Turbomachinery,* 111 (4), pp.323-332.

Petrov, I., Polikarpova, M. and Pyrhönen, J., (2013). Rotor surface ferrite magnet synchronous machine for generator use in a hybrid application – electro-magnetic and thermal analysis. *IECON,* Austria.

Pickering, S.J., Lampard, D. and Shanel, M. (2002). Ventilation and heat transfer in a symmetrically ventilated salient pole synchronous machine. *International Conference on Power Electronics, Machines and Drives*, pp.462-467.

Polikarpova, M., Röyttä, P. and Pyrhönen, J. (2013). "Liquid Internal Cooling of High-Power Synchronous Permanent Magnet Generator Winding in Arctic Conditions", International Review of Mechanical Engineering (IREME), 7 (2), pp.301-307.

Ponomarev, P., Polikarpova, M., Heinikainen, O. and Pyrhönen, J. (2011). Design of integrated electro-hydraulic power unit for hybrid mobile working machines. *European Conference on Power Electronics and Applications*, UK.

Ponomarev, P. (2013). *Tooth-coil permanent magnet synchronous machine design for special applications*. Doctoral Thesis, Acta Universitatis Lappeenrantaensis, Finland.

Popiel, C.Z.O. and Boguslawski, L., (1975). Local heat-transfer coefficients on the rotating disk in still air. *International Journal Heat Mass Transfer,* 18, pp.167-170.

Product Technical Data (2001). *PEKASOL L*. KUHLSOLE GmbH, Germany. [Retrieved 2001], url: www.pekasol.de.

Product Technical Data (2008). *Low voltage water cooled motors*. ABB LV Motors. [Retrieved 2011], url: www.abb.com.

Product Technical Data (2011). *Neodymium-Iron-Boron magnets*. TDK. [Retrieved 2008], url: www.tdk.co.jp.

Product Technical Data (2001). *GLYKOSOL N*. KUHLSOLE GmbH, Germany. [Retrieved 2001], url: www.pekasol.de.

Product Technical Data (2011). *Thermophysical Properties of Brines*. M. Conde Engineering, Zurich, Switzerland.

Product Technical Data (2012). *ECOCUT HS*. FUCHS, Germany. [Retrieved 2012], url: fuchs-europe.de.

Product Technical Data (2012). *Liquid cooling for inductive and resistive components*. REO ELECTRONIK AG, Germany.

Product Technical Data (2008). *Safe handling and storage of Synfluid Polyalphaolefins (PAO)*. Chevron Phillips Chemical Company LLC. [Retrieved 2008], url: www.cpchem.com.

Product Technical Data. *Siemens hydrogen-cooled generators SGen-2000H series*. Siemens. [Retrieved 2008], url: energy.siemens.com.

Product Technical Data. *Ultramax HVLP46*. Valvoline. [Retrieved 2010], url: www.valvolineeurope.com.

Pyrhönen, J., Jokinen, T., Hrabovcova, V. (2008). *Design of rotating electrical machines*. John Wiley & Sons, Ltd.

Pyrhönen, J., Jokinen, T., Hrabovcova, V. (2014). *Design of rotating electrical machines*. second edition, John Wiley & Sons, Ltd.

Rahman, P., Caricchi, F. and Crescimbini, F., (2004). Application of direct drive wheel motor for fuel cell electric and hybrid electric vehicle propulsion system. *Industry Application Annual Meeting*.

Ranchy, E., Malinowska, B. and Cassir, M. (1998). Design of de-ionized water cooling of power converters. *Power Electronic Specialists Conference*, pp. 1931-1936.

Rilla, M. (2012). *Design of salient pole PM synchronous machines for a vehicle traction application – analysis and implementation*. Doctoral Thesis, Acta Universitatis Lappeenrantaensis, Finland.

Saari, J. (2001). *Thermal analysis of high-speed induction machines*. Doctoral Thesis, Helsinki University of Technology, Finland.

Saums, D.L. (2009). Vaporizable dielectric fluid cooling of IGBT power semiconductors for vehicle power trains. *5th IEEE Vehicle Power and Propulsion Conference*, USA.

Saums, D.L. (2010). Vaporizable dielectric fluid cooling for IGBT power semiconductors. *International Conference on Integrated Power Electronic Systems*, pp.1-7.

Saums, D.L. (2011). Applications of vaporizable dielectric fluid cooling for IGBT power semiconductors. *IEEE SEMI-THERM Symposium*, pp. 253-264.

Saums, D.L. (2012). Liquid cooling systems for electronics thermal management. *IMAPS Chesapeake Symposium*, USA.

Saums, D.L. (2012). Classifying and understanding thermal interface materials for power LED applications. I*MAPS European Advanced Technology Workshop On Thermal Management and Micropackaging*, France.

Schrittwieser, M., Marn, A., Farnleitner, E. and Kastner, G. (2012). Numerical analysis of heat transfer and flow of stator duct models. *International Conference on Electrical Machines*, pp.383-388.

Schulz - Harder, J. (2009). Efficient cooling of power electronics. *International Conference on Power Electronics Systems and Applications*, pp.1-6.

Scowby, S.T., Dobson, R.T. and Kamper, M.J. (2004). Thermal modelling of an axial flux permanent magnet machine. *Applied Thermal Engineering*, 24, pp. 193-207.

Seghir-Oualil, S., Harmand, S. and Laloy, D. (2003). Study of the thermal behavior of a synchronous motor with permanent magnets. *International Journal of Engineering*, 3, pp.229-256.

Seghir-Ouali, S., Saury, D., Harmand, S., Phillipart, O. and Laloy, D. (2006). Convective heat transfer inside a rotating cylinder with axial air flow. *International Journal Thermal Science*, 45 (12), pp.1166-1178.

Semenov, D. (2014). *Computational studies for the design of process equipment with complex geometries*. Doctoral Thesis, Acta Universitatis Lappeenrantaensis, Finland.

Semken, S., Polikarpova, M., Röyttä, P., Alexandrova, J., and Pyrhönen, J. (2012). Direct-drive permanent magnet generator for high-power wind turbines – benefits and limiting factors. *IET Renewable Power Generation*, 6 (1), pp.1-8.

Service Catalog of Manifolds. *Lebentech*. [Retrieved 2010], url: www.lebentech.com.

Shanel, M., Pickering, S.J. and Lampard, D. (2003). Conjugate heat transfer analysis of a salient pole rotor in an air cooled synchronous generator. *International Conference on Electrical Machines and Drives*, 2, pp.737-741.

Sharar, D.L., Jankowski, N.R. and Morgan, B. (2010). *Review of two-phase electronics cooling for army vehicle applications*. Army Research Laboratory, US.

Shi, P. and Lo, K. L. (2009). Thermal effect of intermittent generation on conventional generator. *Proceedings of the 44th International Universities Power Engineering Conference*, UK, pp.1-5.

Shikun, C. (2000). *Electrical machine design*. Beijing: China Machine Press.

Shrestha, G., Polinder, H., Bang, D. and Ferreira, J. (2008). Review of energy conversion system for large wind turbines. *European Wind Energy Conference*.

Sikora, M., Vlach, R. and Navratil, P. (2011). The unusual water cooling applied on small asynchronous motor. In *Engineering Mechanics*, 18 (2), pp.143-153.

Simons, R.E. (1996). Direct liquid immersion cooling for high power density microelectronics. In *Electronics Cooling*, 1.

Skuriat, R. and Johnson, C.M., (2008). Direct substrate cooling of power electronics. *International Conference on Integrated Power Systems*, pp.1-5.

Smolders, L., Long, H., Feng, Y. and Tavner, P., (2010). Reliability analysis and prediction of wind turbine gearboxes. *European Wind Turbine Conference*.

Snieckus, D., (2013). Supersizing the turbine test bench. *Recharge*, 8, pp. 43-45.

Staton, D., Boglitti, A. and Cavagnino, A. (2005). Solving the more difficult aspects of electrical motor thermal analysis. *IEEE Transactions on Energy Conversion*, 20 (3), pp.620-628.

Stachowiak, G. and Batchelor, A. (2005). *Engineering Tribology*. 3rd ed. Burlington, UK: Elsevier Butterworth-Heinemann.

Svoboda, R. and Palmer, D.A. (2008). Behaviour of copper in generator stator cooling-water systems. *Symposium on Hydrothermal Geochemistry*, Germany.

Syrett, B. and Stein, J. (2001). Generator cooling system operating guidelines: cooling system maintenance and performance guidelines during startup, operation and shutdown. *EPRI*, Final Report, USA.

Tachibana, F. and Fukui, S. (1964). Convective heat transfer of the rotational and axial flow between two concentric cylinders. *Bulletin of JSME*, 7 (26), pp.385-391.

Technical Data Sheet (2014). *ABB Low voltage industrial performance motors*. [Retrieved 2014], url: www.abb.com

Technical Data Sheet (2011). *ACC Silicones*. [Retrieved 2011], url: www.acc-silicones.com.

Technical Data Sheet (2010). *AREMCO*. [Retrieved 2010], url: www.aremco.com.

Technical Data Sheet (2014). *High-performance thermal solutions heat pipe & engineering solutions for power electronics*. CRS Engineering. [Retrieved 2014], url: www.heat-pipes.com.

Technical Data Sheet (2012). *CR - customised solutions*. Grundfos. [Retrieved 2012], url: www.grundfos.com.

Technical Handbook (2011). *Raccorderie Metalliche*. Grundfos. [Retrieved 2011], url: www.racmet.com.

Technical Letter (2008). *90/10 copper-nickel vs. Type 316 stainless steel a functional comparison of two condenser tube alloys*. Fineweld Tube, USA.

Technical Letter (2009). *Ferritic/Duplex/Austenitic steel grades for condenser tubes*. Fisher Group, Germany.

Technical Letter (2012). *EATON*. [Retrieved 2012], url: www.lusanga.com.

Technical Report (2008). *ENEA*. [Retrieved 2008], url: www.frascati.enea.it.

Technical Report (2010). Failure rate and event data for use within land use planning risk assessments. *HSE, UK*.

Thompson, D.R., Gill, S., Louvar, T., Sathe, A. and Thompson, D. (2009). Vaporizable dielectric fluid cooling of IGBT power semiconductors for vehicle powertrains. *IEEE Vehicle Power and Propulsion Conference*.

Tomas, T. (2010). Ice-cold physics. *Sun & Wind Energy*, vol. 1.

Tong, W., Wu, S., An, Z., Dong, Y., Zhang, H. and Tang, R. (2010). Cooling system design and thermal analysis of multibrid permanent magnet wind generator. *International Conference on Electrical and Control Engineering*, pp.3499-3502.

Tong, W., Wu, S., An, Z. and Tang, R. (2010). Thermal analysis of direct-drive permanent magnet wind generator using both lumped parameter network and finite element method. *Asia-Pacific Power and Energy Engineering Conference*, pp.1-4.

Turek, L.J., Rini, D.P., Saarloos, B.A. and Chow, L.C. (2008). Evaporative spray cooling of power electronics using high temperature coolant. *11th Intersociety Conference on Thermal and Thermomechanical Phenomena in Electronic Systems*, 2, pp.346-351.

Villemeur, A. (1992). *Reliability, availability, maintainability and safety assessment*. John Wiley & Sons, UK.

Vlach, R., Grepl, R. and Krejci, P. (2005). Control of stator winding slot cooling by water using prediction of heating. In *Proceedings of International Conference on Mechatronics*, Japan, pp.1-5.

Wagner, J.M., Shamir, U., and Marks, D.H. (1988). *Water distribution reliability: simulation method*. ASCE, J. Water Resources Planning and Management.

Wang, H.Y., Su, P.S. and Wang, X.H. (2005). Calculation on the thermal field of the water cooling stator of three-gorge hydro-generator. *International Conference on Electrical Machines and Systems*, 3, pp.2231-2235.

Wildi, T. (2006). *Electrical machines, drives, and power systems.* 6th edition, New Jersey:Pearson Education.

Wolpert, T. (1982). The reliability of power and cooling systems. *Telecommunications Energy Conference*, pp. 181-186.

Wollf, D. (2009). Hydrogen for generator cooling – the pressure, purity and dewpoint difference. *11th Annual Electric and Power Conference & Exhibition*.

Wong, W.Y. (1977). *Heat transfer for engineers.* N.Y. Longman, White Plains.

Worden, J.A. and Mundulas, J.M. (2001). Understanding, diagnosing and repairing leaks in water-cooled generator stator winding. *GE Power Systems*, Schenectady, NY.

Yao, Y., Gu, L., Fan, T., Sun, W. and Luo, J. (2011). Evaluation of heat transfer characteristic of aluminum nitride (AlN) potting compound for the end windings of permanent magnet synchronous machines. *ICECE*.

Yu, Q., Laudensack, C. and Gerling, D. (2010). Improved lumped parameter thermal model and sensitivity analysis for SR drives. *International Conference on Electrical Machines*, pp.383-388.

Yuzwa, G.F. and Eng, P. (1990). Water treatment program for glycol systems. *ALBERTA Public Works*, Supply & Services.

Zhang, H.Y., Pinjala, D. and Poi-Siong Teo (2003). Thermal management of high power dissipation electronic packages: from air cooling to liquid cooling. *IEEE Electronics Packaging Technology Conference*, pp.620-625.

Zhe, H., Hui, G. and Guobiao, G. (2009). Review of liquid cooling technology for rotor of turbo generator and application research of open channel evaporative cooling technology. *IEEE Conference on Electrical Machines and Systems*, pp.1-4.

Zheng, P., Liu, R., Thelin, P., Nordlund, E., Sadarangani, C. and Mahkamov, K. (2008). Research on the cooling system of a 4QT prototype machine used for HEV. In *IEEE Transaction on Energy Conversation*, 23 (1), pp.61-67.

Zhenyu, L. and Huier, C. (2008). Multi-objective optimization design analysis of primary surface recuperator for microturbines. *Applied Thermal Engineering*, 28 (5-6), pp.601-610.

Zukauskas, A. (1972). Heat transfer from tubes in cross flow. *Advances in Heat Transfer*, 8.

Appendix A: CFD modelling of radial-flux permanent magnet synchronous machine (Chapter 3)

(a) 4 mm × 40 mm cooling duct with convection coefficient 5500 W/(m^2·K)

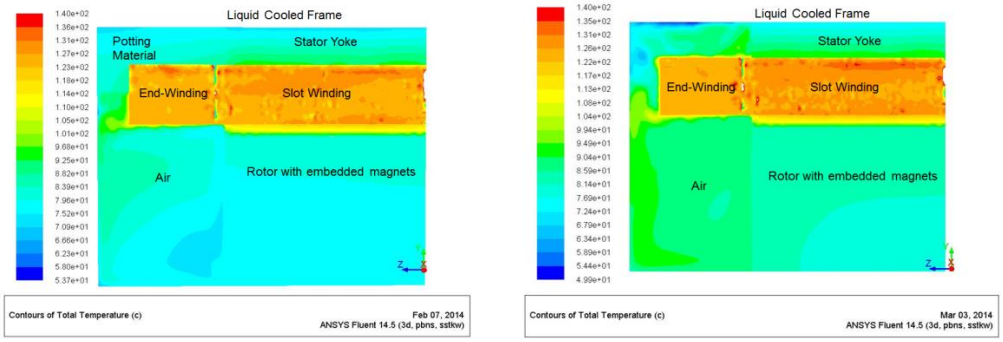

(b) 2 mm × 40 mm cooling duct with convection coefficient 10000 W/(m^2·K)

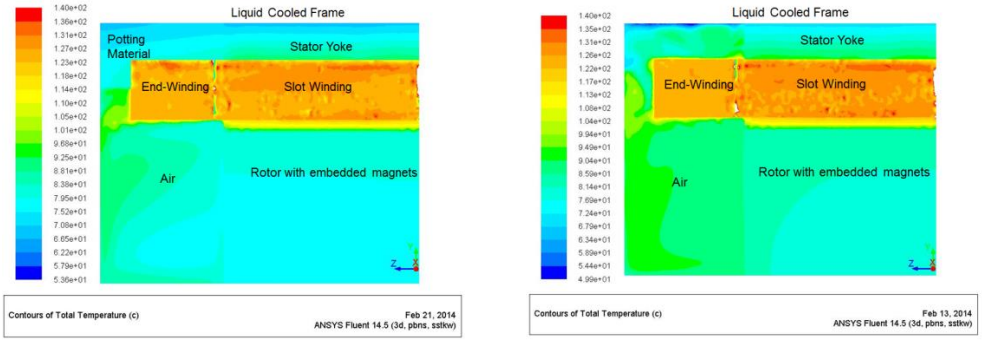

Figure A.1: Temperature distributions within machine parts for different performances of the liquid jacket.

(a) Temperature distribution within the machine parts and velocity field inside the machine (cooling systems are based on liquid jacket and potting material (upper part of the end winding is potted)).

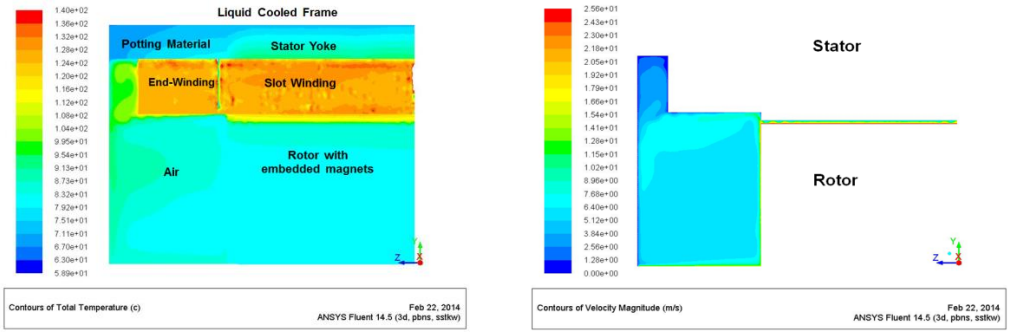

(b) Temperature distribution within the machine parts and velocity field inside the machine (cooling systems are based on a liquid jacket and potting material (half of the end-winding region is potted))

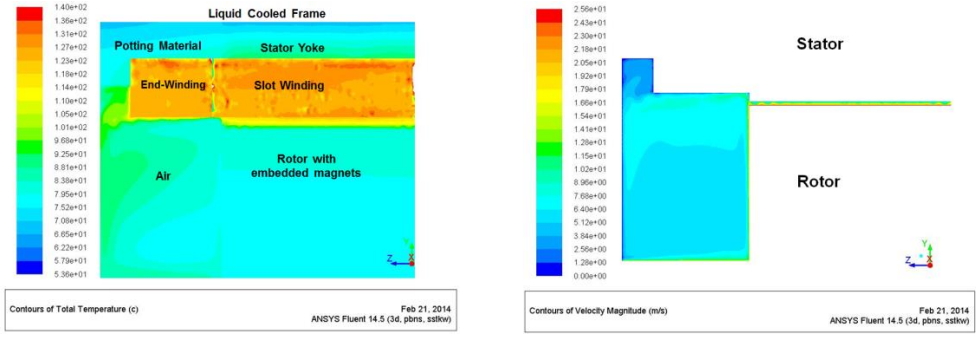

(c) Temperature distribution within machine parts and velocity field inside the machine (cooling systems are based on a liquid jacket and potting material (all the end-winding region is potted))

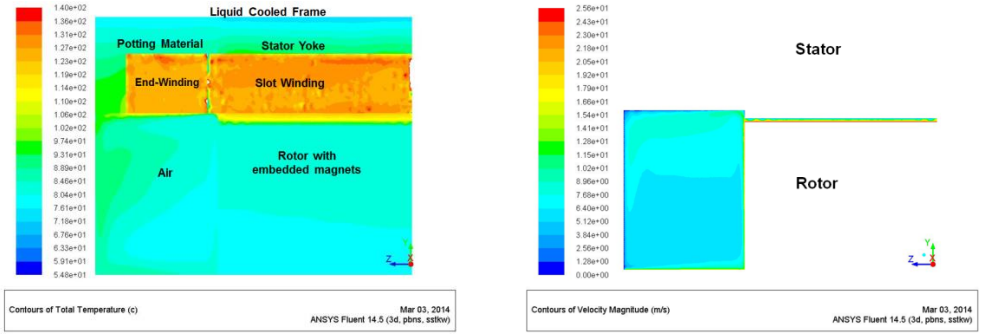

Figure A.2: Temperature distribution within machine parts.

Appendix B: Definition of thermal resistances for DD PMSG (Chapter 4)

Table B.1 Definition of the machine parameters

Parameter		Quantity
Stator Yoke Outer and Inner Radiuses	r_{styout} , r_{styin}	3.382 m, 3.342 m
Stator Slot Outer and Inner Radiuses	r_{stslout} , r_{stslin}	3.464 m, 3.382 m
Stator Tooth Outer and Inner Radiuses	r_{sttout} , r_{sttin}	3.464 m, 3.382 m
Rotor Yoke Outer and Inner Radiuses	r_{ryout} , r_{ryin}	3.545 m, 3.5 m
Magnets' Outer and Inner Radiuses	r_{rmagout} , r_{rmagin}	3.5 m, 3.472 m
Shaft Outer Radius	r_{sh}	1 m
Equivalent Winding Radius	$r_{\text{eqwind}} = \left(s_{\text{sl}}^2 / \pi \right)^2$	0.044 m
Stainless Steel Tube Radius	r_{sst}	0.00275 m
Length of Rotor and Stator	l_{r} , l_{st}	1.15 m
Length of End-Winding	l_{endw}	0.115 m
Length of End-Cap	l_{endcap}	0.1383 m
Length of Support Structure	l_{ss}	0.07 m
Number of Slots and Magnets	N_{sl}, N_{mag}	144, 120
Number of Conductors in Slot	N_{c}	20
Number of Support Structure Bars	N_{ss}	48
Width of Slot	W_{sl}	0.0742 m
Width of Stator Tooth	W_{stt}	0.0803 m
Width of Insulation	W_{ins}	0.00033 m
Width of Magnet	W_{rmag}	0.1708 m
Height of Magnet	h_{rmag}	0.028 m
Width of Support Structure Bars	W_{ss}	0.08 m
Diameter of Air Gap	D_{ag}	7.082 m
Diameter of Rotor	D_{r}	7.09 m
Cross-Section of Slot	s_{sl}	$4.9 \cdot 10^{-2}$ m
	Convection Coefficients	
Convection Coefficient between Fluid and Copper Winding (Eq. (2.6)-(2.9))	$\alpha_{\text{f/c}}$	10200 W/(m^{2}K)
Convection Coefficient in Air Gap (Eq. (4.18)-(4.21))	α_{ag}	53 W/(m^{2}K)
Convection Coefficient in between Stator and End-Cap Air (Eq. (4.16)-(4.17))	$\alpha_{\text{st/air}}$	17 W/(m^{2}K)
Convection Coefficient for Rotor Outer Surface and in between Rotor and End-Cap Air (Eq. (4.14)-(4.15))	$\alpha_{\text{ryout/amb}}$, $\alpha_{\text{r/air}}$	18 W/(m^{2}K), 33 W/(m^{2}K)
	Thermal Conductivities	
Thermal Conductivity of Steel Lamination in radial and axial directions	λ_{lam} , λ_{lama}	4.43 W/(m·K), 39 W/(m·K)
Thermal Conductivity of Steel Lamination in radial and axial directions	λ_{curad} , λ_{cu}	0.8 W/(m·K), 386 W/(m·K)
Thermal Conductivity of Insulation	λ_{ins}	0.26 W/(m·K)
Thermal Conductivity of Permanent Magnets	λ_{pm}	9 W/(m·K)
	Coefficients	
Lamination Stacking Factor	K	0.97
Hot-Spot To Mean Temperature Ratio	K_{w}	1.5
Radial Conductivity Factor	F_{r}	2.5
Filling Factor	F_{fil}	0.8

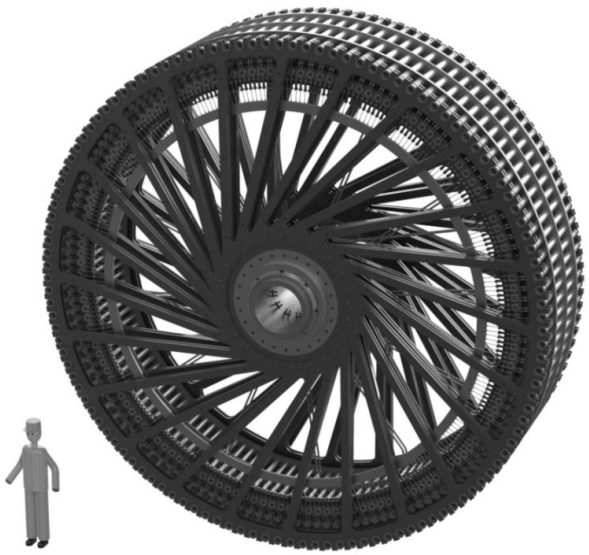

Figure B.1: Machine design.

Table B.2 Definition of the thermal resistances for LPTN

Parameter	Meaning of thermal resistance
$R_1 = \frac{1}{\alpha_{\mathrm{ryout/amb}} \cdot \pi \cdot r_{\mathrm{ryout}}^2 \cdot l_{\mathrm{r}}}$	Radial Resistance from Rotor Yoke to Ambient
$R_2 = \frac{(-1) \cdot \left(\left(r_{\mathrm{ryout}}^2 + r_{\mathrm{ryin}}^2 \right) - \frac{4 \cdot r_{\mathrm{ryin}}^2 \cdot r_{\mathrm{ryout}}^2 \cdot \ln\left(r_{\mathrm{ryout}} / r_{\mathrm{ryin}} \right)}{r_{\mathrm{ryout}}^2 - r_{\mathrm{ryin}}^2} \right)}{4 \cdot \pi \cdot \lambda_{\mathrm{lam}} \cdot l_{\mathrm{r}} \cdot \left(r_{\mathrm{ryout}}^2 - r_{\mathrm{ryin}}^2 \right)}$	Interconnecting Resistances of Rotor Yoke
$R_3 = \frac{D_{\mathrm{r}} \cdot \left(\frac{2 \cdot r_{\mathrm{ryout}}^2 \cdot \ln\left(r_{\mathrm{ryout}} / r_{\mathrm{ryin}} \right)}{r_{\mathrm{ryout}}^2 - r_{\mathrm{ryin}}^2} - 1 \right)}{2 \cdot \lambda_{\mathrm{lam}} \cdot l_{\mathrm{r}} \cdot K \cdot W_{\mathrm{rmag}} \cdot N_{\mathrm{mag}}}$,	Radial Resistances between Rotor Magnets and Rotor Yoke
$R_4 = \frac{D_{\mathrm{r}} \cdot \left(1 - \frac{2 \cdot r_{\mathrm{rmagin}}^2 \cdot \ln\left(r_{\mathrm{rmagout}} / r_{\mathrm{rmagin}} \right)}{r_{\mathrm{rmagout}}^2 - r_{\mathrm{rmagin}}^2} \right)}{2 \cdot \lambda_{\mathrm{pm}} \cdot l_{\mathrm{r}} \cdot N_{\mathrm{mag}} \cdot W_{\mathrm{rmag}}}$	

$$R_5 = \frac{\left(-D_r\right)\cdot\left(\left(r_{rmagout}^2 + r_{rmagin}^2\right) - \dfrac{4\cdot r_{rmagout}^2\cdot r_{rmagin}^2\cdot \ln\left(r_{rmagout}/r_{rmagin}\right)}{r_{rmagout}^2 - r_{rmagin}^2}\right)}{4\cdot\lambda_{pm}\cdot W_{rmag}\cdot l_r\cdot\left(r_{rmagout}^2 - r_{rmagin}^2\right)}$$

Interconnecting Resistances of Rotor Permanent Magnets

$$R_6 = \frac{D_r\left(\dfrac{2\cdot r_{ryout}^2\cdot\ln\left(r_{ryout}/r_{ryin}\right)}{r_{ryout}^2 - r_{ryin}^2} - 1\right)}{2\cdot\lambda_{lam}\cdot l_r\cdot K\cdot\left(\pi\cdot D_{ag} - \cdot N_{mag}\cdot W_{rmag}\right)},$$

$$R_7 = \frac{D_r}{\alpha_{ag}\cdot r_{ryin}\cdot l_r\cdot\left(\pi\cdot D_{ag} - \cdot N_{mag}\cdot W_{rmag}\right)}$$

Radial Resistances between Rotor Yoke and Air Gap

$$R_8 = \frac{D_r\cdot\left(1 - \dfrac{2\cdot r_{rmagout}^2\cdot\ln\left(r_{rmagout}/r_{rmagin}\right)}{r_{rmagout}^2 - r_{rmagin}^2}\right)}{2\cdot\lambda_{pm}\cdot l_r\cdot N_{rmag}\cdot\left(W_{rmag} + 2\cdot h_{rmag}\right)},$$

$$R_9 = \frac{D_r}{\alpha_{ag}\cdot r_{rmagin}\cdot l_r\cdot\left(W_{rmag} + 2\cdot h_{rmag}\right)\cdot N_{rmag}}$$

Radial Resistances between Rotor Magnets and Air Gap

$$R_{10} = \frac{D_{ag}}{\alpha_{ag}\cdot r_{sttout}\cdot l_{st}\cdot W_{stt}\cdot N_{sl}},\quad R_{11} = \frac{D_{ag}\cdot\left(1 - \dfrac{2\cdot r_{sttin}^2\cdot\ln\left(r_{sttout}/r_{sttin}\right)}{r_{sttout}^2 - r_{sttin}^2}\right)}{2\cdot\lambda_{lam}\cdot l_{st}\cdot K\cdot N_{sl}\cdot W_{stt}}$$

Radial Resistances between Tooth and Air Gap

$$R_{12} = \frac{D_{ag}}{\alpha_{ag}\cdot r_{stslout}\cdot l_{st}\cdot W_{sl}\cdot N_{sl}},\quad R_{13} = \frac{D_{ag}\cdot\left(1 - \dfrac{2\cdot r_{stslin}^2\cdot\ln\left(r_{stslout}/r_{stslin}\right)}{r_{stslout}^2 - r_{stslin}^2}\right)}{2\cdot\lambda_{curad}\cdot l_{st}\cdot N_{sl}\cdot W_{sl}}$$

Radial Resistances between Coils and Air Gap

$$R_{14} = \frac{W_{stt}\cdot\left(r_{sttout}^2 + r_{sttin}^2\right)}{\lambda_{lam}\cdot rK\cdot l_{st}\cdot D_{ag}\cdot N_{sl}\cdot\left(r_{sttout}^2 - r_{sttin}^2\right)}$$

$$R_{15} = \frac{2\cdot W_{ins}}{\pi\cdot\alpha_{ins}\cdot l_{st}\cdot r_{eqwind}\cdot N_{sl}} + \frac{1}{2\cdot\pi\cdot\alpha_{curad}\cdot l_{st}\cdot F_{rad}\cdot N_{sl}}$$

Radial Resistances between Tooth and Coils

$$R_{16} = \frac{\left(-D_{ag}\right)\cdot\left(\left(r_{sttout}^2 + r_{sttin}^2\right) - \dfrac{4\cdot r_{sttin}^2\cdot r_{sttout}^2\cdot\ln\left(r_{sttout}/r_{sttin}\right)}{r_{sttout}^2 - r_{sttin}^2}\right)}{4\cdot\lambda_{lam}\cdot W_{stt}\cdot l_{st}\cdot\left(r_{sttout}^2 - r_{sttin}^2\right)}$$

Interconnecting Resistances of Stator Tooth

$$R_{17} = \frac{\left(W_{sl} - D_{ag}\right)\left(r_{stslout}^2 + r_{stslin}^2\right)}{\lambda_{cu} \cdot N_{sl}^2 \cdot l_{st} \cdot D_{ag} \cdot W_{sl} \cdot \left(r_{stslout}^2 - r_{stslin}^2\right)},$$

Resistance between Coils and Coolant

$$R_{18} = \frac{2}{\alpha_{f/c} \cdot \pi \cdot D_{stt} \cdot l_{st} \cdot N_c \cdot N_{sl}}$$

$$R_{19} = \frac{D_{ag} \cdot \left(\frac{2 \cdot r_{stslout}^2 \cdot \ln\left(r_{stslout} / r_{stslin}\right)}{r_{stslout}^2 - r_{stslin}^2} - 1 \right)}{2 \cdot \lambda_{curad} \cdot l_{st} \cdot W_{sl} \cdot N_{sl}},$$

Radial Resistances between Coils and Stator Yoke

$$R_{20} = \frac{D_{ag} \cdot \left(1 - \frac{2 \cdot r_{styout}^2 \cdot \ln\left(r_{styout} / r_{styin}\right)}{r_{styout}^2 - r_{styin}^2} \right)}{2 \cdot \lambda_{lam} \cdot l_{st} \cdot K \cdot N_{sl} \cdot W_{sl}}$$

$$R_{21} = \frac{D_{ag} \cdot \left(\frac{2 \cdot r_{sttout}^2 \cdot \ln\left(r_{sttout} / r_{sttin}\right)}{r_{sttout}^2 - r_{sttin}^2} - 1 \right)}{2 \cdot \lambda_{lam} \cdot l_{st} \cdot K \cdot W_{stt} \cdot N_{sl}},$$

Radial Resistances between Tooth and Yoke

$$R_{22} = \frac{D_{ag} \cdot \left(1 - \frac{2 \cdot r_{styout}^2 \cdot \ln\left(r_{styout} / r_{styin}\right)}{r_{styout}^2 - r_{styin}^2} \right)}{2 \cdot \lambda_{lam} \cdot l_{st} \cdot K \cdot N_{sl} \cdot W_{stt}}$$

$$R_{23} = \frac{(-1) \cdot \left(\left(r_{styout}^2 + r_{styin}^2\right) - \frac{4 \cdot r_{styin}^2 \cdot r_{styout}^2 \cdot \ln\left(r_{styout} / r_{styin}\right)}{r_{sttout}^2 - r_{sttin}^2} \right)}{4 \cdot \pi \cdot \lambda_{lam} \cdot l_{st} \cdot \left(r_{styout}^2 - r_{styin}^2\right)}$$

Interconnecting Resistances of Stator Yoke

$$R_{24} = \frac{1}{\pi \cdot \alpha_{st} \cdot r_{styin} \cdot l_{st}}, \quad R_{25} = \frac{\left(\frac{2 \cdot r_{styout}^2 \cdot \ln\left(r_{styout} / r_{styin}\right)}{r_{styout}^2 - r_{styin}^2} - 1 \right)}{2 \cdot \pi \cdot \lambda_{lam} \cdot l_{st} \cdot K}$$

Radial Resistances between Stator Yoke and Air in Support Structure

$$R_{26} = \frac{1}{\pi \cdot \alpha_{r/air} \cdot r_{sh} \cdot l_{sh}}, \quad R_{27} = \frac{1}{4 \cdot \pi \cdot r_{sh} \cdot \lambda_{lam} \cdot l_{sh}}$$

Radial Resistances between Air in Support Structure and Shaft

$$R_{1a} = \frac{l_r}{6 \cdot \pi \cdot \lambda_{lama} \cdot \left(r_{ryout}^2 - r_{ryin}^2\right)},$$

$$R_{2a} = \frac{1}{\pi \cdot \alpha_{r/air} \cdot \left(r_{ryout}^2 - r_{ryin}^2\right)}$$

Axial Resistance between Rotor Yoke and End-Cap Air

$$R_{3a} = \frac{l_{st} \cdot D_{ag}}{6 \cdot N_{sl} \cdot \lambda_{lama} \cdot W_{stt} \cdot \left(r_{sttout}^2 - r_{sttin}^2\right)},$$

Axial Resistance between Tooth and End-Cap Air

$$R_{4a} = \frac{1}{\pi \cdot \alpha_{\text{stator/air}} \cdot \left(\left(r_{\text{styout}}^2 - r_{\text{styin}}^2 \right) - \left(N_{\text{sl}} \cdot s_{\text{sl}} \right) \right)}$$

$$R_{5a} = \frac{l_{\text{st}}}{6 \cdot \pi \cdot N_{\text{st}} \cdot \lambda_{\text{cu}} \cdot s_{\text{sl}} \cdot F_{\text{fil}}}, \; R_{6a} = \frac{l_{\text{endw}} \cdot K_{\text{w}}}{N_{\text{sl}} \cdot s_{\text{sl}} \cdot \lambda_{\text{cu}} \cdot F_{\text{fil}}}$$

Axial Resistance between Coils and End-Winding

$$R_{7a} = \frac{2}{\alpha_{\text{f/c}} \cdot \pi \cdot D_{\text{hole}} \cdot l_{\text{endw}} \cdot K_{\text{w}} \cdot N_{\text{c}} \cdot N_{\text{sl}}}, \quad R_{8a} = \frac{1}{\pi \cdot \alpha_{\text{stator/air}} \cdot \left(\left(r_{\text{styout}}^2 - r_{\text{styin}}^2 \right) \right)}$$

Resistance between End-Winding and Coolant

$$R_{8a} = \frac{\left(W_{\text{sl}} - D_{\text{hole}} \right) \cdot \left(r_{\text{styout}}^2 + r_{\text{styin}}^2 \right)}{\lambda_{\text{cu}} \cdot N_{\text{sl}}^2 \cdot l_{\text{endw}} \cdot K_{\text{w}} \cdot W_{\text{sl}} \cdot D_{\text{ag}} \cdot \left(r_{\text{styout}}^2 - r_{\text{styin}}^2 \right)}$$

$$R_{9a} = \frac{2 \cdot K_{\text{w}}}{16 \cdot \pi^2 \cdot \lambda_{\text{cuins}} \cdot F_{\text{r}} \cdot \left(r_{\text{stslout}} - r_{\text{stslin}} \right)},$$

Axial Resistance between End-Cap Air and End-Winding

$$R_{10a} = \frac{K_{\text{w}} \cdot \left(3.5 \cdot r_{\text{eqwind}} \right)^2}{8 \cdot \pi \cdot . l_{\text{endw}} \cdot \lambda_{\text{cuins}} \cdot F_{\text{r}} \cdot N_{\text{sl}} \cdot \left(r_{\text{eqwind}} \right)^2},$$

$$R_{11a} = \frac{1}{w \cdot \pi^2 \cdot \alpha_{\text{st/air}} \cdot N_{\text{sl}} \cdot r_{\text{endw}} \cdot \left(r_{\text{stslout}} - r_{\text{stslin}} \right)}$$

$$R_{12a} = \frac{l_{\text{r}}}{6 \cdot \pi \cdot \lambda_{\text{lama}} \cdot \left(r_{\text{styout}}^2 - r_{\text{styin}}^2 \right)}, \; R_{13a} = \frac{1}{\pi \cdot \alpha_{\text{r/air}} \cdot \left(r_{\text{styout}}^2 - r_{\text{styin}}^2 \right)}$$

Axial Resistance between Stator Yoke and End-Cap Air

$$R_{14a} = \frac{l_{\text{r}} \cdot 2 \cdot r_{\text{styin}}}{\lambda_{\text{lama}} \cdot \left(r_{\text{styout}}^2 - r_{\text{styin}}^2 \right) \cdot W_{\text{ss}} \cdot N_{\text{ss}}}, \; R_{15a} = \frac{l_{\text{r}} \cdot 2 \cdot r_{\text{styin}}}{0.5 \cdot \lambda_{\text{lam}} \cdot r_{\text{sh}}^2 \cdot W_{\text{ss}} \cdot N_{\text{ss}}}$$

Radial Resistance between Stator Yoke and Shaft

$$R_{16a} = \frac{l_{\text{r}} \cdot 2 \cdot r_{\text{ryin}}}{\lambda_{\text{lama}} \cdot \left(r_{\text{ryout}}^2 - r_{\text{ryin}}^2 \right) \cdot W_{\text{rss}} \cdot N_{\text{rss}}}, \; R_{17a} = \frac{l_{\text{r}} \cdot 2 \cdot r_{\text{ryin}}}{0.5 \cdot \lambda_{\text{lam}} \cdot r_{\text{sh}}^2 \cdot W_{\text{ss}} \cdot N_{\text{ss}}}$$

Radial Resistance between Stator Yoke and Shaft

For cooling Matrix

$$R_{\text{f}} = \frac{1}{\rho_{\text{f}} \cdot c_{\text{f}} \cdot \upsilon_{\text{f}} \cdot \pi \cdot r_{\text{sst}}^2 \cdot N_{\text{sl}}}$$

Thermal Resistance of Fluid Flow

$$R_{\text{ag}} = \frac{2}{\rho_{\text{air}} \cdot c_{\text{pair}} \cdot \upsilon_{\text{air}} \cdot \pi \cdot \left(r_{\text{rmag}}^2 - r_{\text{styout}}^2 \right)}$$

Thermal Resistance of Air Flow in Air Gap

$$R_{\text{air in ss}} = \frac{2}{\rho_{\text{air}} \cdot c_{\text{pair}} \cdot \upsilon_{\text{air}} \cdot \pi \cdot \left(r_{\text{styoutin}}^2 - r_{\text{sh}}^2 \right)}$$

Thermal Resistance of Air Flow in Support Structure

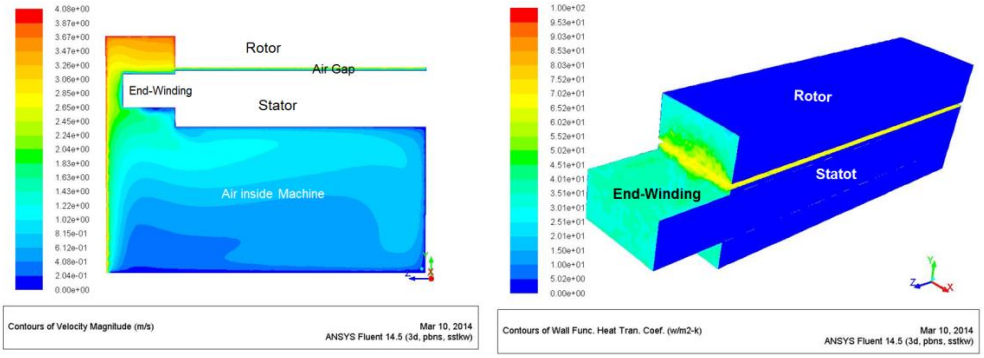

(a) (b)

Figure B.2: CFD models of the generator: velocity field in the air gap and support structure (a) and convection coefficient on the back surfaces (b).

Appendix C: Definition of thermal resistances for PMSM (Chapter 5)

Table C.1 Definition of the machine parameters

Parameter		Quantity
Frame Outer Radius	r_{frout}	0.195 m
Stator Yoke Outer and Inner Radiuses	r_{styout} , r_{styin}	0.190 m, 0.17 m
Stator Slot Outer and Inner Radiuses	$r_{stslout}$, r_{stslin}	0.17 m, 0.13 m
Stator Tooth Outer and Inner Radiuses	r_{sttout} , r_{sttin}	0.17 m, 0.13 m
Upper Rotor Yoke Outer and Inner Radiuses	$r_{upryout}$, r_{upryin}	0.127 m, 0.124 m
Magnets' Outer and Inner Radiuses	$r_{rmagout}$, r_{rmagin}	0.124 m, 0.112 m
Down Rotor Yoke Outer and Inner Radiuses	r_{dryout} , r_{dryin}	0.112 m, 0.091 m
Shaft Outer Radius	r_{sh}	0.05 m
Inlet Duct	$r_{inletduct}$	0.005 m
Equivalent Winding Radius	$r_{eqwind} = \left(s_{sl}^2 / \pi \right)^2$	0.0174 m
Length of Rotor and Stator	l_r , l_{st}	0.052 m
Length of End-Winding	l_{endw}	0.0234 m
Length of End-Cap	l_{endcap}	0.0273 m
Number of Slots and Magnets	N_{sl}, N_{mag}	18, 16
Width of Slot	W_{sl}	0.0238 m
Width of Stator Tooth	W_{stt}	0.0238 m
Width of Insulation	W_{ins}	0.00033 m
Width of Magnet	W_{rmag}	0.04 m
Width of Support Structure	W_{sup}	0.02 m
Diameter of Air Gap	D_{ag}	0.273 m
Diameter of Rotor	D_r	0.254 m
Cross-Section of Slot	s_{sl}	$8.971 \cdot 10^{-4}$ m
	Convection Coefficients	
Convection Coefficient between Frame and Outer Air (Eq. (2.2)-(2.5))	$\alpha_{frout/amb}$	3.7 W/(m^{2}K)
Convection Coefficient in Air Gap (Eq. (4.18)-(4.21))	α_{ag}	2100 W/(m^{2}K)
Convection Coefficient in between Stator and End-Cap Oil (Eq. (5.1)-(5.2))	$\alpha_{stator/oil}$	702 W/(m^{2}K)
Convection Coefficient in between Rotor and End-Cap Oil (Eq. (5.1)-(5.2))	$\alpha_{rotor/oil}$	1500-2000 W/(m^{2}K)
	Thermal Conductivities	
Thermal Conductivity of Aluminum	λ_{al}	237 W/(m·K)
Thermal Conductivity of Steel Lamination in radial and axial directions	λ_{lam} , λ_{lama}	4.43 W/(m·K), 39 W/(m·K)
Thermal Conductivity of Steel Lamination in radial and axial directions	λ_{curad} , λ_{cu}	0.7 W/(m·K), 386 W/(m·K)
Thermal Conductivity of Insulation	λ_{ins}	0.26 W/(m·K)
Thermal Conductivity of Permanent Magnets	λ_{pm}	9 W/(m·K)
	Coefficients	
Lamination Stacking Factor	K	0.97
Hot-Spot To Mean Temperature Ratio	K_w	1.5
Radial Conductivity Factor	F_r	2.5
Filling Factor	F_{fil}	0.63

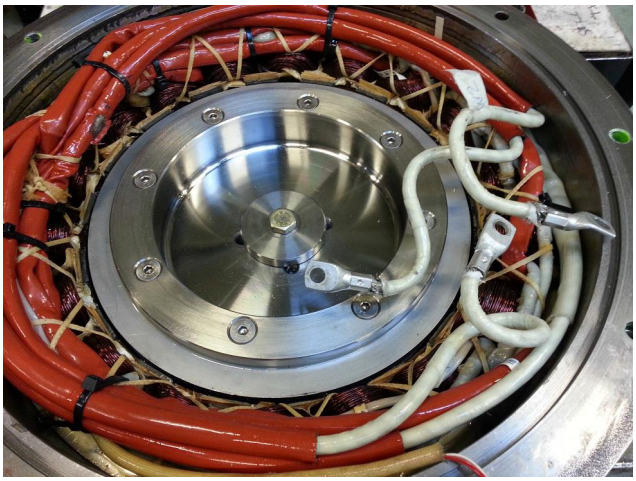

Figure C.1: Machine design (Ponomarev, 2013).

Table C.2 Definition of the thermal resistances for LPTN

Parameter	Meaning of thermal resistance
$R_1 = \frac{1}{\alpha_{\text{frout/amb}} \cdot \pi \cdot r_{\text{frout}}^2 \cdot l_r}$	Radial Resistance from Stator Frame to Ambient
$R_2 = \frac{\left(\frac{2 \cdot r_{\text{frout}}^2 \cdot \ln\left(r_{\text{frout}} / r_{\text{styout}} \right)}{r_{\text{frout}}^2 - r_{\text{styout}}^2} - 1 \right)}{2 \cdot \lambda_{\text{al}} \cdot l_{\text{st}}}$, $R_3 = \frac{\left(1 - \frac{2 \cdot r_{\text{stslout}}^2 \cdot \ln\left(r_{\text{styout}} / r_{\text{stslout}} \right)}{r_{\text{styout}}^2 - r_{\text{stslout}}^2} \right)}{2 \cdot \pi \cdot \lambda_{\text{lam}} \cdot l_{\text{st}} \cdot K}$	Radial Resistances between Stator Frame and Stator Yoke
$R_4 = \frac{(-1) \cdot \left(\left(r_{\text{styout}}^2 + r_{\text{styin}}^2 \right) - \frac{4 \cdot r_{\text{styin}}^2 \cdot r_{\text{styin}}^2 \cdot \ln\left(r_{\text{styout}} / r_{\text{styin}} \right)}{r_{\text{styout}}^2 - r_{\text{styin}}^2} \right)}{4 \cdot \pi \cdot \lambda_{\text{lam}} \cdot l_{\text{st}} \cdot \left(r_{\text{styout}}^2 - r_{\text{styin}}^2 \right)}$	Interconnecting Resistances of Stator Yoke
$R_5 = \frac{D_{\text{ag}} \cdot \left(\frac{2 \cdot r_{\text{styout}}^2 \cdot \ln\left(r_{\text{styout}} / r_{\text{styin}} \right)}{r_{\text{styout}}^2 - r_{\text{styin}}^2} - 1 \right)}{2 \cdot \lambda_{\text{lam}} \cdot l_{\text{st}} \cdot K \cdot N_{\text{sl}} \cdot W_{\text{sl}}}$	Radial Resistances between Stator Yoke and Coils
$R_6 = \frac{D_{\text{ag}} \cdot \left(1 - \frac{2 \cdot r_{\text{stslin}}^2 \cdot \ln\left(r_{\text{stslout}} / r_{\text{stslin}} \right)}{r_{\text{stslout}}^2 - r_{\text{stslin}}^2} \right)}{2 \cdot \lambda_{\text{curad}} \cdot l_{\text{st}} \cdot W_{\text{sl}} \cdot N_{\text{sl}}}$	

$$R_7 = \frac{D_{ag}\cdot\left(1-\frac{2\cdot r_{styout}^2\cdot\ln\left(r_{styout}/r_{styin}\right)}{r_{styout}^2-r_{styin}^2}-1\right)}{2\cdot\lambda_{lam}\cdot l_{st}\cdot K\cdot N_{sl}\cdot W_{stt}}$$

Radial Resistances between Stator Yoke and Stator Tooth

$$R_8 = \frac{D_{ag}\cdot\left(1-\frac{2\cdot r_{sttin}^2\cdot\ln\left(r_{sttout}/r_{sttin}\right)}{r_{sttout}^2-r_{sttin}^2}\right)}{2\cdot\lambda_{lam}\cdot l_{st}\cdot K\cdot W_{stt}\cdot N_{sl}}$$

$$R_9 = \frac{W_{stt}\cdot\left(r_{sttout}^2+r_{sttout}^2\right)}{\lambda_{lam}\cdot N_{sl}\cdot K\cdot D_{ag}\cdot l_{st}\cdot\left(r_{sttout}^2-r_{sttout}^2\right)},$$

Radial Resistances between Tooth and Coils

$$R_{10} = \frac{2\cdot W_{ins}}{\pi\cdot\lambda_{ins}\cdot l_{st}\cdot r_{eqwind}\cdot N_{sl}} + \frac{1}{2\cdot\pi\cdot\lambda_{curad}\cdot l_{st}\cdot F_{rad}\cdot N_{sl}}$$

$$R_{11} = \frac{\left(-D_{ag}\right)\cdot\left(\left(r_{sttout}^2+r_{sttin}^2\right)-\frac{4\cdot r_{sttin}^2\cdot r_{sttout}^2\cdot\ln\left(r_{sttout}/r_{sttin}\right)}{r_{sttout}^2-r_{sttin}^2}\right)}{4\cdot\lambda_{lam}\cdot W_{stt}\cdot l_{st}\cdot\left(r_{sttout}^2-r_{sttin}^2\right)}$$

Interconnecting Resistances of Stator Tooth

$$R_{12} = \frac{D_{ag}\cdot\left(\frac{2\cdot r_{stslout}^2\cdot\ln\left(r_{stslout}/r_{stslin}\right)}{r_{stslout}^2-r_{stslin}^2}-1\right)}{2\cdot\lambda_{curad}\cdot l_{st}\cdot N_{sl}\cdot W_{sl}} \quad R_{13} = \frac{D_{ag}}{\alpha_{ag}\cdot r_{stslin}\cdot l_{st}\cdot W_{sl}\cdot N_{sl}}$$

Radial Resistances between Coils and Air Gap (Oil in Air Gap)

$$R_{14} = \frac{D_{ag}\cdot\left(\frac{2\cdot r_{sttout}^2\cdot\ln\left(r_{sttout}/r_{sttin}\right)}{r_{sttout}^2-r_{sttin}^2}-1\right)}{2\cdot\lambda_{lam}\cdot l_{st}\cdot K\cdot N_{sl}\cdot W_{stt}} \quad R_{15} = \frac{D_{ag}}{\alpha_{ag}\cdot r_{sttin}\cdot l_{st}\cdot W_{stt}\cdot N_{sl}}$$

Radial Resistances between Stator Tooth and Air Gap (Oil in Air Gap)

$$R_{16} = \frac{D_r}{h_{ag}\cdot r_{upryup}\cdot l_r\cdot\pi}, \quad R_{17} = \frac{D_{ag}\cdot\left(1-\frac{2\cdot r_{upryin}^2\cdot\ln\left(r_{ryout}/r_{upryin}\right)}{r_{upryout}^2-r_{upryin}^2}\right)}{2\cdot\pi\cdot\lambda_{lam}\cdot l_r\cdot K}$$

Radial Resistances between Upper Rotor Yoke and Air Gap (Oil in Air Gap)

$$R_{18} = \frac{(-1)\cdot\left(\left(r_{upryout}^2+r_{upryin}^2\right)-\frac{4\cdot r_{upryin}^2\cdot r_{upryout}^2\cdot\ln\left(r_{upryout}/r_{upryin}\right)}{r_{upryout}^2-r_{upryin}^2}\right)}{4\cdot\pi\cdot\lambda_{lam}\cdot l_r\cdot\left(r_{upryout}^2-r_{upryin}^2\right)}$$

Interconnecting Resistances of Upper Rotor Yoke

$$R_{19}=\frac{D_r\cdot\left(\frac{2\cdot r_{upryout}^2\cdot\ln\left(r_{upryout}/r_{upryin}\right)}{r_{upryout}^2-r_{upryin}^2}-1\right)}{2\cdot\lambda_{lam}\cdot l_r\cdot K\cdot W_{rmag}\cdot N_{mag}},$$

Radial Resistances between Upper Rotor Yoke and Rotor Embedded Magnets

$$R_{20}=\frac{D_r\cdot\left(1-\frac{2\cdot r_{rmagin}^2\cdot\ln\left(r_{rmagout}/r_{rmagin}\right)}{r_{rmagout}^2-r_{rmagin}^2}\right)}{2\cdot\lambda_{pm}\cdot l_r\cdot W_{rmag}\cdot N_{mag}}$$

$$R_{21}=\frac{\left(-D_r\right)\cdot\left(\left(r_{rmagout}^2+r_{rmagin}^2\right)-\frac{4\cdot r_{rmagout}^2\cdot r_{rmagin}^2\cdot\ln\left(r_{rmagout}/r_{rmagin}\right)}{r_{rmagout}^2-r_{rmagin}^2}\right)}{4\cdot\lambda_{pm}\cdot W_{rmag}\cdot l_r\cdot\left(r_{rmagout}^2-r_{rmagin}^2\right)}$$

Interconnecting Resistances of Rotor Permanent Magnets

$$R_{22}=\frac{D_r\cdot\left(\frac{2\cdot r_{upryout}^2\cdot\ln\left(r_{upryout}/r_{upryin}\right)}{r_{upryout}^2-r_{upryin}^2}-1\right)}{2\cdot\lambda_{lam}\cdot l_r\cdot K\cdot\left(\pi\cdot D_r-2\cdot W_{rmag}\cdot N_{rmag}\right)},$$

Radial Resistances between Upper Rotor Yoke and Down Rotor Yoke

$$R_{23}=\frac{D_r\cdot\left(1-\frac{2\cdot r_{dryin}^2\cdot\ln\left(r_{dryout}/r_{dryin}\right)}{r_{dryout}^2-r_{dryin}^2}\right)}{2\cdot\lambda_{lam}\cdot l_r\cdot K\cdot\left(\pi\cdot D_r-2\cdot W_{rmag}\cdot N_{rmag}\right)}$$

$$R_{24}=\frac{\left(-1\right)\cdot\left(\left(r_{dryout}^2+r_{dryin}^2\right)-\frac{4\cdot r_{dryin}^2\cdot r_{dryout}^2\cdot\ln\left(r_{dryout}/r_{dryin}\right)}{r_{dryout}^2-r_{dryin}^2}\right)}{4\cdot\pi\cdot\lambda_{lam}\cdot l_r\cdot\left(r_{dryout}^2-r_{dryin}^2\right)}$$

Interconnecting Resistances of Down Rotor Yoke

$$R_{25}=\frac{D_r\cdot\left(\frac{2\cdot r_{rmagout}^2\cdot\ln\left(r_{rmagout}/r_{rmagin}\right)}{r_{rmagout}^2-r_{rmagin}^2}-1\right)}{2\cdot\lambda_{pm}\cdot l_r\cdot W_{rmag}\cdot N_{rmag}}$$

Radial Resistances between Rotor Embedded Magnets and Down Rotor Yoke

$$R_{26}=\frac{D_r\cdot\left(1-\frac{2\cdot r_{dryin}^2\cdot\ln\left(r_{upryout}/r_{upryin}\right)}{r_{upryout}^2-r_{upryin}^2}\right)}{2\cdot\lambda_{lam}\cdot l_r\cdot K\cdot W_{rmag}\cdot N_{rmag}},$$

$$R_{27} = \frac{D_r \cdot \left(\frac{2 \cdot r_{dryin}^2 \cdot \ln\left(r_{dryout} / r_{dryin} \right)}{r_{dryout}^2 - r_{dryin}^2} - 1 \right)}{2 \cdot \lambda_{lam} \cdot l_r \cdot K \cdot W_{sup}}, \quad R_{28} = \frac{D_r}{4 \cdot W_{sup} \cdot \lambda_{lama} \cdot l_r \cdot r_{sh}}$$

Radial Resistances between Down Rotor Yoke and Shaft

$$R_{31a} = \frac{1}{\pi \cdot \alpha_{stator/oil} \cdot 4 \cdot r_{styout} \cdot l_{endcap}}$$

Axial Resistance between Frame and End-Cap Oil

$$R_{1a} = \frac{l_{st}}{6 \cdot \pi \cdot \lambda_{lama} \cdot \left(r_{styout}^2 - r_{styin}^2 \right)}, \quad R_{2a} = \frac{1}{\pi \cdot \alpha_{stator/oil} \cdot \left(r_{styout}^2 - r_{styin}^2 \right)}$$

Axial Resistance between Stator Yoke and End-Cap Oil

$$R_{3a} = \frac{l_{st} \cdot D_{ag}}{6 \cdot N_{sl} \cdot \lambda_{lama} \cdot W_{stt} \cdot \left(r_{sttout}^2 - r_{sttin}^2 \right)},$$

Axial Resistance between Stator Teeth and End-Cap Oil

$$R_{4a} = \frac{1}{\pi \cdot \alpha_{stator/oil} \cdot \left(\left(r_{styout}^2 - r_{styin}^2 \right) - \left(N_{sl} \cdot s_{sl} \right) \right)}$$

$$R_{5a} = \frac{l_{st}}{6 \cdot \pi \cdot \lambda_{cu} \cdot N_{sl} \cdot s_{sl} \cdot F_{fil}}, \quad R_{6a} = \frac{l_{endw} \cdot K_w}{\lambda_{cu} \cdot N_{sl} \cdot s_{sl} \cdot F_{fil}}$$

Axial Resistance between Coils and End-Winding

$$R_{7a} = \frac{2 \cdot K_w}{16 \cdot \pi^2 \cdot \lambda_{cuins} \cdot F_r \cdot \left(r_{stslout} - r_{stslin} \right)},$$

Axial Resistance between End-Cap Oil and End-Winding

$$R_{8a} = \frac{K_w \cdot \left(3.5 \cdot r_{eqwind} \right)^2}{8 \cdot \pi \cdot l_{endw} \cdot \lambda_{cuins} \cdot F_r \cdot N_{sl} \cdot \left(r_{eqwind} \right)^2},$$

$$R_{9a} = \frac{1}{w \cdot \pi^2 \cdot \alpha_{stator/air} \cdot N_{sl} \cdot r_{endw} \cdot \left(r_{stslout} - r_{stslin} \right)}$$

$$R_{10a} = \frac{l_r}{6 \cdot \pi \cdot \lambda_{lama} \cdot \left(r_{upryout}^2 - r_{upryin}^2 \right)}, \quad R_{11a} = \frac{1}{\pi \cdot \alpha_{rotor/oil} \cdot \left(r_{upryyout}^2 - r_{upryin}^2 \right)}$$

Axial Resistance between Upper Rotor Yoke and End-Cap Oil

$$R_{12a} = \frac{l_r}{6 \cdot \pi \cdot \lambda_{lama} \cdot \left(r_{rmagout}^2 - r_{ryin}^2 \right)}, \quad R_{11a} = \frac{1}{\pi \cdot \alpha_{rotor/oil} \cdot \left(r_{rmagout}^2 - r_{rmagin}^2 \right)}$$

Axial Resistance between Rotor Yoke and End-Cap Air

$$R_{14a} = \frac{l_r}{6 \cdot \pi \cdot \lambda_{lama} \cdot \left(r_{dryout}^2 - r_{dryin}^2 \right)}, \quad R_{11a} = \frac{1}{\pi \cdot \alpha_{rotor/oil} \cdot \left(r_{drout}^2 - r_{drin}^2 \right)}$$

Axial Resistance between Down Rotor Yoke and End-Cap Oil

For Cooling Matrix

$$R_f = \frac{1}{\rho_f \cdot c_f \cdot \upsilon_f \cdot \pi \cdot r_{inletduct}^2}$$

Thermal Resistance of Fluid Flow (Oil)

ACTA UNIVERSITATIS LAPPEENRANTAENSIS

555. HEINONEN, JARI. Chromatographic recovery of chemicals from acidic biomass hydrolysates. 2013. Diss.

556. HELLSTÉN, SANNA. Recovery of biomass-derived valuable compounds using chromatographic and membrane separations. 2013. Diss.

557. PINOMAA, ANTTI. Power-line-communication-based data transmission concept for an LVDC electricity distribution network – analysis and implementation. 2013. Diss.

558. TAMMINEN, JUSSI. Variable speed drive in fan system monitoring. 2013. Diss.

559. GRÖNMAN, KAISA. Importance of considering food waste in the development of sustainable food packaging systems. 2013. Diss.

560. HOLOPAINEN, SANNA. Ion mobility spectrometry in liquid analysis. 2013. Diss.

561. NISULA, ANNA-MAIJA. Building organizational creativity – a multitheory and multilevel approach for understanding and stimulating organizational creativity. 2013. Diss.

562. HAMAGUCHI, MARCELO. Additional revenue opportunities in pulp mills and their impacts on the kraft process. 2013. Diss.

563. MARTIKKA, OSSI. Impact of mineral fillers on the properties of extruded wood-polypropylene composites. 2013. Diss.

564. AUVINEN, SAMI. Computational modeling of the properties of TiO2 nanoparticles. 2013. Diss.

565. RAHIALA, SIRPA. Particle model for simulating limestone reactions in novel fluidised bed energy applications. 2013. Diss.

566. VIHOLAINEN, JUHA. Energy-efficient control strategies for variable speed controlled parallel pumping systems based on pump operation point monitoring with frequency converters. 2014. Diss.

567. VÄISÄNEN, SANNI. Greenhouse gas emissions from peat and biomass-derived fuels, electricity and heat – Estimation of various production chains by using LCA methodology. 2014. Diss.

568. SEMYONOV, DENIS. Computational studies for the design of process equipment with complex geometries. 2014. Diss.

569. KARPPINEN, HENRI. Reframing the relationship between service design and operations: a service engineering approach. 2014. Diss.

570. KALLIO, SAMULI. Modeling and parameter estimation of double-star permanent magnet synchronous machines. 2014. Diss.

571. SALMELA, ERNO. Kysyntä-toimitusketjun synkronointi epävarman kysynnän ja tarjonnan toimintaympäristössä. 2014. Diss.

572. RIUNGU-KALLIOSAARI, LEAH. Empirical study on the adoption, use and effects of cloud-based testing. 2014. Diss.

573. KINNARINEN, TEEMU. Pressure filtration characteristics of enzymatically hydralyzed biomass suspensions. 2014. Diss.

574. LAMMASSAARI, TIMO. Muutos kuntaorganisaatiossa – tapaustutkimus erään kunnan teknisestä toimialasta. 2014. Diss.

575. KALWAR, SANTOSH KUMAR. Conceptualizing and measuring human anxiety on the Internet. 2014. Diss.

576. LANKINEN, JUKKA. Local features in image and video processing – object class matching and video shot detection. 2014. Diss.

577. AL-SAEDI, MAZIN. Flexible multibody dynamics and intelligent control of a hydraulically driven hybrid redundant robot machine. 2014. Diss.

578. TYSTER, JUHO. Power semiconductor nonlinearities in active d*u*/d*t* output filtering. 2014. Diss.

579. KERÄNEN, JOONA. Customer value assessment in business markets. 2014. Diss.

580. ALEXANDROVA, YULIA. Wind turbine direct-drive permanent-magnet generator with direct liquid cooling for mass reduction. 2014. Diss.

581. HUHTALA, MERJA. PDM system functions and utilizations analysis to improve the efficiency of sheet metal product design and manufacturing. 2014. Diss.

582. SAUNILA, MINNA. Performance management through innovation capability in SMEs. 2014. Diss.

583. LANA, ANDREY. LVDC power distribution system: computational modelling. 2014. Diss.

584. PEKKARINEN, JOONAS. Laser cladding with scanning optics. 2014. Diss.

585. PELTOMAA, JYRKI. The early activities of front end of innovation in OEM companies using a new FEI platform as a framework for renewal. 2014. Diss.

586. ROZHANSKY, IGOR. Resonant tunneling effects in semiconductor heterostructures. 2014. Diss.

587. PHAM, THUY DUONG. Ultrasonic and electrokinetic remediation of low permeability soil contaminated with persistent organic pollutants. 2014. Diss.

588. HOKKANEN, SANNA. Modified nano- and microcellulose based adsorption materials in water treatment. 2014. Diss.

589. HINKKANEN, JUHA. Cooperative strategy in emerging markets – analysis of interfirm R&D cooperation and performance in Russian manufacturing companies. 2014. Diss.

590. RUSKOVAARA, ELENA. Entrepreneurship education in basic and upper secondary education – measurement and empirical evidence. 2014. Diss.

591. IKÄHEIMONEN, TUULI. The board of directors as a part of family business governance – multilevel participation and board development. 2014. Diss.

592. HAJIALI, ZUNED. Computational modeling of stented coronary arteries. 2014. Diss.

593. UUSITALO, VILLE. Potential for greenhouse gas emission reductions by using biomethane as road transportation fuel. 2014. Diss.

594. HAVUKAINEN, JOUNI. Biogas production in regional biodegradable waste treatment – possibilities for improving energy performance and reducing GHG emissions. 2014. Diss.

595. HEIKKINEN, JANNE. Vibrations in rotating machinery arising from minor imperfections in component geometries. 2014. Diss.

596. GHALAMCHI, BEHNAM. Dynamic analysis model of spherical roller bearings with defects. 2014. Diss.